Development and Application of Saturable Absorbers to Femtosecond Solid-State Laser Mode-Locking

by

Rohit Prativadi Prasankumar

B.S.E.E., University of Texas at Austin (1997)
M.S. Massachusetts Institute of Technology (1999)

Submitted to the Department of Electrical Engineering and Computer Science In Partial Fulfillment of the Requirements for the Degree of

Doctor of Philosophy

at the

Massachusetts Institute of Technology

June 2003

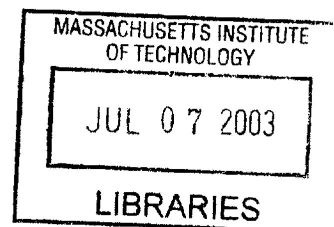
MASSACHUSETTS INSTITUTE OF TECHNOLOGY
JUL 07 2003
LIBRARIES

©2003 Massachusetts Institute of Technology
All Rights Reserved

Signature of Author ______
Department of Electrical Engineering and Computer Science
May 23, 2003

Certified by ______
James G. Fujimoto
Professor of Electrical Engineering
Thesis Supervisor

Accepted by ______
Arthur C. Smith
Chairman, Departmental Committee on Graduate Studies

BARKER

Development and Application of Saturable Absorbers to Femtosecond Solid-State Laser Mode-Locking

by

Rohit Prativadi Prasankumar

Submitted to the Department of Electrical Engineering and Computer Science on May 23, 2003
in Partial Fulfillment of the Requirements for the Degree of Doctor of Philosophy

ABSTRACT

Semiconductor saturable absorbers have had a major impact on the field of ultrashort pulse generation by increasing the stability and reliability of ultrashort pulse lasers, making them more useful in many applications. These versatile devices can be grown both epitaxially with molecular beam epitaxy and non-epitaxially using RF sputtering. In this thesis, the development and application of both types of saturable absorbers to self-starting mode-locking in solid-state lasers was examined.

The first part of this thesis describes the use of an epitaxially grown saturable Bragg reflector to mode-lock an extended cavity femtosecond Cr:LiSAF laser. Inexpensive single mode diodes were used as a pump source and a multi-pass cavity was used to lower the laser repetition rate. Pulses with durations of 39 fs and energies of 0.75 nJ were generated at an 8.6 MHz repetition rate. These pulse energies and durations are comparable to those produced from commercially available Ti:sapphire lasers that have a significantly higher cost.

The second part of this thesis explored the further development and application of non-epitaxially grown semiconductor-doped silica films. A novel pump-probe system with independent pump and probe wavelength tunability from 700 to 1000 nm and a time resolution of 17 fs was developed for device characterization. The linear and nonlinear optical properties of InAs-doped silica films deposited by RF sputtering were characterized as a function of fabrication parameters, including nanocrystallite size, pump and probe wavelength relative to the absorption edge, and rapid thermal annealing temperature. Guidelines for the optimization of semiconductor-doped silica films for saturable absorber applications were extracted from the experimental data. Large nanocrystallites, high annealing temperatures, and an operating wavelength close to the absorption edge were found to optimize saturable absorber performance, with a low saturation fluence of 640 $\mu J/cm^2$ obtained at 1.54 μm. These saturable absorber devices were then designed to self-start mode-locking in a Cr:forsterite laser, obtaining self-starting 25 fs pulses with 91 nm bandwidth at 1.3 μm. These versatile devices can be designed for any solid-state laser system using the guidelines developed in this work and have the potential to replace epitaxially grown saturable absorbers in many applications.

Thesis Supervisor: Professor James G. Fujimoto
Title: Professor of Electrical Engineering and Computer Science

Acknowledgments

It is hard to believe that I am finally writing this section of my thesis, after reading so many other "acknowledgments" sections over the years I have been here at MIT and wondering what I would say when I finally wrote mine. Many people have helped me along the way and deserve thanks for their assistance and support, and at this point I'm afraid I will forget people, so please accept my apologies in advance.

I would first like to thank my thesis advisor, Professor James Fujimoto. I have learned how to do science from him and his influence will have a lasting impact on my career. I have been fortunate to work in his laboratory from the beginning of my graduate school education and can safely say that I have learned more every year I have been here. I would also like to thank Professor Franz Kaertner for his many helpful suggestions and ideas during the course of my thesis work as well as his willingness to always give them regardless of how busy he was. Thanks go to Professor Mildred Dresselhaus for serving on my thesis committee and taking the time to go over my thesis in great detail, offering many improvements along the way. I would also like to thank Professor Erich Ippen for much helpful advice over the years, and Professor Herman Haus for his help as well as for serving on both of my qualifying exam committees. Thanks also go to Cindy Kopf, Mary Aldridge, Donna Gale, and Dorothy Fleischer for keeping all the administrative activities of the group running smoothly during the most stressful times.

I would like to thank Dr. Jim Walpole and Leo Misaggia who gave me much assistance at Lincoln Labs and were always willing to spend time working with me. It was a pleasure to collaborate with Professor Michael Ruane at Boston University and his insight and advice was always appreciated. Thanks also go to Paul Mak, whose skill and knowledge of the sputtering and annealing systems at BU averted many problems and saved me many wasted afternoons. I would also like to thank Dr. Wayne Knox for providing the SBR samples used in the Cr:LiSAF work.

I have been very lucky to work with many talented postdocs and graduate students who have helped me both in and out of the lab during my years here and have provided many fond memories of my time at MIT. Igor Bilinsky introduced me to the lab and gave me a great start in research work. I was very fortunate to learn from him during my first projects here. Boris Golubovic, Steve Boppart, Xingde Li, Wolfgang Drexler, Uwe Morgner, and Costas Pitris were also very helpful in the first few years here and I enjoyed working with them. Seong-Ho Cho gave me lots of assistance in the lab and was always available and willing to answer my questions.

I would like to thank Ingmar Hartl and Christian Chudoba for teaching me the finer details of pump-probe and autocorrelation measurements and also for lots of help with the saturable absorber work. Thanks also go to Kaoru Minoshima for helping me with organizing my trip to Japan as well as for helpful advice. It was always very helpful to talk to Thomas Schibli and discuss his many insights and ideas. It was a pleasure to collaborate with Stephane Bourquin on measuring pump-probe signals using his detector. Thanks also go to Yasu Hirakawa for his work on the Cr:LiSAF project. I would also like to thank Alphan Sennaroglu for helpful advice and insights, and I admire his desire to work on and ability to get results out of the Cr:forsterite laser system which has caused me many hours of frustration.

I would like to thank Pei-lin Hsiung, John Fini, Juliet Gopinath, Juhi Chandalia, and Aurea Zare for being great officemates and somehow managing to put up with my incessant drumming on things for many years. We had many interesting discussions that were always a nice diversion from the daily grind of lab work. Drew Kowalevicz shared many late nights in the lab with me before CLEO deadlines, and it was a pleasure to work with him and figure out things together. I would also like to thank Ravi Ghanta, Aaron Aguirre, Paul Herz, Tony Ko, and Desmond Adler for many good times and discussions in and out of the lab. I wish Vikas Sharma and Aurea Zare luck in continuing all the laser work in our group and thank them for their help with the latter stages of my projects. Thanks also go to Matt Grein for lots of good discussions about after-graduation plans and how UT-Austin is a much better school than A&M, and Dan Ripin for sharing the pain of working with Cr:based lasers. I would also like to thank the other members of the optics group, including Erik Thoen, Onur Kuzucu, Felix Grawert, Jason Sickler,

Peter Rakich, Charles Yu, Rebecca Younkin, Leaf Jiang, Kazi Abedin, and Hanfei Shen for their camaraderie.

Outside of the lab, all the friends I met and became close to during graduate school are all very much appreciated for helping me relax and take my mind off lab work, and making all the fun times and great memories we had together possible. I would also like to thank all my teachers throughout my educational career for inspiring and helping me along the way.

This section would not be complete without acknowledging my parents. They served to motivate me to explore the limits of what I could achieve when I was younger, and were always there when I needed them throughout the years. This accomplishment would not be possible without their love and support. My brother has also always supported me during all sorts of ups and downs, and been there to ground me and provide a realistic perspective on things as well as to help me relax and have fun playing video games on ancient Nintendo systems late at night. My sister's boundless energy and her million stories about all the exciting things going on in her life were always a welcome distraction from lab frustrations as well, and her courage in facing adversity has amazed me. I would also like to thank my aunt, uncle, grandmother, and cousins in New Hampshire for providing a home away from home and a place to get some real food whenever I needed it. Thanks also go to my family in India, San Francisco, and Australia for always expressing their pride for my smallest accomplishment during my years in school.

Finally, I would like to thank my fiancé, Anu, for all her love and support during the last few years of this thesis. It seems like an incredibly fortuitous series of coincidences that led to the beginning of our relationship a few summers ago, for which I would like to thank my good friend and future brother-in-law Sameer for persisting through all sorts of adversity in his attempts to win his wife's love and therefore get me introduced to his sister-in-law. I don't really know where to start in expressing how much I have learned from Anu about the things that are important in life. Her caring, thoughtfulness, courage, and strength have set a high standard for me to aspire to. My life has been enriched by her and I hope to give back to her even a small amount of the happiness she has given me during the rest of our lives together.

Table of Contents

Chapter 1

Introduction 18

Chapter 2

Laser mode-locking 23

2.1 Introduction 23

2.2 Passive mode-locking with slow and fast saturable absorbers 27

2.3 Self phase modulation 29

2.4 Dispersion 32

2.5 Gain filtering 34

2.6 The master equation for fast saturable absorber mode-locking 34

2.7 Kerr lens mode-locking 39

2.8 Self-starting mode-locked operation 42

2.9 Soliton mode-locking 44

2.10 Saturable absorbers for laser mode-locking 46

2.10.1 Modulation depth and non-saturable loss 47

2.10.2 Absorption saturation intensity and fluence 48

2.10.3 Absorption saturation recovery time 51

2.10.5 Wavelength dependence and other characteristics 53

2.11 Design of a mode-locked laser 55

2.11.1 Four mirror cavity 55

2.11.2 Dispersion compensation using prism pairs 59

2.11.3 Dispersion compensation using double-chirped mirrors 60
2.11.4 Optimization of laser cavities for Kerr lens mode-locking 64

2.12 Pulse measurement 69

Chapter 3

Previous Work on Semiconductor Saturable Absorbers and Diode-Pumped Solid-State Lasers 75

3.1 Introduction 75

3.2 Epitaxially grown semiconductor saturable absorbers 76
3.2.1 General principles of epitaxially grown saturable absorber design 76
3.2.2 High finesse A-FPSA 77
3.2.3 AR-coated SESAM 80
3.2.4 Low-finesse A-FPSA (SBR) 81
3.2.5 Broadband SESAMs 82
3.2.6 Semiconductor saturable absorbers for Cr:forsterite and Cr:LiSAF 83
3.2.7 Summary of previous work on epitaxially grown semiconductor saturable absorbers 84

3.3 Non-epitaxially grown semiconductor saturable absorbers 85
3.3.1 Semiconductor-doped glass structures 85
3.3.2 Semiconductor-doped silica film saturable absorbers 87

3.4 Diode-pumped solid state lasers 92

Chapter 4

An extended cavity femtosecond Cr:LiSAF laser mode-locked with an epitaxially grown saturable absorber 100

4.1 Introduction 100

4.2 Laser properties of Cr:LiSAF 101

4.3 Diode pump source design **103**

4.4 Operation of the Cr:LiSAF laser in a four mirror cavity **107**

4.5 Design of a multi-pass cavity for increasing laser pulse energies **110**

4.6 Saturable Bragg reflector design **120**

4.7 Mode-locked operation of the extended cavity Cr:LiSAF laser with and without prisms **122**

Chapter 5

Fabrication and characterization of semiconductor-doped silica film saturable absorbers **127**

5.1 Introduction **127**

5.2 Optical properties of semiconductor quantum dots **129**

5.2.1 Energy states in bulk semiconductors 129

5.2.2 Energy levels and linear absorption of quantum dots 131

5.2.3 Nonlinear optical properties of quantum dots 137

5.3 Experimental setup-fabrication **142**

5.3.1 RF sputtering system 142

5.3.2 Photolithography 145

5.3.3. Rapid thermal annealing 146

5.4 Pump-probe spectroscopy **146**

5.4.1 General principles 146

5.4.2 Novel pump-probe system with independent pump and probe wavelength tunability from 700 to 1000 nm 150

5.4.3 Pump-probe systems operating at 1.26 and 1.5 microns 156

5.5 Linear and nonlinear optical characterization of semiconductor-doped silica film saturable absorbers **157**

5.5.1 Linear transmission measurements 157

5.5.2 Pump-probe measurements on films with different InAs/SiO_2 ratios........................161
5.5.3 Wavelength dependence of the saturation fluence..163
5.5.4 Fluence-dependent pump-probe measurements at 1.54 μm.......................................166
5.5.5 Pump-probe measurements at 1.26 μm...168
5.5.6 Effect of RTA temperature variance on absorption saturation dynamics..................169
5.5.7 Effect of other fabrication parameters on absorption saturation dynamics................173

5.6 X-ray diffraction measurements on semiconductor-doped silica film saturable absorbers...........175

5.7 Fast dephasing times in semiconductor nanocrystallites and their effect on the saturation fluence...........177

5.8 Guidelines for the design of non-epitaxially grown semiconductor-doped silica films saturable absorbers...........182

Chapter 6

Self-starting mode-locking in a Cr:forsterite laser using non-epitaxially grown semiconductor-doped silica films...........185

6.1 Introduction...........185

6.2 Cr:forsterite laser system...........186

6.3 Transmissive saturable absorber device design...........187

6.4 Laser cavity design...........189

6.5 Self-starting Kerr lens mode-locking...........191

Chapter 7

Conclusion...........198

Appendix A

RF sputtering procedure...204

Appendix B

Optics used in the Cr:LiSAF laser 207

References...209

List of Figures and Tables

Figure 2-1. Intensity as a function of time for N=4 (gray) and N=10 (black) phase-locked modes. 25

Figure 2-2. Active mode-locking in the time domain 26

Figure 2-3. Pulse formation with slow saturable absorber mode-locking........ 28

Figure 2-4. Pulse formation with fast saturable absorber mode-locking (from ref [50])........ 29

Figure 2-5. (a) Electric field of a Gaussian pulse envelope with a carrier frequency defined by equation (2.8). (b) Electric field of the pulse in (a) after propagating through a Kerr medium and undergoing self-phase modulation 31

Figure 2-6. (a) Chirp, (b) pulse duration, (c) stability, and (d) bandwidth plotted as functions of the dispersion........ 36

Figure 2-7. Schematic of Kerr-lens mode-locking with a soft aperture........ 41

Figure 2-8. Nonlinear absorption change with increasing intensity........ 49

Figure 2-9. Nonlinear absorption change of a saturable absorber as a function of pulse fluence. 50

Table 2-1. Summary of the ideal characteristics of a saturable absorber........ 54

Figure 2-10. Schematic of a z-fold cavity. 56

Figure 2-11. Calculated beam waist size as a function of *b* for a symmetric four mirror cavity.57

Figure 2-12. Calculated beam waist size as a function of *b* for an asymmetric four mirror cavity. 58

Figure 2-13. Dispersion compensation using a prism pair........ 59

Figure 2-14. (a) Standard Bragg high reflector structure. (b) Single chirped mirror structure. (c) Double chirped mirror structure........ 61

Figure 2-15. Reflectivity and group delay of chirped mirrors. The upper portion is the enlarged top part of the reflectivity. The dotted curves display the reflectivity and group delay of a chirped mirror. The dashed curve shows the result for a double chirped mirror with a linear chirp of the thickness of the high index layers. The solid curve shows the result for a double chirped mirror with a quadratic chirp of the high index layer thickness........ 63

Figure 2-16. Contour lines of the Kerr-lens sensitivity (parameter of the curves) in (a) the tangential plane and (b) the sagittal plane as functions of b, the distance between the curved

mirrors, and a, the distance from M1 to the crystal as defined in figure 2-10, for a symmetric cavity with $d_1=d_2=85$ cm 65
Figure 2-17. Same as in figure 2-16, for an asymmetric cavity with $d_1=50$ cm and $d_2=110$ cm. 67
Figure 2-18. Schematic of an interferometric autocorrelator. 70
Figure 2-19. Schematic of a non-collinear, background-free intensity autocorrelator. 72
Figure 3-1. Schematic of a typical Z cavity incorporating a saturable absorber (SA) with a focusing mirror (CM2) with curved mirrors CM1 to focus the light into the crystal and an output coupler OC. 77
Figure 3-2. Different SESAM designs in historical order. (a) High-finesse A-FPSA. (b) AR-coated SESAM. (c) Low-finesse A-FPSA, or SBR 79
Figure 3-3. Schematic of the Ti:sapphire laser cavity used in demonstration of self-starting mode-locking with non-epitaxially grown saturable absorbers. 86
Figure 3-4. Linear absorption measurement of the InAs-doped silica films. 88
Figure 3-5. Compositional maps of an InAs-doped silica film taken with STEM. The image sizes are 80 by 80 nm. BF: bright field image; O:oxygen; As:arsenic; In:indium 89
Figure 3-6. Absorption saturation dynamics of InAs-doped silica films for different annealing temperatures. 90
Figure 3-7. Autocorrelation (a) and spectrum (b) of self-starting pulses from a KLM Ti:sapphire laser incorporating an InAs-doped silica film saturable absorber. 91
Figure 3-8. Schematic of the diode-pumped KLM Cr:LiSGAF laser (from [175]). 96
Figure 3-9. Schematic of the compact, single mode diode-pumped Cr:LiSAF laser (from [131]). 98
Table 4-1. Physical and optical properties of some common solid-state laser crystals 102
Table 4-2. Diode beam sizes measured in the tangential and sagittal planes using a ThorLabs beam profiler. 104
Figure 4-1. Schematic of the diode pump source. 105
Table 4-3. Measured beam radius for each diode in the tangential and sagittal planes at a distance of 5.4 cm from M1. 105
Figure 4-2. Absorption and emission cross sections for Cr:LiSAF for the electric field polarized both parallel (top plot) and perpendicular (lower plot) to the crystal axis at a temperature of 295 K. 106

Figure 4-3. Schematic of the x cavity Cr:LiSAF laser. 107

Figure 4-4. Measured transmission of the ARO high reflecting mirrors used in the Cr:LiSAF laser cavity. (a) Full scale. (b) Close up of the reflectivity. The transmission is <0.1% from 785-935 nm. 108

Figure 4-5. Measured transmission of the output coupler used in the Cr:LiSAF laser cavity. The transmission is <1.5% from 818-895 nm. 108

Figure 4-6. Schematic of a multi-pass cavity with four bounces on each mirror. The beam is introduced and extracted through notches in the mirrors 112

Figure 4-7. Possible unit cells for the unity q transformation in an MPC. The cavity is unfolded, representing the mirrors with lenses, and the reference planes are depicted with vertical lines. 112

Figure 4-8. Schematic of the MPC used in this work.. 114

Figure 4-9. Calculation of the mirror separation for the flat-curved mirror cavity as a function of n, for different values of m.. 116

Figure 4-10. Calculation of the repetition rate for the flat-curved mirror cavity as a function of n, for different values of m. 116

Figure 4-11. (a) Reflectivity of the DCMs used in the Cr:LiSAF laser. The step in the data at 800 nm is due to a detector change. This figure shows the high reflectivity bandwidth of these DCMs. (b) Calculated and measured dispersion of the DCMs (obtained from V. Scheuer). 118

Figure 4-12. Schematic of the extended cavity Cr:LiSAF laser.. 120

Figure 4-13. Device structure (a) and reflectivity bandwidth (b) of the SBR [128]. 120

Figure 4-14. Schematic of the x cavity Cr:LiSAF laser with an SBR..................................... 121

Figure 4-15. Experimental setup of the extended cavity femtosecond Cr:LiSAF laser............ 122

Figure 4-16. Autocorrelation (a) and spectrum (b) of the extended cavity Cr:LiSAF laser using prisms for dispersion compensation. The output power in this configuration was 5.5 mW at an 8.4 MHz repetition rate, resulting in pulse energies of 0.66 nJ. 123

Figure 4-17. Autocorrelation (a) and spectrum (b) of the extended cavity Cr:LiSAF laser using only DCMs for dispersion compensation. The output power in this configuration is 6.5 mW at an 8.6 MHz repetition rate, resulting in pulse energies of 0.75 nJ. 124

Figure 4-18. Mode-locked and cw output power of the extended cavity Cr:LiSAF laser as a function of (a) D1 pump power, with D2 and D3 held constant at a total power of 90 mW, (b) D2 pump power, with D1 and D3 held constant at a total power of 90 mW, and (c) D3 pump power, with D1 and D2 held constant at a total power of 90 mW. The mode-locked slope efficiency is 12.8% for D1, 11.6% for D2, and 8.3% for D3. 125

Figure 5-1. Density of states $g^{0d}(\varepsilon)$ for a quantum dot compared to the bulk density of states $g^{3d}(\varepsilon)$ 133

Figure 5-2. Schematic depiction of spectral hole burning: (a) The absorption of the semiconductor before (solid line) and after (dashed line) the pump pulse. (b) The absorption change calculated from (a) 138

Figure 5-3. Calculated effect of band-gap renormalization. The curve labeled "1" shows the absorption of the semiconductor before high intensity optical excitation; the peaks are due to exciton absorption. The curve labeled "2" depicts the absorption after pulsed excitation and clearly shows the shift of the band gap to lower energies due to band gap renormalization, along with the disappearance of the excitonic peaks 139

Figure 5-4. RF sputtering system.. 143

Figure 5-5. Schematic of the sputtering target used to deposit InAs-doped silica films............ 144

Figure 5-6. Schematic of the 5.4 fs Ti:sapphire laser described in ref. [90]. 151

Figure 5-7. (a) Spectrum and (b) autocorrelation of the 5.4 fs Ti:sapphire laser.. 152

Figure 5-8. Schematic of the pump-probe system with independent pump and probe wavelength tunability from 700-1000 nm. 152

Figure 5-9. Prism compressor used to select spectral components within the 700-1000 nm bandwidth of the Ti:sapphire output spectrum.. 153

Figure 5-10. Cross-correlation of the independently wavelength tunable pump-probe system based on a ultrashort pulse Ti:sapphire laser, measured by phase-matched second harmonic generation in a 100 μm BBO crystal. 155

Figure 5-11. Linear transmission measurement before annealing of a 150 nm thick 10%InAs/90% SiO_2 film deposited on a sapphire substrate. 158

Figure 5-12. Comparison of semiconductor-doped silica films with different InAs/SiO_2 ratios. The absorption edge shifts to longer wavelengths with increasing InAs/SiO_2 ratio........... 160

Figure 5-13. Linear transmission measurement of 150 nm thick 10% InAs/90% SiO_2 films annealed at different temperatures for 60 seconds in nitrogen.. 161

Figure 5-14. Degenerate pump-probe measurements at 800 nm on InAs-doped silica films with different InAs/SiO_2 ratios. The black lines show the results of fitting the data with exponential or double exponential functions, and the relaxation time constants are labeled for each curve.. 162

Figure 5-15. Degenerate pump probe measurement of a 10% InAs/90% SiO_2 film as a function of wavelength, showing a decrease in saturation fluence with excitation closer to the absorption edge. 163

Figure 5-16. Tunable degenerate pump-probe measurements at wavelengths of 1.54 μm, 1.48 μm, and 1.43 μm on a 40% InAs/60% SiO_2 film.. 165

Figure 5-17. Fluence-dependent pump-probe measurement at 1.54 μm on the 40% InAs/60% SiO_2 film with the transmission curve shown in figure 5-12... 167

Figure 5-18. Degenerate pump-probe measurement at 1.26 μm of the 40% InAs/60% SiO_2 film with the transmission curve shown in figure 5-12. 168

Figure 5-19. Degenerate pump probe measurement of a 150 nm thick 10% InAs/90% SiO_2 film at 800 nm as a function of rapid thermal anneal temperature. Discrete changes in the dynamics as a function of annealing temperature are observed.. 170

Figure 5-20. Degenerate pump probe measurement of a 150 nm thick 10% InAs/90% borosilicate glass film at 800 nm as a function of RTA temperature. The absorption saturation dynamics change continuously as a function of RTA temperature.................. 172

Figure 5-21. X-ray diffraction measurement of 10% InAs/90% SiO_2 films annealed at different temperatures for 60 seconds in nitrogen; the nonlinear optical properties of these films are shown in figure 5-19 175

Figure 6-1. Linear transmission of the 40% InAs/60% SiO_2 films used in Cr:forsterite laser mode-locking experiments 188

Figure 6-2. Pump-probe measurement at 1.26 μm on a thin 40% InAs/60% SiO_2 film used for mode-locking a Cr:forsterite laser.. 189

Figure 6-3. (a) Reflectivity of the DCMs used in the Cr:forsterite laser. The reflectivity is greater than 99.8% from 1.1 to 1.5 μm. (b) Group delay dispersion of the Cr:forsterite crystal, PBH71 prisms, and DCMs, plotted with the total intracavity dispersion.............. 190

Figure 6-4. Schematic diagram of Cr:forsterite laser with additional fold 191

Figure 6-5. Interferometric autocorrelation (a) and spectrum (b) of self-starting KLM in Cr:forsterite using non-epitaxially grown InAs-doped silica films. Self-starting 25 fs pulses with a bandwidth of 91 nm were generated. 192

Figure 6-6. Intensity autocorrelations at different dispersion operating points for saturable absorber mode-locking without KLM. The peak intensity of the longer background pulse decreases as the negative dispersion increases... 194

Figure 6-7. Spectra at different dispersion operating points for saturable absorber mode-locking without KLM.. 194

Figure 6-8. Measured mode-locking build-up time for pure saturable absorber mode-locking with large negative dispersion.. 195

Chapter 1
Introduction

The ability to produce ultrashort pulses with durations shorter than 100 femtoseconds (fs) has led to many fascinating advances in science and technology. These include the generation of radiation at extreme wavelengths in the x-ray [1-3] and terahertz [4] regimes, frequency metrology [5, 6], biomedical imaging [7, 8], optical communications [9, 10], ultrafast carrier dynamics [11], coherent control [12], and attosecond pulse metrology [13-16]. These applications all benefit from one or more of the unique properties of femtosecond pulses including short time duration, large optical bandwidth, and high peak intensity. Ultrashort pulse technology has advanced to the point where pulses shorter than one femtosecond [13-15], bandwidths comparable to the optical carrier frequency [17], and intensities comparable to those at the core of stars [18] can be generated with laboratory scale, tabletop systems. A better feeling for the time scales involved can be obtained by noting that one femtosecond compares to one second as 5 minutes compares to the age of the universe.

Since the first proposal [19] and subsequent demonstration [20] of the laser, the many applications of laser technology have spurred research in this field. The first demonstration of mode-locking in a helium-neon laser generated nanosecond pulses [21], and subsequent efforts generated picosecond (ps) pulses from solid-state lasers including ruby and Nd:YAG [22, 23]. The narrow gain bandwidth of these materials limited pulse durations to a few tens of ps. The development and mode-locking of dye lasers [24] resulted in the generation of the first femtosecond pulses [25], and eventually pulses as short as 6 fs were generated from a mode-locked dye laser [26]. However, dye lasers are inconvenient to operate, since the dyes degrade and therefore must be continuously circulated, and the dyes are also often toxic and carcinogenic. Tunable vibronic solid-state lasers based on materials such as Ti:sapphire [27, 28], revolutionized ultrashort pulse generation. These crystals have broad gain and absorption bandwidths due to their vibrationally broadened energy states. Ultrashort pulse generation in solid-state lasers was accomplished by the discovery of Kerr lens mode-locking (KLM) in

Ti:sapphire [29], demonstrating a method that has been used to generate sub-100 fs pulses from several different solid-state laser systems, covering much of the visible and near-infrared frequency range.

Recent advances have enabled the routine generation of 10 fs pulses from the Ti:sapphire laser, which has become the workhorse of the ultrashort pulse laser industry. KLM has been employed to generate pulses as short as 5 fs directly from the Ti:sapphire laser oscillator [17]. Pulse compression techniques have been used external to the laser cavity to generate the shortest sub-5 fs optical pulses [30, 31]. In this regime, effects sensitive to the relative phase between the carrier and envelope of an optical pulse, such as high harmonic generation [32] and above threshold ionization [33, 34], can be observed and controlled [35], culminating in the recent generation of trains of attosecond pulses [13-15].

These many applications necessitate the further development of reliable, inexpensive femtosecond lasers, both for experiments for which the relatively low pulse energies (picojoules to nanojoules) directly from the laser oscillator are sufficient and also to serve as the seed oscillator for amplified systems producing pulses with high energies (microjoules-joules) and ultrashort durations. Semiconductor saturable absorbers are a recently developed technology that provides an intensity-dependent absorption for passive mode-locking of solid-state lasers [36-38]. These devices are typically grown by molecular beam epitaxy (MBE) and consist of one or more quantum wells grown in a mirror structure. Semiconductor saturable absorbers have several advantages: they make mode-locking more stable and insensitive to perturbations, simplify laser cavity alignment, and often provide self-starting operation. Semiconductor saturable absorbers have been used alone to generate sub-100 fs pulses in several laser systems, and with soliton-like pulse shaping have generated pulses as short as 13 fs in a Ti:sapphire laser [39]. They have also been used in conjunction with KLM to generate self-starting pulses as short as 5.5 fs from Ti:sapphire [40]. Sub-100 fs pulses have also been generated from other laser systems with semiconductor saturable absorbers, including Cr:LiSAF [41], Cr:LiSGAF [42], Cr:forsterite [43], and Cr:YAG [44].

In this thesis, the development and application of semiconductor saturable absorbers to femtosecond solid-state laser mode-locking was explored. The presented work can be logically divided into two major parts. The first part focuses on the application of an epitaxially grown saturable absorber to mode-locking a Cr:LiSAF laser pumped by inexpensive single spatial mode diodes. The goal of this work was to develop a femtosecond laser source with pulse energies and durations comparable to those of standard Ti:sapphire systems, which have pump sources that are nearly two orders of magnitude more expensive.

The second part of this work extended previous work on the development of non-epitaxially grown saturable absorbers based on semiconductor nanocrystallites doped into silica films that were deposited by RF sputtering on sapphire substrates. Non-epitaxial growth overcomes many of the limitations of epitaxially grown devices, including lattice matching constraints that limit the choice of materials and device design, bandwidth limitations, and the high cost and complexity of MBE systems. These devices were previously used to self-start KLM assisted 25 fs pulses from a Ti:sapphire laser [45, 46]. In this thesis, methods for reducing the high saturation fluence of these devices, which limits pulse generation, were investigated. The linear and nonlinear optical properties as well as the structural properties were characterized while varying fabrication parameters in an attempt to extract trends aiding in device optimization. The guidelines developed from these experiments were used to develop devices for mode-locking a Cr:forsterite laser.

The organization of this thesis is as follows:

Chapter 2 provides a detailed background on the principles of laser mode-locking. Passive mode-locking techniques and pulse shaping mechanisms are discussed in detail. The desired properties of saturable absorbers are also described. Finally, a description of important issues in mode-locked laser design is given.

Chapter 3 describes previous research on semiconductor saturable absorbers. Epitaxially grown saturable absorbers and their different designs and applications are reviewed, as well as non-epitaxially grown saturable absorbers based on bulk semiconductor-doped glasses and

semiconductor-doped silica films. Previous work on diode-pumped solid-state lasers of the colquirite family (Cr:LiSAF, Cr:LiSGAF, and Cr:LiCAF) is also described to provide background on the Cr:LiSAF laser developed as part of this thesis.

Chapter 4 describes the development of an extended cavity femtosecond Cr:LiSAF laser pumped by low cost single spatial mode diodes. The design of the key elements that make this novel laser possible, in particular the diode pump source, saturable Bragg reflector (SBR), and multi-pass cavity (MPC), is detailed. Ultrashort pulse generation using dispersion compensation with prisms and also in a prismless cavity using double-chirped mirrors (DCMs) is described, and the lasing threshold and slope efficiencies as a function of various combinations of the pump diodes are also measured.

Chapter 5 describes the characterization of semiconductor-doped silica film saturable absorbers. It starts with an overview of the linear and nonlinear optical properties of semiconductors, in particular semiconductor quantum dots. The fabrication techniques of RF sputtering and rapid thermal annealing are discussed. The pump-probe method used to measure nonlinear optical properties is explained and the development of a novel pump-probe system based on a broad bandwidth Ti:sapphire laser is described. Experiments characterizing the nonlinear optical properties of the semiconductor-doped silica films as functions of the pump and probe wavelengths, nanocrystallite size, rapid thermal annealing temperature, and other fabrication parameters are presented. The results of x-ray diffraction measurements performed on the films as a function of annealing temperature are also presented. An explanation for the high saturation fluence of these films, based on the fast dephasing time in semiconductor nanocrystallites, is discussed. Finally, guidelines for saturable absorber optimization based on the experimental results presented in this chapter are given.

Chapter 6 discusses the design and application of a semiconductor-doped silica film to self-starting mode-locking in a Cr:forsterite laser. The guidelines developed in chapter 5 are applied to design a semiconductor-doped silica film with a minimized saturation fluence at the lasing wavelength. Linear transmission and pump-probe measurements of the film used in laser mode-locking are described. The pulse durations and bandwidths generated from applying the

saturable absorber to self-starting KLM in Cr:forsterite are also presented. Further experiments on self-starting pure saturable absorber mode-locking as well as optimizing the pulse duration for self-starting KLM will also be discussed.

Chapter 7 summarizes the results presented in this thesis and proposes future research based on this work.

Appendix A details the RF sputtering procedure used in film fabrication. Appendix B lists the optics used in the Cr:LiSAF laser cavity.

Chapter 2
Laser mode-locking

2.1 Introduction

Mode-locking is the most widely used method of ultrashort pulse generation, enabling the generation of pulses down to two cycles in duration. The term mode-locking refers to the description of this process in the frequency domain as the phase locking of many axial modes simultaneously oscillating in the laser cavity. This can be understood by describing the correspondence between the output of a laser in the frequency and time domains [47]. In the time domain, the steady state electric field $E(t)$ periodically repeats itself in each pass through the laser cavity, ending at the output coupler. This can be represented by

$$E^N(t) = \sum_{n=0}^{N-1} E(t - nT_R) \tag{2.1}$$

Here N is the number of passes through the cavity and T_R is the cavity round trip time, given by $2L/c$, where L is the cavity length and c is the speed of light. For large N, this can also be represented by [48]

$$E^N(t) = E(t) \otimes \sum_{n=0}^{\infty} \delta(t - nT_R). \tag{2.2}$$

The Fourier transform of this function into the frequency domain results in

$$E^N(\omega) = \frac{2\pi}{T_R} E(\omega) \sum_{n=0}^{\infty} \delta(\omega - n\frac{2\pi}{T_R}) \tag{2.3}$$

where $E(\omega)$ is the Fourier transform of $E(t)$ with ω the frequency. From this expression, it can be seen that the laser spectrum is a series of axial frequency modes spaced by $\omega_{ax}=2\pi/T_R$. Normally, the relative phases of these modes are unsynchronized and vary randomly in time, resulting in continuous wave (cw) laser operation with the energy concentrated within a few modes around the gain peak. This produces an approximately constant output power. Locking

the relative phases of the modes causes them to constructively interfere at a certain point in the cavity, resulting in an intense light pulse. As the mode amplitudes change with time, the point in the cavity at which they constructively interfere changes and the pulse propagates through the cavity. This can be seen from the following simple analysis. The laser field can be represented as the superposition of axial frequency modes with varying amplitudes and phases,

$$E(z,t)=\sum_{n=0}^{N-1} E_n e^{i((\omega_0+n\omega_{ax})t-k_n z+\varphi_n)}\ , \tag{2.4}$$

where φ_n is the phase, ω_0 is the center frequency, and E_n is the amplitude of a given mode. If the axial modes are assumed to have the same amplitude (E_n=1 for simplicity) and phase (let φ_n=0), then their output can be described as

$$E(z,t)=\sum_{n=0}^{N-1} e^{i((\omega_0+n\omega_{ax})t-k_n z)}=\frac{e^{iN\omega_{ax}(t-z/c)}-1}{e^{i\omega_{ax}(t-z/c)}-1}e^{i\omega_0(t-z/c)}\ , \tag{2.5}$$

for $k_n=\dfrac{\omega_0+n\omega_{ax}}{c}$, and the intensity for z=0 is given by

$$I(t)=\left|E(t)\right|^2=\frac{\sin^2[N\omega_{ax}(t-z/c)/2]}{\sin^2[\omega_{ax}(t-z/c)/2]} \tag{2.6}$$

Figure 2-1 illustrates the temporal intensity profile for N=4 and N=10 modes locked in phase in a standard solid state laser cavity. This shows that the modes constructively interfere to produce a pulse train spaced by the round trip time $T_R=2\pi/\omega_{ax}$=10 ns. The inverse of the round trip time is the pulse repetition rate $f_{rep}=1/T_R=c/2L$=100 MHz. It is clear that as the number of locked modes increases, the pulse duration gets shorter and the pulse peak intensity increases. The pulse duration can be approximated by $\tau=T_R/N$, implying that as more modes are phase-locked, the pulse duration gets shorter. In most mode-locked laser systems the gain bandwidth of the laser limits the number of axial modes that can be locked together and therefore sets a lower bound on the pulse duration. For a typical Ti:sapphire laser, the gain bandwidth spans ~350 nm, implying a minimum pulse duration of about 2.7 fs or one optical cycle. A typical ultrashort pulse has a bandwidth of about 100 nm, or ~50 THz, implying that ~500,000 modes are phase-locked for a 100 MHz Ti:sapphire laser.

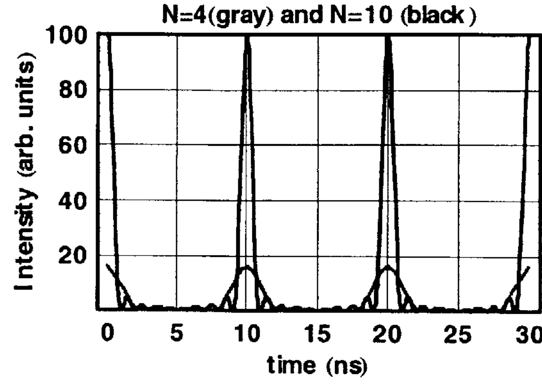

Figure 2-1. Intensity as a function of time for N=4 (gray) and N=10 (black) phase-locked modes.

These ultrashort optical pulses formed by the superposition of many axial modes are most often described in the time domain by the slowly varying envelope approximation. This represents the electric field in terms of a sinusoidal carrier wave modulated by an envelope that changes very slowly compared to the fast modulations in the carrier wave. This can be derived by simplifying equation (2.4)

$$E(z,t) = e^{i\omega_0(t-z/c)} \sum_{n=0}^{N-1} E_n e^{i(n\omega_{ax}(t-z/c)+\varphi_n)}, \tag{2.7}$$

and with the envelope given by $A(t - z/c) = \sum_{n=0}^{N-1} E_n e^{i(n\omega_{ax}(t-z/c)+\varphi_n)}$,

then

$$E(z,t) = A(t - z/c)e^{i\omega_0(t-z/c)}. \tag{2.8}$$

This expression is also a solution of Maxwell's wave equation. This description of an ultrashort optical pulse has been shown to be valid down to pulse durations of one optical cycle [34]. It should be noted that the peak of the electric field can be offset from the peak of the envelope and effects due to this "carrier-envelope phase" become significant for few cycle pulses [34, 49]. This is represented by

$$E(z,t) = A(t - z/c)e^{i(\omega_0(t-z/c)+\varphi)}, \tag{2.9}$$

where φ is the carrier-envelope phase. This phase factor does not affect the amplitude or spacing of the axial modes in the frequency domain and therefore was not explicit in equations (2.4)-(2.8). The carrier-envelope phase is due to the difference between phase and group velocities in the laser cavity and therefore changes from pulse to pulse. This manifests itself in the frequency

domain as an offset of the frequency comb from integer multiples of the repetition rate. Recent research has demonstrated control of the pulse-to-pulse change in phase, which has implications in both the time and frequency domains. A detailed discussion of this is beyond the scope of this thesis; the interested reader is referred to references [34] and [5].

Although the above discussion has mostly focused on the frequency domain representation, mode-locking is usually easier to analyze in the time domain using the carrier-envelope formalism. Mode-locking can be viewed in the time domain as a periodic modulation of the intracavity gain or loss that generates short pulses. This can be accomplished with both active and passive techniques. Active mode-locking relies on an intracavity modulator to change the cavity loss at a frequency synchronized to the cavity round trip time. This was used in the first demonstration of mode-locking [21]. In the time domain, the modulator introduces a periodic loss modulation into the cavity at frequency f_m equal to the cavity repetition rate *c/2L*, creating a short modulation window during which the loss is less than the gain (figure 2-2). However, once the pulse is shorter than this window, it cannot decrease further in duration, and therefore the pulse duration is limited by the modulator speed.

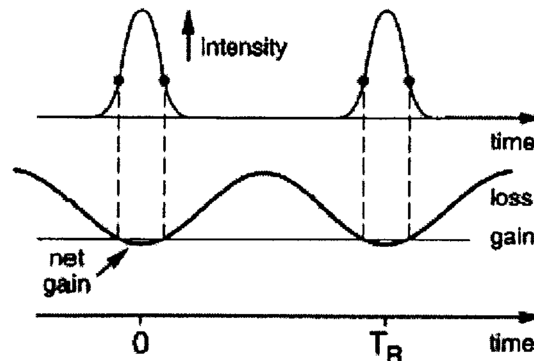

Figure 2-2. Active mode-locking in the time domain (from ref [50]). The pulse is shown on the top axis and is formed by the net gain window due to loss modulation.

This process can also be viewed in the frequency domain as the generation of sidebands at frequencies $\nu_0 \pm f_m$ on the laser mode at frequency ν_0. Since the cavity modes are spaced by f_m, the sidebands are phase-locked to the carrier frequency ν_0. On subsequent passes through the modulator, the sidebands at $\nu_0 \pm f_m$ will be modulated and develop sidebands themselves at

frequencies $\nu_0 \pm 2f_m$. Repetition of this process generates a comb of modes separated by the repetition rate of the laser. This has also been used in optical frequency metrology to bridge gaps between optical frequency standards, enabling measurement of unknown frequencies near the comb frequencies [5].

Passive mode-locking is the most common method of generating ultrashort pulses and was used to generate the first sub-picosecond pulses from a dye laser. This technique relies on modulating the intracavity gain or loss by the pulse itself and has resulted in pulses as short as 5 fs directly from the laser oscillator [17]. In this chapter, fundamental principles of passive mode-locking will be reviewed. Slow and fast saturable absorption models will be discussed in section 2.2. The dominant pulse shaping mechanisms including self amplitude modulation, self phase modulation, dispersion, and gain filtering, will be described in sections 2.3-2.5 and incorporated into the master equation for mode-locking. Solutions to this equation and the influence of pulse shaping mechanisms on the output pulse duration, chirp, bandwidth, and stability will be discussed in section 2.6. Dispersion managed mode-locking will also briefly be described in this section. Kerr lens mode-locking, the mechanism by which the shortest pulses have been generated, will be described in detail in section 2.7. Conditions for self-starting mode-locked operation will be reviewed in section 2.8. Section 2.9 will describe the technique of soliton mode-locking. Optimum parameters for saturable absorber design will be described in detail in section 2.10. Finally, a discussion of the important issues in designing a mode-locked laser will be given in section 2.11, and techniques for pulse measurement will be discussed in section 2.12.

2.2 Passive mode-locking with slow and fast saturable absorbers

Passive mode-locking requires a mechanism that favors pulsed over cw operation. This is usually an intensity dependent loss or gain in the laser cavity provided by a saturable absorber. Saturable absorbers are intracavity elements that introduce lower loss for higher intensities. This can be used to discriminate between high intensity pulses and low intensity cw radiation. Saturable absorbers can be classified as either slow or fast depending on their response time relative to the pulse duration. A slow saturable absorber recovers its absorption on a time scale

longer than the pulse duration, and its transmission scales with the pulse fluence. A fast saturable absorber responds instantaneously to changes in the pulse intensity, and therefore its transmission scales with the pulse intensity. In general, saturable absorbers help form a net gain window that determines the pulse duration and stabilizes the pulse against perturbations.

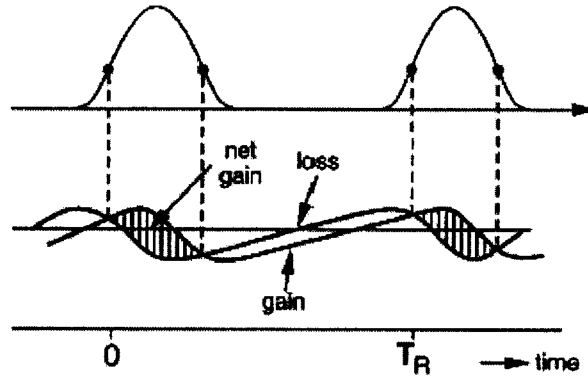

Figure 2-3. Pulse formation with slow saturable absorber mode-locking (from ref [50]). The net gain window is formed by the combination of absorber and gain saturation.

Slow saturable absorbers cannot usually support short pulse formation alone, requiring gain saturation to help produce ultrashort pulses (figure 2-3) (except in the case of soliton mode-locking, to be described in section 2.9). The slow saturable absorber responds to the leading edge of the pulse, decreasing the cavity loss, which recovers on a long time scale. Gain saturation subsequently occurs and attenuates the trailing edge of the pulses. The combination of the two pulse shaping effects results in a window of net gain, forming an ultrashort pulse. This technique was used to generate pulses as short as 27 fs [51] in a laser using dyes as both gain and saturable absorber media. The theory of slow saturable mode-locking is described in ref. [52]. Most real saturable absorbers (usually semiconductors) respond on a time scale of nanoseconds or faster, necessitating a gain medium that responds on a similar time scale to generate an ultrashort pulse. Solid-state laser media that are the focus of most current research respond on a time scale of microseconds and therefore cannot be mode-locked using this technique.

Fast saturable absorber mode-locking is the preferred method for mode-locking most solid-state laser systems. In this technique, the saturable absorber responds instantaneously to changes in the pulse intensity, creating a net gain window with a width determined by the pulse duration

(figure 2-4). Gain saturation is not a factor in fast saturable absorber mode-locking. The challenge in using this method is to find absorbers that relax on a fast enough time scale.

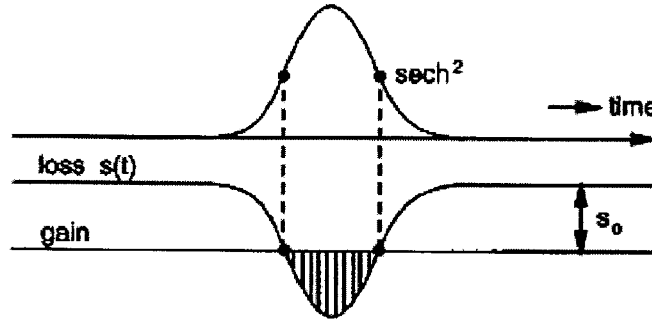

Figure 2-4. Pulse formation with fast saturable absorber mode-locking (from ref [50]). The net gain window is formed by the fast response of the saturable absorption.

In general, the theory of fast saturable absorber mode-locking describes a saturable absorber as an element shaping the pulse by self-amplitude modulation (SAM). Pulses usually form from noise fluctuations in the free running cw laser that are amplified by SAM since it favors the higher intensity noise fluctuations over the low intensity cw radiation. Self-amplitude modulation efficiently reduces the pulse duration down to picoseconds, after which other pulse shaping mechanisms such as self phase modulation, dispersion, and gain filtering take over to bring the pulse duration down to the femtosecond range. These pulse shaping processes are also incorporated into the theory of fast saturable absorber mode-locking and will be discussed below.

2.3 Self phase modulation

Self phase modulation (SPM) is a result of the optical Kerr effect. This occurs due to the nonlinear polarization response induced when a strong electric field is applied to an optical medium, given by

$$P = \varepsilon_0[\chi^{(1)}E + \chi^{(2)}E^2 + \chi^{(3)}E^3 + ...], \tag{2.10}$$

where the first term gives the normal linear response and the successive terms are the nonlinear polarization. In isotropic, homogenous media, the $\chi^{(2)}$ term vanishes; however, the $\chi^{(3)}$ term is present in all media. From the constitutive relation for the electric displacement $D = \varepsilon E$, an

intensity dependent index of refraction due to the nonlinear third order susceptibility $\chi^{(3)}$ can be derived,

$$n = n_0 + n_2 I , \tag{2.11}$$

where n_0 is the linear index of refraction, n_2 is the nonlinear index of refraction, and the pulse envelope $A(t)$ is normalized such that $I = |A|^2$ is the peak intensity of the laser pulse. The Kerr effect is a nonresonant effect in most laser gain media and therefore can respond on extremely fast time scales (a few fs) [53]. In most optical crystals, n_2 is positive and on the order of 10^{-16} cm^2/W.

The Kerr effect gives rise to two important ultrafast pulse phenomena: self-focusing and self-phase modulation (SPM). Self-focusing will be discussed in section 2.7 when describing Kerr lens mode-locking. Self-phase modulation is an important shaping mechanism for ultrashort pulses. Neglecting dispersion, pulse propagation through any medium with self-phase modulation can be described by an equation for the pulse envelope

$$\frac{\partial A(z,t)}{\partial z} = -i\delta |A|^2 A(z,t) \tag{2.12}$$

where $\delta = k_0 n_2$ is the SPM coefficient and $k_0 = 2\pi / \lambda$. This results in an intensity-dependent nonlinear phase shift for a pulse described by equation (2.8), given by

$$\Delta\varphi(t) = -k_0 n_2 L I(t) , \tag{2.13}$$

where L is the length of the optical medium. The time derivative of the phase shift gives the instantaneous frequency shift,

$$\Delta\nu(t) = \frac{d}{dt}\Delta\varphi(t) = -k_0 n_2 L \frac{dI(t)}{dt} . \tag{2.14}$$

This implies that the frequency will vary across the pulse as the intensity envelope changes, an effect called “chirp”. In most materials, the nonlinear index n_2 is positive, implying that the leading edge of the pulse with $dI/dt>0$ will down shift (red shift) the instantaneous frequency, and the trailing edge of the pulse ($dI/dt<0$) will up shift the frequency (blue shift) (figure 2-5). This can be explained by noting that the high intensity pulse peak sees a higher index of refraction than the low intensity pulse wings. The pulse peak will travel slower than the wings, causing the field oscillations to bunch up towards higher frequencies on the trailing edge of the

pulse and spread out towards lower frequencies on the leading edge. SPM only introduces a phase shift on the pulse and therefore does not affect the temporal intensity envelope. However, the pulse spectrum broadens due to the new frequencies generated on the leading and trailing edges of the pulse by SPM.

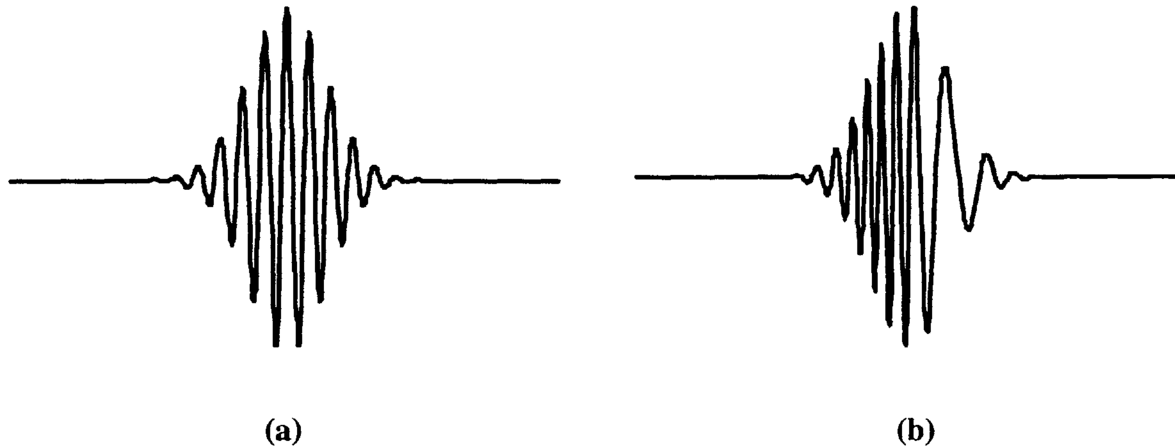

(a) **(b)**

Figure 2-5. (a) Electric field of a Gaussian pulse envelope with a carrier frequency defined by equation (2.8). (b) Electric field of the pulse in (a) after propagating through a Kerr medium and undergoing self-phase modulation. The chirp on the pulse has the same effect as normal dispersion, with higher frequencies delayed relative to lower frequencies

In a dispersive medium where the index of refraction varies with frequency, the additional frequency components on the leading and trailing edges of the pulse travel with different speeds. This can either increase or decrease the pulse duration depending on the sign of the dispersion. Pulse propagation in a medium with positive dispersion (low frequencies travel faster than high frequencies) causes the high frequencies on the trailing edge to lag behind the low frequencies on the leading edge, broadening the pulse in time. However, propagation in a medium with negative dispersion (high frequencies travel faster than slow frequencies) causes the blue-shifted components on the trailing edge of the pulse to catch up to the red-shifted frequencies on the leading edge, compressing the pulse in time. This interplay between SPM and dispersion, often called soliton-like pulse shaping, is the effect responsible for soliton generation and propagation. Solitons are waveforms that can travel over long distances without changing their shape, due to a balance between SPM and dispersion. Soliton-like pulse shaping can be

exploited in an ultrafast laser to obtain very short pulses. This underlines the importance of dispersion in an ultrafast laser, which will be discussed in the following section.

2.4 Dispersion

Ultrashort pulse propagation is strongly influenced by dispersion in the laser cavity. In general, an ultrashort pulse contains many spectral components that propagate at different speeds in the laser cavity due to dispersion, the variation of the refractive index with frequency. . Without proper dispersion management, this will cause the pulse envelope to change shape and spread out in time. Therefore, careful consideration of dispersive effects is extremely important in generation of the shortest pulses.

In general, propagation of light through a dispersive optical system causes a frequency dependent phase shift given by $\varphi(\omega)$. Ultrashort pulses described by the slowly varying envelope approximation (equation (2.8)) have a spectral phase given by

$$\varphi(L,\omega) = \omega_0 L n(\omega)/c, \tag{2.15}$$

for propagation through a dispersive medium with refractive index $n(\omega)$ and length L. An expression for the group delay can be derived by expanding the spectral phase around the carrier frequency ω_0 (usually the center of the frequency spectrum, although more complicated expressions can be used [34, 54]),

$$\varphi(\omega) = \varphi_0 + (\omega-\omega_0)(d\varphi/d\omega)_{\omega_0} + \frac{1}{2}(\omega-\omega_0)^2(d^2\varphi/d\omega^2)_{\omega_0} + \ldots, \tag{2.16}$$

with the group delay (GD) given by $T_g(\omega_0) = \left(d\varphi/d\omega\right)_{\omega_0}$ and the group delay dispersion (GDD) given by $GDD(\omega_0) = \left(d^2\varphi/d\omega^2\right)_{\omega_0}$ at the carrier frequency. Therefore, the pulse envelope propagates at the group velocity $v_g(\omega_0) = L/T_g(\omega_0)$ and the carrier wave propagates with the phase velocity $v_p(\omega) = c/n(\omega)$. Physically, the group delay refers to the time relative to the pulse envelope that different frequency components arrive at a given point in space. The group delay dispersion is a measure of how strongly the material spreads the pulse components; the larger the GDD, the larger the difference in arrival times between nearby frequency components

for a certain amount of optical path length through the material. For extremely short pulses (<10 fs), higher order dispersion terms become important, including the third order dispersion, given by $TOD(\omega_0) = \left(d^3\varphi / d\omega^3\right)_{\omega_0}$ and the fourth order dispersion, $FOD(\omega_0) = \left(d^4\varphi / d\omega^4\right)_{\omega_0}$ [55]. For example, the broadening of a 10 fs transform limited Gaussian pulse is the same for a *GDD*=100 fs^2, *TOD*=1000 fs^3, and *FOD*=10,000 fs^4.

The index of refraction is often given as a function of wavelength for many materials. Therefore, it is useful to express the GDD as a function of wavelength, given by [56]

$$GDD(\lambda) = \left(\frac{\lambda^3}{4\pi^2 c^2}\right)\left[2\left(\frac{d\varphi}{d\lambda}\right) + \lambda\left(\frac{d^2\varphi}{d\lambda^2}\right)\right]. \tag{2.17}$$

For a given transparent material, the refractive index is usually given in the form of a Sellmeier equation,

$$n^2 - 1 = \sum_k \frac{B_k \lambda^2}{\lambda^2 - C_k}, \tag{2.18}$$

where B_k and C_k are coefficients that are given for the substance under consideration. The GD and GDD can easily be calculated from equations (2.17) and (2.18) for a particular material.

Equation (2.12) can be modified to describe pulse propagation including both dispersion and SPM. The modified equation is called the nonlinear Schrödinger equation and is given by

$$i\frac{\partial A(z,t)}{\partial z} = -\frac{k_n''}{2}\frac{\partial^2 A(z,t)}{\partial t^2} + \delta |A|^2 A(z,t), \tag{2.19}$$

where $k_n'' = \frac{\partial^2 k}{\partial \omega^2}$, the GDD per unit length. This equation is used to describe the propagation of solitons in optical fibers [57]. A stationary solution of this equation is the fundamental soliton, described by a hyperbolic secant function,

$$A_s(z,t) = A_0 \,\text{sech}^2\left(\frac{t}{\tau}\right) e^{-i\delta A_0^2 z}. \tag{2.20}$$

This pulse shape is also common in passively mode-locked solid state lasers, and this equation can indeed be used to describe the pulses generated from a femtosecond solid state laser with appropriate modifications, described in section 2.6.

2.5 Gain filtering

Gain filtering is another important pulse shaping mechanism that must be considered in understanding passive mode-locking. The gain of a laser is frequency dependent, arising from the linewidth of the atomic transitions involved in the lasing process. In a real laser system, these transitions are not ideally sharp but are broadened by different homogeneous and inhomogeneous processes. Homogeneous broadening occurs when each atom has the same frequency response and arises from processes such as the finite upper state lifetime of the laser material or the coupling to vibrational phonon modes in the crystal lattice. Effects such as crystal imperfections cause the atomic lineshape to vary between atoms, giving rise to inhomogeneous broadening. In most solid state lasers, homogenous broadening is the dominant mechanism. The shape of the gain is a Lorentzian, which can be approximated by a parabolic gain profile near the center wavelength, given by

$$G(\omega) = g\left[1 - \frac{(\omega - \omega_0)^2}{\Omega_g^2}\right], \qquad (2.21)$$

where g is the laser gain at the center, ω_0 is the center frequency, and Ω_g is the gain bandwidth. This frequency dependent gain tends to act as a bandwidth limiting filter that broadens pulses passing through the laser crystal, particularly for extremely short laser pulses. Pulse perturbations including multiple pulsing and cw breakthrough are also influenced by the finite gain bandwidth of the lasing transition [58] and will be discussed further in sections 2.6 and 2.10.2.

2.6 The master equation for fast saturable absorber mode-locking

The above pulse shaping processes can be incorporated into a master equation describing the time evolution of the pulse envelope $A(t)$ for fast saturable absorber mode-locking in the steady state, first formulated by Haus [59, 60, 61] and given by

$$\left[g\left(1+\frac{1}{\Omega_g^2}\frac{d^2}{dt^2}\right)-(l+ix)-i\psi+iD\frac{d^2}{dt^2}+(\gamma-i\delta)|A(t)|^2\right]A(t)=0\,. \qquad (2.22)$$

In this equation, the first term is due to gain filtering, obtained by Fourier transforming equation (2.21) to get a time domain expression. The linear loss and phase shift per pass are incorporated in the $l+jx$ term. The $i\psi$ term incorporates the phase shift due to deviations of the carrier frequency from an axial resonator frequency. Dispersion is taken into account by the $iD(d^2/dt^2)$ term, where D is given by $k''L/2$ for a path length L through the resonator (similar to equation (2.19)). The $\gamma|A(t)|^2$ term accounts for self-amplitude modulation (saturable absorber action) and the $-i\delta|A(t)|^2$ operator incorporates self-phase modulation. The solutions of this equation have the form

$$A(t)=A_0\,\text{sech}\left(\frac{t}{\tau}\right)\exp[i\beta\ln(\text{sech}(t/\tau))] \qquad (2.23)$$

where β is the chirp parameter and τ is the pulse width [62]. The pulse duration, chirp, bandwidth, and stability parameters can be determined by substituting this expression back into the master equation [60]. This reduces to two complex equations, one with terms proportional to sech and one with terms proportional to sech^3, which can individually be set to zero. These equations can be solved for the pulse width and chirp for a known amplitude A_0 of the pulse. The amplitude can be determined by setting the saturated gain, g, equal to the loss, l, in which case the saturated gain is given by the condition

$$g=\frac{g_0}{1+E_p/P_sT_R} \qquad (2.24)$$

with the pulse energy given by $E_p=2A_0^2\tau$. A_0 can be obtained from solving equation (2.24), and this can be introduced into the master equation to obtain the pulse width and chirp parameter. Normalized parameters are used for the pulse width,

$$\tau_n=(E_p\Omega_g^2/2g)\tau \qquad (2.25)$$

dispersion,

$$D_n=(\Omega_g^2/g)D \qquad (2.26)$$

and bandwidth (obtained directly from the solutions for the chirp and pulse width):

$$\omega_n=(1+\beta^2)^{1/2}(1/\tau_n)\,. \qquad (2.27)$$

The normalized pulse width and bandwidth, as well as the chirp β and the stability criterion, are plotted in figure 2-6 as functions of the normalized dispersion D_n while varying the SPM parameter δ. The pulses are stable if the gain before and after the pulse is less than the loss to prevent the growth of disturbances, setting the stability criterion, $l\text{-}g>0$. The balance of saturable absorber action and gain filtering is crucial in determining pulse stability and will be discussed more thoroughly below.

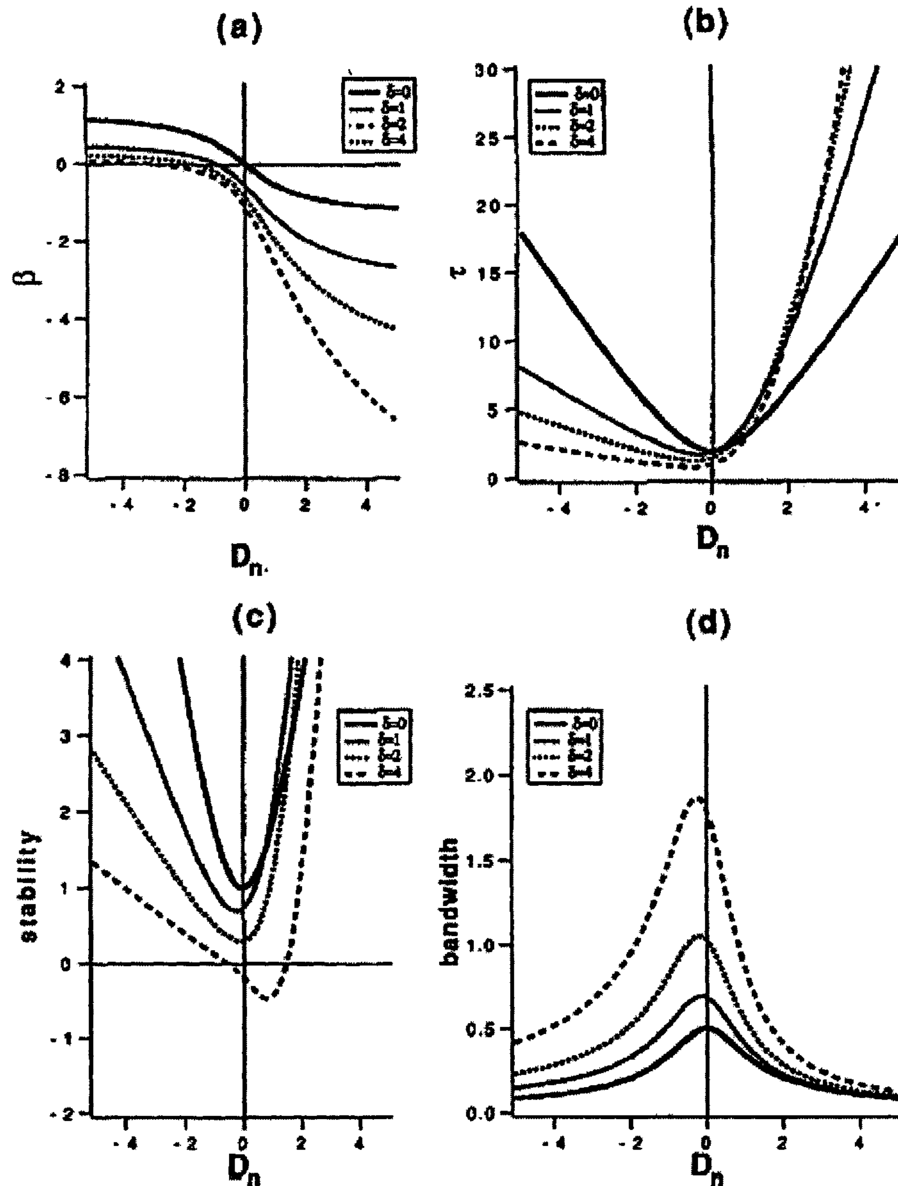

Figure 2-6. (a) Chirp, (b) pulse duration, (c) stability, and (d) bandwidth plotted as functions of the dispersion (from reference [60]).

Mode-locked operation can be qualitatively understood from these graphs. By inspecting the graph for the chirp parameter β, it is clear that there are two different regimes of operation depending on the sign of the dispersion. In the positive dispersion regime, the pulses are strongly chirped and the duration is long. Gain filtering actually acts to decrease the pulse duration in this regime by balancing the pulse broadening resulting from SPM and positive dispersion. The high and low ends of the pulse spectrum are cut off, reducing the bandwidth and also the duration for a chirped pulse. The pulse duration is primarily determined by the strength of the saturable absorber.

In the negative GDD regime, soliton-like pulse shaping dominates pulse generation and shaping. The balance of negative GDD and SPM, as described in section 2.3, results in short, unchirped pulses (often referred to as "solitons" in this thesis). The SPM parameter δ has a much stronger influence on the pulse width than the SAM parameter γ in this regime. Therefore, in this regime the solutions to the master equation can be approximated by an ideal soliton-like hyperbolic secant pulse, given by solutions of the nonlinear Schrödinger equation (2.19). An approximate expression for the full width at half maximum (FWHM) pulse duration can be obtained by substituting the hyperbolic secant solution, equation (2.20), into (2.19) [58]:

$$\tau_{FWHM} = 1.76 \cdot \frac{4|D|}{\delta E_p}, \tag{2.28}$$

where E_p is the pulse energy. This expression is applicable to most solid-state lasers mode-locked by a fast saturable absorber. Soliton-like pulse shaping has been shown to reduce the pulse duration by a factor of 2-2.75 as compared to lasers mode-locked purely by a fast saturable absorber without SPM and GDD [58, 60].

It appears from equation (2.28) that the pulse duration does not depend on the saturable absorption, which is not really true. In the negative dispersion regime, the saturable absorber is necessary to stabilize the soliton by providing a window of net gain for the pulse, where the gain before and after the pulse must be less than the loss (which is equal to the saturated value of the cw gain) in order to suppress noise perturbations. The finite gain bandwidth imposes additional loss on a soliton as compared to cw oscillation at the gain peak, and therefore saturable

absorption is necessary to favor pulsed over cw operation. Shorter pulses require stronger saturable absorber action due to their broad bandwidths.

Similarly, from figure 2-6 it is clear that larger values of SPM lead to shorter pulses if the negative dispersion is increased to balance the SPM-induced broadening. However, for increasingly large values of SPM (occurring as the pulse gets shorter), gain filtering causes the broad bandwidth pulse to lose energy and become unstable. This can also occur for operation near zero dispersion, when the pulses are very short and have broad bandwidths. As described in the previous paragraph, efficient saturable absorber action can keep the pulse stable by compensating for the losses due to gain filtering. However, for high pulse energies, the absorber is fully saturated and cannot stabilize the pulse any further. In contrast, SPM does not saturate with increased pulse energy, and therefore the pulse continues to get shorter as the pulse energy increases until either the cw radiation breaks through or the pulse breaks up into multiple pulses. Multiple pulsing occurs because two or more solitons with lower energy and longer duration will saturate the absorber more effectively and incur lower loss from gain filtering; this will be described in more detail in section 2.10.2. A stability criterion can be derived for the saturable absorber to overcome losses due to gain filtering [58], given by

$$\frac{D_g}{\tau^2} < 2q_0, \tag{2.29}$$

where $D_g = g / \Omega_g^2$ is the gain dispersion and q_0 is the saturable loss (often called the "modulation depth", described in section 2.10.1) of the absorber. The minimum pulse duration that can be supported for a given saturable loss is obtained by setting the two sides of equation (2.29) equal to one another. Equation (2.29) shows that as the pulse duration decreases due to soliton shaping (from equation (2.28)), the saturable absorber strength must increase to keep the pulse stable against multiple pulsing and cw breakthrough. These instabilities are very important and must be carefully considered in ultrashort pulse lasers, especially those with extremely short pulse durations or very high pulse energies.

The master equation approach is valid as long as the pulse envelope does not significantly change per round trip. However, for extremely short pulses with durations in the 10 fs regime, higher order dispersion (not included in the master equation) becomes important [55], as well as

ordering of the elements in the resonator [63]]. The pulse shape changes significantly during propagation through each element in the resonator, necessitating a different approach for describing ultrashort pulse generation in this regime, called dispersion managed mode-locking [64].

In this model, ultrashort pulse propagation is equated to dispersion managed soliton propagation [64], in which the pulse passes through segments of positive and negative dispersion in which the pulse width changes significantly. For ultrashort pulse lasers, it can be shown using this model that in a linear cavity with one arm containing the negative dispersion (such as a cavity using only a prism pair for dispersion compensation) and the crystal providing positive dispersion, the pulse is shortest in the arm containing the negative dispersion. If the negative dispersion is equally distributed between both arms, the pulse is shortest at each end of the cavity and also has the same shape both times it passes through the crystal in a round trip (as opposed to a cavity with the negative dispersion only in one arm). Finally, the pulse is found to be transform limited in the center of the positive and negative dispersion cells. The pulse shapes in this regime can be fit by a $sinc^2$ function. This model gives guidelines for designing and understanding lasers producing sub-10 fs pulses. However, for most laser systems the intuitive conclusions drawn from the master equation approach are still a helpful guide to understanding mode-locking dynamics.

2.7 Kerr lens mode-locking

Kerr lens mode-locking (KLM) is the dominant method of generating extremely short, sub-50 fs pulses from solid-state lasers. KLM is an artificial fast saturable absorber based on the optical Kerr effect. As mentioned in section 2.3, the intensity dependent index of refraction given by equation (2.11) can result in the effects of self-phase modulation and self-focusing. Self-focusing in combination with an intracavity aperture is the basis of the artificial fast saturable absorber used in Kerr lens mode-locking. In this section, a physical description of KLM will be given, while the optimal cavity design for a Kerr lens mode-locked laser is discussed in section 2.11.4.

Generally, the transverse profile of an optical pulse takes a Gaussian shape, with higher intensity in the center than in the wings. When a pulse propagates through a Kerr medium, the higher intensity center modifies the refractive index through the Kerr effect, while the lower intensity outer portions do not. This creates an intensity dependent lens within the Kerr medium that counteracts the normal diffractive beam divergence (for a positive n_2). At a power equal to the critical power for self-focusing [65], given by

$$P_{crit} = \frac{a\lambda^2}{8\pi n_0 n_2}, \tag{2.30}$$

where a is a correction factor between 3.7-6.4, the beam becomes collimated and propagates without divergence. For powers greater than P_{crit}, the beam theoretically collapses to a singularity; in reality, higher order effects or damage of the medium occur before this happens.

Self-focusing can be utilized in combination with an intracavity aperture to generate ultrashort pulses. The intracavity transverse beam profile is modified for high intensities as compared to low intensities; for example, high intensity pulses will have a different spatial profile than the low intensity cw radiation. By introducing an aperture to discriminate between high and low intensities, an intensity dependent loss mechanism is created, equivalent to a fast saturable absorber.

Solid-state laser crystals typically have a positive n_2 and therefore act as a positive lens for high intensities, such that the high intensity radiation has a smaller mode size within the laser crystal than low intensity radiation. An intracavity aperture can therefore be placed at a position within the cavity where the high intensity mode is smaller than the low intensity mode, favoring pulsed operation. This has been accomplished using both "hard" and "soft" apertures. A "hard" aperture is usually a physical slit placed at a position in the cavity to create more loss for the cw radiation and favor pulsed operation [66]. "Soft" apertures rely on the overlap of the laser mode and pump mode within the laser crystal (figure 2-7).

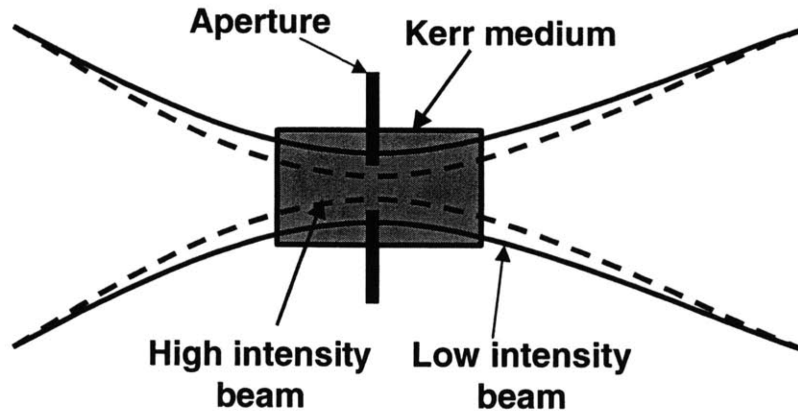

Figure 2-7. Schematic of Kerr-lens mode-locking with a soft aperture.

The pump mode is first set to be smaller than the cw laser mode within the laser crystal. The high intensity pulsed mode will self-focus to a smaller mode size than the cw mode within the crystal and will therefore overlap better with the pump mode, experiencing more gain than the cw radiation. Soft or gain aperture KLM is generally favored for the generation of extremely short pulses due to bandwidth limitations present in hard aperture KLM, and was used in the KLM laser systems described in this thesis.

KLM has been used to generate pulses down to 5 fs in duration [17] and is the only method for generating sub-10 fs pulses. However, it requires very precise cavity alignment (to be discussed in section 2.11.4) and is usually not self-starting. Self-starting (when the pulse evolves from noise fluctuations without any external energy input) is difficult in KLM lasers, because the Kerr nonlinearity that is strong for ultrashort pulses is much less significant for longer pulses and negligible for cw radiation. Similarly, any nonlinearity that is strong for longer pulses or cw radiation will be overdriven in the ultrashort pulse regime. For example, in a standard femtosecond laser, the peak power changes by six orders of magnitude between cw and mode-locked operation. Self-starting KLM lasers have been demonstrated with pulse durations down to 50 fs, but the cavity alignment is extremely sensitive and no shorter self-starting pulses have been demonstrated [67, 68]. Most KLM lasers can be started by tapping an end mirror or shaking a mirror or prism stage; this provides a sufficient noise perturbation to enable KLM.

2.8 Self-starting mode-locked operation

The buildup of a laser pulse from noise perturbations has been analyzed by several authors [69, 70, 71] with the goal of deriving optimum parameters for self-starting laser mode-locking. In general, a noise perturbation can be represented as a perturbation $s(t)$ on the steady state photon flux S_0, which affects the round trip gain through

$$\Delta g_a = ks(t), \tag{2.31}$$

where k is a proportionality constant that depends on the strength of the fast saturable absorber [69]. A short fluctuation will see more gain than cw radiation, as well as more gain for the peak than the wings; this increased gain enables the initial fluctuation to build into a steady state mode-locked pulse. For a gain medium with a relaxation time longer than the cavity round trip time (usually true for solid-state lasers with relaxation times of microseconds) such that the gain saturates only with the average power, mode-locking will always self-start, with a rate determined by the width of the initial perturbation and the strength of the SAM provided by the saturable absorber.

When dynamic gain saturation is taken into account, a more careful analysis must be performed to determine a self-starting condition [69]. For a gain medium with recovery time long compared to the width of the fluctuation, the perturbation changes the gain by

$$\Delta g_s = -\sigma g \int_{-\infty}^{t} s(t)dt \tag{2.32}$$

with σ the emission cross-section of the gain and g the saturated gain prior to the perturbation. The effect of the change in gain on the perturbation due to the sum of equations (2.31) and (2.32) can be calculated by calculating the overlap integral between Δg_a+Δg_s and $s(t)$ to get

$$k/g > \sigma \left\{ \frac{\left[\int_{-\infty}^{\infty} s(t)dt \right]^2}{\int_{-\infty}^{\infty} s^2(t)dt} \right\}. \tag{2.33}$$

The ratio of integrals in (2.33) is generally given by $\beta\tau_p$, where τ_p is the width of the perturbation and β is a scaling factor that depends on the shape of the perturbation (β=0.85 for a $sech^2$ shape,

0.75 for a Gaussian shape) and is usually near unity. Therefore, the self-starting condition is given by

$$k / g > \beta \sigma \tau_p . \tag{2.34}$$

This shows that the gain cross section is an important parameter in self-starting mode-locking. A shorter perturbation width also makes start up of mode-locking easier, as does stronger saturable absorber action. The gain dependence of this condition implies that mode-locking will start as soon as the laser threshold is reached if the nonlinearity is large enough compared to the gain saturation. However, experiments have shown that in most laser systems, there are two thresholds, one for cw lasing and one for mode-locking, which contradicts this prediction.

The existence of a separate threshold for mode-locking was examined in [70]. A condition similar to (2.34) was first derived for self-starting mode-locking with dynamic gain saturation. However, this condition also did not predict the existence of a mode-locking threshold, motivating an investigation based on the introduction of a decay time for the perturbation. Generally, the mode-locked pulse will evolve from the most intense mode-beating fluctuation in the cw laser, which has a finite coherence time since the modes dephase after a certain period of time. If the pulse does not get significantly shorter within the coherence time, then it will break up. A coherence time τ_c can be included to obtain the condition for self-starting,

$$k' P_i > \frac{1}{\ln(m_i)} \frac{T_r}{\tau_c} , \tag{2.35}$$

where $k' = \hbar \omega A_g k$, with A_g the beam cross section in the gain medium, P_i the cw intracavity power, and m_i the initial number of modes. This shows that a longer cavity round trip time makes self-starting more difficult, and also defines a threshold power for self-starting. Subsequent work identified spurious reflections in the laser cavity as a possible source of decoherence between modes, and found that the ratio of the perturbation width to the cavity round trip time was important in determining self-starting behavior [71].

In summary, self-starting laser mode-locking is easier for stronger saturable absorber action, smaller gain cross-sections, shorter perturbation widths, and shorter cavity lengths. As

previously discussed, Kerr lens mode-locking is usually not self-starting, necessitating other mode-locking techniques or devices to obtain a self-starting source of ultrashort pulses.

2.9 Soliton mode-locking

Soliton mode-locking is a mode-locking technique that relies on the combination of soliton-like pulse shaping and a slow saturable absorber for ultrashort pulse generation [39, 58, 72-74]. The mode-locking dynamics can be described in a similar manner as the discussion of fast saturable absorber mode-locking with soliton-like pulse shaping in section 2.6. The primary difference between these techniques is the use in soliton mode-locking of a slow saturable absorber that responds on time scales much longer than the final pulse duration. Self-starting soliton mode-locking can be achieved over the full cavity stability region, in comparison to KLM in which pulse generation is very sensitive to the stability operating point. Soliton mode-locking can also be distinguished from slow saturable absorber mode-locking since no dynamic gain saturation is necessary for short pulse formation. This technique has been used to generate self-starting 13 fs pulses from a Ti:sapphire laser [75].

Soliton mode-locking relies on the interplay of SPM and GDD to form an ultrashort pulse [39, 58]. As described in section 2.6, a soliton is unstable without a saturable absorber to stabilize the pulse against the growth of noise perturbations. The soliton loses energy due to gain dispersion, and this energy is in the form of a longer background pulse (called the "continuum"). This background pulse sees more gain than the soliton due to its smaller bandwidth near the gain peak, and the long recovery time of the slow saturable absorber leaves a net gain window after the short soliton pulse for the continuum to grow. The continuum creates negligible SPM but is spread out in time by GDD. Therefore, the continuum is spread into the region of the slowly recovering saturable absorber loss, which prevents it from reaching threshold and destabilizing the soliton.

A mathematical treatment of soliton mode-locking is given in refs. [73] and [39] and will be briefly summarized here. Beginning with the master equation (2.22), the $\gamma|A(t)|^2$ term for

self-amplitude modulation in the fast saturable absorber model is replaced by a separate differential equation describing the saturable absorber response to the pulse in each round trip,

$$\frac{\partial q(T,t)}{\partial t} = -\frac{q - q_0}{T_A} - \frac{|A(T,t)|^2}{E_{sat}}, \tag{2.36}$$

where T_A is the absorber recovery time, assumed to be shorter than the time between pulses, and E_{sat} is the saturation energy of the absorber. In the soliton mode-locking model, the pulse duration is given by equation (2.28) (since soliton-like pulse shaping is dominant), and full saturation of the absorber is assumed (i.e., the pulse energy is much larger than E_{sat}). When the soliton is stable, the net gain per round trip is zero and the saturated gain is equal to the total loss, $g=l+D_{g,f}/3\tau^2$, where $D_{g,f}$ accounts for the gain and intracavity filter dispersion and the second term accounts for the additional loss for the soliton due to the saturable absorber and the finite filter and gain bandwidths when the absorber is fully saturated [39, 58, 72, 73]. The soliton loses energy to the continuum as it passes through the filters and the slowly recovering saturable absorber. Soliton perturbation theory can be used to obtain an equation for the decay of the continuum. It is found that the soliton is stable if the continuum solutions to this equation decay in time, which occurs if there is enough dispersion to spread the continuum into the region of the slowly recovering absorber loss. An equation can then be obtained for the minimum pulse width that the absorber can support [39, 73, 74], given by

$$\tau = \left(\frac{1}{\sqrt{6}\Omega_g}\right)^{3/4} \left(\frac{T_A g^{3/2}}{q_0}\right)^{1/4} (\varphi)^{-1/8}, \tag{2.37}$$

with

$$\varphi = \frac{\delta E_p}{4\tau} = \frac{|D|}{\tau^2}, \tag{2.38}$$

where Ω_g is the gain bandwidth and φ is the nonlinear phase shift, also given in equation (2.13). This can be compared to the minimum pulse duration obtained from the fast saturable absorber model, given in equation (2.29). The ratio of the pulse durations in the soliton mode-locking and fast saturable absorber cases, $\tau / \tau_{FSA} \approx (T_A \Omega_g)^{1/4}$, shows that the pulse widths are comparable in both mode-locking techniques and the ratio decreases slowly with the absorber recovery time.

The saturable absorber device parameters and design are very important in optimizing soliton mode-locking. The pulsewidth is proportional to the square root of the saturable absorber strength (saturable loss), and pulses up to 30 times shorter than the absorber response time can be initiated and stabilized [75]. Therefore, it is important to carefully design the absorber recovery time and strength to minimize the pulse duration. In general, increasing the saturable absorber strength should enable generation of shorter pulses, since it is inversely proportional to the pulsewidth in pure fast saturable absorber mode-locking without SPM and GDD [59]. However, real saturable absorbers always introduce undesirable non-saturable loss along with the desired saturable loss, causing the laser to operate less efficiently. Therefore, there is a limit in practice on how much saturable loss can be introduced before the laser is unable to reach threshold. For a given absorber strength, soliton-like pulse shaping is critical to achieve the minimum pulse duration.

The drawbacks in soliton mode-locking are primarily in the optimization of saturable absorber properties, since the saturable and non-saturable loss, recovery time, and bandwidth play an essential role in ultrashort pulse generation. This differs from KLM, in which the artificial fast saturable absorber due to the nonlinear index of refraction responds essentially instantaneously and does not introduce any non-saturable loss or bandwidth limitations. These effects can explain why KLM is the only technique currently demonstrated to generate sub-10 fs pulses. However, many lasers are mode-locked with real saturable absorber devices and therefore it is appropriate to discuss the ideal properties of a saturable absorber in the next section.

2.10 Saturable absorbers for laser mode-locking

Saturable absorbers can be used in three different regimes for laser mode-locking. The first case is when the saturable absorber starts mode-locking for relatively low intracavity intensities, but only weakly supports further pulse shaping. In this case, the saturable absorber can be saturated by a small intracavity change in intensity (like a noise perturbation) and amplify this into a long pulse, with durations of nanoseconds to picoseconds. At this point, another

mode-locking mechanism (such as KLM) that is more efficient for higher intracavity intensities takes over and further shortens the pulse while stabilizing mode-locking. The second case is when another mechanism initiates mode-locking at low intensities where the absorber is only weakly saturated. This reduces the duration of the pulse into a regime where the absorber saturates and provides further pulse shortening. Finally, the third case is when the saturable absorber is effective for low and high intracavity intensities and can both start mode-locking and provide further pulse shortening.

Saturable absorbers used in laser mode-locking are designed to optimize several important parameters. These include linear absorption, absorption saturation intensity and fluence, modulation depth, ratio of saturable to non-saturable losses, wavelength dependence and bandwidth of operation, and damage threshold [38, 36]

2.10.1 Modulation depth and non-saturable loss

The saturable absorber must be designed to provide optical absorption at the operating wavelength of the laser. This absorption can be separated into two components: saturable and non-saturable loss. Saturable loss is nonlinearly dependent absorption that decreases for higher intensity incident light. In the semiconductor saturable absorbers considered in this thesis, this occurs through band filling due to the Pauli exclusion principle. Additional effects including excitonic effects and bandgap renormalization must often be taken into account near the band edge [76]. Non-saturable loss is not intensity dependent and causes the laser to operate less efficiently while increasing the threshold.

The modulation depth is the total amount of saturable loss introduced by a saturable absorber, which can decrease to zero ("bleaching") by absorption of an infinitely high pulse energy. In all mode-locking theories, the pulse duration is inversely proportional to the modulation depth of the saturable absorber [38, 58, 59], as given by

$$\tau \propto \frac{1}{q_0^{\eta}}, \tag{2.39}$$

where $2q_0$ is the modulation depth and η is a factor that depends on the mode-locking theory. In general, a high modulation depth is always desirable for the generation of shorter pulses.

The total absorption should be low enough such that the laser can still reach both the cw and mode-locking thresholds. It should also be high enough to introduce an appreciable amount of saturable loss to discriminate between low and high intensities. The ratio of saturable to non-saturable loss should be maximized, since any additional non-saturable loss only degrades the laser performance and makes it operate farther above threshold, which can increase the tendency for instabilities. Non-saturable losses are usually from material defects and can sometimes lower the damage threshold for the device.

2.10.2 Absorption saturation intensity and fluence

The absorption saturation intensity and fluence are important parameters influencing mode-locked operation. In the initial stages of pulse evolution when noise fluctuations are amplified into pulses, the saturable absorber acts like a fast saturable absorber since the width of the noise fluctuations is long compared to the recovery time of the absorber, and therefore the cw intensity incident on the absorber determines the amount of absorption saturation. The absorption coefficient for a two level system is given by [47]

$$\alpha = \frac{\alpha_0}{1 + \frac{I}{I_{sat}}}, \tag{2.40}$$

where α_0 is the small signal absorption coefficient (linear absorption), I is the cw intensity, and I_{sat} is the saturation intensity, given by

$$I_{sat} = \frac{h\nu}{\sigma_A T_A}, \tag{2.41}$$

where $\hbar\nu$ is the photon energy, σ_A is the absorption cross section of the transition, and T_A is the absorption saturation recovery time. Therefore, as the intensity increases, the absorption coefficient approaches zero and the absorption saturates. In general, the saturation intensity should be large enough such that the absorption is not saturated by the cw intensity, since otherwise there would not be enough modulation in absorption for pulse formation. However, it

is worth mentioning that the intensity can always be tailored by changing the spot size on the absorber, so in general lower saturation intensity is better. Figure 2-8 shows the variation of absorption with the cw intensity.

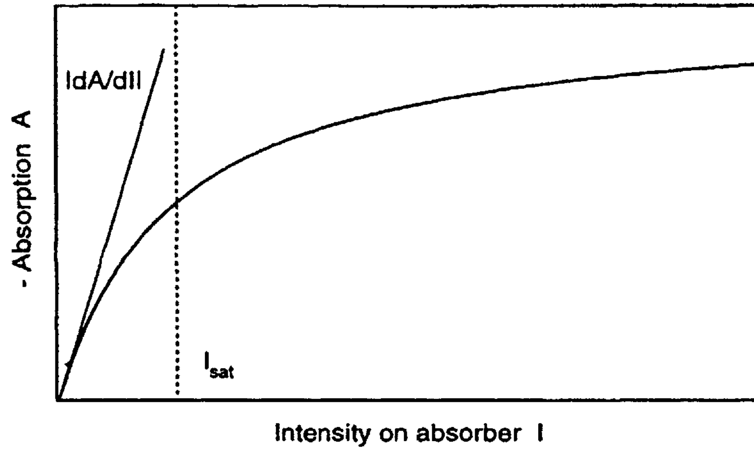

Figure 2-8. Nonlinear absorption change with increasing intensity.

Maximum and minimum bounds for the saturation intensity can be obtained by considering the mode-locking build-up time and the condition for stability against Q-switching. The mode-locking build-up time is a good measure of self-starting performance and can be approximated by [74]

$$T_{mlb} \propto \frac{1}{\left.\frac{dA}{dI}\right|_{I=0} I}, \tag{2.42}$$

where dA/dI is the slope as shown in fig. 2-8. From this expression it is clear that a faster build-up time can be achieved by increasing this slope. This can be accomplished by lowering the saturation intensity of the device. However, if the saturation intensity is too small, the laser can start to Q-switch. To avoid Q-switching, the laser must satisfy the inequality given by

$$\left|\frac{dA}{dI}\right| I < r\frac{T_R}{\tau_2}, \tag{2.43}$$

where T_R is the round trip time as before, r is the pump parameter determining how many times above threshold the laser is pumped, and τ_2 is the upper state lifetime of the gain medium [74, 77]. From this equation, it is clear that Q-switching can be suppressed by using a device with a high saturation intensity, a low repetition rate laser, or a laser pumped far above threshold.

Physically, this equation can be interpreted by independently examining the left and right hand sides. The left-hand side is a measure of the absorber saturation and the corresponding reduction in cavity loss, causing the intracavity intensity to increase. The right-hand side is a measure of how fast the gain can respond to compensate for the reduction in loss to keep the intracavity intensity constant. If the gain responds too slowly, than the intensity will increase until the absorber is completely bleached, causing Q-switching. The combination of equations (2.42) and (2.43) sets upper and lower bounds for the saturation intensity. In practice, optimal laser performance is almost always achieved with lower saturation intensities.

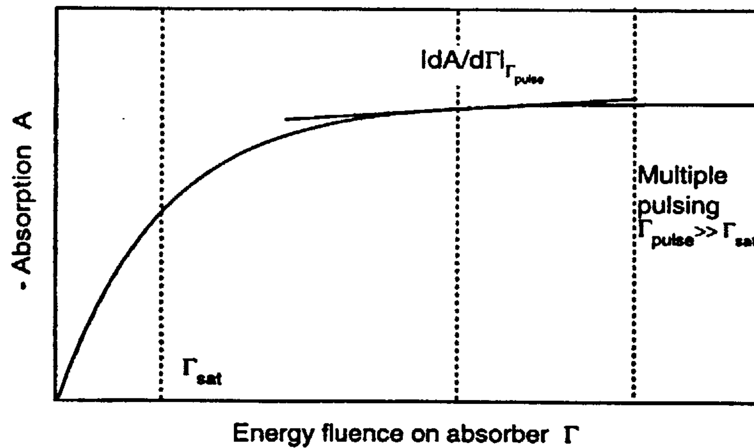

Figure 2-9. Nonlinear absorption change of a saturable absorber as a function of pulse fluence.

When the laser pulse is comparable to or shorter than the absorption saturation recovery time, then the saturable absorber acts as a slow saturable absorber and saturates with the pulse fluence $\Gamma(t) = \int_{-\infty}^{t} I(t)dt$. The absorption coefficient is then given by

$$\alpha = \alpha_0 \exp(-\Gamma / \Gamma_{sat}) \tag{2.44}$$

where Γ_{sat}, the saturation fluence, is given by

$$\Gamma_{sat} = \frac{h\nu}{\sigma_A}. \tag{2.45}$$

Figure 2-9 shows the absorption change of a saturable absorber with the pulse fluence.

Upper and lower bounds for the saturation fluence can also be derived in a similar manner as the saturation intensity. If the absorption saturation recovery time is shorter than the cavity round trip time, then the condition for no Q-switching given by (2.43) is usually fulfilled. However, another condition must be satisfied to prevent Q-switched mode-locking, given by

$$\left|\frac{dA}{d\Gamma}\right|\Gamma < r\frac{T_R}{\tau_2}. \tag{2.46}$$

This condition is satisfied by choosing the pulse energy very high, such that the slope of the curve in figure 2-9 is very small [36]. Equivalently, the saturation fluence can also be chosen to be very low such that it is much lower than the pulse fluence for moderate pulse energies. The modulation depth can be seen from figure 2-9 as the difference in the amount of absorption for low fluences and the amount of absorption at the pulse energy of interest. Operating at higher pulse energies also increases the modulation depth and therefore decreases the pulse duration.

However, there is an upper limit to the pulse fluence, given by the onset of multiple pulsing. As described in section 2.6, multiple pulsing occurs when the pulse bandwidth is broad, causing the short pulse to see reduced gain compared to cw radiation at the gain peak. When the pulse energy is many times higher than the saturation fluence, then the absorption is no longer a strong function of the pulse energy, as can be seen from fig. 2-9. Therefore, beyond a certain pulse energy, multiple pulses with reduced energy and longer duration are favored over a single short pulse since they see a larger average gain but the same amount of absorption as the single pulse. Pulses with energy more than three to five times the saturation fluence are likely to become unstable and break up into multiple pulses [58, 74]. This criterion sets an upper limit on pulse energies and a lower limit on the saturation fluence. For a given saturable absorber design, the pulse fluence relative to the saturation fluence can be adjusted by changing the mode area on the saturable absorber, optimizing mode-locking operation.

2.10.3 Absorption saturation recovery time

The absorber recovery time influences many aspects of mode-locked operation, particularly self-starting performance and the minimum achievable pulse duration. It should be faster than the cavity round trip time to provide sufficient discrimination between pulsed and cw

operation. This can be seen by comparing the absorption bleaching factors for pulsed and cw operation, $x_p = \Gamma / \Gamma_{sat}$ and $x_{cw} = I / I_{sat}$. In general, the pulse energy Γ is related to the intensity by $\Gamma = I \cdot T_R$. Therefore, the ratio of absorption bleaching factors is given by

$$x_p = \frac{\Gamma}{\Gamma_{sat}} = \frac{IT_R}{I_{sat}\tau_a} = x_{cw}\frac{T_R}{\tau_a}, \tag{2.47}$$

with the absorption saturation recovery time τ_a. This demonstrates that faster recovery times can provide better discrimination between pulsed and cw operation. As previously discussed, making the absorber recovery time shorter than the cavity round trip time also satisfies the condition for no Q-switching (2.43).

Longer absorption saturation recovery times result in better self-starting performance [36, 38]. This can be seen by examining the expression for the mode-locking build-up time, equation (2.42). As previously discussed, shorter mode-locking build-up times result from making the slope *dA/dI* larger, which occurs for lower saturation intensities. This can be done by increasing the absorption cross section or by increasing the absorber recovery time. The extremely fast response time of KLM makes it unsuitable for self-starting, although this fast response time enable generation of the shortest pulses.

In the fast saturable absorber mode-locking model, the minimum pulse duration is influenced by the absorber recovery time, since the response of the absorber must be fast enough to keep the pulse stable against noise perturbations that grow outside the net gain window. With soliton mode-locking, the shortest pulses generated are up to 30 times shorter than the absorption saturation recovery time, emphasizing the strong influence of this parameter on the shortest achievable pulse as discussed in section 2.9 [74].

The semiconductor saturable absorbers considered in this thesis have a bitemporal response time [78]. The fast time constant is determined by the fast relaxation of carriers out of the excited state into a thermalized distribution, which typically happens within less than one picosecond. The slow time constant is given by the time for the excited electron-hole pairs to recombine and happens within tens of picoseconds to nanoseconds. This bitemporal response is advantageous in saturable absorber applications since the slow time constant aids in self-starting

and the fast time constant enables generation of short pulses. In epitaxially grown semiconductor saturable absorbers, the recovery time can be controlled using techniques such as low temperature growth or proton bombardment. This decreases the recovery time but also usually adds non-saturable loss to the device. Carrier dynamics in semiconductors will be described in more detail in chapter 5.

2.10.5 Wavelength dependence and other characteristics

The absorption saturation would ideally be wavelength independent, since otherwise it would introduce a gain filter that would limit ultrashort pulse generation. Kerr lens mode-locking is theoretically wavelength independent; however, a frequency dependent mode size [79] may limit generation of the shortest pulses. Semiconductor saturable absorbers are strongly wavelength dependent, since the absorption coefficient, saturation fluence, and recovery dynamics are strong functions of energy in relation to the band edge. This can limit the spectral operation range of a semiconductor saturable absorber. The device structure can also limit the bandwidth of operation; this will be discussed in detail in chapter 3. Ideally, the saturable absorber device would be wavelength independent and would also introduce a controlled amount of dispersion (usually zero) into the laser cavity.

The damage threshold of a saturable absorber should also be significantly higher than the incident intracavity pulse intensity in order to avoid damage during laser operation. An ideal saturable absorber should not require critical alignment nor impose constraints on laser design. Finally, the absorber should be easy to fabricate and inexpensive.

Overall, careful design of the saturable absorber parameters is essential for optimizing mode-locked operation. The saturable absorber modulation depth should be maximized and the non-saturable losses minimized. The absorption saturation intensity should be high enough such that it is not saturated by the cw intensity and avoids Q-switching, but low enough for efficient self-starting. The absorption saturation fluence should be low enough to avoid Q-switched mode-locking, but high enough to prevent multiple pulsing. The absorption saturation recovery time should be shorter than the cavity round trip time, providing better discrimination between

pulsed and cw operation, and also short to minimize the pulse duration. However, higher absorption saturation recovery times aid in effective self-starting. Finally, the bandwidth of operation is ideally wavelength independent, and the damage threshold is ideally much higher than the expected pulse intensity. These desired absorber characteristics are summarized in table 2-1.

Characteristic	**Ideal saturable absorber**
Modulation depth	high
Non-saturable loss	none
Saturation intensity	-higher than cw intracavity intensity -low enough to faciliate self-starting
Saturation fluence	-low enough to avoid Q-switching and provide high modulation depth -high enough to prevent multiple pulsing
Absorption saturation recovery time	-faster than the cavity round trip time and fast for effective pulse shortening -slow enough to faciliate self-starting
Wavelength dependence	none
Damage threshold	high
Laser design and alignment constraints	none
Device design constraints	none
Fabrication technique	simple
Cost	low

Table 2-1. Summary of the ideal characteristics of a saturable absorber.

2.11 Design of a mode-locked laser

Proper design of a mode-locked laser resonator is critical for optimal laser performance. Lasers are very sensitive to alignment, in cw operation and particularly in pulsed operation. Therefore, cavity design is crucial in building a robust, stable mode-locked laser producing ultrashort pulses. This section will briefly review the description of a Gaussian beam in terms of the q parameter and ABCD matrices, after which the standard four mirror cavity used in most solid-state lasers will be described. Dispersion compensation with both prisms and double chirped mirrors (DCM) will be explained and the optimization of a laser resonator for KLM will also be described in detail.

2.11.1 Four mirror cavity

The four mirror cavity, consisting of two curved mirrors to focus the laser mode into the crystal, an end mirror, and an output coupler, is the most widely used cavity in ultrashort pulse generation from solid-state lasers due to its relative simplicity and ability to create a tightly focused mode within the laser crystal [80]. It is usually referred to as a "z" or "x" fold cavity depending on the particular layout. A schematic of a standard four mirror "z" cavity is shown in figure 2-10. This cavity consists of an end mirror HR, an output coupler OC, and two curved mirrors M1 and M2 separated by a distance b, with a crystal CR positioned between them at a distance a from M1. The crystal is cut for Brewster's angle incidence, to minimize unwanted reflections that would increase laser loss; this sets the polarization of the laser beam. The HR and M1 are separated by a distance d_1, while the OC and M2 are separated by d_2. The angle of each of the curved mirrors is set to compensate the astigmatism of the crystal; this will be discussed below.

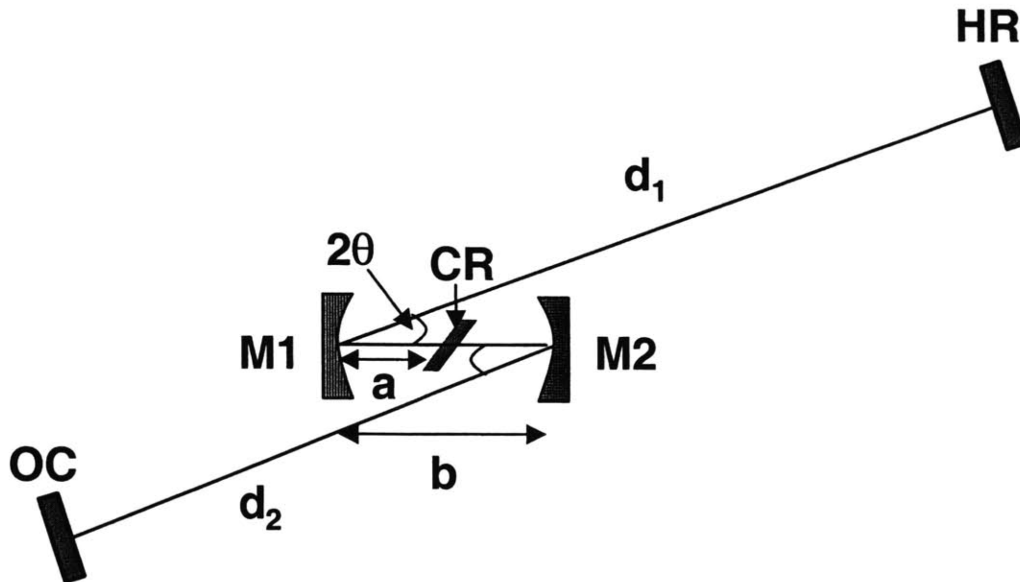

Figure 2-10. Schematic of a z-fold cavity.

The electric field profile in a laser resonator is described by the paraxial wave equation, with the solutions given by Hermite-Gaussian functions. Therefore, the powerful analysis techniques based on the representation of a Gaussian beam in terms of the q parameter and ABCD matrices can be used to calculate the spot sizes and stability regions of any laser resonator [81]. The beam waist size w (defined as the transverse radius where the amplitude is $1/e$ of its value on axis) as a function of b at any position in the four mirror cavity of figure 2-10 can be calculated using ABCD matrices for given curved mirror radii, d_1, and d_2. The cavity can either be symmetric ($d_1=d_2$) or asymmetric (d_1 and d_2 are different). Figure 2-11 shows the beam waist at the center of the crystal for a symmetric cavity as a function of d. The parameters for the calculation are stated in the figure caption. This cavity has one stability region (a region where lasing modes can exist), a characteristic of symmetric cavities.

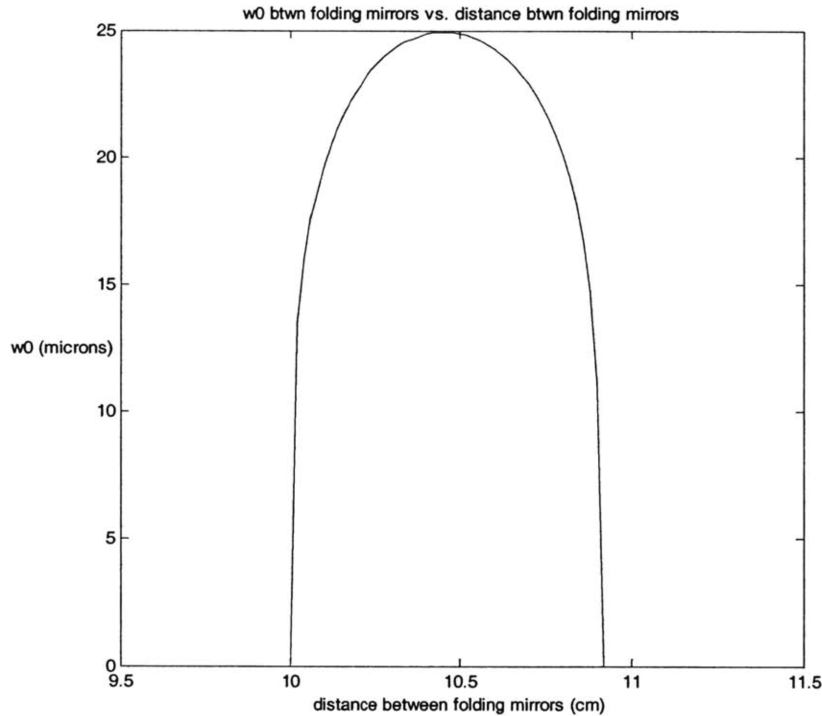

Figure 2-11. Calculated beam waist size as a function of b for a symmetric four mirror cavity. The parameters for the calculation are $d_1=d_2=60$ cm and the radius of curvature (ROC) is 10 cm for both curved mirrors (see figure 2-10). The wavelength is 860 nm.

The more widely used asymmetric cavity is modeled in figure 2-12, with the calculation parameters also given in the figure caption. This cavity shows two stability regions as a function of b, with a region where no lasing modes exist in between. In an asymmetric cavity, the separation between the two stability regions depends on the ratios of the two arms. In both symmetric and asymmetric cavities, the beam waist in the crystal decreases as the arm lengths are increased, and also as the radii of the curved mirrors M1 and M2 are decreased. Therefore, the laser mode within the crystal can be scaled to a desired value by varying these parameters. Smaller laser spot sizes within the crystal can increase the self-phase modulation and generate broader spectra; care must be taken to avoid pulse instabilities due to the high nonlinearities. The pump mode is usually set to match the laser mode within the crystal, providing maximum gain. The pump beam is usually focused through M1 or M2 (through an anti-reflection coating on the back of the mirror) into the laser crystal, with appropriate focusing optics chosen to set the pump mode size within the crystal.

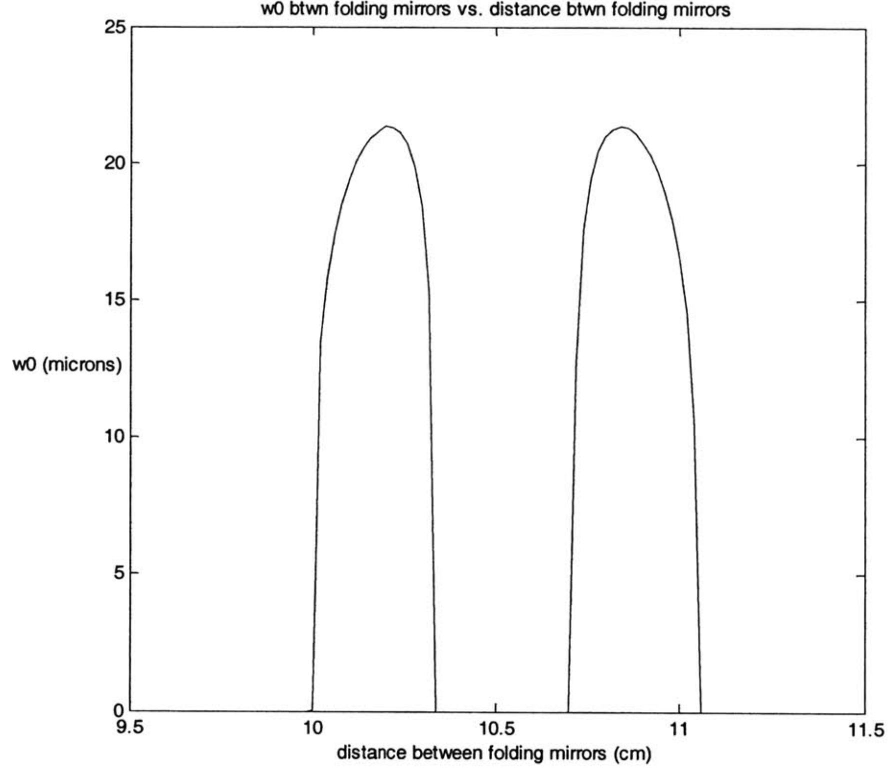

Figure 2-12. Calculated beam waist size as a function of *b* for an asymmetric four mirror cavity. The parameters for the calculation are d_1=80 cm and d_2=40 cm and the radius of curvature (ROC) is 10 cm for both curved mirrors (see figure 2-10). The wavelength is 860 nm.

The Brewster cut crystal causes the laser mode to be astigmatic, having different sizes in the tangential (parallel to the plane of incidence) and sagittal (perpendicular to the plane of incidence) plans. This astigmatism can reduce the gain due to the poor overlap with the pump beam (ideally circular), reducing the maximum output power from the laser, and is also detrimental to Kerr lens mode-locking. The angle of the curved mirrors M1 and M2 can be set to compensate the astigmatism introduced by the crystal, using the expression

$$f\left(\frac{1}{\cos\theta}-\cos\theta\right)=t\frac{\sqrt{1+n^2}}{n^2}\left(1-\frac{1}{n^2}\right) \quad (2.48)$$

where t is the crystal thickness, n is the refractive index of the crystal, and f is the focal length of the curved mirrors [82]. This expression is typically used to set the incidence angles of the curved mirrors in a z or x cavity, depending on the crystal thickness.

2.11.2 Dispersion compensation using prism pairs

Prism pairs are the most common method of dispersion compensation in a femtosecond laser cavity. Prism pairs provide both angular dispersion from their separation, which is anomalous (negative), and material dispersion from the insertion of each prism into the laser beam, which is usually normal (positive) dispersion but can be negative for certain prism materials at a given wavelength. The prism pair is usually designed to introduce anomalous dispersion into the laser cavity to compensate the normal dispersion of the solid state laser crystal; this also aids in soliton-like pulse shaping with SPM and GDD as previously discussed in section 2.3. It should be noted that angular dispersion can also be generated using grating pairs [83]; these devices are too lossy for dispersion compensation within the laser cavity, but are useful for providing large amounts of dispersion for external pulse compression.

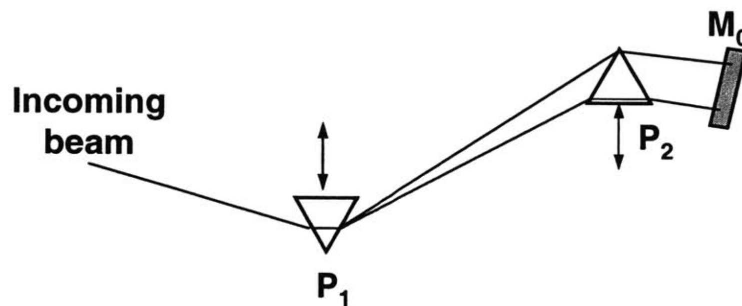

Figure 2-13. Dispersion compensation using a prism pair.

Figure 2-13 depicts a standard geometry for dispersion compensation using a prism pair. The laser beam enters the prism sequence, passes through the two prisms and the distance separating them, and is spectrally dispersed on the end mirror. It is then retro-reflected back through the prism sequence, spatially recompressing the beam. Two additional prisms separated by the same distance can also be used instead of an end mirror to recollimate the spatially dispersed beam after the first prism pair [26, 84]. The apex angle of the prisms is cut such that the laser beam enters and leaves each prism at Brewster's angle, traveling parallel to the base of the prism within the material. The amount of negative GDD introduced by the prism separation can be obtained by calculating the path length between the two prisms as a function of wavelength and taking the second derivative of the associated phase change. This can be approximated by [54]

$$GDD_{ang}(\lambda_c) \approx -4l \frac{\lambda_c^3}{2\pi c^2} \left(\frac{dn}{d\lambda} \right)^2, \tag{2.49}$$

where l is the distance between the prisms and $n(\lambda)$ is given in equation (2.18). The positive dispersion introduced by the prism pair is calculated from knowing the amount of prism material traversed by the laser beam, expressed by

$$GDD_{mat}(\lambda_c) = \frac{\lambda_c^3}{2\pi c^2} L \frac{d^2 n}{d\lambda^2}, \tag{2.50}$$

where L is the amount of material traversed by the beam. The sum of these two expressions gives

$$GDD_{tot}(\lambda_c) \approx \frac{\lambda_c^3}{2\pi c^2} \left[Ln'' - 4n'^2 l \right], \tag{2.51}$$

the total dispersion introduced by the prism sequence. It is clear from this expression that a continuously variable amount of GDD can be introduced by varying the prism separation and insertion. Prism pairs have been used to generate pulses as short as 8.5 fs [85]. Third and fourth order dispersion terms introduced by the prism pair limit generation of pulses below this duration, since there are an insufficient number of adjustable parameters to control both the GDD and TOD except in certain wavelength ranges for particular prism materials [85-87]. Other disadvantages of the prism pair include insertion loss due to imperfections in the prism material or Brewster cut of the prisms. However, the simplicity and low cost of this technique make it the preferred method for generating all but the shortest sub-10 fs pulses.

2.11.3 Dispersion compensation using double-chirped mirrors

Double-chirped mirrors are a powerful technology enabling the generation of few-cycle pulses in many laser systems, including Ti:sapphire, Cr:LiCAF, Cr:forsterite, and Cr:YAG [40, 88-91]. These mirrors are designed to compensate GDD as well as higher order dispersion over a very broad wavelength range, and have been designed to cover one octave of bandwidth. Double chirped mirrors can be used both with and without prisms to generate ultrashort pulses.

Standard Bragg reflectors consist of alternating pairs of high and low index layers that are typically made of TiO_2/SiO_2 pairs grown by ion beam sputtering on an SiO_2 substrate (Figure 2-14 (a)). The bandwidth of these mirrors is determined by the refractive index of the two materials along with the number of pairs that are used [81]. The dispersion of these mirrors is usually constant as a function of wavelength.

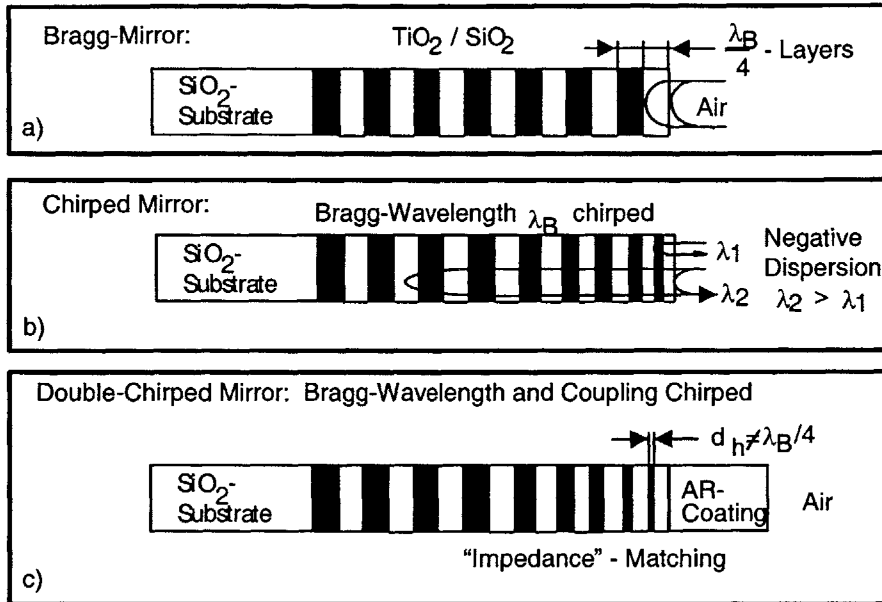

Figure 2-14. (a) Standard Bragg high reflector structure. (b) Single chirped mirror structure. (c) Double chirped mirror structure (figure reprinted from ref [92]).

The development of chirped mirrors provided a way to incorporate dispersion compensation into the mirror structure (Figure 2-14 (b)) [93, 94]. Changing the Bragg wavelength of the quarter-wave stack as a function of depth into the mirror causes longer wavelengths to penetrate deeper into the mirror than shorter wavelengths. Therefore, longer wavelengths traverse a larger path length than shorter wavelengths, introducing dispersion. This can be tailored to introduce a controlled amount of dispersion over a large wavelength range. The starting point of this design is a mirror with a linearly chirped Bragg wavelength. However, these mirrors exhibit large oscillations in the GDD, which tend to break up a broadband pulse and limit the achievable bandwidth. The oscillations are due to light reflected at the surface of the mirror, which interferes with the reflections from deeper in the mirror and leads to Gires-Tournois-like interference, creating strong spectral oscillations in the dispersion. A computer

optimization algorithm is therefore used to minimize the oscillations. These mirrors have been used to generate pulses as short as 7.5 fs [95].

An analytic understanding of chirped mirrors was obtained by the application of coupled-mode and transmission line theory [92, 96, 97]. The goal was to further understand the origin of the oscillations in the group delay and obtain insight into the best starting design to achieve a certain group delay characteristic. It was found that the oscillations in the group delay could be modeled as an impedance matching problem with coupled mode theory. A Bragg mirror composed of high and low index pairs can be described by:

$$\frac{dA}{dm} = -i\delta(m)A(m) - i\kappa(m)B(m)$$
$$\frac{dB}{dm} = +i\kappa(m)A(m) + i\delta(m)B(m) \tag{2.52}$$

In these equations, A and B are the amplitudes of the forward and backward propagating waves (leftward and rightward in figure 2-14), respectively. The detuning coefficient δ and the coupling coefficient κ are functions of the normalized distance m, which is the thickness of a single layer pair and may vary within the mirror structure. Exact expressions for the coupling and detuning coefficients can be obtained [96]. When the reflectivity, r, at an index discontinuity is much less than 1, these equations can be approximated by $\delta(m) \approx \phi_h(m) + \phi_l(m)$ and $\kappa(m) \approx -2r\sin[\phi_h(m)]$, with ϕ_h and ϕ_l the phase shifts in the high and low index layers, respectively. This shows that the coupling coefficient is uniquely determined by the thickness of the high index layer and therefore the detuning coefficient is determined by the thickness of the low index layer.

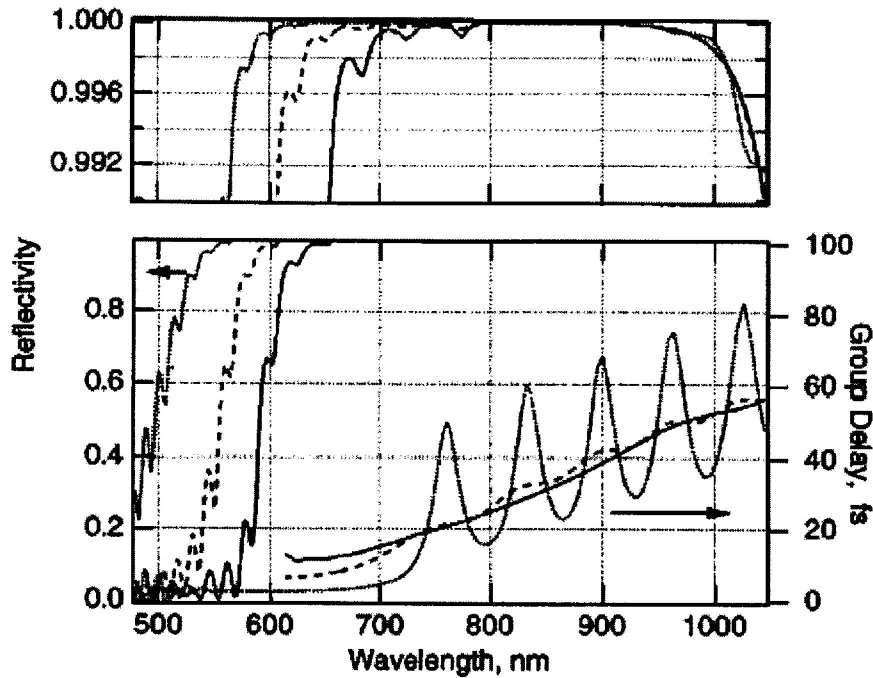

Figure 2-15. Reflectivity and group delay of chirped mirrors. The upper portion is the enlarged top part of the reflectivity. The dotted curves display the reflectivity and group delay of a chirped mirror. The dashed curve shows the result for a double chirped mirror with a linear chirp of the thickness of the high index layers. The solid curve shows the result for a double chirped mirror with a quadratic chirp of the high index layer thickness (reprinted from ref. [92, 97]).

The coupled-mode equations (2.52) can be shown to be equivalent to transmission line equations [96]. From transmission line theory, it is known that unwanted reflections can be minimized by slowly varying the impedance. This is accomplished in the mirror structures by smoothly varying the thickness of the high index layer as well as the Bragg wavelength of the mirror as a function of the penetration depth, resulting in a "double-chirped" mirror. The thickness of the high index layer goes from nearly zero to a standard quarter wave layer. An anti-reflection coating on the front surface of the mirror is also added to impedance match the incident and transmitted waves at the air-mirror interface (Figure 2-14 (c)), after which the whole structure is further optimized [92, 96-98]. The combination of the impedance chirp, Bragg wavelength chirp, and anti-reflection coating enables dispersion compensation over a wide wavelength range with minimal oscillations and high reflectivity [92, 97]. A comparison of the

group delay dispersion and reflectivity for a linearly chirped mirror (the starting point for the chirped mirror design) and a double chirped mirror is shown in figure 2-15.

Limitations in the use of double chirped mirrors for ultrashort pulse generation usually arise from the ion beam sputtering process used to fabricate the mirrors, since extremely high control over the thickness of the dielectric layers is required to minimize dispersion oscillations over a broad bandwidth. The group delay and group delay dispersion of double chirped mirrors, as well as other dispersive optical elements, can be measured with white light interferometry. This is a standard technique for measuring group delay dispersion from different optical elements and is described in reference [99].

The oscillations in a double chirped mirror structure are more difficult to suppress for broader bandwidths around one octave. Therefore, recent experiments have used pairs of mirrors designed to have oscillations out of phase with each other, such that when the dispersion oscillations are added over all the cavity elements, they cancel out and produce a smooth spectral dispersion variation [100]. This technique has enabled the shortest pulses generated directly from a laser oscillator, with durations of 5 fs [17]. Other groups have used DCMs, chirped mirrors, and/or prisms external to the laser cavity in combination with spectral broadening techniques based on SPM in fibers or hollow gas-filled waveguides to compress pulses to durations of 4 fs [101, 30].

2.11.4 Optimization of laser cavities for Kerr lens mode-locking

Many research groups have studied the optimization of laser cavities for Kerr lens mode-locking [66, 80, 102-107]. KLM is very sensitive to several cavity parameters, particularly the separation between the two curved mirrors (in a four mirror cavity) and the crystal position between the two mirrors. The dispersion operating point must also be carefully chosen for a given crystal thickness, and the astigmatism compensation angle of the curved mirrors must be set correctly. Careful cavity alignment is essential for stable, reproducible KLM, particularly in low gain, thermally sensitive lasers like Cr:forsterite and Cr:LiSAF.

The general procedure for designing a KLM laser is to calculate the value of a parameter sensitive to Kerr lensing as a function of cavity settings to determine the operating point at which KLM is optimized. The most common choice is to calculate the change of the beam waist between the high and low intensity laser modes at a certain point in the cavity [67, 68, 103, 108]. This parameter, called the Kerr-lens sensitivity, is given by the derivative of the beam waist with respect to power [67, 68, 103]:

$$\delta = \left(\frac{1}{w} \frac{dw}{dP} \right)_{P=0} \tag{2.53}$$

Other definitions have been suggested for a parameter sensitive to Kerr lensing, based on the transmission of the laser mode through an intracavity slit, the change in gain between the high and low intensity laser modes, or the change in power between the high and low intensity laser modes [80, 109].

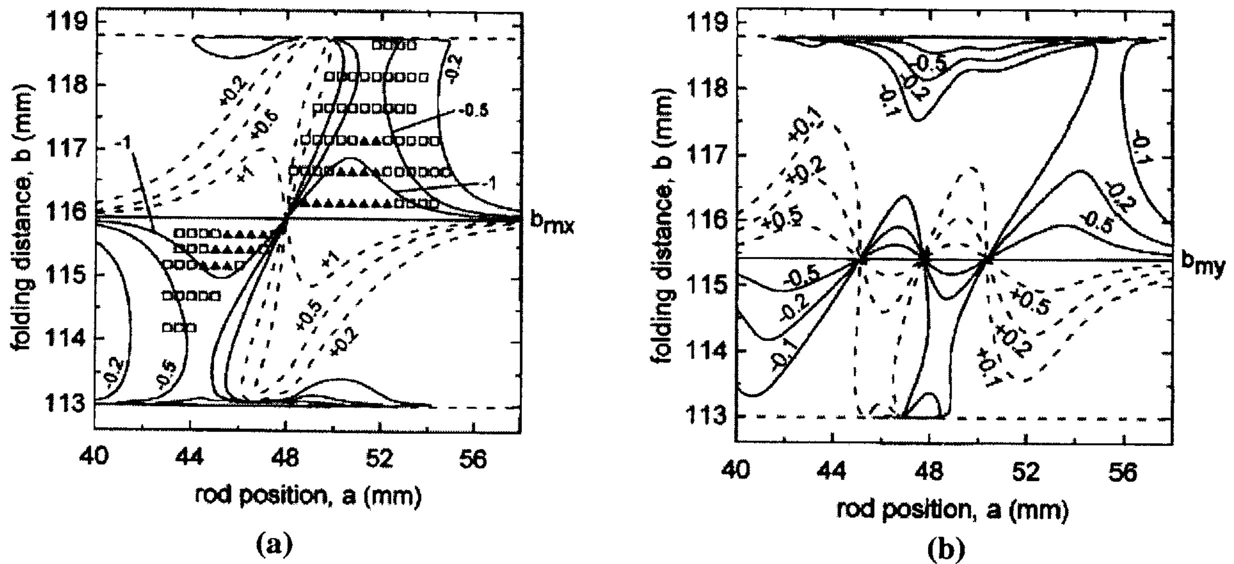

Figure 2-16. Contour lines of the Kerr-lens sensitivity (parameter of the curves) in (a) the tangential plane and (b) the sagittal plane as functions of b, the distance between the curved mirrors, and a, the distance from M1 to the crystal as defined in figure 2-10, for a symmetric cavity with d_1=d_2=85 cm (reprinted from ref [103]). The Kerr-lens sensitivity is calculated at the HR shown in figure 2-10. The squares are the points where KLM was initiated by tapping an end mirror, while the filled triangles are the points at which KLM was self-starting. A hard aperture was used to cut the beam in the tangential plane.

In hard aperture KLM, δ is typically calculated near one of the cavity end mirrors, at which a physical aperture can be placed. The Kerr lens sensitivity is calculated within the crystal in soft aperture KLM. Contour plots of δ as functions of the crystal position and curved mirror separation can be made for both symmetric and asymmetric cavities [103]. The Kerr lens sensitivity is calculated for a hard-aperture KLM symmetric cavity in the tangential (*xz*, horizontal plane, or the plane of the laser cavity) and sagittal (*yz*, vertical plane, orthogonal to the plane of the laser cavity) planes, and the resulting contour plots are depicted in figure 2-16.

From these plots it is clear that the Kerr-lens sensitivity is maximized near the middle of the stability region in a symmetric cavity, with the crystal also near the center of the two curved mirrors. Self-starting was obtained at the points of largest sensitivity, and non-self-starting KLM was obtained over a wide range of crystal positions and mirror separations. Astigmatism causes the Kerr-lens sensitivity to increase in the tangential plane and decrease in the sagittal plane; therefore, in hard-aperture KLM the aperture should cut the beam in the tangential plane with a vertical slit [66, 103]. The symmetric configuration results in strong changes of the beam waist with pump intensity and was shown to enable self-starting KLM operation [103, 67]. Self-starting pulse durations were limited to 50 fs in this cavity. The large Kerr lens sensitivity values for a symmetric resonator occur very near the stability boundary and therefore these cavities are sensitive to environmental perturbations.

Figure 2-17 plots the Kerr-lens sensitivity for an asymmetric cavity. In an asymmetric cavity the Kerr-lens sensitivity is maximized near the outer edge of the inner stability region and the inner edge of the outer stability region. The crystal position should be set closer to M2 for optimized operation in the inner stability region and closer to M1 for operation in the outer stability region, when $d_1>d_2$. As in the symmetric case, KLM action is stronger in the tangential plane, demonstrating that proper astigmatism compensation is important in generating ultrashort pulses. It has been shown that operation near the inner edge of the outer stability region is most favorable for stable KLM [68, 106], although KLM can be achieved in the inner stability region as well. This is because the laser cavity is more sensitive to misalignment in the inner stability region, making stable KLM more difficult. This was experimentally observed in figure 2-17, as KLM was obtained over a larger range in the outer stability region. The outer stability region is

referred to as the "LMS" (low misalignment sensitivity) region and the inner stability region is called the "HMS" (high misalignment sensitivity) region in some of the literature [68].

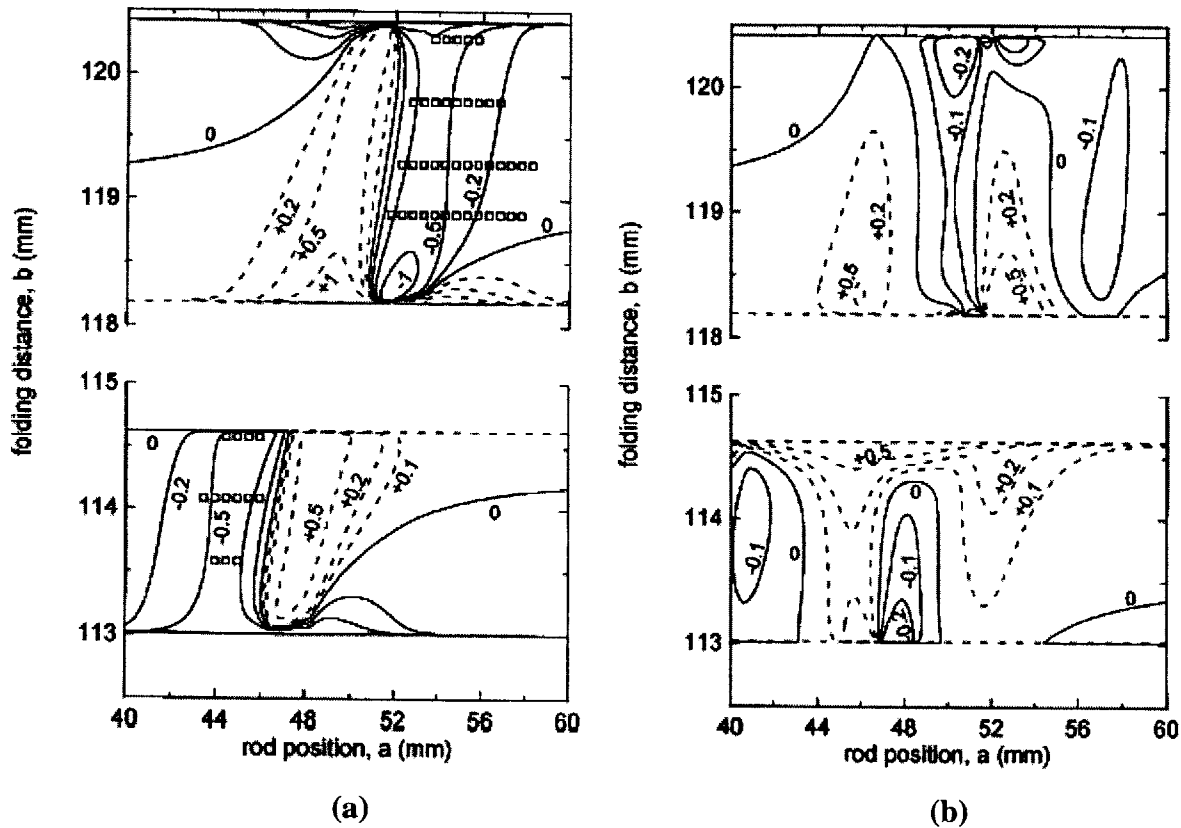

Figure 2-17. Same as in figure 2-16, for an asymmetric cavity with d_1=50 cm and d_2=110 cm (reprinted from ref [103]).

The ratio of arm lengths d_1 and d_2 has also been shown to influence KLM performance. In an asymmetric cavity the optimal arm length ratio is generally thought to be ~1.5-2 [56, 80]. This provides stability against environmental perturbations while keeping a high Kerr lens sensitivity. The length of the long arm is often set by the prism separation (typically 50-100 cm) in cavities that use prisms for dispersion compensation. It has also been shown that hard aperture KLM is most effective when the aperture is placed in the short cavity arm (usually near the output coupler) [66, 68].

The simulations and experiments shown in figures 2-16 and 2-17 were derived for hard aperture KLM. Soft aperture KLM generally follows the same trends; the KLM strength in an

asymmetric cavity is maximized near the inner edge of the outer stability region, with the crystal closer to M1 [80, 106]. In soft aperture KLM, the cavity and pump mode focusing are designed to make the pump mode smaller than the cw laser mode within the crystal for operation near the inner edge of the outer stability region. This optimizes the overlap between the pump mode and the mode-locked laser mode due to the self-focusing induced smaller mode size of the latter. This often results in powers nearly a factor of 2 higher for mode-locked operation as compared to cw operation.

A detailed model of soft aperture KLM must consider the overlap of the laser and pump modes throughout the crystal, not just at a single plane. One method of doing this integrates δ along the propagation direction within the crystal [108]. Another technique considers the crystal as a succession of thin Kerr lenses and determines the laser intensity after each lens using ABCD matrices, inputting the result into the next lens matrix; this is called the split-step method [107, 109]. In practice, it is usually sufficient to calculate the beam waist sizes of the pump and cw laser modes within the crystal and set the pump mode to be smaller than the cw laser mode near the inner edge of the outer stability region. A laser mode that gives optimized overlap typically has a confocal parameter that is approximately equal to the length of the laser crystal [80, 105].

In summary, optimized cavity design is critical for generation of ultrashort pulses using KLM. The curved mirror separation and crystal position are the most important parameters for generating short pulses. Operation near the middle of the stability region for a symmetric cavity and near the inner boundary of the outer stability region for an asymmetric cavity has been shown to provide the strongest change of the intracavity laser mode with intensity, optimizing KLM operation. Careful choice of the aperture position and size in hard aperture KLM or the pump and laser mode sizes in soft aperture KLM is essential for optimizing KLM action. It should be noted that the above guidelines have been derived for the standard z or x four mirror resonators. However, other cavity designs have been used in KLM lasers, including extremely compact cavities [104, 110], ring lasers [111], curved mirrors with different radii of curvature [112], and cavities with additional folds [17]. Thermal lensing modifies the modes within the crystal and often must also be taken into account, particularly in Cr:forsterite and Cr:YAG lasers [89, 113-115].

2.12 Pulse measurement

Femtosecond laser pulses are too short to be measured by conventional methods, since the detectors used to measure longer pulses have a time response of ~ps at best. Ultrashort pulses can be measured if a shorter reference pulse is available by measuring the intensity cross-correlation,

$$A_c(\tau) = \int_{-\infty}^{\infty} I_s(t) I_r(t-\tau) dt \,, \tag{2.54}$$

where $I_s(t)$ is the signal to be measured and the reference pulse is given by $I_r(t)$. An ideal reference pulse is a delta function in time. By taking the Fourier transform of the cross-correlation, dividing by the known Fourier transform of the reference pulse, and taking the inverse Fourier transform of the result, the intensity profile of the signal pulse can be obtained. However, this technique does not give any information on the phase content of the signal pulse [54].

In many cases, a shorter reference pulse is not available, and therefore the signal itself is used as a reference. This technique, called autocorrelation, is perhaps the most common method of measuring femtosecond pulses [54]. In an autocorrelation measurement, the pulse is split into two identical replicas, which are delayed in time with respect to each other. A nonlinear process with a quasi-instantaneous response is used to generate a signal proportional to the temporal overlap of the two replicas. By precisely varying the delay between the two pulses and measuring the nonlinear signal at each point, the overlap between the two intensity envelopes is scanned as a function of delay. Autocorrelations can be performed in either a non-collinear or collinear geometry, depending on the application. The nonlinear process is usually a second order effect, since the nanojoule pulse energies from femtosecond oscillators limit the use of higher order processes. The most commonly used techniques for generating a nonlinear signal are second harmonic generation (SHG) in a nonlinear crystal or two photon absorption (TPA) in a semiconductor photodiode [116, 117].

A schematic of an interferometric autocorrelator is shown in figure 2-18. It consists of a Michelson interferometer with a variable delay in one arm. The input pulse is split at the beam splitter (BS1), and the two replicas travel down the respective arms of the interferometer and are retroreflected by two 45 degree angled mirrors. The pulses are recombined at the second beam splitter (BS2) and propagate collinearly to the second harmonic generating crystal (CR). The generated second harmonic signal (due to sum frequency mixing between the two beams) is measured as a function of time delay and focused onto a detector D after passing through a filter to eliminate the fundamental. The detector is usually a photomultiplier tube or photodiode. Two beam splitters are used in order for the two beams to pass through the same amount of material. The use of identical beam splitters and mirrors in each arm ensures dispersion balance between the two arms.

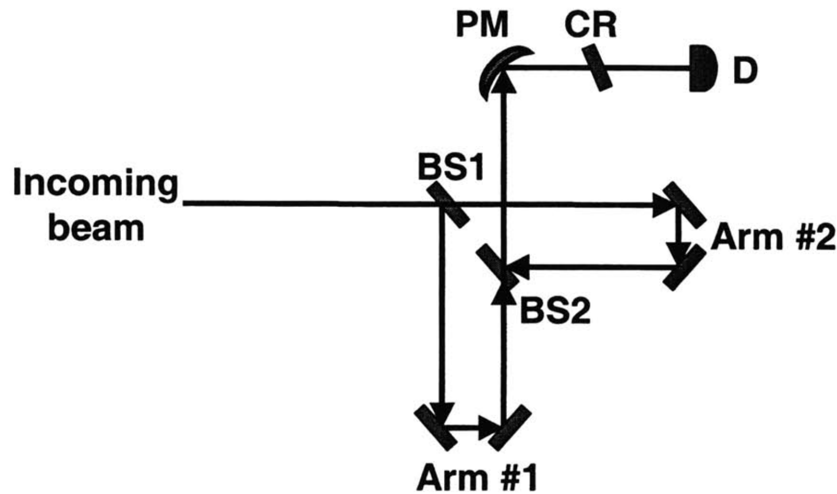

Figure 2-18. Schematic of an interferometric autocorrelator.

The pulse duration can be obtained by considering the signal measured by the detector:

$$G_2(\tau) = \int_{-\infty}^{\infty} \{[E_1(t-\tau) + E_2(t)]^2\}^2 dt \tag{2.55}$$

Here E_1 and E_2 are the electric fields of each pulse, and τ is the time delay between the pulses. This expression can be rewritten as

$$G_2(\tau) = 1 + 2A(\tau) + 4\,\mathrm{Re}[B(\tau)e^{-i\omega_c\tau}] + \mathrm{Re}[C(\tau)e^{-2i\omega_c\tau}] \tag{2.56}$$

where

$$A(\tau) = \int_{-\infty}^{\infty} I(t)I(t-\tau)dt \tag{2.57}$$

$$B(\tau) = \frac{1}{2}\int_{-\infty}^{\infty} \{I(t) + I(t-\tau)\} E(t)E^*(t-\tau)dt \tag{2.58}$$

$$C(\tau) = \int_{-\infty}^{\infty} E^2(\tau)E^{2*}(t-\tau)dt\,. \tag{2.59}$$

For these expressions the normalization $\int_{-\infty}^{\infty} |I(t)|^2 dt = 1$ is used. At zero delay (τ=0) the sum of the terms is at its maximum of $G_2(0)$=8. When the delay is one-half an optical cycle the fields destructively interfere and the signal is zero. For large delays, the fields do not interfere any more and the signal is a superposition of two frequency doubled pulses, $G_2(\infty) = 1$. Therefore, an interferometric autocorrelation (IAC) trace has a peak to background ratio of 8:1. A typical IAC is shown in figure 6-5 (a). It is important to use a scan speed slower than the detector response time to resolve the interference fringes in this trace.

The pulse duration can be extracted from the full-width at half maximum (FWHM) of the autocorrelation by assuming a pulse shape and relating the measured FWHM of the autocorrelation and the FWHM of the pulse intensity profile through a known scaling factor for the pulse shape. These scaling ratios are given by $\tau_{ac} / \tau_p = 2\ln 2$ for a Gaussian pulse and $\tau_{ac} / \tau_p = 1.7627$ for a sech^2 pulse, where τ_{ac} and τ_p are the FWHM of the autocorrelation and pulse intensities. More accurate determinations of the pulse duration are obtained by various pulse reconstruction algorithms that fit the IAC by taking the measured power spectrum and searching for the spectral phase that gives the best agreement with the measured autocorrelation. The pulse duration and shape can be determined by Fourier transforming the best fitting phase profile. An interferometric autocorrelation can qualitatively show the presence of chirp on the pulse; this is discussed in more detail in reference [54].

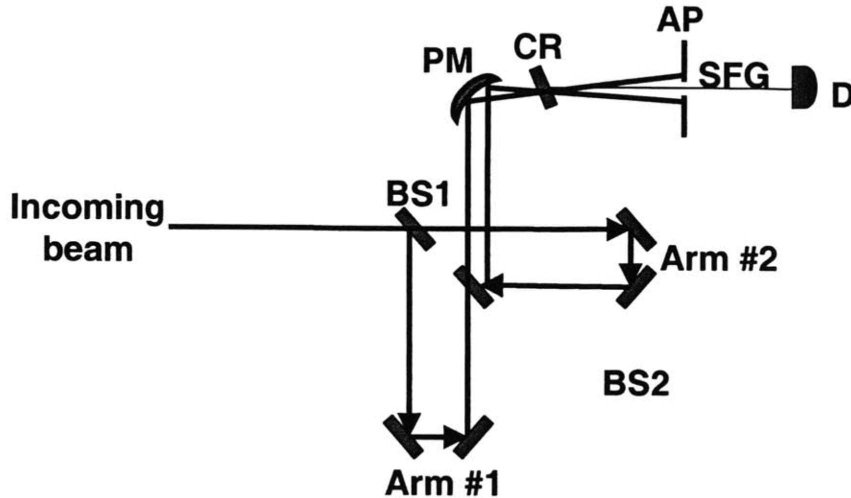

Figure 2-19. Schematic of a non-collinear, background-free intensity autocorrelator.

An intensity autocorrelation can be obtained by averaging over the interference terms $B(\tau)$ and $C(\tau)$. This can be done with time averaging (by choosing a detector that is too slow to resolve these terms) or spatially averaging (using non-collinear beams that average between different phases of the interference terms). This reduces equation (2.56) to

$$D(\tau) = 1 + 2A(\tau). \tag{2.60}$$

where $D(\tau)$ is the intensity autocorrelation. This is most commonly done using a non-collinear geometry (figure 2-19). The beams are made to propagate parallel to one another without overlapping after reflecting from the second beam splitter. The lens or mirror focuses the two beams to overlap on the same spot in the nonlinear crystal. The phase-matched second harmonic signal due to sum frequency generation (SFG) from the two beams propagates to the detector in a direction between the SHG from each of the two original beams. The peak to background ratio of this signal is 3:1 from equation (2.60). Spatial filtering can be used in the intensity autocorrelation to eliminate the background signal due to the SHG from each beam, as shown in figure 2-20. This is called the background-free intensity autocorrelation ($D(\tau) = 2A(\tau)$) and is often used to make measurements with a high dynamic range [54, 118]. The pulse duration can be calculated from the intensity autocorrelation in a similar manner as the interferometric autocorrelation, by assuming a pulse shape and relating the measured FWHM of the autocorrelation and the FWHM of the pulse intensity profile. The scaling factors for the

intensity autocorrelation are $\tau_{ac} / \tau_p = 1.414$ for a Gaussian pulse and $\tau_{ac} / \tau_p = 1.543$ for a $sech^2$ pulse.

Several important issues must be considered when performing autocorrelation measurements. If a nonlinear crystal is used for second harmonic generation, the thickness must be chosen such that phase matching occurs over a bandwidth larger than the pulse spectrum to avoid errors due to spectral filtering; the crystal also must not introduce significant dispersion. For sub-10 fs pulses, the crystal thickness is usually less than 100 μm to satisfy these conditions. In addition, when measuring pulses with bandwidths exceeding an octave, the second harmonic signal will overlap with the fundamental spectrum; the SHG signal can still be distinguished by its orthogonal polarization, but care must be taken to suppress the fundamental since the SHG signal is very small due to the thin crystal that must be used. When using two-photon absorption in a photodiode for pulse measurement, the bandgap of the photodiode must be chosen to measure only the second harmonic wavelength and not the fundamental wavelength (for a non-octave spanning spectrum). Finally, the interferometric autocorrelation is preferred over the simpler intensity autocorrelation for measuring extremely short pulses due to errors introduced by the non-collinear overlap of the beams within the nonlinear element [56, 89] that limit the time resolution of the system.

Recently, other pulse characterization techniques have been developed to extract the complete amplitude and phase profile of the ultrashort pulses. The most widely used are frequency-resolved optical gating (FROG) [119-123] and spectral phase interferometry for direct electric field reconstruction (SPIDER) [124-126]. FROG is essentially an autocorrelator followed by a spectrometer, with which the signal spectrum as a function of time delay can be plotted. From this data, an iterative deconvolution algorithm is used to find the electric field that best reproduces the data. Several configurations have been demonstrated with different geometries and methods for obtaining a nonlinear signal [121]; the version based on second-harmonic generation has proven the most useful for measuring ultrashort pulses, as it has been used to measure pulse durations down to 4.5 fs [123]. This technique has the advantage of a simple experimental setup, since the signal from an autocorrelator must simply be sent into a

spectrometer. However, the data set is large and the algorithms required to reconstruct the electric field are complex.

SPIDER, in contrast to FROG, enables direct reconstruction of the electric field from the measured data. In this measurement, the input pulse is split into two replicas, with a fixed time delay between them. Each replica is upconverted using sum-frequency generation (SFG) with a chirped, stretched pulse (usually derived from the original pulse) in a nonlinear crystal. The time delay between the replicas causes each replica to be frequency mixed with a different temporal slice of the stretched pulse, and therefore a different frequency since the pulse is chirped. An interferogram is then recorded with a spectrometer. No moving parts are used in the experimental setup and only one interferogram is measured. A fast, non-iterative algorithm can be used to directly extract the electric field. This technique has been used to measure sub-6-fs pulses [126]. Compared to FROG, the extraction of the amplitude and phase of the electric field is much simpler; however, the experimental setup is much more complex. Both FROG and SPIDER can be used for single shot pulse measurements from amplified systems as well as pulse trains from oscillators, and are important tools in ultrashort pulse characterization.

Chapter 3

Previous Work on Semiconductor Saturable Absorbers and Diode-Pumped Solid-State Lasers

3.1 Introduction

The passive mode-locking techniques discussed in the previous chapter all rely on an intensity-dependent loss or gain to favor pulsed laser operation. This can be implemented using semiconductor saturable absorbers. These are devices that introduce saturable loss into the laser cavity, favoring high intensity pulsed operation over cw operation at low intensities. These devices offer many advantages in comparison to other passive mode-locking techniques, including increased laser stability and robustness as well as operation that is often self-starting. When compared to KLM, they have the additional advantages of decoupling the gain and mode-locking mechanisms as well as relaxing the critical cavity alignment required for KLM.

Until recently, the majority of semiconductor saturable absorbers were grown with molecular beam epitaxy (MBE). These devices, called semiconductor saturable absorber mirrors (SESAM) [36, 38, 127] or saturable Bragg reflectors (SBR) [37, 128] have been very successful in mode-locking solid state lasers, either by starting and stabilizing KLM, generating two-cycle pulses [40, 129], or by independently mode-locking a laser, enabling simpler cavity designs and more compact lasers. In combination with diode pumping, epitaxially grown saturable absorbers have enabled the development of extremely compact, robust, and inexpensive lasers, demonstrating the potential of these systems for replacing Ti:sapphire lasers in some applications [130, 131]. Recently, non-epitaxially grown saturable absorbers based on semiconductor nanocrystallites doped into silica films and deposited on sapphire substrates have also been developed and applied to self-starting mode-locking in a Ti:sapphire laser [45, 46]. These

devices offer several advantages, including increased versatility and reduced cost, over epitaxially grown saturable absorbers.

In this chapter, the development of both epitaxially and non-epitaxially grown saturable absorbers will be described in detail, along with previous research on the diode-pumped colquirite-based lasers that were used in part of this work. Section 3.2 will describe epitaxially grown semiconductor saturable absorbers, describing several different designs to demonstrate the concept of scaling these devices for different applications by changing design parameters. The development of non-epitaxially grown saturable absorbers will be discussed in section 3.3. Finally, cw and mode-locked operation of colquirite-based lasers pumped by ion lasers, broad stripe diodes, and single mode diodes will be discussed in section 3.4.

3.2 Epitaxially grown semiconductor saturable absorbers

3.2.1 General principles of epitaxially grown saturable absorber design

In the past, bulk semiconductors were used to mode-lock color-center [132] and diode lasers [133]. They were also considered for solid-state laser mode-locking, but their undesirable properties including high insertion loss, low saturation intensity, long carrier lifetimes, and low damage threshold made them unsuitable for this application. This problem was solved with the invention of the semiconductor saturable absorber mirror (SESAM) [36, 127] and saturable Bragg reflector (SBR) [37]. These are the most common saturable absorber devices used in solid-state laser mode-locking, based on semiconductor quantum wells grown by molecular beam epitaxy (MBE) in a mirror structure.

In general, these devices consist of two mirror structures, forming a Fabry-Perot resonator, with the saturable absorber layer in between. The bottom mirror is typically a high reflectivity mirror, often a distributed Bragg reflector (DBR) grown by MBE and consisting of alternating high and low index semiconductor layers. Dispersion and bandwidth properties of DBRs are usually poor compared to standard dielectric mirrors due to the small index contrast

between the high and low index materials; choice of these materials is limited by the lattice matching requirements imposed by the epitaxial growth process. A saturable absorber consisting of one or more quantum wells, sometimes with transparent spacer layers, is grown on top of the DBR, and then a top reflector is added with reflectance properties tailored for the specific application. The reflectivity of the top mirror controls most aspects of device operation since it determines the intensity entering the device, which establishes the fluence incident upon the saturable absorber layer and also either accentuates or de-emphasizes the properties of the bottom mirror. Absorption saturation is provided by band filling in the semiconductor. These devices can be regarded as nonlinear mirrors that replace a high reflector within the laser cavity. A schematic of a typical solid-state laser cavity with a saturable absorber is shown in figure 3-1. In the following sub-sections different device designs will be discussed in more detail.

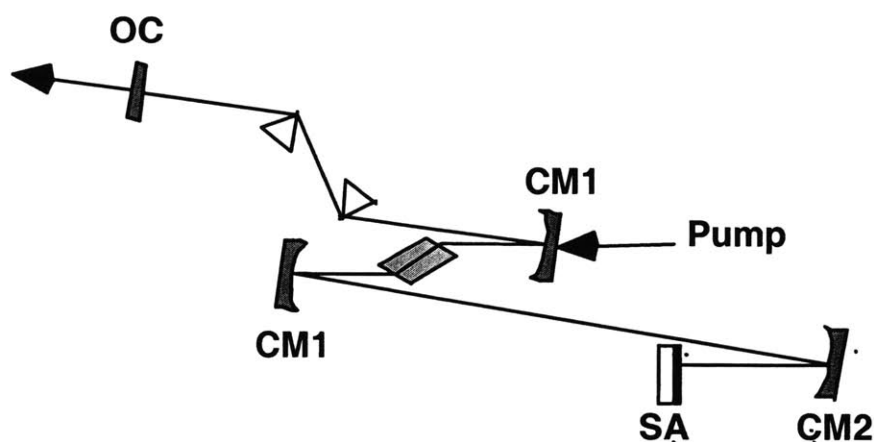

Figure 3-1. Schematic of a typical Z cavity incorporating a saturable absorber (SA) with a focusing mirror (CM2) with curved mirrors CM1 to focus the light into the crystal and an output coupler OC.

3.2.2 High finesse A-FPSA

The first demonstration of solid-state laser mode-locking using semiconductor saturable absorbers was achieved using an antiresonant Fabry-Perot saturable absorber (A-FPSA) [36, 127]. This device overcame the problems encountered when using bulk semiconductors by placing a thin semiconductor layer in a Fabry-Perot cavity set to operate at antiresonance.

Operation at antiresonance makes the intensity within the device lower than the incident intensity, which effectively increases the saturation intensity and fluence of the device and also the damage threshold. This mode of operation also results in a device with broad bandwidth and low GDD; the bandwidth is only limited by the reflectivity bandwidth of the top and bottom mirrors.

The condition for antiresonance is given by

$$\varphi_{rt} = 2nkd + \varphi_b + \varphi_t = (2m-1)\pi\ , \tag{2.61}$$

where φ_{rt} is the total round trip phase change after passing through the device, d is the thickness of the Fabry-Perot cavity formed by the top and bottom mirrors, and φ_b and φ_t are the phase changes due to the bottom and top mirrors, respectively. When φ_{rt} is an odd multiple of π after one round trip, the field interferes destructively within the Fabry-Perot, reducing the intensity seen by the saturable absorber layer. The intensity within the device is decreased by a factor of

$$\xi = \frac{1-R_t}{[1+\sqrt{R_t R_b}\exp(-2\alpha d_a)]^2}, \tag{2.62}$$

where R_t and R_b are the reflectivity of the top and bottom mirrors, respectively, and d_a and α are the thickness and field absorption coefficient of the saturable absorber. It is clear from this equation that changing the reflectivity of the top and bottom mirrors, the thickness of the Fabry-Perot cavity, and the absorption coefficient can modify the intensity on the absorber and therefore the effective saturation fluence of the device [134, 74]. The effective saturation fluence of the absorber is increased by a factor of $1/\xi$ compared to a free standing absorber:

$$\Gamma_{sat,eff} = \frac{1}{\xi}\Gamma_{sat} \tag{2.63}$$

The saturation intensity is also increased by the same amount, and the damage threshold of the device is similarly increased since the absorber sees a lower intensity. The top mirror reflectivity of the A-FPSA is adjusted in the different device designs to change the effective saturation fluence of the absorber. By scaling the laser mode area on the saturable absorber, the ratio of the incident fluence to the effective saturation fluence can be modified.

Another important parameter in mode-locking with a semiconductor saturable absorber is the carrier lifetime. In general, carrier lifetimes in bulk semiconductor materials are relatively

long, on the order of nanoseconds, which is comparable to the pulse repetition rate. In order for the absorber to completely recover between pulses, the carrier recombination time must be shortened. This is often done by low temperature growth [135], which can easily be incorporated with standard epitaxial fabrication techniques. Low temperature growth is thought to reduce carrier lifetimes by increasing the concentration of group-V elements that form point defects that act as trap sites for carriers [136]. The photogenerated carriers rapidly fall into the mid-gap trap states and then recombine. This technique typically increases the nonsaturable loss while reducing the carrier lifetime from tens of nanoseconds to picoseconds [134]. Adjusting the growth temperature enables control of the carrier recombination dynamics for particular applications [137]. In the first high-finesse A-FPSA, described in the next paragraph, growth at low temperatures reduced the carrier lifetimes in the saturable absorber to 69 ps, significantly shorter than the pulse repetition rate of 4.5 ns.

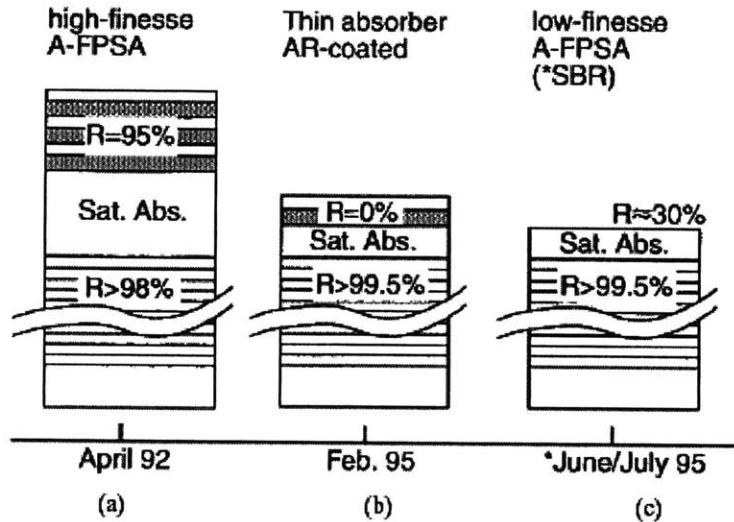

Figure 3-2. Different SESAM designs in historical order. (a) High-finesse A-FPSA. (b) AR-coated SESAM. (c) Low-finesse A-FPSA, or SBR. (from ref. [36])

The first application of these principles was realized with a device known as the high-finesse A-FPSA [127]. In this design, the reflectivity of the top mirror is very high, increasing the effective saturation fluence and de-emphasizing the narrow bandwidth and poor dispersion properties of the bottom mirror. The structure of the high-finesse A-FPSA is shown in figure 3-2(a). The bottom mirror is a DBR consisting of 16 pairs of alternating GaAs and AlAs layers grown by molecular beam epitaxy. The reflectivity of the bottom mirror was ~96%. The

saturable absorber layer was a low temperature grown InGaAs/GaAs multiple quantum well structure deposited in the same MBE run. The top mirror was a 98% reflectivity TiO_2/SiO_2 dielectric structure evaporated onto the saturable absorber.

This device was used to mode-lock an Nd:YLF laser, generating self-starting 3.3 ps pulses at 1047 nm [127]. Similar designs have been used to mode-lock other laser systems [138-140]. The saturation fluence of the high finesse A-FPSA used in the initial demonstration was high, ~3.5 mJ/cm^2 for the top and bottom mirror reflectivities given above. One drawback of this device is that the reduced intensity on the absorber leads to a modulation depth of ~1%, limiting the minimum achievable pulse duration. However, using a high-finesse A-FPSA design, 19 fs KLM-assisted pulses and 40 fs soliton mode-locked pulses were generated from a Ti:sapphire laser [141].

3.2.3 AR-coated SESAM

The opposite limit of the high-finesse A-FPSA design is to make the reflectivity of the top mirror zero by anti-reflection (AR) coating the device (figure 3-2(b)). This increases the modulation depth and lowers the saturation fluence and intensity by increasing the field seen by the absorber, improving the self-starting performance. This device was also fabricated using MBE, with the DBR identical to that of the high-finesse A-FPSA. A single thin GaAs quantum well was used as the saturable absorber layer to reduce the insertion loss, and transparent spacer layers were used to set the Fabry-Perot cavity for operation at antiresonance. The saturation fluence of the AR-coated SESAM was 18 μJ/cm^2 and the modulation depth was 4.9%. This device was used to self-start 34 fs soliton mode-locked pulses from a Ti:sapphire laser, with mode-locking build up times as low as 2.6 μs [141]. Stable mode-locking could be obtained throughout the cavity stability region. The main drawback of the AR-coated SESAM is that although its high modulation depth can support very short pulses, the AR coating emphasizes the poor bandwidth and dispersion properties of the bottom DBR, which act as a strong limitation to pulse shortening in this regime.

3.2.4 Low-finesse A-FPSA (SBR)

The low-finesse A-FPSA, also known as the saturable Bragg reflector, is an intermediate design between the high-finesse A-FPSA and the AR-coated SESAM [36, 37, 128]. In this device, shown in figure 3-2(c), the top mirror is formed by the ~30% Fresnel reflection of the semiconductor-air interface, and a single quantum well with a thickness of ~10 nm is used as the saturable absorber. The bottom mirror is a DBR structure consisting of ~30 high and low index semiconductor layer pairs.

The thin quantum well used as the saturable absorber layer here, as well as in the AR-coated SESAM, opens up the possibility of controlling the saturation fluence and wavelength dependence of the saturable absorber device by positioning the quantum well at a specific point in the electric field pattern [37]. For any electromagnetic wave reflected from a mirror, a standing wave pattern is formed by the incident and reflected light. When the quantum well thickness of a few nm is much smaller than the wavelength, then the absorber can be placed at a certain point in the standing wave pattern to control the electric field on the absorber and therefore the effective saturation fluence. Since the standing wave pattern is wavelength dependent, several absorber layers can be placed at different positions in the wave pattern to partially compensate for the wavelength dependence of the absorption in the semiconductor itself, resulting in a device with broader bandwidth [141].

In the low-finesse A-FPSA, the quantum well can be placed at any point in the standing wave pattern of the DBR to control the incident field on it. Placing the absorber closer to the surface of the DBR increases its effective saturation fluence, while positioning the absorber deeper in the structure increases the saturation fluence. This device can be thought of as a DBR with a weakly perturbing saturable absorber layer [37, 128]. An advantage of this design is that it can be fabricated in one MBE run and does not require any post-processing such as AR or HR coatings; however, the bandwidth of the DBR still limits ultrashort pulse generation. Pulses as short as 70 fs were obtained from a Cr:LiSAF laser using only the SBR for mode-locking, and in a Ti:sapphire laser with KLM 25 fs self-starting pulses were obtained with this device [37].

3.2.5 Broadband SESAMs

To support the generation of ultrashort sub-15 fs pulses, the bottom DBR must be replaced by another mirror with broader reflectivity bandwidth. Several different methods of doing this have been realized recently. Initially, the bottom DBR was replaced by a silver mirror [75]. The silver mirror has a reflectivity of over 98% from 500 nm to the mid-infrared and therefore does not limit the laser bandwidth. This device required extensive post processing due to the lattice matching requirements of MBE growth, which prevented the semiconductor from being grown directly on the silver mirror. Therefore, the absorber was grown on a semiconductor substrate that was subsequently etched off, and the back surface was coated with silver and bonded to a Si substrate for heat sinking. Transparent spacer layers were also used to position the saturable absorber at a desired point in the standing wave pattern and minimize the wavelength dependence of the absorption.

A silver mirror was incorporated into both low-finesse A-FPSA and AR-coated SESAM designs [75]. Self-starting KLM assisted 10 fs pulses were obtained from a Ti:sapphire laser with the low-finesse A-FPSA on a silver mirror. The modulation depth of this device was only 1%, not large enough to stabilize soliton mode-locking [38]. This limitation was overcome using the AR-coated SESAM on a silver mirror. The modulation depth was increased to ~6% by adding an AR coating and additional GaAs quantum well layers, generating 13 fs soliton mode-locked pulses over the full cavity stability range without KLM [39]. The disadvantage of this device is that the AR coating is only correct for one wavelength, increasing the wavelength dependence of the reflectivity.

With improved dispersion compensation based on DCMs, self-starting KLM assisted 6.5 fs pulses were obtained using the low-finesse A-FPSA on a silver mirror [129]. The SESAM design was further modified by introducing three distinct absorber layers: 11 nm GaAs, 20 nm $In_{0.22}Ga_{0.78}As$, and 4 nm GaAs, positioned at different points in the standing wave pattern to increase the device bandwidth. This resulted in a modulation depth of 4% over a 400 nm bandwidth and a saturation fluence of 180 $\mu J/cm^2$. This device supported self-starting sub-two-

cycle pulses when used with an output coupler designed to improve spectral shaping and DCMs with minimized dispersion oscillations [40].

Other SESAM designs were also explored to avoid the extensive post-processing required for silver mirror based devices. Bragg reflectors based on AlGaAs/CaF_2 high and low index pairs were investigated due to the large index difference between the materials, which would allow for an MBE-grown DBR exhibiting broad bandwidth with fewer layer pairs [142]. Devices using four pairs were grown using MBE, with a GaAs quantum well used as the saturable absorber. These devices also supported generation of sub-6 fs pulses, but they required a very complicated growth process to avoid cracking and defects in the mirror structures.

The combination of dispersion compensation and saturable absorption in a single device is an important goal in ultrashort pulse generation due to the desire for compact resonators with a limited number of components. This was accomplished using a structure known as the dispersion compensating saturable absorber mirror (D-SAM) [143]. In this device, the Fabry-Perot is operated at resonance in a Gires-Tournois-like cavity formed by the semiconductor-air interface and the bottom DBR. It introduces negative dispersion of ~400 fs^2 at the laser wavelength of 840 nm and was used to generate 160 fs pulses from a Cr:LiSAF laser without any additional dispersion compensation. Another interesting design demonstrated an output-coupling SESAM that had 10% transmission. This device was used to passively Q-switch a Nd:YVO_4 microchip laser, yielding 143 ps pulses [144].

3.2.6 Semiconductor saturable absorbers for Cr:forsterite and Cr:LiSAF

Most of the previously described semiconductor saturable absorbers were used to mode-lock Ti:sapphire lasers. However, similar designs have been extensively applied to mode-locking of Cr:forsterite and Cr:LiSAF lasers. A low-finesse A-FPSA design based on a 16 AlAs/GaAs pair DBR and a single InGaAs quantum well was used to obtain self-starting 36 fs pulses from a Cr:forsterite laser [145, 146]. The SESAM design was improved by replacing the DBR with a gold mirror. The gold mirror was coated with a semiconductor-SiO_2 double layer stack to enhance its reflectivity, and a single InGaAs quantum well was used as the saturable

absorber. The mirror structure was carefully designed to maximize the reflectivity by using a semiconductor-SiO_2 double layer stack to enhance the reflectivity of the gold film. The bandwidth of this SESAM was extremely broad, with reflectivity >97% over 400 nm centered at 1.3 μm. When used in a Cr:forsterite laser, self-starting 20 fs pulses with 90 nm bandwidth were generated [43].

Semiconductor saturable absorbers have also been applied in several designs to mode-lock Cr:LiSAF lasers. Initial work used a high-finesse A-FPSA to generate 98 fs pulses with average powers of 50 mW from a diode-pumped Cr:LiSAF laser [147]. This laser was then used with a broader bandwidth low-finesse A-FPSA and improved pump beam shaping to generate 45 fs pulses with 105 mW output power [148]. Soliton mode-locking was started and stabilized by the SESAM and wavelength tunability over a range of 50 nm was obtained. As previously described in section 3.2.4, an SBR was also used to mode-lock a Cr:LiSAF laser, resulting in 70 fs pulses at 866 nm with up to 88 mW output power [37]. A low-finesse A-FPSA was used to generate 50 fs pulses from a diode-pumped Cr:LiSAF laser with average powers of 340 mW [36, 149]. This laser generated 1.4 W cw output power [149, 150]. Further results obtained using semiconductor saturable absorbers to mode-lock colquirite-based lasers will be described in section 3.4.

3.2.7 Summary of previous work on epitaxially grown semiconductor saturable absorbers

In summary, epitaxially grown saturable absorbers have been applied in a variety of designs to mode-lock solid-state lasers. The reflectivity of the top mirror is the main factor in determining device performance in most designs. The high-finesse A-FPSA has a high reflectivity top mirror, giving it a high saturation fluence as compared to bulk semiconductors. This mirror also de-emphasizes the poor properties of the bottom DBR mirror; however, the low intensity on the saturable absorber limits the modulation depth and therefore the minimum pulse duration. The AR-coated SESAM is the opposite design limit, with a low saturation fluence and high modulation depth. The poor dispersion and bandwidth properties of this device limit ultrashort pulse generation. The SBR or low-finesse A-FPSA is an intermediate choice between the two extreme designs. These designs can also be modified by replacing the bottom DBR with

a broader bandwidth metal or fluoride-based mirror to support ultrashort pulses. In general, soliton mode-locking is best supported by AR-coated SESAMs since the saturable absorber provides significant pulse shaping. In KLM-assisted lasers, a high-finesse A-FPSA works well since it starts mode-locking with only minor bandwidth limitations, after which KLM can provide the majority of the pulse shaping. The low-finesse A-FPSA and SBR designs have been shown to support both regimes of pulsed operation. Therefore, the choice of saturable absorber design must be tailored to the particular application.

3.3 Non-epitaxially grown semiconductor saturable absorbers

Although epitaxially grown semiconductor saturable absorbers have been very successful in mode-locking solid state lasers, they possess some disadvantages that motivate the desire to explore non-epitaxial growth techniques. Molecular beam epitaxy systems are expensive and require a well trained operator. The lattice matching constraints imposed by the epitaxial growth process limit the choice of absorber and substrate materials. Finally, the bottom mirror imposes additional constraints on the device. In low finesse or AR-coated A-FPSA designs, the poor reflection bandwidth and dispersion properties of the bottom DBR limit the minimum achievable pulse duration. High-finesse A-FPSA designs avoid the poor properties of the bottom DBR at the expense of the modulation depth of the saturable absorber, which also limits the pulse duration. Other designs based on broader bandwidth bottom mirrors require extensive post-processing, making the device costly and complex. Therefore, alternatives to epitaxial growth were explored in previous research.

3.3.1 Semiconductor-doped glass structures

The non-epitaxial device designs demonstrated so far are generally based on semiconductor nanocrystallites doped into glass structures that utilize the quantum confinement effect to create devices for a particular wavelength. Colored glass filters are usually composed of semiconductor nanocrystallites grown from a glass melt; changing the size of the nanocrystallites changes the optical absorption edge of the glass filters through the quantum size

effect (see section 5.2 for details). Initial research used a HOYA IR76 colored glass filter to mode-lock a Ti:sapphire laser [151]. The filter was polished down to a thickness of 90 μm for appropriate absorption. Pulses with durations of 2.7 ps were obtained and the laser could be tuned from 785-855 nm. Similar results were obtained using a PbS-doped glass grown from a melt and polished down to a 150 μm thickness to mode-lock a Cr:forsterite laser, generating 4.6 ps pulses tunable from 1207-1307 nm [152].

Shorter pulses were obtained using standard Schott RG-780, RG-830, and RG-850 (labeled by the wavelength below which the filter is strongly absorbing) colored glass filters polished down to thin wedges and glued to sapphire substrates to self-start mode-locking with and without KLM in a Ti:sapphire laser [153]. The colored glass filters were polished down to a thin wedge to introduce a continuously variable thickness down to 20 μm into the laser cavity. This enabled the absorption introduced by the device to be tuned by varying its insertion into the laser beam.

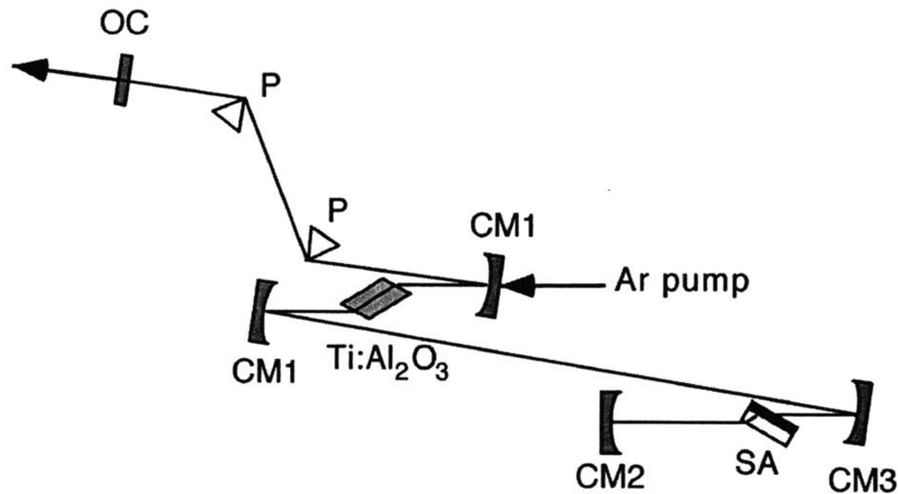

Figure 3-3. Schematic of the Ti:sapphire laser cavity used in demonstration of self-starting mode-locking with non-epitaxially grown saturable absorbers.

When the semiconductor-doped glass saturable absorbers were introduced into the Ti:sapphire cavity in a transmissive geometry (figure 3-3), self-starting KLM was obtained, with pulse durations of 52 fs and bandwidths of 15 nm. The bandwidth was limited on the short

wavelength side by the increasing absorption of the saturable absorber and on the long wavelength side by the reflectivity of the mirrors in the laser cavity.

When the cavity was not set for KLM, self-starting 2 ps pulses were obtained with average powers of 200 mW. Mode-locked operation was sustained over a tuning range of 780-860 nm. Pump-probe experiments were also performed to measure the absorption saturation dynamics of these devices. The saturation fluence was measured to be 1 mJ/cm^2. A photodarkening effect was observed, where the carrier recovery times decreased with increasing exposure to the laser intensity. This is expected to limit mode-locked operation in some cavity designs. For example, a 3% output coupler was also tested, since the intracavity power would be higher and the mode-locking build-up time would be faster; however, it was found that mode-locking was not stable with this output coupler and the performance deteriorated with time, most likely due to the photodarkening effect.

3.3.2 Semiconductor-doped silica film saturable absorbers

The use of semiconductor-doped glass structures to mode-lock Ti:sapphire lasers motivated the search for a more versatile non-epitaxially grown saturable absorber device design. Non-epitaxially grown semiconductor saturable absorbers based on semiconductor-doped silica films were developed [45, 46, 154], possessing several advantages when compared to epitaxially grown absorbers. Semiconductor-doped silica film saturable absorbers are grown using RF sputtering and are based on semiconductor nanocrystallites doped into a silica film and deposited on a substrate. RF sputtering is a much simpler, faster, and cheaper technique than MBE, and has been used by several research groups to deposit semiconductor-doped silica films on different substrates [155-157]. This technique has no lattice matching constraints, making the choice of film and substrate materials almost unlimited. The optical absorption edge can be controlled by varying the semiconductor material or size of the nanocrystallites, while the amount of absorption is determined by the thickness of the film. The large distribution of nanocrystallite sizes leads to a smooth optical absorption edge, which is advantageous in supporting ultrashort laser pulses and also enables a broad laser tuning range. Finally, semiconductor-doped silica films can be deposited on mirror structures, raising the possibility of

depositing a semiconductor-doped silica film on a double-chirped mirror to provide saturable absorption and dispersion compensation in a single structure.

InAs-doped silica films were deposited on sapphire substrates using a non-magnetron RF sputtering system (described in section 5.3.1). The sputtering target had a 10% InAs/ 90% SiO_2 ratio. These films were deposited on sapphire substrates due to the high thermal conductivity of sapphire. A rapid thermal annealing treatment (RTA) in a nitrogen atmosphere for 60 seconds at temperatures ranging from 500-750 C was performed. It will be shown later in this section that this modified the absorption saturation dynamics of the saturable absorbers.

A comprehensive set of film characterization measurements was performed, including measurements of linear absorption, femtosecond absorption saturation dynamics, nanocrystallite size, film composition, element distribution within the film, and the crystalline structure of the nanocrystallites [46, 154]. The optical absorption edge of the films was measured by linear transmission to be 1200 nm. Unlike epitaxially grown saturable absorbers based on quantum wells, the transmission curve of the semiconductor-doped silica films was smooth as a function of wavelength due to the broad size distribution of the nanocrystallites, which was expected to result in a broad tuning range when used in laser mode-locking. Figure 3-4 depicts a linear absorption measurement of these films.

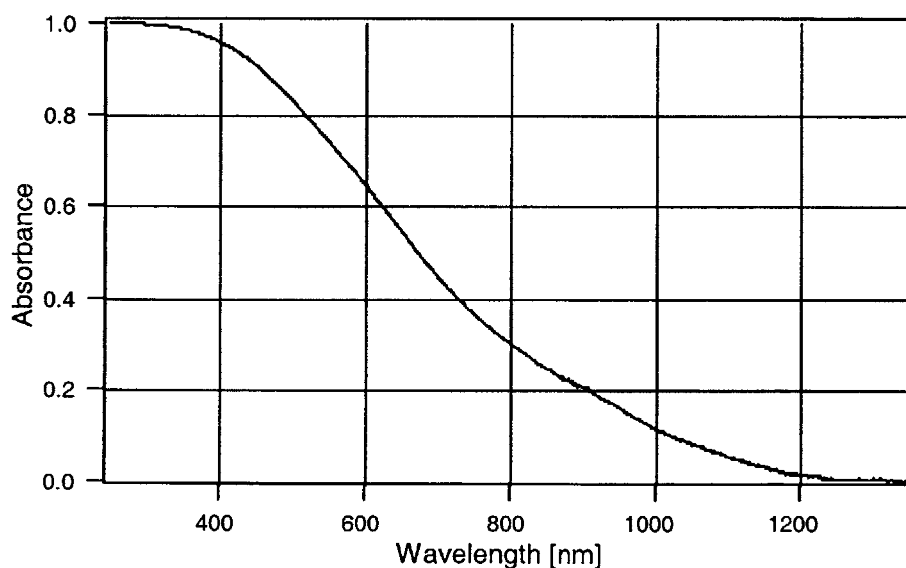

Figure 3-4. Linear absorption measurement of the InAs-doped silica films.

X-ray photoelectron spectroscopy (XPS) measurements were performed to determine the chemical composition of the semiconductor-doped silica films. It was found that both In and As are present in the film, and they existed in the form of InAs. Transmission electron microscopy (TEM) measurements were also taken to determine the structural composition of the InAs-doped silica films. From these measurements it was found that the films consisted of nanocrystallites in a background matrix, with maximum particle sizes of ~8 nm.

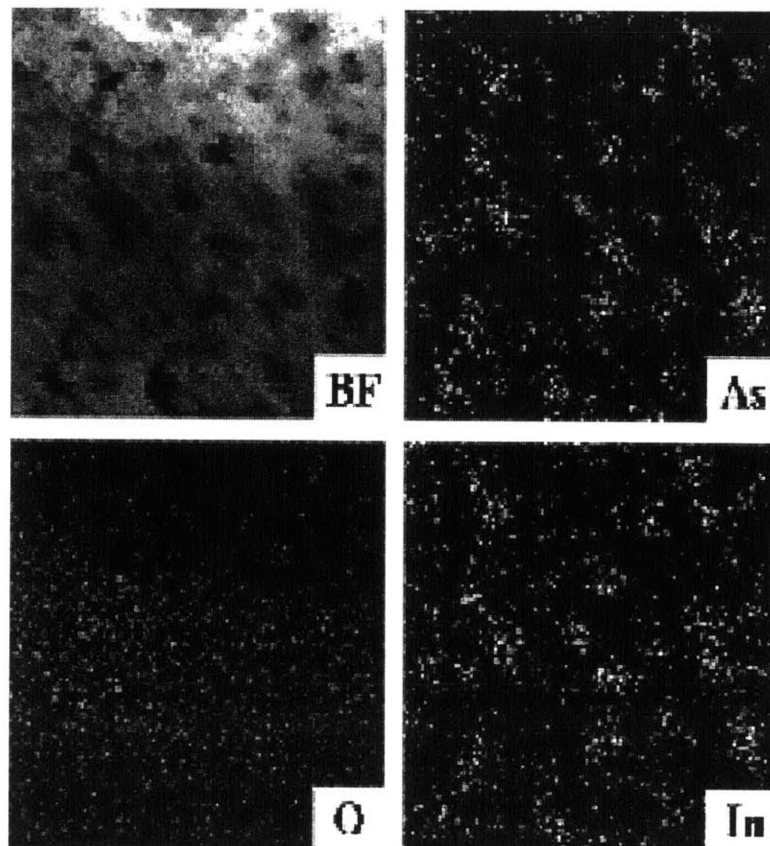

Figure 3-5. Compositional maps of an InAs-doped silica film taken with STEM. The image sizes are 80 by 80 nm. BF: bright field image; O:oxygen; As:arsenic; In:indium.

The distribution of elements within the film was investigated by using scanning transmission electron microscopy (STEM) in conjunction with energy dispersive x-ray spectroscopy (EDX). The results of these measurements are shown in figure 3-5. Examination of these images reveals that In and As are distributed in the same positions as the nanocrystallites seen in the bright field (BF) image. The distribution of oxygen and silicon (not shown) was

uniform, as expected. Therefore, these measurements verify that the films consist of InAs nanocrystallites in a silica matrix.

Electron diffraction measurements were also performed to determine the crystalline structure of the nanocrystallites. The material was found to be polycrystalline, retaining the zincblende structure of bulk InAs. The lattice constant was calculated to be 0.582 nm, comparable to that of 0.605 nm for bulk InAs.

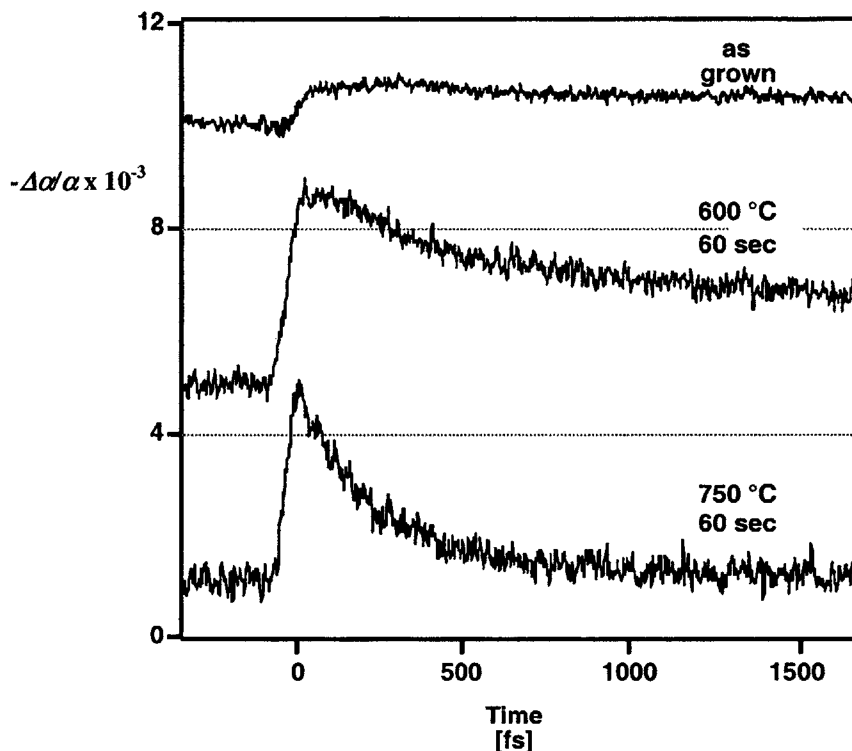

Figure 3-6. Absorption saturation dynamics of InAs-doped silica films for different annealing temperatures. The traces are vertically displaced for clarity.

The nonlinear optical properties of the semiconductor-doped silica films were measured using femtosecond pump-probe experiments (figure 3-6). It was found that rapid thermal annealing had a significant effect on the dynamics of the semiconductor-doped silica films. The magnitude of the pump probe signal, which is inversely proportional to the absorption saturation fluence, increased by a factor of two for the annealed films, indicating a decrease in the saturation fluence by the same amount. The saturation fluence was extracted from this data and found to be 25 mJ/cm^2, significantly higher than the ~100 μJ/cm^2 saturation fluence of typical

epitaxially grown absorbers. The modulation depth of these devices was measured to be 0.5%. The carrier recovery times also decreased with increasing annealing temperature.

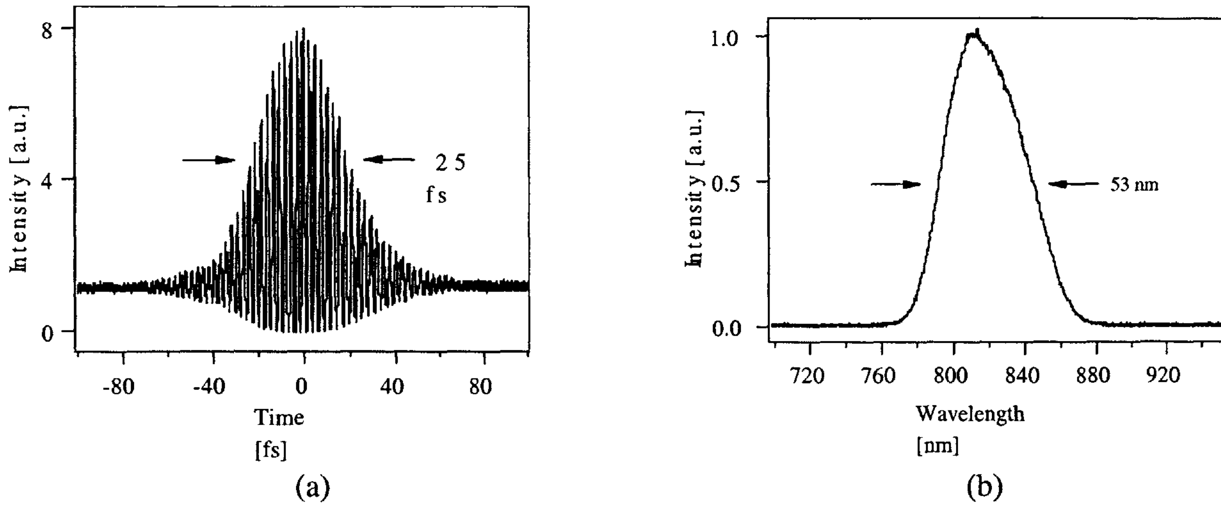

Figure 3-7. Autocorrelation (a) and spectrum (b) of self-starting pulses from a KLM Ti:sapphire laser incorporating an InAs-doped silica film saturable absorber.

Semiconductor-doped silica film saturable absorbers were applied to mode-locking of a Ti:sapphire laser. The laser cavity was identical to that in figure 3-3, with the semiconductor-doped silica film saturable absorber deposited on a sapphire substrate and placed at the focus of the second cavity fold (in the position labeled "SA"). With this configuration, self-starting KLM was obtained, with 25 fs pulses and a bandwidth of 53 nm (figure 3-7) [45, 154]. The pulses were not transform limited due to excess self-phase modulation in the sapphire substrates. The wavelength could be tuned from 800 to 880 nm while maintaining self-starting operation.

This was the first demonstration of laser mode-locking using non-epitaxially grown semiconductor-doped silica films. Subsequently, research was performed to incorporate these devices into a reflective structure [158], with the goal of replacing a cavity mirror with a saturable absorber device, as in the earlier research on SESAMs and SBRs. The device structure consisted of an InAs-doped film placed between two sapphire spacer layers, all deposited on a gold mirror. This design positioned the InAs-doped silica film at the peak of the electric field by using the spacer layers to set the thickness of the spacer layer/saturable absorber film combination for a half wave layer at 800 nm. The whole structure, including the gold mirror,

was deposited by RF sputtering on a sapphire substrate. However, self-starting operation could not be obtained. This could be due to several effects, such as spurious reflections introduced by the saturable absorber mirror that prevented self-starting or by variations in the thickness of the InAs-doped film and spacer layers that positioned the saturable absorber film away from the electric field peak. The reflectivity of these devices was relatively low (85-90%), supporting the second hypothesis. Kerr lens mode-locking was significantly easier to start and extremely stable once started by lightly tapping the table; the stability region over which KLM could be obtained also increased as compared to operation without a saturable absorber. In this work, semiconductor-doped silica films were also deposited on dielectric mirrors, but mode-locking performance was not improved with these devices. Finally, GaSb was tested as the semiconductor dopant. GaSb-doped films were fabricated; however, upon annealing their optical quality significantly decreased, making them unsuitable for laser mode-locking applications.

Semiconductor-doped silica films are a very promising technology for mode-locking solid-state lasers. However, the high absorption saturation fluence limits self-starting mode-locking without KLM and the low modulation depth limits the minimum pulse duration. Therefore, one focus of the research presented in this thesis was to comprehensively characterize the linear and nonlinear optical properties of these devices, with the goal of reducing the saturation fluence and developing guidelines for the design of semiconductor-doped silica film saturable absorbers for any laser system.

3.4 Diode-pumped solid state lasers

Diode-pumped solid-state laser systems are the focus of much current research in ultrashort pulse generation. These systems are very desirable when compared to ion-laser-pumped laser systems since they require significantly less electrical power, can be air-cooled, and are much more compact, reliable, and inexpensive. Ultrashort pulse generation with diode-pumped solid state lasers is focused on crystals of the colquirite family, including Cr:LiSAF, Cr:LiSGAF, and Cr:LiCAF, due to their broad gain bandwidths in the near infrared comparable

to that of Ti:sapphire. These crystals also have absorption bands peaking around 670 nm, where red AlGaInP laser diodes are readily available. The combination of broad gain bandwidth and diode pumpability means these laser systems have the potential to replace Ti:sapphire in some low power applications including optical coherence tomography, frequency metrology, and terahertz generation. Initial studies used krypton laser pumping at 647 nm in order not to be limited by the poor beam quality of broad stripe laser diodes. The emission characteristics and thermal properties of these crystals were measured (given in table 4-1) and cw lasing was successfully demonstrated [159-161]. The main disadvantage of colquirite-based lasers when compared to Ti:sapphire lasers is their lower thermal conductivity, which limits the maximum pump power that can be used. In general, thermal problems in Cr:LiSAF make pumping with more than 1.5-2 W of power from an ion laser difficult, restricting this material to relatively low power applications; to date these problems have not been encountered in Cr:LiSGAF based lasers due to their higher thermal conductivity and lower, more isotropic thermal expansion coefficients [42]. However, a high power cw Cr:LiSAF laser pumped by a diode laser array has been demonstrated [150]. This laser used an elliptical 2 mm x 150 μm pump spot to efficiently distribute the heat within the laser crystal, enabling the crystal to be kept at 10 °C. The laser mode was matched to the pump spot within the crystal using a cylindrical mirror within the laser cavity. This laser produced 1.1 W cw power for 5.5 W absorbed pump power.

Mode-locking of Cr:LiSAF, Cr:LiSGAF, and Cr:LiCAF has been demonstrated with several different pump sources and with dispersion compensation provided either by prisms or by dispersion-compensating mirrors. Initial mode-locking efforts focused on Cr:LiSAF and Cr:LiCAF pumped by krypton or argon lasers and lasing near 840-860 nm. Cr:LiSAF absorbs light from a krypton laser at 647 nm much more efficiently than the argon laser at 476-488 nm, and therefore Cr:LiSAF lasers pumped by krypton lasers usually exhibit better performance. Active mode-locking using an acousto-optic modulator (AOM) was used to mode-lock Cr:LiSAF for the first time [162]. Using SF-10 prisms for dispersion compensation, pulse durations of 150 fs were obtained with 50 mW average power for 1 W pump power from a krypton laser.

The first demonstration of KLM in Cr:LiSAF generated 50 fs pulses using SF-14 prisms for dispersion compensation [163]. Mode-locking was initiated in a standard x cavity by an AOM; after mode-locking was initiated, the modulator could be turned off without interrupting pulsed operation. This laser generated average powers of 150 mW for 2 W pump power at 476 nm from an argon laser. At nearly the same time, 170 fs pulses were generated from Cr:LiCAF using the same cavity configuration as in ref. [162]. This laser was purely Kerr lens mode-locked and did not require an AOM to initiate mode-locking [164]. Self-starting 50 fs pulses were generated using a saturable absorber dye to initiate KLM in a Cr:LiSAF laser pumped by an argon laser at 488 nm [165]; subsequently, improved dispersion compensation enabled the generation of self-starting 33 fs pulses from the same laser [166]. In Cr:LiSGAF, mode-locking was demonstrated with 64 fs pulses and 200 mW output power pumped by 2 W from a krypton laser [167]. These powers are comparable to those from Ti:sapphire based systems.

The laser systems described in the previous paragraph all incorporated prisms for dispersion compensation; however, the shortest pulses have been obtained with the aid of chirped mirrors for dispersion compensation. The shortest pulses obtained in both Cr:LiSAF and Cr:LiSGAF using ion laser pumping were 14 fs, with average powers of 100 mW in Cr:LiSGAF and 70 mW in Cr:LiSAF for 2 W absorbed power from a krypton laser [168, 169]. This laser used only two low-loss chirped mirrors for dispersion compensation in a simple x cavity design. Finally, a Cr:LiCAF laser pumped by a Ti:sapphire laser at 693 nm has recently generated pulses as short as 9 fs [88]. In this laser, 10 fs pulses could be generated using only DCMs for dispersion compensation. With the addition of a fused silica prism pair to fine tune the dispersion, 9 fs pulses were generated with 220 mW average power for 2.1 W pump power.

Broad stripe laser diode pumping has been extensively investigated in colquirite-based laser systems. These diodes are much less expensive ($1000-3000) and offer significant advantages in compactness and reliability when compared to ion lasers (typical prices of $50,000 for a 5 W laser). Broad stripe laser diodes emit an asymmetric output beam from an aperture with typical dimensions of 1 μm x 100 μm. The beam is nearly diffraction limited in the direction perpendicular to the diode junction, but is many times diffraction limited in the other

direction. Cylindrical lenses can be used to make the pump spot more circular, although the focused spot within the laser is usually highly elliptical.

The first diode-pumped, mode-locked Cr:LiSAF laser was both actively mode-locked with an acousto-optic modulator and passively mode-locked using a multiple quantum well saturable absorber in an external cavity, each case resulting in picosecond pulses [170]. The first KLM diode-pumped Cr:LiSAF laser generated 97 fs pulses, with average powers of 3 mW using a 250 mW pump diode laser [171]. In this laser, hard-aperture KLM was initiated with an AOM and fused silica prisms were used for dispersion compensation. Two 400 mW diodes were used to pump the same laser, resulting in 34 fs pulses with 42 mW output power [172]. A hard-aperture KLM Cr:LiSAF laser generated 70 fs pulses with 50 mW output power when pumped by two 400 mW red diodes; this laser was unique in that it was self-starting when the 1% output coupler was replaced by the high reflector, generating 55 fs pulses with 10 mW output power [173].

An optimized prism dispersion compensation scheme was used to generate 12 fs pulses from a Cr:LiSAF laser pumped by 350 and 500 mW diode lasers [112]. The dispersion compensation and pump and laser mode matching in this laser were further improved to generate 9.9 fs pulses [174]. Several different prism materials, including fused silica, BK7, LaKL21, K5, and N-ZK7 were tested. Dispersion compensation with the fused silica prisms produced the longest pulses of 28 fs, while use of the N-ZK7 prisms generated the shortest 9.9 fs pulses. The output powers from this laser were low (a few mW) since a high reflector was used as an output coupler when generating the shortest pulses. However, a 99.3% output coupler was tested with the BK-7 prisms, producing 14 fs pulses with 23 mW output power.

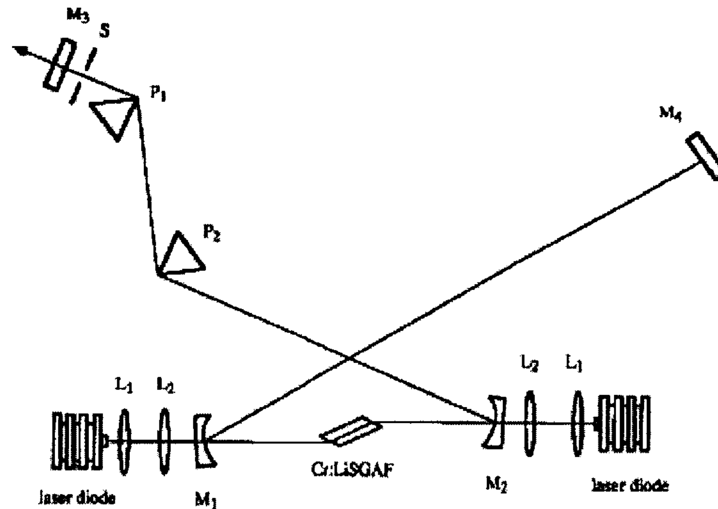

Figure 3-8. Schematic of the diode-pumped KLM Cr:LiSGAF laser (from [175]).

In Cr:LiSGAF, the first demonstration of KLM with diode pumping used a hard aperture in an x cavity to generate 100 fs pulses with 35 mW average power for 680 mW pump power [175]. Figure 3-8 depicts the laser cavity used in this research. Subsequently, 50 fs pulses were generated from the same laser with soft-aperture KLM [42]. Stable KLM was achieved over a wavelength range of 810-860 nm.

The previously cited studies all used prisms for dispersion compensation. A diode-pumped Cr:LiSGAF laser pumped by two 500 mW diode lasers was completely dispersion compensated by chirped mirrors, producing 65 fs pulses with 70 mW output power [176]. The first diode-pumped, mode-locked Cr:LiCAF laser was also demonstrated using low-loss chirped mirrors for dispersion compensation [177]. This laser produced 52 fs pulses with 75 mW output power from a 1.95% output coupler for 630 mW pump power. Using a low percentage 0.1% output coupler, pulses as short as 20 fs were generated with 13 mW output power. Recently, a combination of chirped mirrors and prisms was used to generate 10 fs pulses in both Cr:LiSAF and Cr:LiSGAF lasers [178]. A diode-pumped Cr:LiCAF laser based on the Ti:sapphire pumped resonator described earlier has also recently been demonstrated to generate 12 fs pulses, with 25 mW output power when pumped with two 500 mW diodes [179]. These results demonstrate the feasibility of generating 10 fs pulses from all three of the colquirite-based materials. The

primary limitation on generating shorter pulses is most likely the low nonlinearity in these crystals, which is nearly a factor of four smaller than Ti:sapphire, limiting SPM and Kerr lensing.

Although mode-locking with broad stripe diodes has generated the shortest pulses from Cr^{3+}-based laser systems, their poor mode quality and relatively high price has motivated the search for alternatives, with the goal of developing more efficient, inexpensive laser systems. Single mode diodes have recently become available at wavelengths around 670 nm with powers of 50-60 mW. These diodes have significantly better mode quality than broad stripe diodes, enabling more efficient matching of the pump and laser modes within the crystal. This is expected to improve KLM performance as well. Another major advantage of these diodes is their extremely low cost of ~$20 per diode, much cheaper than that of broad stripe diodes.

The first demonstration of this concept used one single mode diode at 680 nm with 33 mW output power to pump a novel three mirror cavity Cr:LiSAF laser [180]. A high reflector was used as the output coupler and a regenerative prism mode locker was used to initiate KLM. Initially, the laser was directly pumped with the elliptical mode from the laser diode, without shaping the beam, and 75 fs pulses with 0.73 mW output power (in two beams) were obtained for an incident pump power of 36 mW. Only 9.5 mW pump power was required to reach the cw threshold, and 22 mW for the mode-locking threshold. With two pump diodes, 60 fs pulses with 3.14 mW total output power were obtained for 76 mW pump power. The regenerative mode-locker could be turned off once the mode-locking became stable in this configuration. The laser diode power supply could also be replaced with three AA batteries, allowing 18 hours of stable pump operation.

Subsequently, two single mode diodes were used to pump a Cr:LiSAF laser mode-locked with a SESAM and two fused silica prisms for dispersion compensation [181]. Use of a SESAM allowed improvement of the output power by an order of magnitude with a 1.5% output coupler. Pulse durations as short as 57 fs were achieved with output powers up to 9 mW for a maximum incident pump power of 80 mW. Using six AA batteries, the pump diodes were stable for 14 hours. As in the previous research, no beam shaping optics were used to shape the output of the pump diodes. More recently, several different cavity designs were explored, with the goal of

developing compact, efficient mode-locked lasers pumped by single mode diodes. The previously described cavity was modified to generate 136 fs pulses at a repetition rate of 470 MHz with an output power of 20 mW for 95 mW incident pump power [131]. The two single mode diodes were shaped by a microlens, combined using a dichroic mirror, and focused into the Cr:LiSAF crystal; these improvements provided more efficient pump coupling and mode matching, resulting in an electrical to optical efficiency of 4% for the full system. The high reflector coatings on the laser mirrors provided negative dispersion near the lasing wavelength of 859 nm; it is important to note that these were not chirped or double chirped mirrors designed to compensate dispersion. The laser was battery powered and extremely compact, fitting on a 22 x 28 cm^2 breadboard, about the size of an 8.5" x 11" piece of paper. A schematic of the laser cavity and pump diodes is shown in figure 3-9. A similar laser was developed using only a single prism for dispersion compensation, generating 113 fs pulses with 20 mW output power in a compact design. The dispersion compensation and pump source design were carefully analyzed [130].

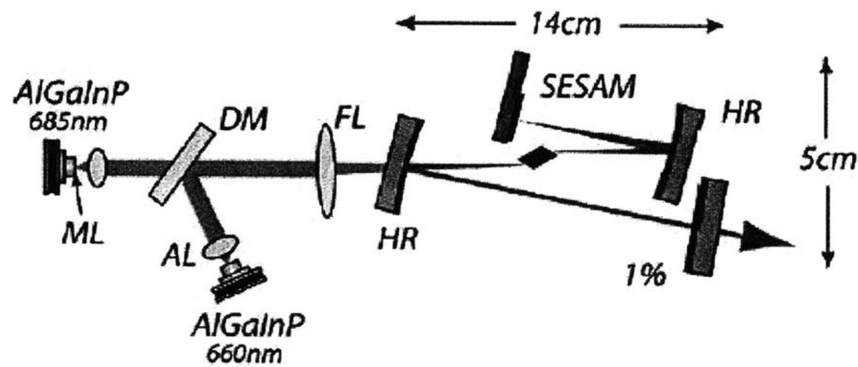

Figure 3-9. Schematic of the compact, single mode diode-pumped Cr:LiSAF laser (from [131]).

By pumping with two pairs of diodes, the laser was then adapted to generate 1.2 kW peak powers with 0.14 nJ pulse energy or 146 fs pulses with 3 mW output power at 1 GHz [131]. The laser was also modified to produce 200 fs pulses with 0.14 nJ pulse energy when pumping with four diodes; the output was frequency doubled to produce a compact, low cost source of 540 fs blue pulses [182]. One disadvantage of these compact, low cost single mode diode pumped Cr:LiSAF lasers is that the pulse energies and pulse durations from these lasers are not comparable to those achieved with standard Ti:sapphire laser systems, which typically generate

sub-100 fs pulses with 1 nJ or greater pulse energy. Therefore, a primary goal of the work performed in this thesis was to develop techniques for increasing pulse energies and reducing pulse durations from single mode diode-pumped Cr:LiSAF lasers. Investigations into this will be discussed in the next chapter.

Chapter 4
An extended cavity femtosecond Cr:LiSAF laser mode-locked with an epitaxially grown saturable absorber

4.1 Introduction

Femtosecond lasers are essential in many applications including ultrafast spectroscopy, high-speed measurement, laser micromachining and biomedical imaging. In order to make femtosecond technology more accessible outside of the laboratory, methods of reducing cost while maintaining high performance must be developed. Current commercial systems producing pulses with durations less than 100 fs are based on the Ti:sapphire laser, which is the workhorse of the ultrashort pulse laser industry due to its high gain and broad bandwidth. However, Ti:sapphire is typically pumped with argon-ion lasers at wavelengths of 488-514 nm or diode-pumped, frequency-doubled Nd:YAG lasers operating at 532 nm. These pump sources are very expensive, with typical prices of ~$50-100K depending on the required power.

Diode-pumped solid-state lasers are an attractive alternative to conventional pumping with expensive gas or solid state lasers. Cr:LiSAF is a widely studied material with a broad emission bandwidth around 850 nm that can be pumped at 670 nm with red laser diodes [161]. As discussed in chapter 3, previous efforts in diode pumping Cr:LiSAF used broad-stripe diodes with powers of hundreds of mW [42, 170, 172, 174, 176]. Pulses as short as 9.9 fs have been generated from a diode-pumped Cr:LiSAF laser [174], and pulse energies of 0.5-1 nJ, comparable to those in standard Ti:sapphire systems, can be achieved with pump powers of several hundred mW [42, 170, 172, 174, 176]. However, these broad-stripe pump diodes are still relatively expensive and have poor mode quality, making efficient mode matching difficult. An attractive alternative is to pump with single spatial mode diodes, which significantly improves

mode matching and laser efficiency [130, 131]. Single mode diodes with powers of 50-60 mW at wavelengths ranging from 660-690 nm are available for only ~$20 each, making this pump source extremely inexpensive. Researchers have demonstrated compact mode-locked Cr:LiSAF lasers pumped by low cost, single spatial mode diodes in several configurations [130, 131]. These lasers typically generated 20 mW output power and 120 fs pulses at 430 MHz, corresponding to a pulse energy of 0.05 nJ. The maximum pulse energy achieved was 0.14 nJ [131], which may be too low for some applications.

The goal of the work described in this chapter was to develop an inexpensive single mode diode-pumped Cr:LiSAF laser generating pulses with durations and energies comparable to those produced from standard Ti:sapphire based systems. A saturable Bragg reflector (SBR) was used for laser mode-locking, and pulse energies were increased by extending the laser cavity with a multi-pass cavity (MPC). Dispersion compensation was accomplished with either double-chirped mirrors (DCMs) or prisms. The pulse energies and durations from this low cost femtosecond source approach those obtained with standard 100 MHz Ti:sapphire lasers, making it a possible substitute for Ti:sapphire in some applications. Section 4.2 briefly describes the properties of the Cr:LiSAF crystal used in this research. In section 4.3, the design of the diode pump source will be discussed. Section 4.4 will describe operation of this laser in a standard four mirror cavity. In section 4.5, the design of a multi-pass cavity (MPC) for increasing pulse energies will be described in detail. The design of the saturable Bragg reflector (SBR) used in this work will be described in section 4.6. Finally, section 4.7 will describe operation of the extended cavity Cr:LiSAF laser with and without prisms.

4.2 Laser properties of Cr:LiSAF

The most common materials used in short pulse diode-pumped solid-state laser systems are crystals of the colquirite family, including Cr:LiSAF, Cr:LiSGAF, and Cr:LiCAF. As discussed in chapter 3, these materials have absorption bands around 670 nm, which is a wavelength range where laser diodes are readily available, and broad gain bandwidths in the near infrared comparable to that of Ti:sapphire. Some important physical and optical properties of

these crystals, along with Ti:sapphire and Cr:forsterite crystals that were also used in this work, are presented in table 4-1. Cr:LiSAF is perhaps the most widely used of the colquirite crystals and was chosen for the work presented in this chapter.

Material	Ti:sapphire	Cr:forsterite	Cr:LiSAF	Cr:LiSGAF	Cr:LiCAF
Gain bandwidth (nm)	700-950	1160-1400	725-945	710-930	710-840
Absorption bandwidth (nm)	450-575	850-1200	600-700	600-700	600-700
Emission cross-section (cm^2)	$3x10^{-19}$	$1.1x10^{-19}$	$4.8x10^{-20}$	$3.3x10^{-20}$	$1.3x10^{-20}$
Upper state lifetime (μs)	3.2	3.9	67	88	170
Refractive index	1.76	1.65	1.4	1.4	1.4
Nonlinear index (cm^2/W)	$3x10^{-16}$	$\sim 2\text{-}6x10^{-16}$	$8x10^{-17}$	$8x10^{-17}$	$8x10^{-17}$
Thermal conductivity (W/m°C)	42	5	3.3	3.6	5.14
Shortest pulses generated (fs)	5	14	9	10	9

Table 4-1. Physical and optical properties of some common solid-state laser crystals (from [28, 89, 113, 114, 159-161, 168, 183]).

The attractiveness of Cr:LiSAF for ultrashort pulse generation lies in its broad gain bandwidth and ability to be diode-pumped. The gain bandwidth is approximately 220 nm [168] which enables the generation of pulses with durations comparable to those from Ti:sapphire lasers [174, 178]. The efficiencies that can be obtained from these lasers are relatively high as well [161]. However, Cr:LiSAF has some disadvantages, making it harder to work with than certain other gain media. The thermal conductivity is much lower than Ti:sapphire, making the laser very sensitive to thermal effects (a property of most Cr:doped crystals, such as Cr:forsterite and Cr:YAG). Pumping with more than 1.5 W risks crystal damage without novel pump focusing designs [150], limiting Cr:LiSAF to relatively low power applications. Cr:LiSGAF has been shown to possess improved thermal conductivity and expansion coefficients, making this material more suitable for higher power lasers [42]. In addition, the relatively low gain cross sections of the colquirite-doped crystals makes them more sensitive to intracavity loss, a problem which is exacerbated when pumping with laser diodes due to their low power and poor mode quality [37]. Upper-state lifetime quenching is also a problem limiting the gain in these crystals at higher temperatures [148, 184]. Finally, the nonlinearity is nearly a factor of four lower than

that of Ti:sapphire, making Kerr lensing difficult in these materials, particularly with the low pump powers available from laser diodes [168, 184]. However, the large bandwidth and diode-pumpability of Cr:LiSAF make it well worth pursuing to satisfy the demand for low cost, efficient, inexpensive femtosecond sources, and indeed a Cr:LiSAF laser running on only six batteries in a compact design has been demonstrated [181], although the pulse energies from this laser are too low for some applications.

4.3 Diode pump source design

Careful design of the pump source for the Cr:LiSAF laser was critical in order to fully utilize all the available pump power. The design of the pump source was similar to that in refs [130] and [131]. The basic concept was to use dichroic mirrors to combine diodes at different wavelengths and polarization multiplexing to combine diodes with different polarization. The diode pump source consisted of two 50 mW single mode diodes at 663 nm (Hitachi HL6503MG) and one 50 mW single mode diode at 685 nm (Mitsubishi ML1013R). Both the HL6503MG and ML1013R are high power AlGaInP laser diodes based on a multiple quantum well (MQW) structure. The threshold currents of these diodes are 30-35 mA, with a maximum operating current of 135-140 mA. The diodes come in a small package with 5.6 mm diameter. The beam divergence of these diodes is approximately 9 degrees parallel to the junction and 20.5 degrees perpendicular to the junction. This necessitated a method of making the tangential and sagittal beam divergences equal. Anamorphic prisms can be used to expand or compress the beam in the tangential plane. In this work, anamorphic prisms were initially used to make the beam divergence the same in the tangential and sagittal planes. However, a simpler technique is to mount a small lens on the diodes that transforms the elliptical laser output into a circular beam. This technology was developed by Blue Sky Research and is a significant improvement upon beam shaping with anamorphic prisms, since the pump source is more compact and the power loss is much lower from the microlenses than the prisms. The diodes used in the presented research were microlensed by Blue Sky Research to provide a circular output beam. The light was collimated with short focal length lenses and each collimated beam was measured with a beam profiler (ThorLabs) in the tangential and sagittal planes to minimize the beam divergence.

It was found that the distance between the diode and the collimating lens was an extremely sensitive parameter, making it difficult to get a well collimated beam. This also made it difficult to set the beam size of each diode in the sagittal and tangential planes to be equal to one another. The collimated sizes of the three diode beams are given in Table 4-2.

Diode	Tangential beam size (mm)	Sagittal beam size (mm)
D1 (Hitachi 663 nm)	1	1.15
D2 (Mitsubishi 685 nm)	1.06	1.09
D3 (Hitachi 663 nm, polarization rotated)	1.1	1.15
Total combined beam	1.02	1.14

Table 4-2. Diode beam sizes measured in the tangential and sagittal planes using a ThorLabs beam profiler. Each beam was individually measured with the other two beams blocked, and the combined beam was measured with all three diodes at a current of 117 mA. The beams were each attenuated to powers of less than 1 mW before the beam profiler with a 3.0 ND filter. D1, D2, and D3 are also described in Figure 4-1 and in the text.

A schematic of the pump source is shown in Figure 4-1. One 663 nm diode (D1) was combined with the 685 nm diode (D2) using a dichroic mirror (DM). Several mirrors were tested for use as dichroic mirrors, with the requirement of high transmission of the 663 nm beam and high reflectivity of the 685 nm beam for a certain angle. It was found that a broadband high reflector for the Cr:LiSAF wavelength range, made by Alpine Research Optics (ARO), was optimal for this application when tilted at an angle of approximately 45 degrees to the 663 nm beam. Diodes D1 and D2 were polarized in the tangential plane, such that the electric field was parallel to the crystal axis. The polarization of the other 663 nm diode (D3) was rotated using a half-wave plate (WP) to be perpendicular to the polarization of the other two beams. A polarizing beam splitter (PBS) was then used to combine the three beams. After the PBS, the three beams had a total power of 139 mW, with 47 mW from D1, 51.5 mW from D2, and 40.5 mW from D3 for each diode driven by a current of 117 mA. For a given current, the Mitsubishi diode (D2) typically offered more output power than the two Hitachi diodes. The lower power from D3 is due to losses in the PBS. Measurements of the laser output power versus pump

power for various combinations of the pump diodes will be described in section 4.8 and are plotted in figure 4-18.

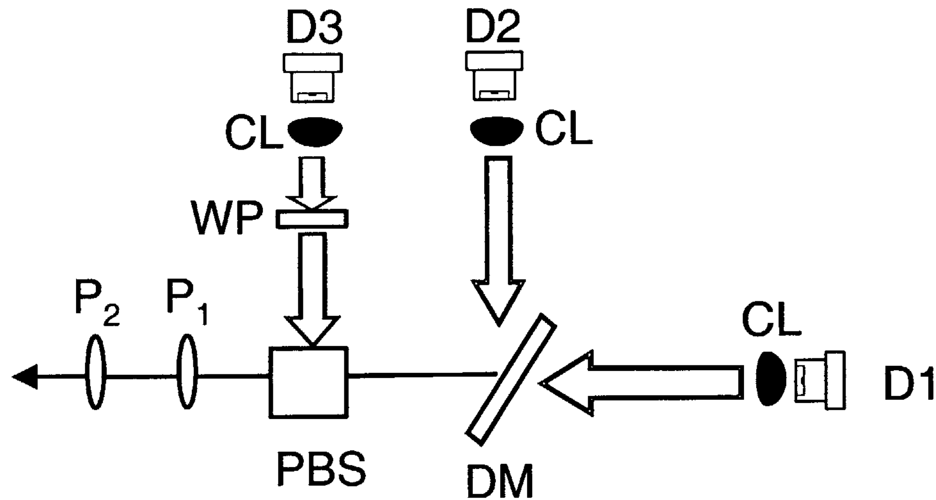

Figure 4-1. Schematic of the diode pump source. D1 and D3 are 50 mW Hitachi 6503MG diodes at 663 nm. D2 is a 50 mW Mitsubishi ML1013R diode at 685 nm. P_1 is an f=-100 mm diverging lens and P_2 is an f=76.3 mm anti-reflection coated achromatic lens. CL are collimating lenses, DM is the dichroic mirror, WP is a half wave plate, and PBS is the polarizing beam splitter.

Diode	Tangential beam radius (μm)	Sagittal beam radius (μm)
D1 (Hitachi 663 nm)	12.5	11.5
D2 (Mitsubishi 685 nm)	10.5	12
D3 (Hitachi 663 nm, polarization rotated)	11.5	11.5
Total combined beam	15	18

Table 4-3. Measured beam radius for each diode in the tangential and sagittal planes at a distance of 5.4 cm from M1.

Several combinations of lenses were tested to focus the pump beam to a small spot within the crystal. The combination producing the smallest spot was found to be an R=-100 mm diverging lens (P1) and an R=76.3 mm antireflection coated achromatic lens (P2), separated by 35 cm. The focused spot size for each beam was measured using the beam profiler after passing through the curved mirror M1 (see figure 4-3). The measurement was performed at a distance of

5.4 cm from M1, corresponding to the typical crystal position in this laser cavity. The results are depicted in Table 4-3.

This lens combination resulted in a minimum radius of 15 x 18 μm for the combined pump beam. This is larger than the individual focused spot size of each beam due to the difficulty in perfectly overlapping all three focused spots. The total power incident upon the crystal was 137 mW after passing through the two lenses and curved mirror.

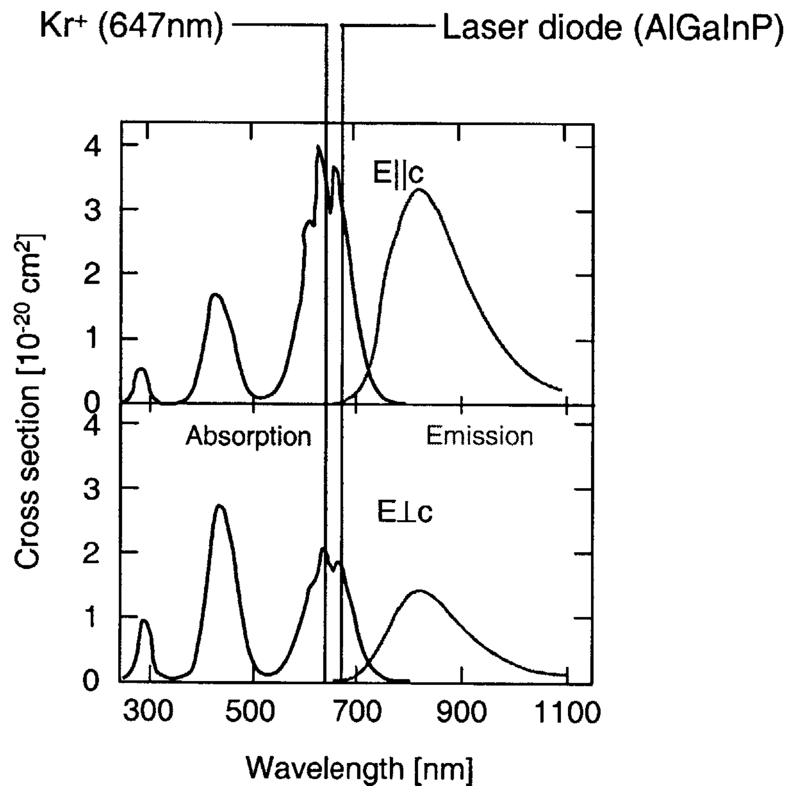

Figure 4-2. Absorption and emission cross sections for Cr:LiSAF for the electric field polarized both parallel (top plot) and perpendicular (lower plot) to the crystal axis at a temperature of 295 K (courtesy of Y. Hirakawa, originally from ref [161]). The wavelengths of a Kr laser and the AlGaInP laser diodes used in this thesis are also shown.

The addition of a fourth pump diode with a wavelength of 685 nm was also considered when designing the pump source. However, the polarization of this diode would have to be rotated in order to multiplex it with the other three diodes. The absorption of the Cr:LiSAF crystal is nearly a factor of two lower for the electric field polarized perpendicular to the crystal

axis, and is also somewhat lower at 685 nm as compared to 663 nm (figure 4-2). Therefore, the improvement in Cr:LiSAF output power that could be expected from adding an additional pump diode was incremental, and three diodes were used for the pump source as previously described. Another possibility for increasing the laser output power could be to pump with another diode pump source based on three diodes from the other side of the laser crystal.

4.4 Operation of the Cr:LiSAF laser in a four mirror cavity

The laser was initially set up to operate in a four mirror x cavity (Figure 4-3) to test the cw laser performance in a standard configuration and attempt to obtain KLM. The pump source was shown in figure 4-1. The 5 mm long Brewster cut, 1.5 % doped Cr:LiSAF laser crystal (CR) was obtained from VLOC Corporation. Two curved mirrors (M_1 and M_2, R=10 cm) identical to the dichroic mirror made by Alpine Research Optics (ARO) used earlier were used to tightly focus the laser mode to a beam waist of 20 μm radius within the crystal. The transmission of the ARO mirrors was measured using a Cary spectrophotometer and is shown in figure 4-4. The measured transmission is less than 0.1% from 785-935 nm, making the mirror reflectivity extremely high, which is necessary for use with the low gain Cr:LiSAF crystal. A table of all optics used in the different iterations of this laser cavity is given in appendix B.

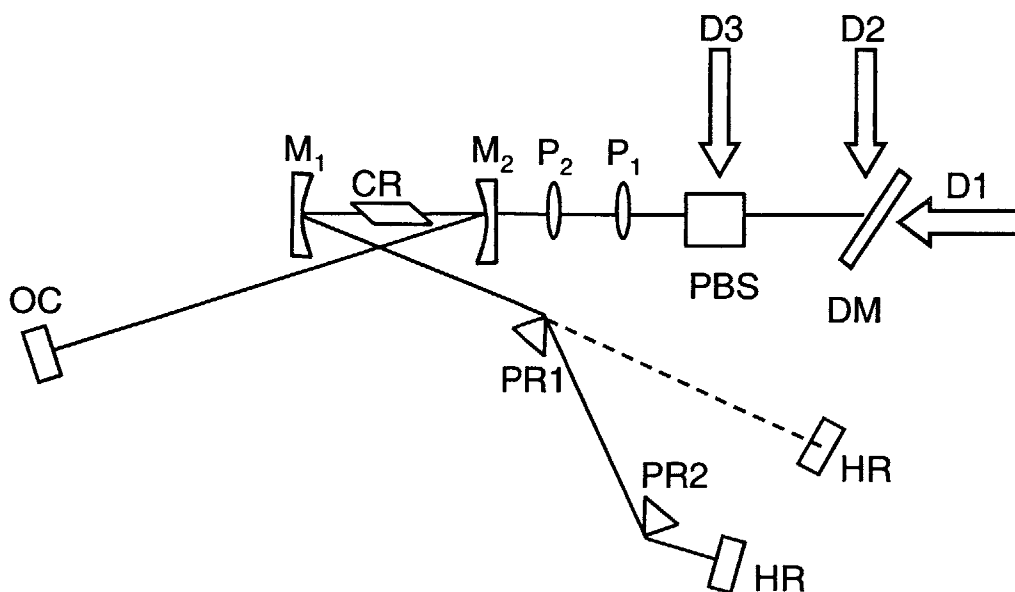

Figure 4-3. Schematic of the x cavity Cr:LiSAF laser.

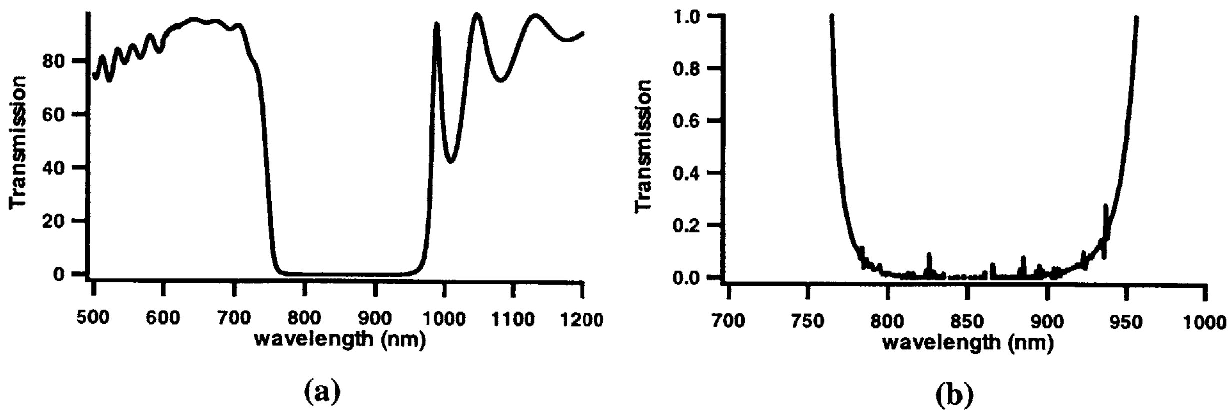

Figure 4-4. Measured transmission of the ARO high reflecting mirrors used in the Cr:LiSAF laser cavity. (a) Full scale. (b) Close up of the reflectivity. The transmission is <0.1% from 785-935 nm.

The transmission of the 3 mm thick output coupler (OC) was also measured and is plotted as a function of wavelength in figure 4-5. The transmission is less than 1.5% between 818 and 895 nm, making the output coupler suitable for use with a Cr:LiSAF laser operating at 860 nm.

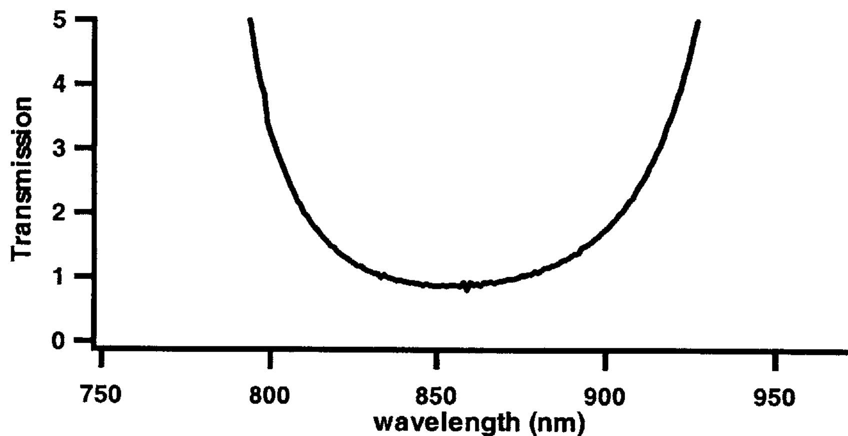

Figure 4-5. Measured transmission of the output coupler used in the Cr:LiSAF laser cavity. The transmission is <1.5% from 818-895 nm.

The high reflecting end mirror (HR) was also an ARO mirror. The arm lengths were initially set to 47 cm (M_1-OC) and 74 cm (M_2-HR). In this configuration, the laser produced 34 mW cw output power as measured using a Coherent Fieldmaster GS power meter with a silicon detector; this power meter was used for all the measurements reported in this chapter. The

Cr:LiSAF laser lased with each diode operating as a single pump beam and the other two diodes blocked. The threshold for lasing with D1 was 22.7 mW (measured at the position of the crystal), 23.3 mW for D2, and 35 mW for D3. This dependence was expected since the absorption of the crystal is highest for D1 due to its electric field polarized parallel to the crystal axis and wavelength of 663 nm, and lowest for D3 with its electric field polarized perpendicular to the crystal axis.

The next step was to attempt mode-locking with KLM. Two fused silica prisms, separated by a distance of 50 cm, were added in the long arm for dispersion compensation as described in section 2.11.3. This choice of prism material and separation has been shown to optimize the second and third order dispersion for Cr:LiSAF [87]. The GDD of the Cr:LiSAF crystal has been measured to be ~225 fs^2 for a round trip through a 5 mm crystal [87]; this value conflicts with that calculated from the Sellmeier equations and reported in ref [185], but agrees approximately with the value reported in ref. [168] and was used in this work. The mirrors in the cavity introduce a negligible amount of dispersion. Therefore, the separation and insertion of the prism pair was set to compensate the crystal dispersion and provide dispersion tunability over a broad range. The cw power obtained after the prisms were inserted was 32 mW.

The end mirror was mounted on a movable stage to initiate KLM. The curved mirror M_2 was systematically translated in increments of 250 μm through the outer stability region, optimizing the power by changing the crystal position, pump lens position, and vertical and horizontal angles of the OC and HR. At each M_2 position, the end mirror stage was shaken in an attempt to initiate mode-locking while varying the dispersion by changing the prism insertion. At several positions in the outer stability region, a mode-locked spectrum was observed on an optical multichannel analyzer (Princeton Applied Research). The observed bandwidth was as large as ~20-30 nm. However, a cw peak always appeared on the short wavelength side of the mode-locked spectrum. This instability always stopped mode-locking after a few seconds, and stable KLM operation for longer than 30 seconds was never observed.

This can be explained by noting that as described in section 2.6, the saturable absorber strength must be large enough to stabilize the pulse against multiple pulsing and cw

breakthrough. CW breakthrough is most likely the dominant source of instabilities in this laser; multiple pulsing typically occurs at high peak intensities and is not a factor here since the pulse energies are relatively small and the nonlinearity of LiSAF is low. The nonlinear phase shift given by equation (2.13) is a good measure of the amount of Kerr lensing within the laser crystal. In this laser, the nonlinear phase shift is only ~0.035 for the low pulse energy of 0.3 nJ out of the laser when assuming a 50 fs pulse, while in Ti:sapphire lasers it is typically ~0.5. Therefore, the self-focusing and subsequently the Kerr lensing is too weak to produce efficient self-amplitude modulation, and the pulse is not stable against cw breakthrough. This is supported by the fact that the pulse was stable for the longest times (~30 seconds) for small bandwidths of 10-15 nm, where the loss in pulse energy due to gain filtering is a weaker effect.

The primary limitation against obtaining pure KLM in this laser is the properties of the pump diodes. Although single spatial mode diodes provide much better mode quality than broad stripe diodes, they still do not offer the mode quality available from gas or solid state lasers. As discussed earlier, these diodes can only be focused to minimum spot sizes of ~15-20 μm, which limits the peak pulse intensity and therefore the KLM strength. Higher power diodes would also help in overcoming this limitation by increasing the Cr:LiSAF output power and therefore the pulse intensity in the laser crystal. A KLM Cr:LiSAF laser pumped by single spatial mode diodes would be an inexpensive, compact source of femtosecond pulses, which can hopefully be attained once better quality pump diodes become available.

4.5 Design of a multi-pass cavity for increasing laser pulse energies

Multi-pass cavities (MPC) providing a unity q parameter transformation of the Gaussian beam have been used to reduce repetition rates from laser oscillators and thereby increase pulse energies without requiring external amplification [186, 187]. The best performance directly out of the laser oscillator in a standard cavity design achieved 720 mW average power with 7.5 fs pulses at 77 MHz repetition rate, resulting in a pulse energy of 9.4 nJ and peak power of 1.25 MW directly from the laser cavity [80]. Focused to a 10 μm radius spot, the peak intensity would be 1.25×10^{12} W/cm^2. However, many interesting nonlinear effects take place at

intensities beyond 10^{13} W/cm^2, including multiphoton and tunneling ionization and the onset of relativistic nonlinear optics. Therefore, amplified systems are necessary for reaching these high intensities. Amplified systems tend to be quite complex and expensive, motivating the desire to increase pulse energies directly from the laser oscillator; in addition to enabling some applications not previously possible with non-amplified systems, the oscillator could also be used to seed an amplified system and reduce its complexity. The reduced repetition rate of the multi-pass cavity oscillator also minimizes thermal effects in studies, such as pump probe spectroscopy.

The basic principle of the multi-pass cavity is to extend the cavity length while leaving the q parameter of the beam within the laser resonator invariant. The average power of the laser is determined by the pump power, resonator loss, and crystal gain and is therefore independent of the cavity length. Increasing the cavity length increases the time between pulses when the laser is mode-locked, and for a given average power this results in more energy per pulse. Extending the arms in a standard four mirror cavity increases the distance between the two stability regions while making each of them smaller, and also makes the mode size smaller in the crystal, leading to instabilities in laser operation. Also, to reduce the repetition rate and increase the pulse energy by a factor of 10, the cavity must be made 10 times longer, which becomes prohibitively large when scaling a standard 100 MHz cavity with a roundtrip length of 3 m down to a 10 MHz cavity with a roundtrip length of 30 m. Therefore, novel techniques of extending the laser cavity in a compact configuration without introducing instabilities are necessary.

The multi-pass cavity developed to address this issue is based on work done in the 1960s by Herriott et al [188, 189]. The cavity consists of two large mirrors between which the beam passes many times, striking the mirror in a circular or elliptical pattern around the circumference of each mirror. For a desired repetition rate, the radius of the curved mirrors, number of bounces on each mirror, and distance between the two large mirrors can be optimized to give a unity q parameter transformation using ABCD matrix analysis. When the MPC is set for unity q and introduced into a laser cavity, the cavity stability region and beam parameters do not change. It is also important to check the angular advance of the beam as it passes between the mirrors, since it must be set such that the beam repeats itself upon a round trip through the cavity. This refers

to the fact that as the beam propagates between the two mirrors in the cavity, it strikes each mirror at a different point around the mirror circumference upon each pass. For example, a cavity with four bounces on each mirror will exhibit a pattern with the bounces at the corners of a diamond or square on each mirror. A schematic of a typical multi-pass cavity is shown in figure 4-6.

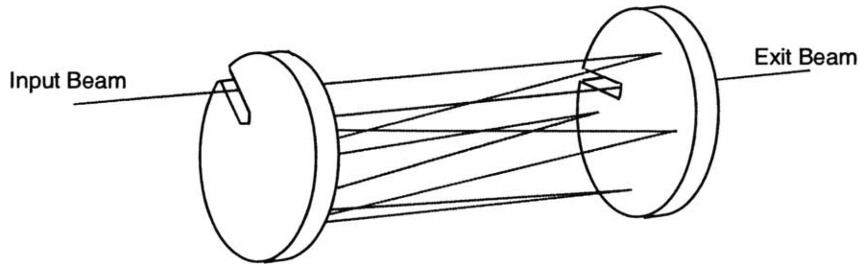

Figure 4-6. Schematic of a multi-pass cavity with four bounces on each mirror. The beam is introduced and extracted through notches in the mirrors (figure reprinted from ref. [190]).

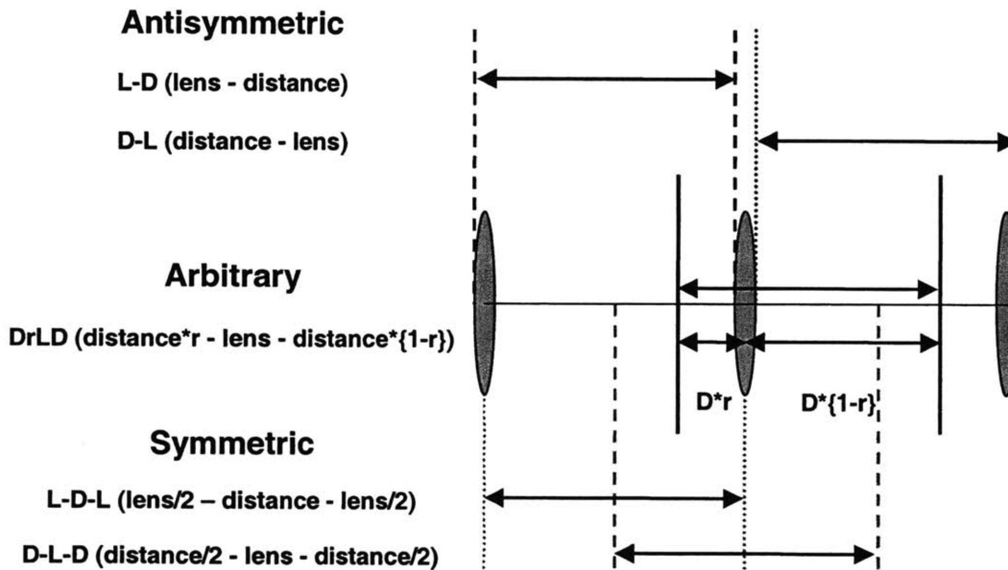

Figure 4-7. Possible unit cells for the unity q transformation in an MPC. The cavity is unfolded, representing the mirrors with lenses, and the reference planes are depicted with vertical lines.

Design of a generalized MPC was analyzed in ref. [191]. Initially, the reference planes and unit cell for calculating the unity q transformation are chosen. Many choices of reference planes are possible, as shown in figure 4-7.

Once this is chosen, the ABCD matrices are determined for the elements in the cavity such as the curved mirrors and the distance between them. The matrix for one round trip, called the ray transfer matrix, is calculated and can be represented in the most general case by

$$M_T = \begin{pmatrix} A & B \\ C & D \end{pmatrix}. \tag{4.1}$$

The determinant of this matrix is unity since a ray entering the MPC comes back to the same region in the cavity after each round trip. The initial ray is represented by a ray vector, given by

$$\vec{r}_i = \begin{pmatrix} r_0 \\ r_0' \end{pmatrix}, \tag{4.2}$$

where r_0 and r_0' give the initial distance from the optical axis and the initial inclination of the ray, respectively. After n round trips, the ray vector becomes

$$\vec{r}_n = M_T^n \vec{r}_i. \tag{4.3}$$

Cavity stability requires that

$$\left| \frac{A+D}{2} \right| \le 1, \tag{4.4}$$

ensuring that the ray will remain confined to the optical axis after n round trips. The eigenvalues and eigenvectors of M_T can be calculated, and then for n round trips the transfer matrix becomes

$$M_T^n = \begin{pmatrix} \frac{A-D}{2}\frac{\sin n\theta}{\sin\theta} + \cos n\theta & B\frac{\sin n\theta}{\sin\theta} \\ C\frac{\sin n\theta}{\sin\theta} & \frac{D-A}{2}\frac{\sin n\theta}{\sin\theta} + \cos n\theta \end{pmatrix}, \tag{4.5}$$

with

$$\cos\theta = \frac{A+D}{2}. \tag{4.6}$$

The angle θ is physically interpreted as the change in angular position of the spots on each mirror after successive round trips, or the angular advance as previously described. In general, the spots

will trace out an elliptical pattern with successive bounces on each mirror; with proper alignment of the initial ray, a circular spot pattern is obtained.

The MPC will have a unity q parameter transformation when $M_T^n = \pm I$, with I the identity matrix. In general, $M_T^n = (-1)^m I$ must be satisfied, which from equation (4.5) occurs when

$$n\theta = m\pi . \tag{4.7}$$

This equation states that the angular advance after n round trips must be a multiple of π in order for the MPC to preserve a unity q transformation. Another way of stating this condition is that the angle θ between successive bounces must be π times a rational number, the ratio of two integers (m/n), for a unity q transformation after n round trips. The parameter m gives the number of semicircular arcs that the beam makes on each of the mirrors before the q parameter returns to its initial value. When m is even, the beam goes around the whole circle an integer number of times before returning to its initial position and exiting the MPC. Examples of a set of possible solutions to (4.7) as well as a example of the application of these equations to the design of an actual MPC are given in ref. [191].

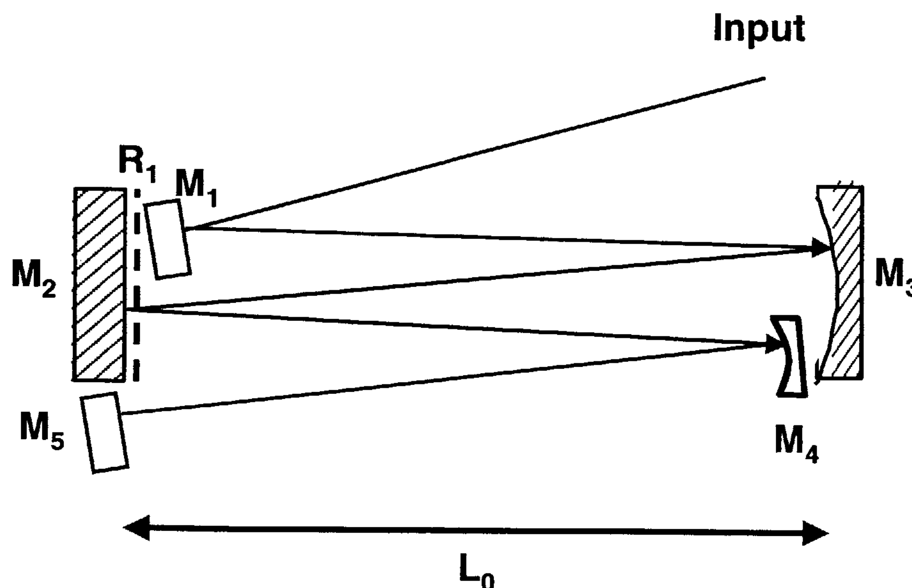

Figure 4-8. Schematic of the MPC used in this work. M_1 is a 0.5” diameter plane mirror. M_2 is a 1.5” diameter plane mirror. M_3 is a 1.5” diameter R=4 m mirror and M_4 is a 0.25” diameter R=4 m mirror. M_5 is the output coupler. The two large mirrors are separated by L_0=2 m. The

reference plane for the unity q transformation is designated by R_1. All mirrors are DCMs, and the beam passes 16 times between the two mirrors.

This approach was followed to design an MPC for the Cr:LiSAF laser described in section 4-4. The initial purpose of the MPC was to increase pulse energies in the hope of obtaining KLM. The MPC used in this work consists of one large plane mirror and one large curved mirror separated by a certain distance, with two smaller mirrors, one plane and one curved, used to introduce and extract the laser beam from the MPC. The smaller plane mirrors are necessary to introduce and extract the beam from the cavity. A schematic of the MPC is shown in figure 4-8.

The ray transfer matrix M_T for this cavity is calculated by multiplying the ABCD matrices for a distance-lens-distance (DLD) unit cell, shown in figure 4-7, since starting at the reference plane R_1, the beam travels a distance L_0, bounces off a mirror with radius of curvature R, and returns through the distance L_0 to the reference plane in one round trip. M_T is given by

$$M_T = \begin{pmatrix} 1-\frac{2L_0}{R} & 2L_0\left(1-\frac{L_0}{R}\right) \\ -\frac{2}{R} & 1-\frac{2L_0}{R} \end{pmatrix}, \tag{4.8}$$

with

$$\cos\theta = 1-\frac{2L_0}{R}. \tag{4.9}$$

For a given R, varying L_0 will give the values of θ that provide a unity q transformation as calculated from equation (4.7). Once L_0 is known, the repetition rate can be calculated since the round trip optical path length introduced by the MPC is $4nL_0$. The repetition rate is given by

$$f_{rep} = \frac{c}{2nR\left(1-\cos\left(\frac{m\pi}{n}\right)\right)}. \tag{4.10}$$

It can be shown that for given values of m and R, there is an optimal value of n that produces the lowest repetition rate [191]. The parameter n gives the number of bounces on each mirror in each single pass through the MPC, and therefore there are $2n$ bounces on each mirror in each roundtrip through the full MPC, or $4n$ total bounces when including both mirrors.

When designing an MPC for the Cr:LiSAF laser, it was important to keep the number of bounces on each mirror low, since the Cr:LiSAF laser is very sensitive to loss due to the low pump powers. To achieve the lowest repetition rate and therefore the highest pulse energy, there is a tradeoff between the number of bounces on each MPC mirror (introducing loss into the cavity which lowers the pulse energy) and the distance between the two mirrors (limited by table space and the desire for a compact design). Equations (4.7) and (4.9) were solved to obtain an expression for the separation L_0 between the two mirrors as a function of n for different values of m in q-preserving configurations. The result of this calculation is depicted in figure 4-9.

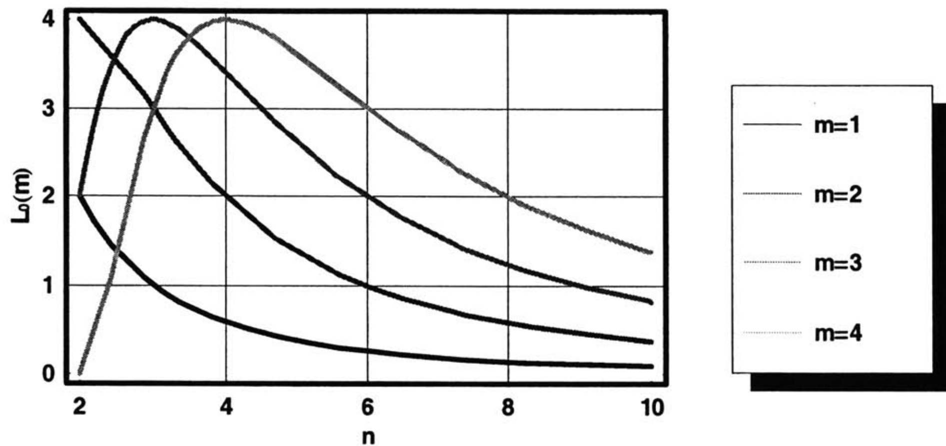

Figure 4-9. Calculation of the mirror separation for the flat-curved mirror cavity as a function of n, for different values of m. The radius of curvature for the curved mirror is 4 meters.

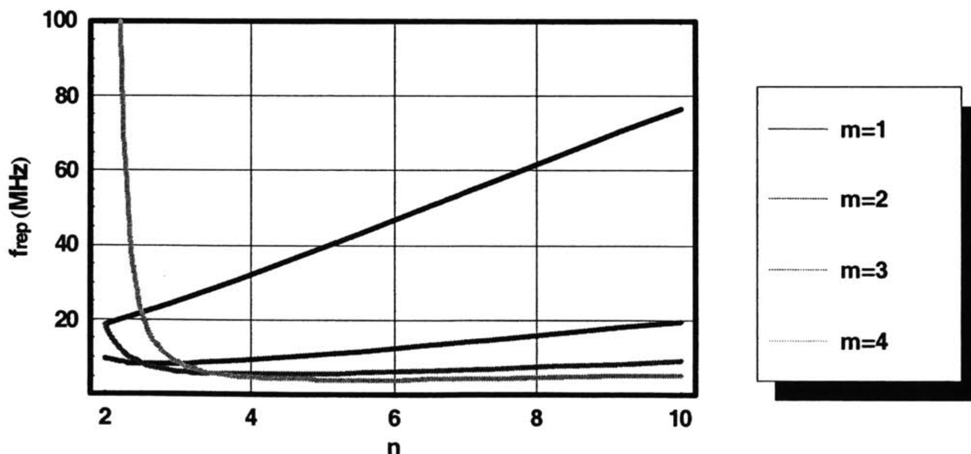

Figure 4-10. Calculation of the repetition rate for the flat-curved mirror cavity as a function of n, for different values of m. The radius of curvature for the curved mirror is 4 meters.

The repetition rate was also calculated using equation (4.10) as a function of n for different m values. In the actual laser, the repetition rate will be lower due to the additional cavity length external to the MPC. The results of this calculation are shown in figure 4-10.

These figures can be used to design an MPC for the Cr:LiSAF laser. One design constraint in this work was the available table space, which limited the maximum possible mirror separation to 2 meters. Another design constraint, as previously mentioned, is the number of bounces on each mirror, limited to a maximum of four to minimize the loss introduced into the cavity. From figure 4-9, it can be seen that for a maximum separation of 2 meters, the m=2 curve gives n=4 bounces, the maximum allowed. The m=3 and m=4 choices have too many bounces for use in a Cr:LiSAF laser with a 2 meter mirror separation. The repetition rate is near the minimum as seen in figure 4-10 for the m=2 curve. Therefore, the choice of m=2 and n=4 seems appropriate for design of a low repetition rate laser. The angular advance is $\theta=\pi/2$, meaning that successive spots are rotated by $\pi/2$ radians on each mirror, forming a diamond or square pattern.

In this MPC, the beam passes 16 times through the cavity in one round trip, for a total added cavity length of 32 m. It is important to account for the dispersion introduced by the many passes through air in the MPC design. If prisms and non-DCM MPC mirrors are used, the prism separation must be set to compensate the additional air dispersion. Low loss double chirped mirrors (DCM) [92] that provide negative dispersion (described in section 2.10.4) can also be used in the MPC to approximately cancel the large amount of air dispersion due to the many passes through the cavity. Therefore, with careful design the MPC can be introduced into the laser cavity without significantly affecting the beam parameters, cavity stability region, or cavity dispersion.

The DCMs used in this work were designed by Dr. Uwe Morgner and Professor Franz Kaertner. These DCMs provided -42 fs^2 group delay dispersion (GDD) per bounce around 860 nm and had a reflectivity bandwidth of 695-895 nm. The reflectivity and dispersion of these mirrors are plotted in figure 4-11. The dispersion of air is approximately 20 fs^2/m at 860 nm [56]. Therefore, for 32 m of air and 16 bounces on the MPC mirrors the total dispersion of the

MPC is approximately –32 fs^2. This design is convenient since each bounce in the MPC approximately compensates the dispersion introduced from one pass through 2 m of air, and therefore the MPC introduces a minimal amount of dispersion into the laser cavity and the prism separation can remain the same.

(a)

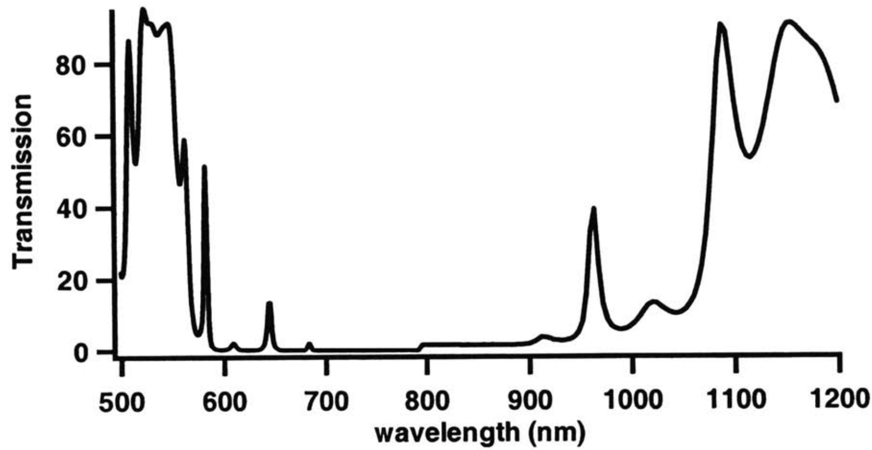

(b)

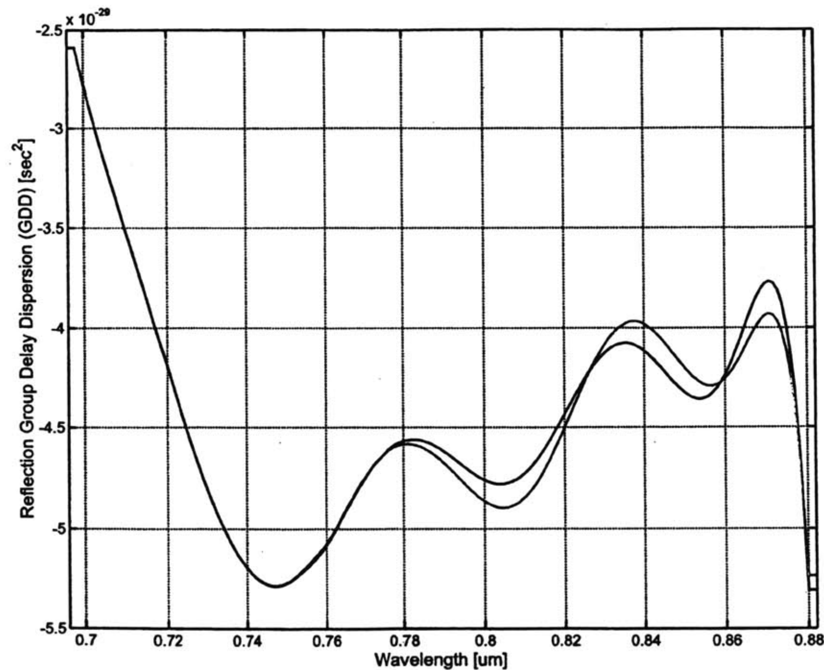

Figure 4-11. (a) Reflectivity of the DCMs used in the Cr:LiSAF laser. The step in the data at 800 nm is due to a detector change. This figure shows the high reflectivity bandwidth of these DCMs. (b) Calculated and measured dispersion of the DCMs (obtained from V. Scheuer).

As described in the previous section, the laser was initially optimized in a standard X cavity with no MPC, obtaining a cw power of 32 mW with prisms. The non-prism arm was extended to 90 cm by folding it with two ARO high reflectors for insertion of the MPC. The MPC must usually be inserted in the long arm of the cavity since the beam is roughly collimated out of this arm in the outer stability region; if the MPC is inserted in the short arm of the cavity, the beam divergence is too large for the beam to fit on the 0.25" R=4 m mirror.

In general, the output beam of the laser is used to roughly align the MPC, after which it is removed and the MPC is adjusted for lasing. However, if the laser output coupler is wedged, then the alignment of the MPC is changed due to the displacement of the output beam through the OC. A special non-wedged, low loss output coupler was used to align the MPC; it was removed once the MPC was aligned and the output was taken out of the MPC arm.

A schematic of this cavity is shown in figure 4-12. The end mirror for the short cavity is labeled "short cavity HR" in the figure. The short cavity was set to a point for optimum KLM, near the inner edge of the stability region where a broad spectrum was observed (although it was not stable as previously described). After the MPC was inserted and aligned, lasing was obtained quickly without changing the laser cavity outside of the MPC. Outputs of 15 mW cw power were obtained. The unity q performance of the MPC was tested by varying M_2 and comparing the extent over which lasing could be obtained with the same measurement in the short cavity; the two measurements were found to be virtually identical, indicating that the MPC did not affect the beam parameters in the laser cavity.

Kerr lens mode-locking was attempted by shaking the end mirror while varying M_2 as before. However, KLM was significantly harder to start in this cavity, and although broad spectra of 30-40 nm were observed, they were not stable for more than a few seconds. This can be explained using equation (2.31). The condition for starting is directly proportional to the cavity round-trip time; if the cavity round-trip time is very long, as in this cavity (117 ns), then a larger perturbation is required to start mode-locking. Shaking the end mirror stage did not

produce a large enough perturbation to start KLM in this cavity. Therefore, the use of a saturable absorber to start and stabilize mode-locking was necessary.

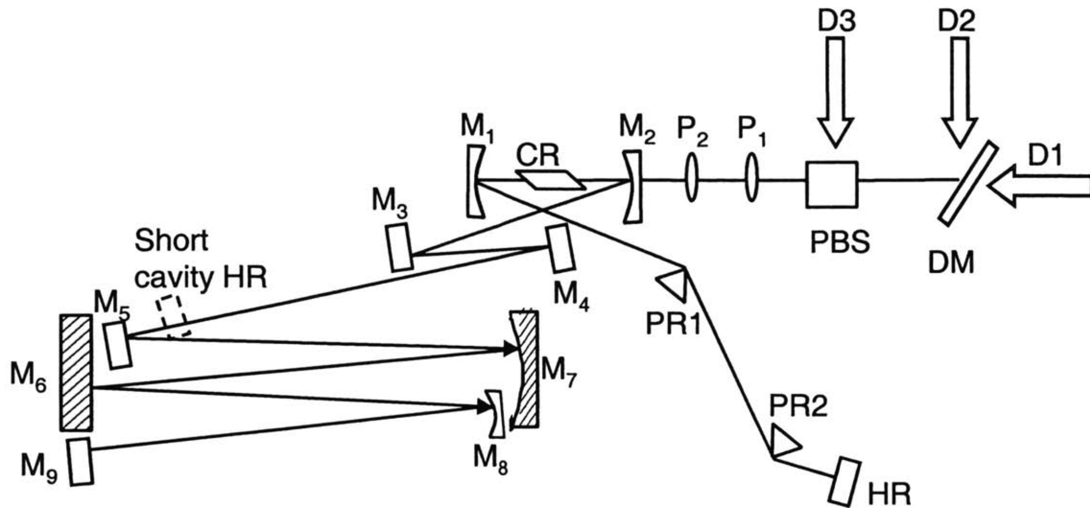

Figure 4-12. Schematic of the extended cavity Cr:LiSAF laser. All mirrors except for M_5-M_9 are ARO high reflectors. Other than the MPC, the cavity is identical to that of figure 4-3.

4.6 Saturable Bragg reflector design

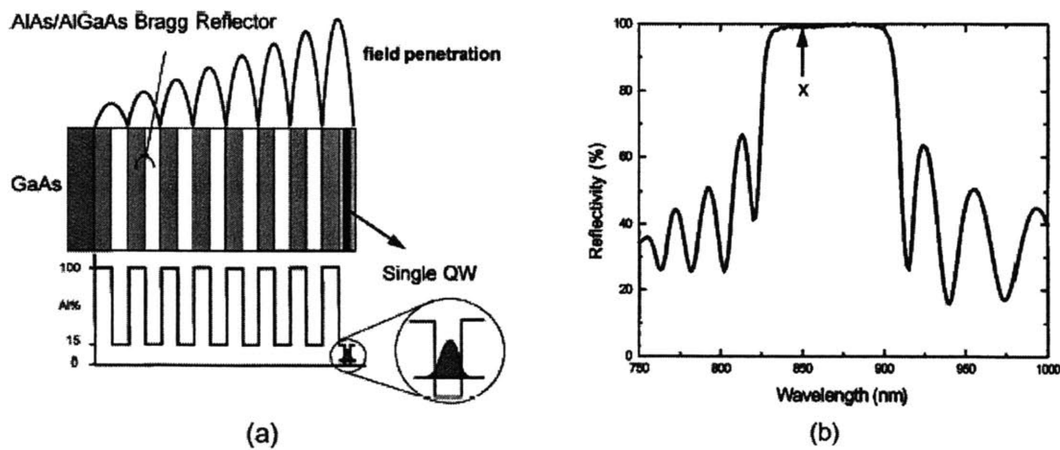

Figure 4-13. Device structure (a) and reflectivity bandwidth (b) of the SBR [128].

The saturable absorber used in this work was identical to that described in ref [128]. It is a saturable Bragg reflector (SBR) device designed for use with Cr:LiSAF and Cr:LiSGAF lasers.

The device design and reflectivity bandwidth is shown in figure 4-13. The device is based on an $AlAs/Al_{0.85}Ga_{0.15}As$ quarter wave layer stack grown by molecular beam epitaxy with minimized scattering losses. A single quantum well (QW) is inserted in the structure to provide saturable absorption, and the saturation intensity of the device can be varied by changing the QW position within the device structure as described in chapter 3. In the device used in this research, the 10 nm GaAs QW is inserted in the top layer of the structure, which consists of 30 high/low index pairs with a reflectivity of 99.5% from 825-900 nm. The dispersion of the SBR is low. The SBR has ~1% saturable absorption, with a low saturation intensity. This SBR has previously been used to self-start 90 fs pulses from a Cr:LiSAF laser [37, 128].

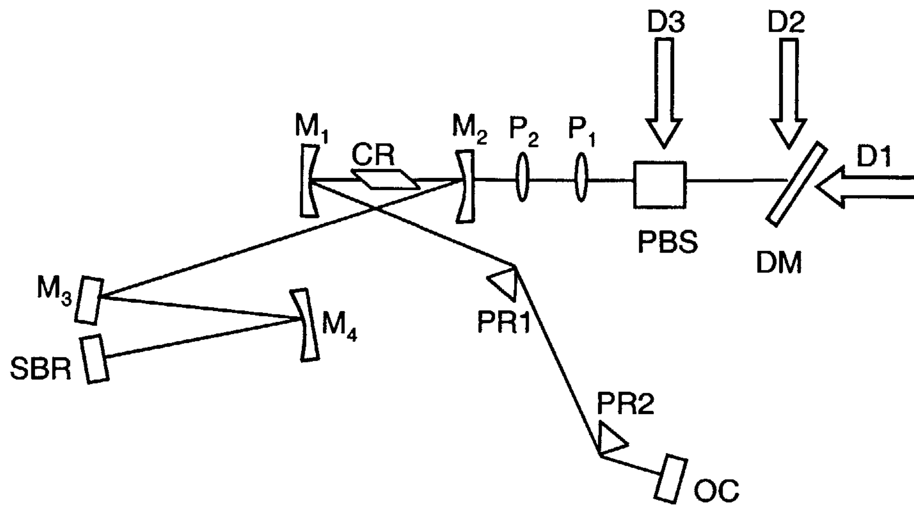

Figure 4-14. Schematic of the x cavity Cr:LiSAF laser with an SBR. M_3 is a plane ARO mirror and M_4 is an R=15 cm Layertec high reflector. All other elements are as described in figure 4-3.

The SBR was tested in the short cavity to determine its suitability for mode-locking the Cr:LiSAF laser. A schematic of the experimental setup is shown in figure 4-14. The output coupler was moved to the prism arm for this experiment. The SBR was mounted on a translation stage and inserted in the non-prism arm, using an R=15 cm mirror (M_4) to generate a small spot size on the device. The separation between M_3 and M_4, and between M_4 and the SBR was adjusted to be equal to the focal length of M_4; this sets the extra fold for a unity q transformation. This can be seen using the same analysis as used in section 4.5 for the multi-pass cavity; the fold after M_3 is a distance-lens-distance unit cell, and this has a unity q transformation when the distance is equal to the focal length. This can also be derived through ABCD matrix analysis.

Therefore, the extra fold with the SBR does not change the cavity stability region or affect the beam parameters within the cavity once the distances are correctly set.

Lasing was first obtained with a standard high reflector in the SBR position. After this mirror was replaced by the SBR and the distances in the extra fold were optimized, a maximum output power of 15 mW was obtained. Mode-locking was self-starting for powers above 7-8 mW and bandwidths up to 20 nm were obtained. Mode-locking did not strongly depend on the curved mirror or crystal positions, suggesting that this was not KLM, but soliton mode-locking.

4.7 Mode-locked operation of the extended cavity Cr:LiSAF laser with and without prisms

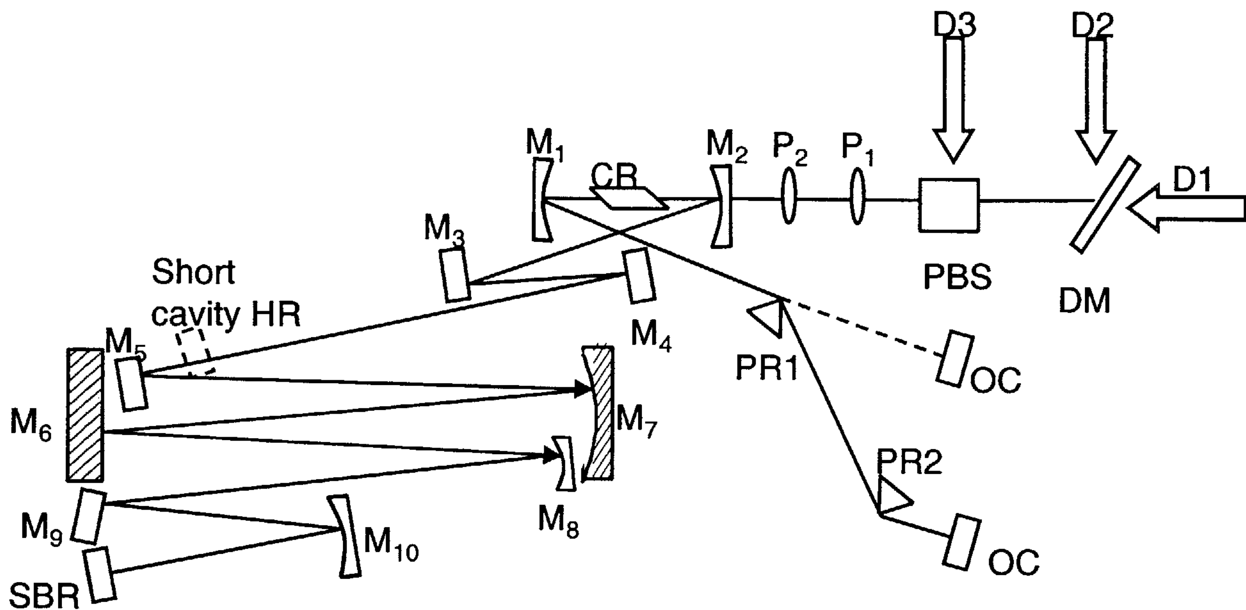

Figure 4-15. Experimental setup of the extended cavity femtosecond Cr:LiSAF laser.

The MPC was introduced into the cavity to generate higher energy pulses [192, 193]. A schematic of the experimental setup is shown in figure 4-15. Initial experiments were performed using prisms for dispersion compensation. The output coupler arm was 70 cm and the MPC arm was 90 cm. The output cw power was 15 mW without the extra fold for focusing onto the SBR. The SBR was subsequently placed in an extra fold after the MPC. An R=20 cm mirror (M_{10})

was used to focus the laser mode to a ~75 μm radius spot on the SBR. The reference planes for a unity q transformation in the MPC are the same as before, at M_6 and M_9. The extra fold in the MPC arm was set for unity q by making the distances from M_9 (the MPC reference plane) to M_{10} and from M_{10} to the SBR equal to the focal length of M_{10} as described above.

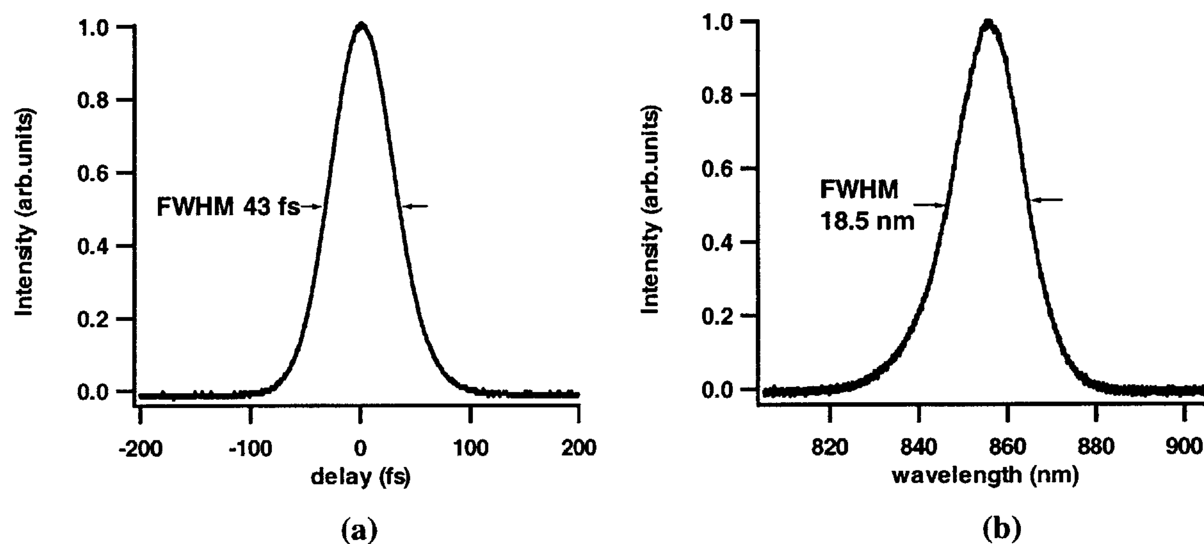

Figure 4-16. Autocorrelation (a) and spectrum (b) of the extended cavity Cr:LiSAF laser using prisms for dispersion compensation. The output power in this configuration was 5.5 mW at an 8.4 MHz repetition rate, resulting in pulse energies of 0.66 nJ.

In this configuration, the laser generated 43 fs pulses with 18.5 nm bandwidth at an 8.4 MHz repetition rate (figure 4-16). The pulse duration was measured by intensity autocorrelation in a 500 μm KDP crystal. The average output power was 5.5 mW, corresponding to a pulse energy of 0.66 nJ. Mode-locking was initiated by shaking the SBR stage and was occasionally self-starting. The SBR and M2 positions could be varied over nearly the full cavity stability range without significantly affecting the output spectrum and pulse duration, although the output power decreased when the mirrors were not at their optimum positions. The dispersion was varied by inserting one of the prisms into the beam, and mode-locking was obtained in both negative and positive dispersion regimes over the full range of prism insertion.

Subsequently, the cavity was reconfigured to operate without prisms. A total of eight bounces on DCMs outside the MPC, providing -336 fs^2 GDD, were used to compensate the

dispersion of the crystal and excess dispersion from air in the cavity. The DCMs were identical to those used in the MPC and described in section 4-5. This set the dispersion operating point for the whole cavity at approximately -83 fs^2. Mirror M_1 was replaced by a R=10 cm DCM and M_3, M_4, and M_9 by flat DCMs. The prisms were removed and M_{10} was replaced by an R=30 cm non-DCM curved mirror. The output coupler arm was 40 cm and the MPC arm was 80 cm. In this prismless cavity, the laser generated 39 fs pulses with 20 nm bandwidth at an 8.6 MHz repetition rate (figure 4-17). The improved power in this configuration is most likely due to loss variations in different positions of the spot on the SBR, since the SBR is inhomogeneous and different positions on the sample have different reflectivities.

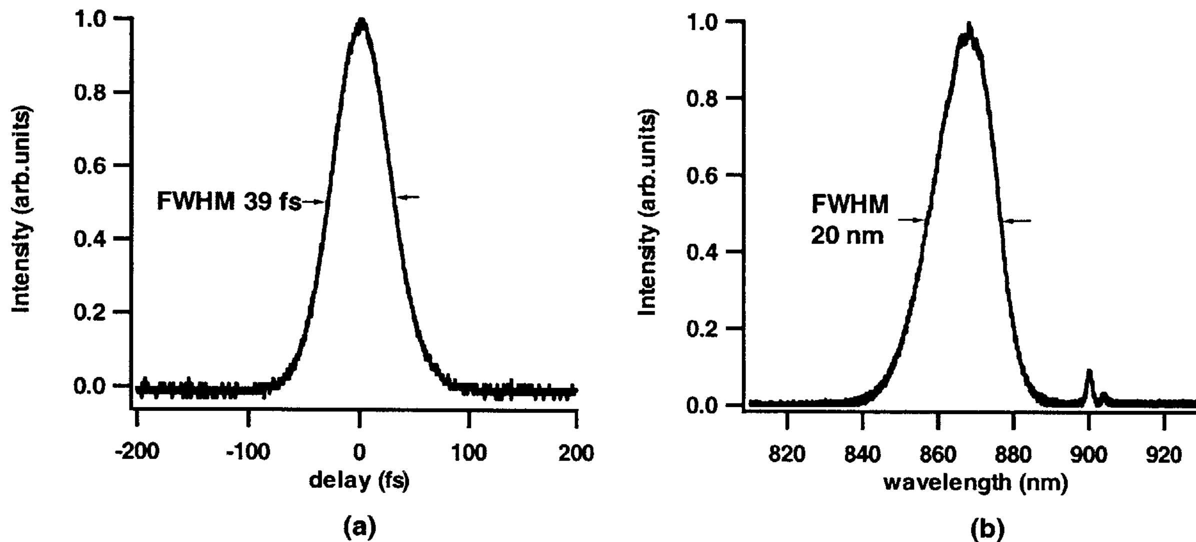

Figure 4-17. Autocorrelation (a) and spectrum (b) of the extended cavity Cr:LiSAF laser using only DCMs for dispersion compensation. The output power in this configuration is 6.5 mW at an 8.6 MHz repetition rate, resulting in pulse energies of 0.75 nJ.

The laser threshold and slope efficiency were also measured in the prismless cavity with different combinations of pump diodes (figure 4-18). The lowest threshold of 69 mW was measured for a combination of 21.8 mW from D2 and 47 mW from D1, with D3 off. The slope efficiency was also measured while varying the power of each diode and keeping the other two at full power. The largest mode-locked slope efficiency was 12.8%, measured for D1 while keeping D2 and D3 at a total power of 90 mW. The mode-locked slope efficiency was 11.6% for D2 and 8.3% for D3. D1 is expected to have the largest slope efficiency since the absorption of

the Cr:LiSAF crystal is maximum for this pump wavelength and polarization, as previously discussed.

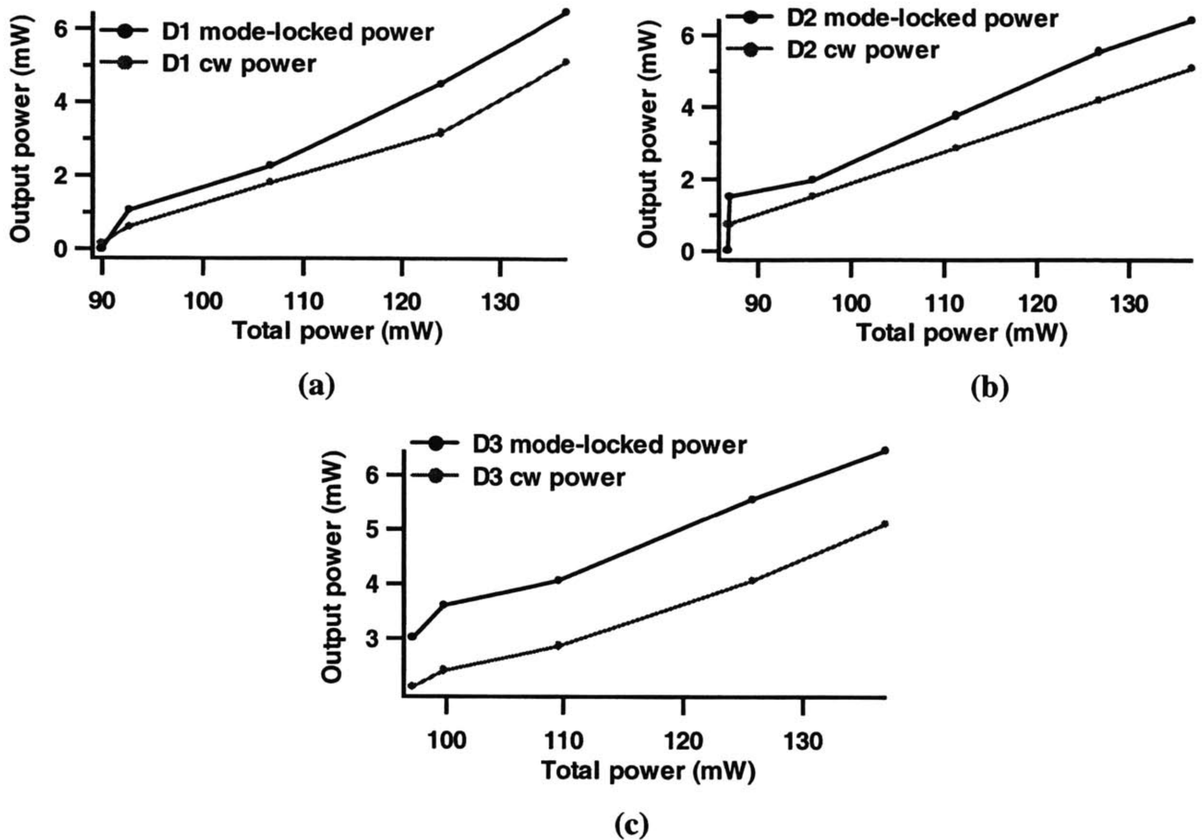

Figure 4-18. Mode-locked and cw output power of the extended cavity Cr:LiSAF laser as a function of (a) D1 pump power, with D2 and D3 held constant at a total power of 90 mW, (b) D2 pump power, with D1 and D3 held constant at a total power of 90 mW, and (c) D3 pump power, with D1 and D2 held constant at a total power of 90 mW. The mode-locked slope efficiency is 12.8% for D1, 11.6% for D2, and 8.3% for D3.

The pulse duration is primarily limited by the SBR bandwidth in both configurations, with and without prisms. This can be seen by noting that a bandwidth of 20 nm was generated when using the SBR to mode-lock the short cavity as described in the previous section. Only ARO mirrors and prisms were used in that cavity. The transmission curve of the ARO mirrors (figure 4-4) shows a broad reflectivity bandwidth from 785-935 nm that would not limit the observed spectra. The dispersion of the ARO mirrors was also measured and found to be negligible over the reflectivity bandwidth. No other elements in the cavity would limit the

bandwidth; therefore, the bandwidth of the SBR must be limiting the minimum pulse duration. Figures 4-16 and 4-17 show that the wings of the spectrum extend almost to the limit set by the SBR bandwidth (830-900 nm). Using broader bandwidth and lower loss SBRs should result in improvements in both pulse duration and output power.

In conclusion, low cost single spatial mode diodes were used to pump an extended cavity femtosecond Cr:LiSAF laser mode-locked with a saturable Bragg reflector. These inexpensive diodes provided efficient matching of the pump and laser modes as compared to broad stripe pump diodes. A multi-pass cavity was demonstrated to lower the repetition rate and improve the pulse energy. Using prisms for dispersion compensation, 43 fs pulses with 18.5 nm bandwidth were produced at an 8.4 MHz repetition rate. The pulse energy was 0.66 nJ in this configuration. In a prismless cavity, the laser generated 39 fs pulses with 20 nm bandwidth. The repetition rate was 8.6 MHz and the pulse energy was 0.75 nJ. Slope efficiencies up to 12.8% were measured, indicating that laser output powers can be scaled to higher output powers and pulse energies as higher power pump diodes become available. This is a low cost source of femtosecond pulses with pulse energies and durations that make this a cost-effective alternative to standard Ti:sapphire lasers in many applications.

Chapter 5

Fabrication and characterization of semiconductor-doped silica film saturable absorbers

5.1 Introduction

Semiconductor saturable absorbers are an important technology for generating stable, reliable ultrashort pulses from solid-state lasers. As discussed in chapter 3, most of these devices are grown using molecular beam epitaxy. Various solid-state laser systems have been mode-locked with epitaxially grown saturable absorbers [36, 37, 44, 86, 127, 194], generating self-starting pulses in compact laser systems, and sub-two-cycle pulses with the aid of KLM [40]. However, as discussed in chapter 3, epitaxially grown semiconductor saturable absorbers have some limitations, such as limited bandwidth without extensive post-processing and lattice matching constraints that limit the choice of materials and device design. An example of these limitations was seen in the experiments performed in the previous chapter, where an epitaxially grown saturable Bragg reflector was applied to mode-lock an extended cavity Cr:LiSAF laser pumped by single mode diodes. Although pulses with energies of 0.75 nJ and durations of 39 fs were achieved, the SBR reflectivity bandwidth limited the generation of even shorter pulses, and its relatively low reflectivity limited the maximum pulse energy. A saturable absorber similar to that in ref. [40] could be applied to improve the laser performance, but this requires extensive post-processing.

Non-epitaxially grown semiconductor saturable absorbers based on semiconductor-doaped silica films deposited by RF sputtering were recently developed as an alternative to epitaxially grown absorbers [45, 46, 154]. These devices offer increased versatility and lower cost when compared to epitaxially grown absorbers. For example, they have several advantages that overcome the limitations of the SBR used to start mode-locking in the Cr:LiSAF laser described in chapter 4.

Semiconductor-doped silica films have no bandwidth limitations when used in a transmissive geometry on a transparent sapphire substrate. Their absorption can easily be scaled by changing the film thickness, introducing a controlled amount of loss into the laser cavity. However, their high saturation fluence limits their use in some laser mode-locking applications, including the Cr:LiSAF laser described in chapter 4. The Cr:LiSAF is very sensitive to cavity loss due to the low pump powers used, which limits the ability to pump many times over threshold. Due to its high saturation fluence, the modulation provided by the saturable absorber is insufficient to self-start mode-locking for a semiconductor-doped silica film thickness small enough to introduce a minimal amount of loss into the cavity. Therefore, in the initial demonstration these absorbers could only be used in conjunction with KLM to start mode-locking in a Ti:sapphire laser [45].

This chapter focuses on the fabrication and characterization of semiconductor-doped films for saturable absorber applications. The goal of this work is to comprehensively characterize the linear and nonlinear optical properties of these devices in order to develop guidelines for designing semiconductor-doped silica film saturable absorbers with optimized saturation fluence for a given solid state laser system. Section 5.2 will briefly describe the optical properties of semiconductor quantum dots, including their nonlinear response to intense laser fields. Section 5.3 will discuss the experimental techniques for fabricating semiconductor-doped silica films, including RF sputtering, photolithography, and rapid thermal annealing. In section 5.4, the pump-probe technique used in characterizing the saturable absorbers is presented. The concepts of pump-probe spectroscopy will be described in detail, and a novel pump-probe system with independent pump and probe wavelength tunability around 800 nm will be presented along with conventional pump-probe systems in the 1300 and 1500 nm wavelength ranges. Experimental results obtained by measuring the effect of varying parameters such as the choice of semiconductor and glass materials, pump/probe wavelengths relative to the absorption edge, annealing time and temperature, and ratio of semiconductor to glass on the film optical properties will be discussed in section 5.5. X-ray diffraction measurements to examine the structural properties of the saturable absorber films will be discussed in section 5.6. A possible explanation for the high saturation fluence of semiconductor-doped silica films, based on the fast dephasing time in RF sputtered semiconductor nanocrystallites, will be given in section 5.7, and

section 5.8 will conclude by discussing guidelines extracted from these experiments for the design of semiconductor-doped silica film saturable absorbers for a given laser system.

5.2 Optical properties of semiconductor quantum dots

Semiconductor quantum dots are a model system for creating "artificial atoms" and studying their properties [195, 196, 197]. Three dimensional quantum confinement effects occur when reducing the particle size until it approaches the exciton Bohr radius for the bulk semiconductor. It will be shown in this section that this gives rise to an energy spectrum consisting of a series of discrete states, much like that of an isolated atom. However, a real quantum dot is composed of many atoms and the wave function can extend over many lattice sites, giving the system unique properties. One advantage in studying quantum dots is that their properties can be controlled and customized for many interesting applications including cavity quantum electrodynamics [195], coherent control [196], quantum dot lasers [198, 199], and quantum computing [200, 201] as well as the saturable absorber applications presented in this thesis. Control of the quantum dot size, shape, composition, and surrounding matrix tailors the dot for a certain application. In this section, basic properties of quantum dots will be briefly reviewed, since the semiconductor nanocrystallite-doped silica films described in this chapter can be theoretically modeled as quantum dots. More comprehensive reviews can be found in refs. [202-204].

5.2.1 Energy states in bulk semiconductors

In a bulk semiconductor, the solution of the Schrödinger equation is in principle a many-electron problem, since the Hamiltonian must contain the interaction between the electrons and the nuclei as well as the interactions between electrons. However, the nearly free electron approximation can be used to obtain a solution of the Schrödinger equation for a single electron in a spatially periodic potential (as in a crystal lattice) [203, 205, 206]. This solution is useful in describing many physical systems. The Schrödinger equation for the bulk semiconductor is given by

$$\left[-\frac{\hbar^2}{2m}\nabla^2 + V(r)\right]\psi(r) = E\psi(r), \tag{5.1}$$

with $V(r) = V(r+R)$ for all lattice vectors R in a crystal. In a periodic potential, the wave functions can be described by Bloch's theorem:

$$\psi_{nk}(r) = u_{nk}(r)e^{ik\cdot r}. \tag{5.2}$$

The wave function consists of an envelope function $u_{nk}(r) = u_{nk}(r+R)$ with the periodicity of the lattice that modulates a plane wave e^{ikr}. In the parabolic band approximation, the energy eigenvalues for electrons and holes are then given by

$$E(k) = \frac{\hbar^2 k^2}{2m^*}, \tag{5.3}$$

with m^* the effective mass of the electron or hole. In this approximation the electrons are regarded as free electrons that are perturbed by the periodic potential of the crystal lattice, with the strength of the perturbation expressed through the effective mass.

Optical absorption in semiconductors occurs when a light source excites a semiconductor with energy greater than the band gap, forming electrons in the conduction band and holes in the valence band. The Coulomb attraction between the electrons and holes can form an exciton, characterized by a wave function that is a product of terms due to the center-of-mass motion and the relative motion of the electrons and holes. The presence of excitons modifies the optical absorption spectrum from the free electron-hole-pair absorption spectrum, resulting in peaks in the absorption near the band edge [207]. The spatial extent of the exciton is given by the exciton Bohr radius, which is 1-20 nm in most semiconductors.

Quantum confinement effects occur when the spatial extent of the electron wave function is confined in one or more dimensions to be smaller than the Bohr radius. Quantum wells (confinement in one dimension), wires (2D confinement), and dots (3D confinement) can be fabricated with high precision using epitaxial and chemical techniques [196, 208] to explore the novel effects arising in this regime. Different regimes of quantum confinement can be identified depending on the ratio of the confined dimension to the Bohr radius. In the next section the energy states and quantum confinement regimes of quantum dots will be discussed.

5.2.2 Energy levels and linear absorption of quantum dots

In the simplest approach, a quantum dot can be viewed as a semiconductor sphere with radius R surrounded by an infinitely high potential barrier representing the dielectric matrix. The envelope function approximation can be used here, where it is assumed that the new wave functions can be described by a modified envelope function given by the product of a new envelope function for electrons and holes $\varphi(r)$ with the periodic Bloch envelope function $u(r)$:

$$\psi(r) = \varphi(r)u(r) \tag{5.4}$$

The new envelope function $\varphi(r)$ is specific to the particle in a spherical potential problem. Then the Hamiltonian for this envelope function is given by

$$\hat{H} = -\frac{\hbar^2}{2m_e}\nabla_e^2 - \frac{\hbar^2}{2m_h}\nabla_h^2 + V_e(r_e) + V_h(r_h) - \frac{e^2}{\varepsilon|r_e - r_h|}, \tag{5.5}$$

where the Coulomb interaction is now taken into account in the last term and the confinement potential is

$$V_{e,h}(r) = \begin{cases} 0 & r < R \\ \infty & r > R \end{cases}. \tag{5.6}$$

Temporarily disregarding the Coulomb interaction enables analytical solution of this problem. For non-interacting electron-hole pairs, the envelope function can be separated into independent contributions from the electrons and holes and is written as a product $\varphi(r_e, r_h) = \zeta_e(r_e)\zeta_h(r_h)$. This solution is well known and can be found in standard quantum mechanics textbooks [209, 210]. The wave functions for electrons and holes are given by

$$\zeta_{nlm}^{e,h}(r) = \sqrt{\frac{2}{R^3}}\frac{J_l\left(k_{nl}\frac{r}{R}\right)}{J_{l+1}(k_{nl})}Y_{lm}(\theta,\phi), \tag{5.7}$$

with $-l \le m \le l$, l=0, 1, 2,..., n=1, 2, 3..., J_l are the Bessel functions and Y_{lm} are the spherical harmonics. The stipulation that the wave function must vanish at the surface of the quantum dot (r=R) can be used as a boundary condition to obtain the energy eigenvalues:

$$J_l\left(k_{nl}\frac{r}{R}\right)\Big|_{r=R} = 0 \tag{5.8}$$

$$E_{nl}^{e} = E_{g} + \frac{\hbar^{2}}{2m_{e}} \frac{k_{nl}^{2}}{R^{2}} \tag{5.9}$$

$$E_{nl}^{h} = \frac{\hbar^{2}}{2m_{h}} \frac{k_{nl}^{2}}{R^{2}} \tag{5.10}$$

The nth root of the Bessel function of order l is given by k_{nl} and $m_{e,h}$ are the effective masses of the electron and hole. Equations (5.9) and (5.10) show the discrete, atom-like energy spectrum of the quantum dot states. The energy of the lowest confined one-electron-hole-pair state has its energy increased compared to the bulk semiconductor band gap by an amount

$$\Delta E = \frac{\hbar^{2}}{2m_{r}} \left(\frac{\pi}{R} \right)^{2} \tag{5.11}$$

where m_r is the reduced effective mass, given by

$$\frac{1}{m_{r}} = \frac{1}{m_{e}} + \frac{1}{m_{h}}. \tag{5.12}$$

The energy difference can be represented in terms of the exciton Bohr radius a_B and exciton Rydberg energy E_R (the binding energy for the lowest energy exciton state [207]) for a more intuitive representation [202]:

$$a_{B} = \frac{\varepsilon \hbar^{2}}{m_{r} e^{2}} \tag{5.13}$$

$$E_{R} = \frac{\hbar^{2}}{2m_{r} a_{B}^{2}} \tag{5.14}$$

$$\Delta E = E_{R} \left(\frac{\pi a_{B}}{R} \right)^{2} \tag{5.15}$$

Here ε is the dielectric constant of the semiconductor. This equation clearly shows that the confinement-induced energy shift scales with the ratio of the dot radius R to the exciton Bohr radius a_B. It is important to note that this equation has been derived by approximating that the Bloch part of the envelope function, $u(r)$, with the parabolic, isotropic bands of a simple two band semiconductor with a direct band gap. This equation is also derived assuming one electron-hole pair per quantum dot, which is a good approximation for low excitation densities [211]. Figure 5-1 depicts the density of states (derived directly from the energy) for quantum dots as compared to a bulk semiconductor. The density of states represents the number of states available in the semiconductor in a certain energy interval [207]. This gives the number of states

available at a certain energy for optical absorption of a photon with that energy and therefore is important in calculating the optical response of a semiconductor. For a more accurate description of the energy levels of a quantum dot, the Hamiltonian can be modified by taking into account the Coulomb interaction, realistic conduction and valence bands including non-parabolicity and valence band mixing, state splitting, and indirect gap semiconductors.

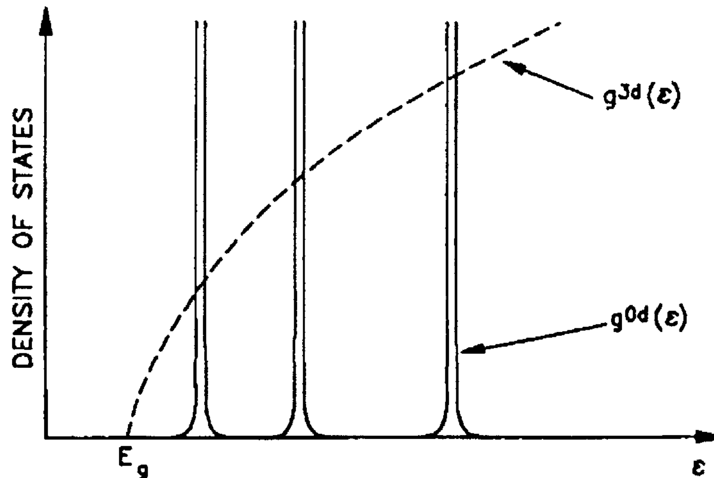

Figure 5-1. Density of states $g^{0d}(\varepsilon)$ for a quantum dot compared to the bulk density of states $g^{3d}(\varepsilon)$ (reprinted from ref [207]).

At this point, it is appropriate to consider the different regimes of quantum confinement [202, 212, 213]. From equation (5.15) it is clear that strongly confined quantum dots ($R \ll a_B$) experience a large energy shift due to quantum confinement. This shift is much larger than the exciton binding energy (proportional to $1/R$), and therefore as a first approximation the Coulomb interaction can be ignored for small dots; this is a useful approximation since the energy states can be obtained analytically. The energy levels for strongly confined quantum dots can therefore be described by the energies given in equations (5.9), (5.10) and (5.15). In this regime, the individual motions of the electron and hole are quantized. When the Coulomb interaction is included, the problem cannot be solved analytically; however, this interaction can be regarded as a small perturbation to the kinetic energy contribution for small quantum dots, and therefore the energy levels are only weakly red shifted due to Coulomb effects [211]. CdSe and CdS quantum dots have large Bohr radii (~3 nm) and therefore can be strongly confined with current fabrication techniques.

The regime of intermediate confinement applies when the Bohr radius for the hole (obtained by modifying equation (5.13) to include the hole effective mass instead of the reduced mass) is smaller than R while the electron Bohr radius is larger than R. This can arise if the effective mass of the holes is much bigger than the electron effective mass. It can be shown that the energy shift due to quantum confinement in this regime can be described by replacing the reduced effective mass by the electron effective mass in equation (5.11) [213]. In the first approximation, the energy shift is determined by the size quantization of the electron.

In the regime of weak confinement ($R >> a_B$), the quantum dot is significantly larger than both the electron and hole exciton Bohr radii. The treatment here is similar to that in a bulk semiconductor, where relative and center-of-mass coordinates for the electron-hole pair are used. It can be assumed that the relative motion of the exciton is unaffected by quantum confinement and therefore only the center-of-mass motion is quantized. In this regime, the energy levels are given by

$$\Delta E = \frac{\hbar^2}{2M}\left(\frac{\pi}{R}\right)^2, \tag{5.16}$$

where $M=m_e+m_h$ is the exciton mass [213]. Weakly confined dots are characterized by a small separation between energy levels. Since these transitions are homogenously broadened, the energy levels may overlap and the spectrum may appear continuous [202]. Some researchers have suggested that higher nonlinearities can be obtained in the weak confinement regime, such that the dots are larger than the Bohr radius but small enough such that discrete optical transitions still exist and the spectrum is not continuous [212]. A good example of a weakly confined system is CuCl since the Bohr radius is only 0.7 nm, and nanocrystallites smaller than this are difficult to fabricate.

The absorption of low intensity light by a semiconductor is determined by the linear absorption coefficient, which can be calculated as a function of frequency using density matrix theory. For a single strongly confined quantum dot, it is given by [202, 207]

$$\alpha(\omega) = \frac{4\pi\omega}{\hbar c\varepsilon}\sum_i |d_{oi}|^2 \frac{\gamma_i}{\gamma_i^2 + (\omega_i - \omega)^2}, \tag{5.17}$$

where d_{oi} is the transition dipole matrix element (this is the same as for the bulk material and is size-independent) for the transition from state o (the ground state) to state i, γ is the homogeneous linewidth of the transition, and $E_i = \hbar\omega_i$ are the one-electron-hole pair energies as given by equations (5.9) and (5.10), which depend on the size R of the quantum dots. Equation (5.17) shows that the absorption spectrum of a single quantum dot is a series of Lorentzian peaks centered at the one-electron-hole pair energies. The transitions are also inhomogeneously broadened due to the size distribution of the dots that occurs in any real system. To calculate the absorption spectrum for the ensemble, one can assume that the dots have a size distribution $f(R)$ centered around a mean dot radius R. The average absorption coefficient is then given by

$$\alpha(\omega)\big|_{avg} = \int_0^\infty f(R)\,\alpha(\omega)\big|_R\, dR\,, \tag{5.18}$$

where $\alpha(\omega)\big|_R$ is the absorption coefficient for a single dot given in equation (5.17).

Linear absorption in quantum dots is analogous to the absorption of excitons in bulk semiconductors [203, 214]. In the bulk, the oscillator strength (to which the absorption coefficient is proportional) is inversely proportional to the volume in k-space required to form the exciton, which is defined by the cube of the exciton Bohr radius a_B. The expression for the absorption in the bulk, including excitonic effects as well as free carrier absorption, is given by

$$\alpha_{bulk}(\omega) = \left(\frac{2\omega|d_{cv}|^2}{n_b c a_B^3}\sum_{n=1}^{\infty}\frac{4\pi}{n^3}\delta(\hbar\omega - E_g + E_R/n^2)\right) + \left(\frac{e^2\omega|d_{cv}|^2}{n_b c\varepsilon}\left(\frac{2m_r}{\hbar^2}\right)^2 \theta(\hbar\omega - E_g)\frac{\pi e^Z}{\sinh Z}\right) \tag{5.19}$$

where the unit-step function $\theta(\hbar\omega - E_g)$ is zero for $\hbar\omega < E_g$ and 1 for $\hbar\omega > E_g$, and the variable Z is given by $Z = \pi\sqrt{E_R/(\hbar\omega - E_g)}$ [207]. The material index is given by n_b, and the other quantities (exciton Rydberg energy E_R, reduced mass m_r, dipole matrix elements d_{cv}) are as previously defined. The first term of this expression gives the discrete excitonic absorption that is significant near the band edge, and the second term describes the absorption for continuum states, which dominates when the photon energy is greater than the band gap. It is clear from this expression that the first term is inversely proportional to the cube of the Bohr radius.

In quantum dots, the oscillator strength is inversely proportional to the spatial restriction of carrier motion in the quantum dot due to quantum confinement. Therefore, the ratio of the bulk and quantum dot oscillator strengths near the band gap is roughly proportional to a_B^3/R^3 [203, 211]. The oscillator strength and therefore the absorption clearly increase for quantum dots smaller than the Bohr radius. This can also be regarded as the shifting of the absorption strength into the lowest bound state as the dot size decreases [214]. This should lead to an increased optical nonlinearity and, along with the potentially narrow linewidth, is one reason for the intense interest in quantum dots for optical switching applications. The change in absorption upon excitation would be much larger before the transition saturates than in bulk semiconductors, enabling effective discrimination between "on" and "off" states [211]. However, inhomogeneous broadening due to the large size distributions present in most quantum dot samples has made the experimental observation of large nonlinearities difficult.

The surrounding dielectric matrix also affects the linear optical absorption properties of the quantum dot. A simple approximation for the absorption of the composite material gives

$$\alpha_{composite} = p\alpha_{semic}, \tag{5.20}$$

where p is the volume fraction of the semiconductor and α_{semic} is the absorption coefficient. However, a more precise treatment includes the local field effects for a composite with a material having a dielectric constant $\varepsilon_1 = \varepsilon_1' + i\varepsilon_1''$ embedded in a non-absorbing matrix with dielectric constant ε_2. Maxwell-Garnett theory [202, 215] can be used to describe the optical properties of quantum dot composites [202, 203]. In this theory, a composite material is described as a homogeneous background medium with spherical inclusions of dopant with small diameters compared to the wavelength of light. The spheres are replaced with electric dipole equivalents and the effective dielectric constant of the composite is calculated. This theory is applicable if the dots are small compared to the wavelength of the light and the volume fraction of the dots is small. The first condition is valid for the materials described in this thesis, since the dot size is typically tens to one hundred nanometers compared to the approximately one micron wavelength of light; however, for some of the higher doped films described in this chapter the second condition may not apply. Under these approximations, however, an expression for the absorption coefficient of the composite material can be derived [203],

$$\alpha_{composite} = p\frac{n_1}{n_c}\frac{9\varepsilon_2^2}{(1-p)^2}\frac{1}{\left(\varepsilon_1' + \varepsilon_2\frac{2+p}{1-p}\right)^2 + \varepsilon_1''^2}\alpha_1 \tag{5.21}$$

where n_1 and n_c are the refractive indices of the semiconductor and composite, respectively, and α_1 is the absorption coefficient of the bulk semiconductor. This expression can be used to calculate the absorption of the composite semiconductor-matrix.

5.2.3 Nonlinear optical properties of quantum dots

The nonlinear optical properties of semiconductors after excitation with an intense light pulse are the subject of much current research. After pulsed excitation, the excited carriers in the conduction and valence bands modify the linear absorption properties of the semiconductor, leading to carrier density dependent optical nonlinearities when the photon energy is greater than the band gap and transient nonlinearities when the incident light is absorbed. When real carriers are generated, the non-equilibrium electrons and holes undergo several relaxation processes that occur on different time scales to return to the ground state.

In general, there are four overlapping regimes of carrier relaxation in a bulk semiconductor [78, 204, 207, 216]. Immediately after the semiconductor is illuminated by an ultrashort laser pulse, the generated excitation has a well-defined phase relationship with the laser field. The laser pulse creates a macroscopic polarization that must be included in Maxwell's equations as a source term, changing both the linear and nonlinear response of the system. The light field couples the valence and conduction band states and induces the electrons to oscillate between them, similar to Rabi flopping in two-level atoms. Many interesting phenomena are observed in this regime, including non-Markovian memory effects, quantum beats of excitons, and carrier-wave Rabi flopping [78, 217, 218]. For excitation below the band gap, virtual carriers are generated, resulting in the optical Stark effect. This shifts the absorption spectrum to higher energies as long as the virtual carriers exist (only during the interaction of the exciting pulse with the semiconductor). The theory of quantum kinetics [218] must be used to understand the coherent regime. The coherent regime usually only lasts for tens to a few

hundred femtoseconds before processes such as carrier-carrier scattering induce dephasing, destroying the coherence.

Many optical nonlinearities resulting from the generation of real carriers can be observed after coherence is destroyed, including band filling, spectral hole burning, plasma screening and band gap renormalization, and exciton ionization [207]. Band filling occurs when all the available states in a band are filled, causing the absorption to bleach and the material to become transparent. Spectral hole burning is observed around the center frequency of the exciting laser pulse, since the excited electrons and holes are just beginning to relax to lower states, and consequently inhibit the absorption at the center frequency by band filling. Figure 5-2 depicts an experimental observation of spectral hole-burning (from [207]).

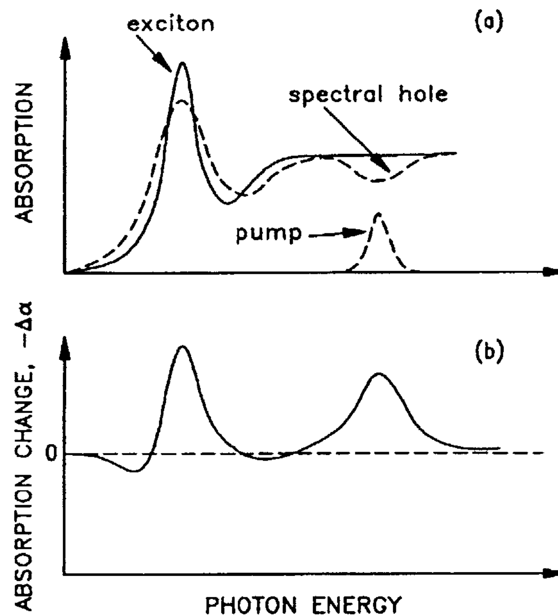

Figure 5-2. Schematic depiction of spectral hole burning: (a) The absorption of the semiconductor before (solid line) and after (dashed line) the pump pulse. (b) The absorption change calculated from (a) (figure reprinted from ref. [207])).

Plasma screening occurs when a carrier excited into an energy band that already contains many equally charged carriers feels repulsion due to the Coulomb force. The Pauli exclusion principle also mandates that carriers with equal spin cannot occupy the same state, and therefore the probability that these carriers are near each other decreases. These two effects cause the

other carriers in the band to redistribute themselves in space by undergoing low energy intraband transitions [211], forming a vacant area around the excited carrier that in effect has the opposite charge. This reduces the effective potential of the carrier, renormalizing the band gap. A calculated absorption spectrum shown in figure 5-3 demonstrates the effects of band gap renormalization.

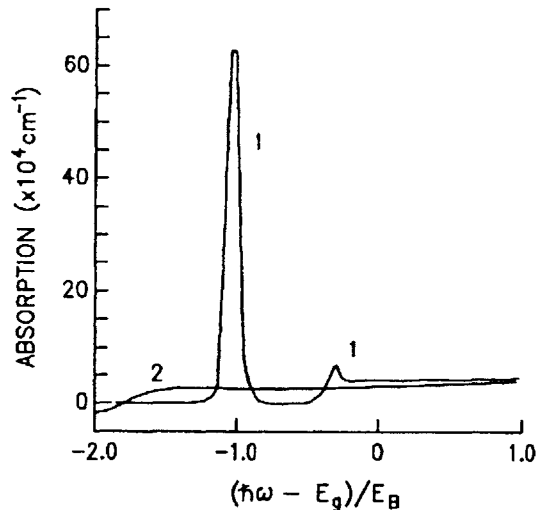

Figure 5-3. Calculated effect of band-gap renormalization. The curve labeled "1" shows the absorption of the semiconductor before high intensity optical excitation; the peaks are due to exciton absorption. The curve labeled "2" depicts the absorption after pulsed excitation and clearly shows the shift of the band gap to lower energies due to band gap renormalization, along with the disappearance of the excitonic peaks (figure reprinted from ref. [207]).

Exciton ionization occurs when an exciton breaks up into a free electron and hole. This is due to screening, which decreases the strength of the Coulomb potential between the electron-hole pair as the carrier density increases. For a large number of carriers, the potential can be lowered enough to ionize the exciton. This manifests itself by a reduction in magnitude of the excitonic peaks near the band gap in the absorption spectrum of the semiconductor, called exciton bleaching. All the nonlinearities due to the excitation of real carriers are strongly dependent on the excited carrier density and consequently the laser pulse intensity.

For real excitations, after coherence is destroyed through dephasing, the distribution of the excited free electron-hole pairs or excitons is typically non-thermal (meaning they cannot be

characterized by a temperature). The non-thermal regime usually lasts for hundreds of femtoseconds to ~2 ps. Carrier-carrier (or exciton-exciton) scattering is the primary means of thermalizing the carrier distributions [78, 216]. The dominant nonlinearities in this regime are exciton bleaching and spectral hole burning through band filling.

The next stage is the hot-carrier regime, characterized by the thermalization of the different carrier distributions with each other and also with the lattice. After the non-thermal regime, the temperatures of different subsystems including holes, electrons, and excitons may differ from each other and are usually elevated from the lattice temperature. In the hot-carrier regime, the electrons and holes reach a common temperature within a few picoseconds through scattering, and through phonon interactions they lose energy and reach the lattice temperature within ~100 ps [78, 216]. The spectral hole disappears and the exciton bleaching is also reduced, although band filling is still significant since the excited electrons and holes have relaxed to the lowest energies in their respective bands.

The final stage is the isothermal regime. After thermalization of the carrier distributions with the lattice and each other in the hot carrier regime, the excitons, carriers, and phonons are all at the lattice temperature. However, there still exists a non-equilibrium distribution of carriers. The excess electron-hole pairs recombine by both radiative and non-radiative processes, returning the semiconductor to equilibrium on a time scale of nanoseconds.

In quantum dots, the relaxation of excited carriers occurs on similar time scales as in bulk semiconductors. The coherent and non-thermal regimes have not been extensively explored in quantum dots and very few experimental or theoretical studies have been reported [78, 204]. However, several techniques have been used to measure dephasing times in quantum dot systems, which will be discussed in detail in section 5.7.

In small quantum dots, band filling is expected to be the dominant optical nonlinearity. The large separation between energy levels makes the small intraband transitions required for the carriers to rearrange themselves in real space very difficult, inhibiting screening. Similarly, the Coulomb interaction is suppressed since the electrons and holes are localized within the quantum

dot and therefore have zero net charge density, making it hard to create an exciton. This also explains why inclusion of the Coulomb interaction has a weak effect on the energy levels in strongly confined dots, as described in section 5.2.2. Therefore, for a small quantum dot, the saturation of the lowest energy level can be treated like a two-level system, and it saturates with a dependence very similar to that given by equation (2.33). Due to the Pauli exclusion principle, the absorption saturates when there is one electron-hole pair per quantum dot in a given energy level [207, 211]. This shows that the most significant mechanism governing quantum dot nonlinearities is band filling, particularly in small quantum dots.

However, when very large carrier densities are generated, two electron-hole pairs per quantum dot can be excited. The Coulomb interaction between the pairs becomes significant, changing the observed nonlinear absorption spectrum [203, 219]. The one pair states are bleached (saturated) and new transitions are allowed. This has been suggested to result in effects such as induced absorption, where the creation of the first pair saturates the absorption, and the Coulomb interaction between the first and second pairs creates more states available for absorption. Induced absorption has been observed in several experiments [219-221].

Relaxation processes in quantum dots are expected to be very different than in the bulk semiconductor due to the large separation between energy levels. This question of how carriers relax in a system of discrete energy levels has generated much experimental and theoretical interest. In higher dimensional semiconductors, relaxation due to phonon absorption and emission is an important process in thermalizing the hot carrier distributions. However, this relaxation only occurs if the difference between the energy levels is near one phonon energy. In small quantum dots, this condition is usually not satisfied due to the large energy difference between initial and final states that is much greater than phonon energies. Therefore, the idea of a "phonon bottleneck" leading to very long relaxation times has been proposed [222]. However, many experiments observed fast relaxation times in quantum dots, contradicting the theoretical expectations [223-225]. One explanation was based on the surface states of quantum dots, which play an important role in carrier relaxation; their quasi-continuous energy distribution could serve as the final state in phonon scattering. Other mechanisms such as Auger processes and electron-hole scattering were also proposed to explain the fast relaxation times [78, 226].

Recently, the observation of a phonon bottleneck was reported in an experiment on epitaxially grown InGaAs quantum dots [227]. This elegant experiment was designed to remove the relaxation processes described above that limited the observation of the bottleneck. The relaxation dynamics of quantum dots are still a subject of much current investigation.

5.3 Experimental setup-fabrication

In this section the experimental techniques and systems used to fabricate the semiconductor-doped silica film saturable absorbers will be described. RF sputtering is used to grow the films, and rapid thermal annealing is used to modify their properties. Photolithography will also briefly be described since this technique is used to measure film thickness and calibrate deposition rates.

5.3.1 RF sputtering system

RF sputtering is a well known technique used to deposit thin films for optical coatings [228, 229]. Several authors have shown that sputtering can be used to deposit semiconductor-doped silica films by using a composite sputtering target. Silica films doped with materials including CdSe, CdTe, GaAs, and CuCl have been fabricated and deposited on different substrates [155-157]. The term "sputtering" refers to the ejection of atoms from a solid target due to the impact of high energy particles. Sputtering can be performed with both DC and RF power sources. Figure 5-4 depicts a typical RF sputtering system.

In this system, a high voltage is applied between the cathode and anode. The target (material to be deposited) is attached to the cathode and the substrates (material on which the thin film is deposited) are placed on the anode. An inert gas (typically argon) at a pressure of $\sim 10^{-3}$-10^{-1} Torr is introduced into the chamber, which is initially in high vacuum ($\sim 10^{-6}$-10^{-8} Torr). The high voltage ionizes the gas, forming a plasma. The plasma ions bombard the negatively biased cathode, ejecting atoms or molecules from the target in a momentum transfer process, and the ejected material condenses on the substrates, forming a thin film. Magnets

placed around the cathode can be used to confine the plasma to the target vicinity, increasing deposition rates by up to an order of magnitude. The substrates are also relatively isolated from the plasma discharge. DC sputtering is often used for depositing conducting materials; however, to deposit insulating materials RF sputtering must be used [228].

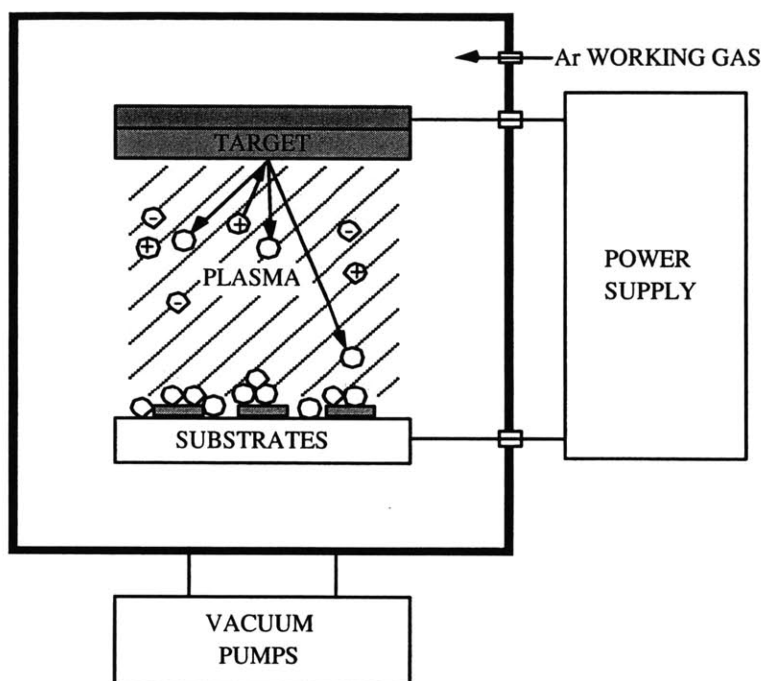

Figure 5-4. RF sputtering system. The target is attached to the negatively charged cathode and the substrates are placed on the positively charged anode. A momentum transfer process between the argon plasma and the target materials enables thin film deposition.

The sputtering system used to deposit the films examined in this thesis was a Denton Discovery 18 magnetron sputtering system located at Boston University that operated at an RF frequency of 13.56 MHz, which is standard in most RF sputtering systems. All sample fabrication (including sputtering, photolithography, and rapid thermal annealing) described in this thesis was performed in collaboration with Paul Mak and Professor Michael Ruane at Boston University. Leo Misaggia and Dr. James Walpole at Lincoln Laboratories collaborated on the device fabrication done in previous research [46, 154, 158] and offered helpful guidance with the research described in this thesis. The system had 3 sputtering targets, allowing sequential deposition of different materials in thin films upon the substrates. Each target was equipped with

a shutter that could shield the target surface from plasma exposure when closed. Samples were loaded and unloaded using a load lock, which is a smaller chamber kept at a pressure of only ~10^{-4} Torr that is connected to the main chamber. A gate valve opens and closes to enable substrates to be inserted and removed from the main chamber. The load lock pumped down in a matter of minutes, enabling several runs to be performed in a single day since the main chamber did not have to be vented after each run to remove the samples. The substrate platform could be set by the user to rotate at a certain speed to ensure uniform deposition of the films on all substrates. Substrate heating up to temperatures of 300 °C was also possible using a radiative heater installed in the system. Control of the RF power and sputtering time enabled films of a desired thickness to be deposited. The argon flow was ~60 sccm to set the argon pressure at 5 mTorr.

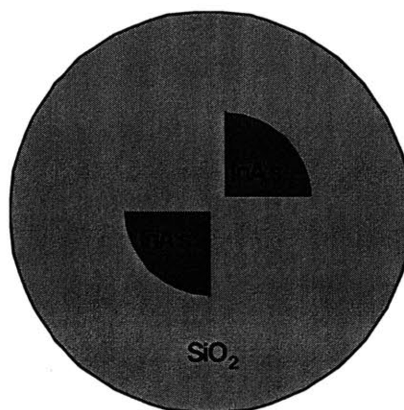

Figure 5-5. Schematic of the sputtering target used to deposit InAs-doped silica films.

The sputtering targets used in these experiments were 3" diameter glass disks, with semiconductor chips glued on top using vacuum-safe epoxy (KL-320K from Kurt J. Lesker Co.). The semiconductor and glass materials as well as the ratio of semiconductor to glass were varied in different experiments, to be described later in this chapter. A schematic of a sputtering target is shown in figure 5-5. A 3" diameter sapphire target was also used in some experiments to deposit a transparent film on top of the semiconductor-doped silica film. The targets were water-cooled and positioned approximately 25 cm from the substrate platform. All films used in optical experiments were deposited on sapphire substrates; the substrates used in laser mode-locking experiments were oriented at zero degrees to minimize birefringence, while those used in

film characterization did not have a particular orientation. All sapphire substrates were 3 mm thick and either 0.5" or 1" in diameter. Both targets and substrates were cleaned with acetone, methanol, and water to minimize contamination when introduced into the sputtering chamber. The sputtering procedure is described in appendix A. It should be mentioned that care was taken to avoid contamination of the films by impurities (particularly carbon contamination from the epoxy) by pre-sputtering the target with the shutter closed, which removed a thin layer from the surface of the target, including contaminants. This has been shown to remove oxygen and carbon impurities from these films [154].

5.3.2 Photolithography

After the films were deposited, photolithography in conjunction with profilometry was performed on some samples to determine the film thickness and calibrate the deposition rate. Silicon substrates were used for this process since they are not etched by hydrofluoric acid (HF). The silicon substrates were placed on top of sapphire substrates during a sputtering run to measure the thickness of the films used in optical experiments as accurately as possible. The deposited films were spin coated with HMDS (hexamethyldisilazene) wetting fluid for ~ 5 seconds and then with photoresist (1813 photoresist) for 30 seconds. They were then placed in an oven at ~80 °C for 20-25 minutes to dry the photoresist. The samples were removed from the oven and placed on the sample stage of a Zeiss mask aligner. A mask with a pattern of lines separated by equal distances from each other was put into contact with the sample and the sample was exposed to UV light for 10 seconds. This created a pattern of exposed and unexposed lines on the film. A photographic developer (Shipley Microdeposit, in a 1:1 ratio with deionized water) was then used to remove the exposed photoresist from the film by immersing the sample in the developer until a clear pattern of bright and dark lines was seen on the film with a microscope. The sample was typically exposed to the developer for ~30 seconds. The sample was subsequently immersed in buffered oxide etch (BOE) fluid (composed primarily of hydrofluoric acid) until the exposed areas of the film were etched down to the substrate. This was done by repeatedly immersing the sample in BOE fluid for ~10 seconds, cleaning it in water, and viewing it under a microscope until the substrate could be seen. At this point, the sample had a pattern of alternating bright and dark lines consisting of the substrate (bright lines) and the

film covered by the photoresist (dark lines). Finally, the sample was cleaned in acetone (followed by deionized water) to remove the photoresist, leaving a series of lines with vertical height equal to the film thickness on the surface of the Si substrate. A profilometer could be used to determine the film thickness by measuring the height of the lines. Typical film thicknesses used in pump-probe experiments were ~100-200 nm, and the deposition rate for a 10% InAs/90% SiO_2 target was measured to be 5 nm/minute for 100 W RF power.

5.3.3. Rapid thermal annealing

Rapid thermal annealing (RTA) has been shown to be an important technique to control the absorption saturation dynamics of semiconductor-doped silica film saturable absorbers [46, 154]. Heating the glass for long periods of time has long been used in the process of making bulk semiconductor-doped glasses [203, 220, 230, 231]. The annealing process enables semiconductor nanocrystallites to grow around nucleation centers in the glass matrix. The final nanocrystallite size is directly proportional to the annealing temperature and duration. In semiconductor-doped silica films, post annealing at temperatures of 500-700 °C for several hours has been shown to increase the nanocrystallite size as well [154, 203, 232]. This red-shifts the optical absorption edge in the films.

Rapid thermal annealing is typically performed at temperatures of 500-800 °C for a few seconds to a few minutes to anneal out structural defects in thin films. This has been shown to modify the chemistry of surface and interface traps [233, 234]. In subsequent sections of this chapter, the effect of RTA times and temperatures on the absorption saturation dynamics of the semiconductor-doped silica films will be described.

5.4 Pump-probe spectroscopy

5.4.1 General principles

Several techniques, including pump-probe spectroscopy, four wave mixing, and time-resolved photoluminescence spectroscopy can be used to measure the semiconductor optical nonlinearities described in the previous section [78, 204, 207, 216, 235]. These techniques generally consist of the excitation of the sample by one or more high intensity "pump" pulses that bring the sample to a non-equilibrium state and the subsequent use of optical methods to monitor the relaxation back to the equilibrium state. Information about the carrier relaxation dynamics, dephasing times, magnitude of absorption saturation, and nonlinear index changes can be obtained with these experiments.

Perhaps the simplest of these techniques is pump-probe spectroscopy, which was used for the nonlinear absorption saturation measurements described in this thesis. The experimental setup is essentially a collinear or non-collinear Michelson interferometer, similar to those used in the autocorrelation measurements of chapter 2 (figure 2-18 depicts a collinear Michelson interferometer and figure 2-19 depicts a non-collinear interferometer). In fact, the only difference between an autocorrelation setup and a standard pump-probe setup is in the beam splitter; an autocorrelator uses a 50/50 beam splitter, while the beam splitter in a pump-probe setup usually sets the pump beam to be at least 10 times more intense than the probe beam. The intensity of the probe pulse is set low enough such that it does not induce changes in the absorption by itself. The time interval between the pump and probe pulses is adjusted using a computer-controlled delay stage, and the pump and probe beams are made to spatially overlap on the sample.

In a standard pump-probe experiment, the high intensity pump pulse excites the sample, inducing a change in its optical properties. The weaker probe pulse is delayed from the pump pulse and its transmission is measured as a function of time delay between the two pulses by varying the delay stage. By comparing the transmission of the probe before the pump pulse to the transmission after the pump pulse as a function of delay, the time evolution of the nonlinear changes in the optical properties of the sample can be measured. The measurement is usually presented in the form of the normalized differential transmission, given by

$$\frac{\Delta T}{T_0} = \frac{T_E - T_0}{T_0}, \tag{5.22}$$

where T_E is the probe transmission in the presence of the pump pulse and T_0 is the probe transmission without the pump pulse. Without pump excitation, the probe measures the linear transmission of the sample. Pump-induced changes in reflectivity can also be detected by modifying the experimental setup to detect the reflected probe beam.

Many different variations on this basic concept have been used to measure ultrafast carrier dynamics in semiconductors. Both low (<1 kHz) and high (>10 kHz) repetition rate lasers can be used to generate the pump and probe beams. The experiments with low repetition rate lasers are essentially single-shot measurements, where the energy of the individual probe pulses is detected. High energy pump pulses are used to generate large $\Delta T/T_0$ signals that can be measured directly, with typical sensitivities of 10^{-2}-10^{-3}. The use of high repetition rate lasers with relatively low pulse energies allows high signal-to-noise measurements by chopping the pump beam at a certain frequency (typically ~1 kHz) and measuring the probe power using a photodiode and lock-in amplifier. The lock-in amplifier only detects signals modulated at the chopper frequency, and therefore only the pump-induced changes in probe transmission are measured, with sensitivities as high as 10^{-5}. Even higher sensitivities of 10^{-6} have been reported by acousto-optically chopping the pump beam at high frequencies (~1 MHz) [235].

Similarly, degenerate (pump and probe at the same wavelength) and non-degenerate (pump and probe at different wavelengths) measurements can be performed. Often, the differential transmission spectrum (DTS) of the sample is measured by detecting the probe spectrum as a function of time delay. This enables time and spectrally resolved measurements of carrier dynamics. A spectrally broad probe pulse is often generated through super-continuum generation by focusing intense laser pulses into a material such as ethylene glycol, water, or glass; this is usually done with amplified, low-repetition rate laser systems due to the high pulse energies required to generate continuum. Part of the laser beam is split off to serve as the pump pulse, and the other part is used to generate the continuum from which the probe is chosen. This allows selection of the excited states being probed. One or more tunable lasers can also be used to generate the pump and/or probe pulses. This enables wavelength-dependent degenerate or non-degenerate (if separate lasers are used for the pump and probe) measurements. If separate lasers are used for the pump and probe, care must be taken to synchronize their repetition rates.

Several experimental details must be carefully considered in pump-probe measurements. The focused pump spot on the sample should ideally be much larger than the probe beam spot size, such that the probe only measures a uniformly excited section of the sample. The pump and probe are often cross-polarized as well. This avoids coherent artifacts [236, 237] and also can be used to eliminate artificial signals due to the pump scattering from the sample into the detector. In a non-collinear pump-probe measurement, apertures can also be used to eliminate scattering of the pump beam into the detector, increasing the sensitivity. The temporal resolution of the pump-probe system is determined by the cross-correlation of the pump and probe pulses at the sample position, making careful dispersion compensation necessary.

In the measurements done in this thesis, the saturation fluence was obtained from the experimentally measured differential transmission. It can be shown [207] that the normalized change in transmission, $\Delta T/T_0$, is proportional to the sample thickness d multiplied by the change in absorption coefficient $\Delta\alpha$, i.e.

$$\frac{\Delta T}{T_0} \approx -\Delta \alpha d \tag{5.23}$$

assuming the pump-induced changes in transmission are small. Assuming that the change in transmission results only from a change in absorption (the reflectivity is unchanged by the pump pulse), the normalized change in the absorption coefficient can be obtained for the intensity I and the absorption A:

$$T = \frac{I}{I_0} = e^{-\alpha d} = 1 - A, \tag{5.24}$$

$$-\Delta T = \Delta A = \Delta(1 - e^{-\alpha d}) = e^{-\alpha_0 d}(1 - e^{-\Delta\alpha d}) \approx \Delta\alpha d e^{-\alpha_0 d} = \Delta\alpha d(1 - A) \tag{5.25}$$

$$\frac{\Delta\alpha}{\alpha_0} \approx \frac{\Delta A}{A(1-A)} \text{ for } e^{\alpha_0 d} \approx 1 - \alpha_0 d. \tag{5.26}$$

Then, from the definition of the saturation fluence,

$$\alpha = \alpha_0 + \Delta\alpha = \alpha_0 e^{-\Gamma/\Gamma_{sat}} \approx \alpha_0(1 - \Gamma/\Gamma_{sat}) \tag{5.27}$$

the saturation fluence can be obtained:

$$\frac{\Gamma}{\Gamma_{sat}} \approx \frac{-\Delta\alpha}{\alpha_0} \approx -\frac{\Delta A}{A(1-A)} \tag{5.28}$$

Therefore, pump-probe experiments can be used to obtain the saturation fluence if Γ, the fluence of the pump pulse, is known. The saturation fluence is inversely proportional to the magnitude of the measured pump-probe signal. The saturation fluence was calculated using this method in ref. [154] and compared favorably to the value obtained from single beam absorption saturation measurements (where the linear transmission of the sample is measured as a function of incident fluence to obtain a curve similar to that shown in figure 2-9).

It is important to note that determining the saturation fluence from pump-probe measurements is not as accurate as determining it from single beam absorption saturation measurements, since difficulty in precisely measuring the spot size (and variations in the spot size due to changes in the laser system), a non-optimized detector alignment, variations in the system alignment (such as variations in the overlap of the focused pump and probe spots), and position of the focused spots on the sample (which is typically inhomeogeneous) can contribute to experimental error. Therefore, some variation in measurement of the $\Delta\alpha/\alpha$ signal when measuring the same sample at different times is often observed. In the work presented in this chapter, the same 10% InAs/90% SiO_2 film was measured at the beginning of each experiment to calibrate the system parameters. However, care should be taken in comparing saturation fluences measured in different experiments, even on the same sample.

5.4.2 Novel pump-probe system with independent pump and probe wavelength tunability from 700 to 1000 nm

One goal of the presented work was to vary the sputtering and RTA fabrication parameters and determine their effect on the linear and nonlinear optical properties of the semiconductor-doped silica films through linear transmission and pump-probe measurements. Linear optical measurements were performed using a Cary spectrophotometer. To fully understand the absorption saturation dynamics in these saturable absorbers, a novel pump-probe system providing independent wavelength tunability from 700 to 1000 nm was developed based on a 5.5 fs Ti:sapphire laser [90]. As discussed in the previous sub-section, wavelength-dependent pump-probe measurements typically require high pulse energy, low repetition rate lasers, limiting the signal-to-noise ratio. Tunable lasers can also be used for high signal-to-noise

ratios, but the pump and probe wavelengths cannot be independently tuned if the same laser is used for both pump and probe beams. If different tunable lasers are used, the system becomes quite complex due to the tight synchronization required between the two pulse trains.

Recent advances in ultrashort pulse generation have resulted in the development of lasers producing sub-two-cycle pulses directly from the laser oscillator [17, 40, 90]. These relatively simple systems (as compared to systems that use extracavity pulse compression to produce ultrashort pulses) produce bandwidths in excess of 300 nm, with pulse durations down to 5 fs. The laser used in this thesis was described in ref. [90] and is shown in figure 5-6.

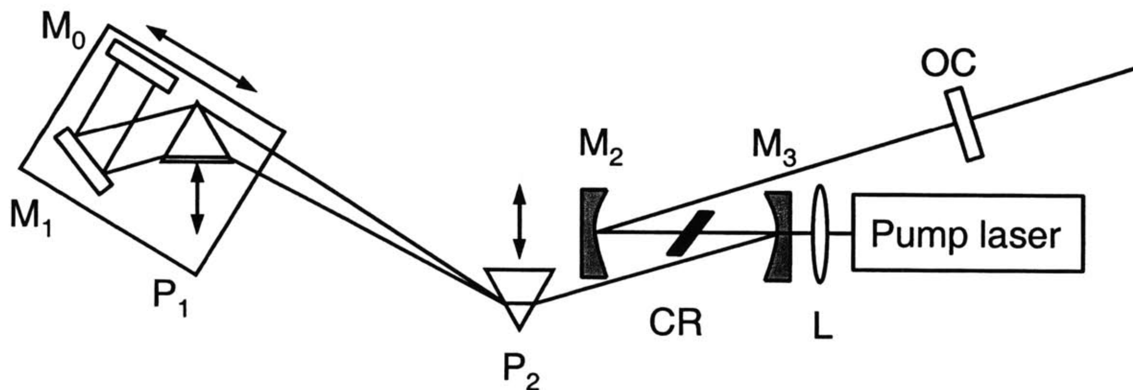

Figure 5-6. Schematic of the 5.4 fs Ti:sapphire laser described in ref. [90].

The Ti:sapphire laser resonator is a standard z cavity design using a combination of DCMs and CaF_2 prisms separated by 65 cm for dispersion compensation. The laser mode is focused into the 2.05 mm thick Brewster-cut Ti:sapphire crystal by two R=10 cm curved DCMs (M_2 and M_3). The output coupler had 1.5% transmission. Two bounces on M_1, a flat DCM, provide a total of 6 bounces on DCMs within the laser cavity. M_0 is a silver mirror. The pump light from a frequency-doubled Nd:YAG laser (Spectra-Physics Millenia) was focused by a 10 cm focal length lens through M_3 into the crystal; the pump power was 5 W. This laser produced 5.4 fs pulses at 90 MHz repetition rate with spectrum extending over 700-1000 nm on a linear scale (figure 5-7). Typical output power used in the experiments described in this chapter was 100-120 mW. In some experiments, the output coupler was replaced by a 2.5% output coupler for 120 mW power; the laser spectrum was typically not as broad with this OC, and the peak in the infrared was about half of its magnitude as compared to that generated with the 1.5% OC.

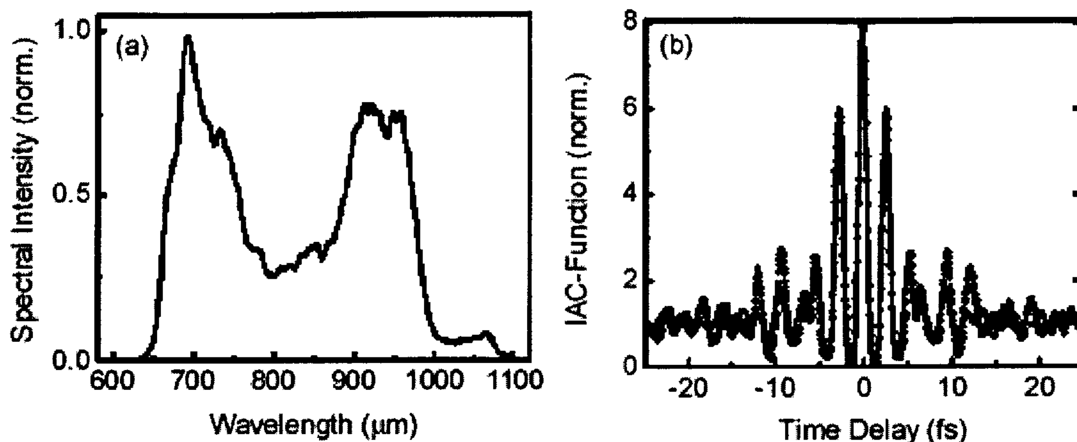

Figure 5-7. (a) Spectrum and (b) autocorrelation of the 5.4 fs Ti:sapphire laser. In (b), the gray line is the measured autocorrelation and the black line is a sinc^2 fit to the data.

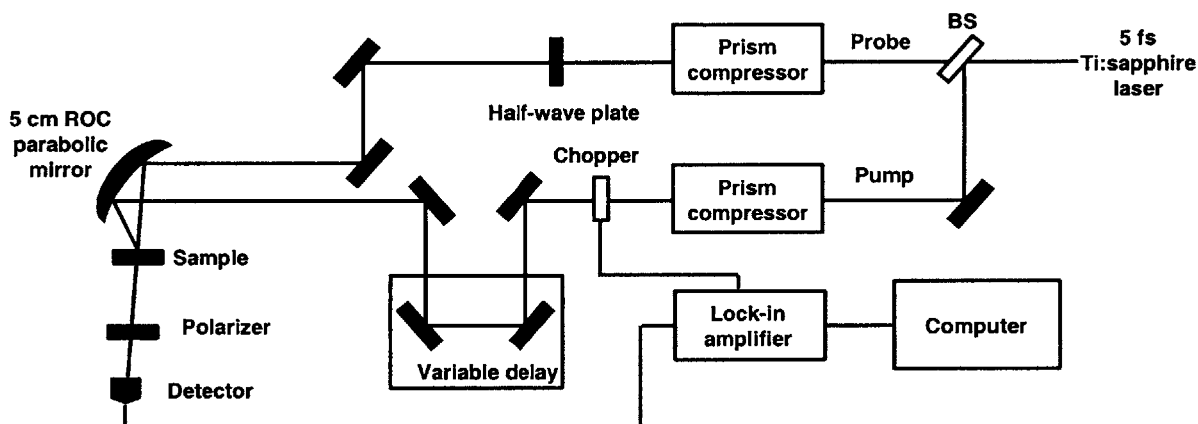

Figure 5-8. Schematic of the pump-probe system with independent pump and probe wavelength tunability from 700-1000 nm.

The broad spectrum of this laser source can be used as the basis for a pump-probe system providing independent pump and probe wavelength tunability at high repetition rates with high sensitivities using a simple design [238, 239]. This system was conceived and developed with the assistance of Dr. Ingmar Hartl. The system is much simpler than typical wavelength tunable systems using two separate tunable lasers or based on continuum generation. It also operates at high repetition rates (90MHz), enabling the use of lock-in detection to achieve high sensitivities. The output from the ultrashort pulse Ti:sapphire laser is sent through an f=1 m lens before the pump-probe system; without this lens, the divergence of the laser output causes the beam size to

increase while traveling through the pump-probe system, eventually aperturing the beam on the mirrors within the system. A schematic of the wavelength tunable pump-probe system is shown in figure 5-8.

A broadband beam splitter splits the output of the laser into pump and probe beams. The two beams are directed into individual prism compressors (similar to those in figure 2-13), each consisting of two fused silica prisms separated by 135 cm (figure 5-9).

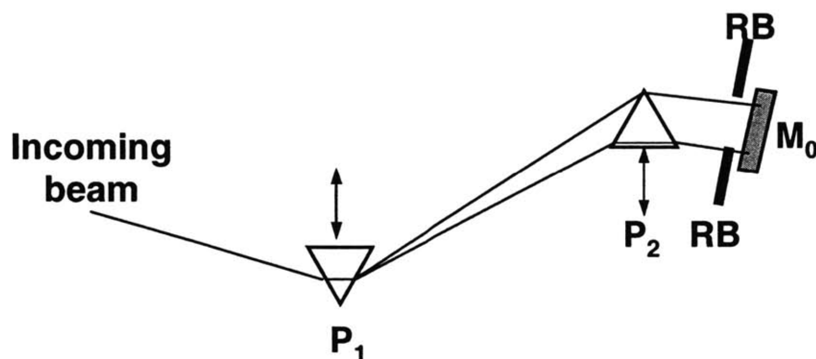

Figure 5-9. Prism compressor used to select spectral components within the 700-1000 nm bandwidth of the Ti:sapphire output spectrum. P_1 and P_2 are fused silica prisms, M_0 is a silver mirror, and RB are the razor blades used to select the desired wavelengths.

In each prism compressor, the pump (probe) beam is spectrally dispersed on a silver mirror after the second prism. Razor blades are positioned near the silver mirror to select the desired pump and probe wavelengths. This enables independent pump and probe wavelength tunability over the laser output spectrum. In practice, the minimum bandwidth that could be selected was ~100 nm; for bandwidths much smaller than this, the pump and/or probe powers were too low to measure a pump-probe signal with good signal-to-noise ratio. The pump (probe) beam is retro-reflected through the prisms in each arm and sent to a standard non-collinear pump probe setup. The pump and probe are cross polarized to avoid pump scattering by inserting a broadband half-wave plate in the probe arm. The two beams are focused to a spot size of 25 μm onto the sample with a 5 cm radius of curvature silver parabolic mirror to minimize additional dispersion. In some experiments, the spot size was larger, up to 70 μm; this is taken into account when calculating the saturation fluence from pump-probe measurements, and did not appear to

affect the observed dynamics. The pump power incident on the sample is typically 80-90 mW and the probe power is 0.3-0.4 mW; this varies with the laser output power. The delay stage had a step size of 0.1 μm, corresponding to 0.3 fs/step. An aperture and linear polarizer are used to block the scattered pump light, and the probe signal is focused by a 5 cm focal length lens onto the amplified silicon detector (ThorLabs PDA55). All mirrors in the system are silver mirrors, with the exception of the last mirror used to send the pump beam to the parabolic mirror, which was gold. The chopper frequency varied between 400 Hz and 2 kHz in these experiments. This system had typical sensitivities of 10^{-4} and when fully optimized could measure signals with a sensitivity of 10^{-5}. A computer was used to synchronize the stage motion and data acquistion from the lock-in amplifier; the program used for data acquisition also had the capability to average an arbitrary number of scans together to increase the signal clarity.

The time resolution of this system was measured by intensity cross-correlation with a 100 μm BBO crystal. The BBO crystal was placed at the focus of the parabolic mirror and the detector was aligned to detect the phase-matched second harmonic signal. The prism separation and insertion in each arm were varied to optimize the experimental time resolution. The minimum width of the cross-correlation was 17 fs for the full laser bandwidth in both pump and probe arms, setting the experimental time resolution. The increased pulse duration was due to broadening of the initial sub-10 fs pulses due to residual uncompensated higher order dispersion in the prism compressors. No significant change in the time resolution was observed when the laser bandwidth was spectrally filtered in the prism compressors, since the minimum laser bandwidth used in these experiments was 100 nm in each arm, enough to support a 17 fs time resolution. The time resolution used in these experiments varied from 17-60 fs; no changes in the absorption saturation dynamics were observed when larger time resolutions of 60 fs were used since the fastest processes in the semiconductor-doped silica films occurred on a time scale of hundreds of fs. Figure 5-10 shows a measured cross-correlation with 17 fs time resolution.

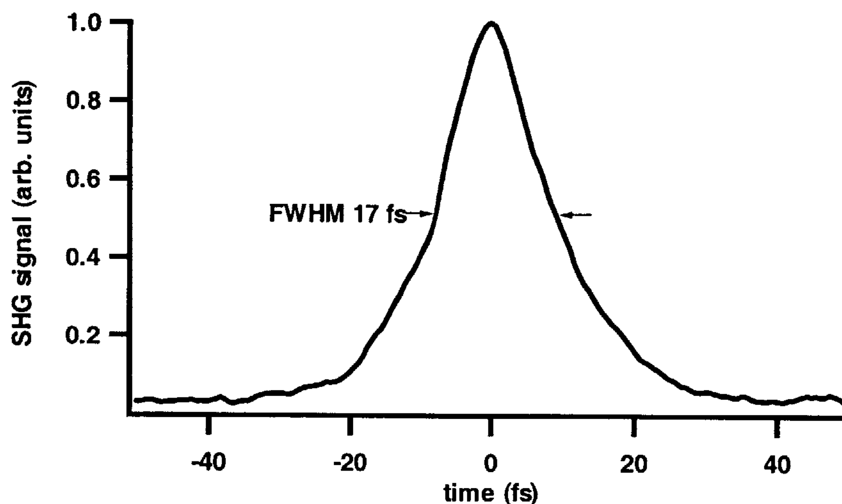

Figure 5-10. Cross-correlation of the independently wavelength tunable pump-probe system based on a ultrashort pulse Ti:sapphire laser, measured by phase-matched second harmonic generation in a 100 μm BBO crystal.

The utility of this system was demonstrated in experiments that used a two-dimensional smart pixel array to measure wavelength and time-resolved carrier dynamics in bulk GaAs [239]. These experiments were performed in collaboration with Dr. Stephane Bourquin. This experiment is similar to standard pump-probe systems based on amplified lasers that use a charge-coupled device (CCD) camera to obtain wavelength-dependent pump-probe measurements. However, high sensitivities are typically not obtained with this method, and therefore amplified lasers must be used to obtain large signals, increasing system complexity. The two-dimensional smart pixel array is essentially a CCD camera with a lock-in amplifier built into each pixel, allowing high sensitivity measurements with wavelength resolution [240, 241]. In these experiments, the smart pixel array had wavelength resolution of 3 nm with typical sensitivities of 10^{-3}. The wavelength-dependent dynamics in GaAs were measured to demonstrate this concept by pumping above the band gap of 870 nm and probing over the whole spectral range of 700-950 nm. Dynamics similar to those seen in previous work [242, 243] were observed, demonstrating the ability of this system to accurately characterize wavelength-dependent time-resolved carrier dynamics. The smart pixel array was not designed for this application, and therefore improvements in the array design tailored specifically for pump-probe applications would significantly increase the sensitivity. The combination of a two-dimensional

smart pixel array with a pump-probe system providing independent wavelength tunability at high repetition rates could be a powerful tool in ultrafast spectroscopy.

5.4.3 Pump-probe systems operating at 1.26 and 1.5 microns

For further understanding of the absorption saturation dynamics in semiconductor-doped silica film saturable absorbers, pump-probe systems based on a mode-locked Cr:forsterite laser with a center wavelength of 1260 nm and a Ti:sapphire-pumped optical parametric oscillator (OPO) tunable between 1400 and 1600 nm were used. The pump-probe system at 1260 nm was based on a Cr:forsterite laser generating pulses as short as 14 fs at 80 MHz repetition rate with 250 nm bandwidth and 80 mW average power [91]. This laser is described in detail in section 6.4. For these experiments, extremely high time resolution was not necessary and more power was desired. Therefore, the laser was configured to operate with average powers of 120 mW, pulse durations of 35 fs, and 60 nm bandwidth for these experiments by increasing the output coupling to 3%. The pump probe system was a standard non-collinear pump probe setup, without any prism compressors for spectral filtering. The setup was essentially the same as shown in figure 5.8 if the prism compressors are removed. A 70/30, broadband beam splitter was used to split the incoming beam into pump and probe. A thin neutral density filter was used to attenuate the probe beam, setting the probe power at 0.7 mW for a pump power of 70 mW. The pump and probe were cross-polarized by inserting a broadband half-wave plate in the probe arm. The beams were both focused to a 20 μm spot on the sample using an R=10 cm parabolic mirror. An aperture and linear polarizer were used after the sample to eliminate pump scattering and the signal was detected with an amplified InGaAs detector. The delay stage had a step size of 1 μm, and the chopper frequency was 400 Hz.

The pump-probe system operating around 1.5 μm was based on a commercial optical parametric oscillator (OPO) (Spectra-Physics Opal). This OPO generated 110-150 fs transform limited pulses at an 82 MHz repetition rate, with signal tunable between 1.4 and 1.6 μm and idler tunable from 1.7 to 2.0 μm. It is pumped by a argon-pumped Ti:sapphire laser producing 100 fs pulses with 2 W power (Spectra-Physics Tsunami). This pump-probe system is described in detail in ref. [244]. Briefly, the system is a collinear pump-probe setup (similar to the

interferometric autocorrelation setup of figure 2-18), with cross-polarized pump and probe beams having pump powers of 124 mW and probe powers of ~8 mW, focused onto the sample with an aspheric lens. The pump spot size on the sample was 20 μm and the time resolution of the system was ~300 fs (measured by the width of the cross-correlation). This system was used in several previous experiments to measure the dynamics of saturable Bragg reflectors [245-248].

5.5 Linear and nonlinear optical characterization of semiconductor-doped silica film saturable absorbers

5.5.1 Linear transmission measurements

Semiconductor-doped silica film saturable absorbers were fabricated under different conditions and their linear transmission was measured to understand the effect of fabrication parameters on linear optical properties. Linear transmission measurements were taken using a Cary 5E UV-Vis-NIR spectrophotometer located in the Center for Materials Science and Engineering at MIT. Initial experiments investigated the effect of varying the nanocrystallite size on the linear optical properties. It has been shown [155, 157, 249] that varying the ratio of semiconductor to glass on the target can be used to control the nanocrystallite size in the sputtered film. Larger semiconductor to glass ratios result in larger nanocrystallite sizes in the deposited film, shifting the optical absorption edge to longer wavelengths. Therefore, the effect of varying the ratio of InAs to SiO_2 on the size of the InAs nanocrystallites in the silica films (inferred from the shift of the optical absorption edge) was tested.

It is worth mentioning here that the goal of the experiments described in this chapter was primarily to characterize the linear and nonlinear optical properties of the semiconductor-doped silica films as functions of fabrication parameters in order to optimize their application as saturable absorber devices. In the previous research (described in chapter 3), a comprehensive characterization of the structural properties of these films was performed, and in most of the films fabricated and characterized in this chapter similar structural properties were assumed. However, some variation in the structural properties of films fabricated under different

conditions has been observed [155-157, 250], and therefore characterization of the film structure as a function of fabrication parameters could also yield valuable data that may be useful in further optimizing film properties. For example, detailed studies of the nanocrystallite growth process could give data about the nanocrystallite size and shape as a function of film thickness, which may influence saturable absorber properties.

Films with a 10% InAs/90% SiO_2 ratio were sputtered in the magnetron system for comparison with the previous films fabricated in a non-magnetron sputtering system [46, 154]. The target was composed of two undoped, single crystal, (100) oriented InAs chips glued to a 3" diameter SiO_2 disk with a 10% InAs/90% SiO_2 area ratio. The sputtering power was 100 W and the deposition time was 30 minutes to deposit 150 nm thick 10% InAs/90% SiO_2 films on a sapphire substrate; the substrate heater was turned off. A linear transmission measurement of a 10% InAs/90% SiO_2 film is shown in figure 5-11.

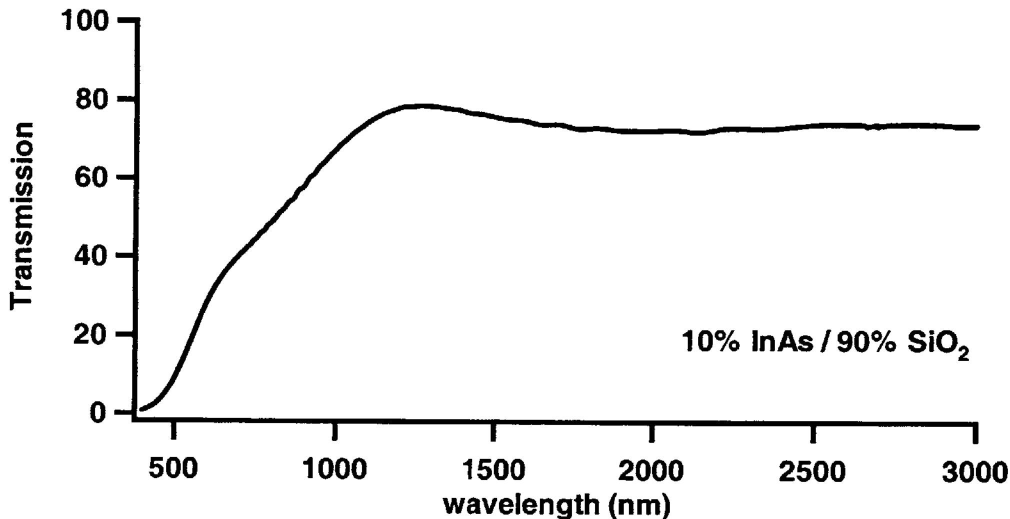

Figure 5-11. Linear transmission measurement before annealing of a 150 nm thick 10%InAs/90% SiO_2 film deposited on a sapphire substrate. The transmission at long wavelengths is less than 100% due to reflection from the sapphire surface.

This transmission characteristic is very similar to that previously obtained [46]. The absorption edge of this sample was approximately 1200 nm and the absorption was ~50% at 800 nm. In the previous work, a nanocrystallite size of 9 nm was estimated from the transmission curve (calculated using equation (5.15) with the absorption edge of 1200 nm and the associated

shift from the 3.5 μm bulk band gap of InAs), which agreed reasonably well with the sizes obtained from TEM measurements. Therefore, a similar nanocrystallite size can be assumed here, which is small compared to the Bohr radius of 32 nm, putting these semiconductor-doped silica films in the strong confinement regime for this InAs/SiO_2 ratio. This sample was subsequently annealed at 600°C for 60 seconds in nitrogen.

Targets with ratios of 3% InAs/97% SiO_2 and 40% InAs/60% SiO_2 were fabricated to deposit films for comparison with the 10%InAs/90% SiO_2 films. A 3% InAs/97% SiO_2 film was deposited at a power of 100 W for 30 minutes on a sapphire substrate. Photolithography (using the procedure described in section 5.3.2) measured the thickness of the sputtered film to be ~160 nm, making the deposition rate 5.3 nm/min at 100 W RF power. Similarly, 40% InAs/60% SiO_2 films were deposited at varying sputtering powers and for different durations. The deposition rate for the 40% InAs/60% SiO_2 films could not be determined by photolithography because the acetone used in the last step of the process to wash off the photoresist also washed off the film itself due to the high InAs concentration. A rough technique based on attaching a piece of tape to the substrate, depositing the film, and removing the tape to expose the substrate, leaving an edge that can be measured by profilometry, was used to estimate a deposition rate of 14 nm/min at 100 W RF power. It was not critical to get a more precise measurement, since the absorption of the film was the important parameter, and this was linearly proportional to the duration of the sputtering run. The deposition rate was found in previous work to be linear with RF power, and the film thickness was linear with both RF power and duration of the sputtering run [158].

Figure 5-12 shows a comparison of linear transmission measurements for a 3% InAs/97% SiO_2 film grown at 200 W for 45 minutes, the 10% InAs/90% SiO_2 film shown in figure 5-9, and a 40% InAs/60% SiO_2 film grown for 3 minutes at 100 W. All films were deposited on sapphire substrates as previously described and annealed in nitrogen for 60 seconds at 600°C. The sputtering powers and durations used with the different targets were chosen to make the film absorption ~40-60%, a good range for pump-probe measurements.

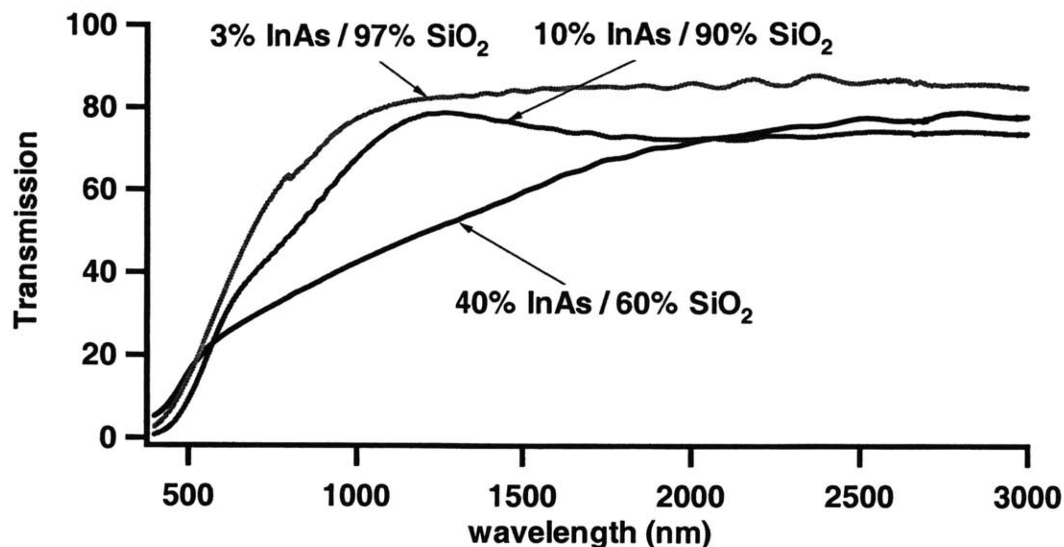

Figure 5-12. Comparison of semiconductor-doped silica films with different $InAs/SiO_2$ ratios. The absorption edge shifts to longer wavelengths with increasing $InAs/SiO_2$ ratio.

Examination of figure 5-12 reveals a shift of the absorption edge to longer wavelengths for higher $InAs/SiO_2$ ratios, agreeing with the expected increase in nanocrystallite size. The absorption edge is ~950 nm for the 3% InAs/97% SiO_2 film and is roughly around 1700 nm for the 40% InAs/60% SiO_2 film, although it is difficult to define an absorption edge since the transmission decreases nearly continuously. The transmission curves become smoother with increasing InAs concentration, which may imply an increase in the nanocrystallite size distribution. Increasing the InAs concentration also makes the nanocrystallites larger, making the quantum confinement weaker. As discussed in section 5.2.2, weak confinement leads to a more continuous spectrum of energy levels. Therefore, the smoother curves are due to the weaker quantum confinement and possibly also to a broadened size distribution. As discussed in chapter 3, this is desirable in saturable absorber applications in order to support a large bandwidth and tuning range. From these experiments, it can be concluded that varying the semiconductor to glass ratio is a simple and effective way of controlling the nanocrystallite size in the sputtered films, enabling fabrication of films for operation at different laser wavelengths over a broad range with only a single semiconductor material.

Samples were also fabricated at different annealing temperatures to measure the variation of the absorption edge as well as pump-probe dynamics with annealing temperature. 10%

InAs/90% SiO_2 films were grown at with 100 W sputtering power for 30 minutes and annealed in nitrogen at different temperatures for 60 seconds. Linear transmission measurements are shown in figure 5-13.

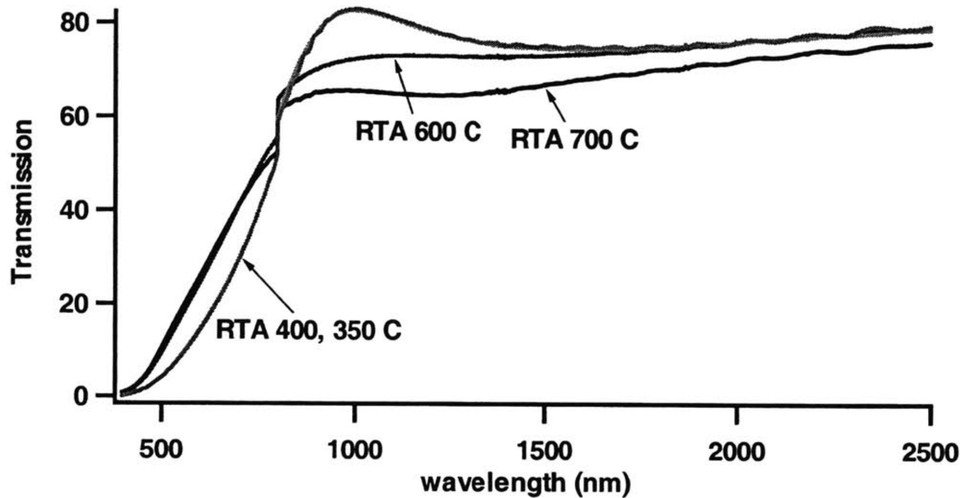

Figure 5-13. Linear transmission measurement of 150 nm thick 10% InAs/90% SiO_2 films annealed at different temperatures for 60 seconds in nitrogen. The discontinuity in the data at 800 nm is due to a detector change.

From these measurements, it is clear that the films annealed at higher temperatures have different transmission characteristics than those annealed at lower temperatures. The films annealed at low temperatures had transmission characteristics similar to the film measured in figure 5-11; the peak near the absorption edge is due to interference effects and the ripples at long wavelengths are due to birefringence in the sapphire substrate, which depended on the sample orientation. The films annealed at 600°C and 700°C had lower transmission near the absorption edge and a smaller interference peak. However, the position of the absorption edge does not change as a function of RTA temperature.

5.5.2 Pump-probe measurements on films with different InAs/SiO_2 ratios

Pump-probe experiments were performed to measure the nonlinear optical properties of the InAs-doped silica films as a function of InAs/SiO_2 ratio. Initial experiments measured the films shown in figure 5-12 at 800 nm using the Ti:sapphire-based pump-probe system operating

with the full laser bandwidth of 250 nm and pump and probe powers of 90 mW and 0.4 mW, respectively, focused to a 20 μm radius spot; all other parameters were as described in section 5.4.2. The results of these measurements are depicted in figure 5-14.

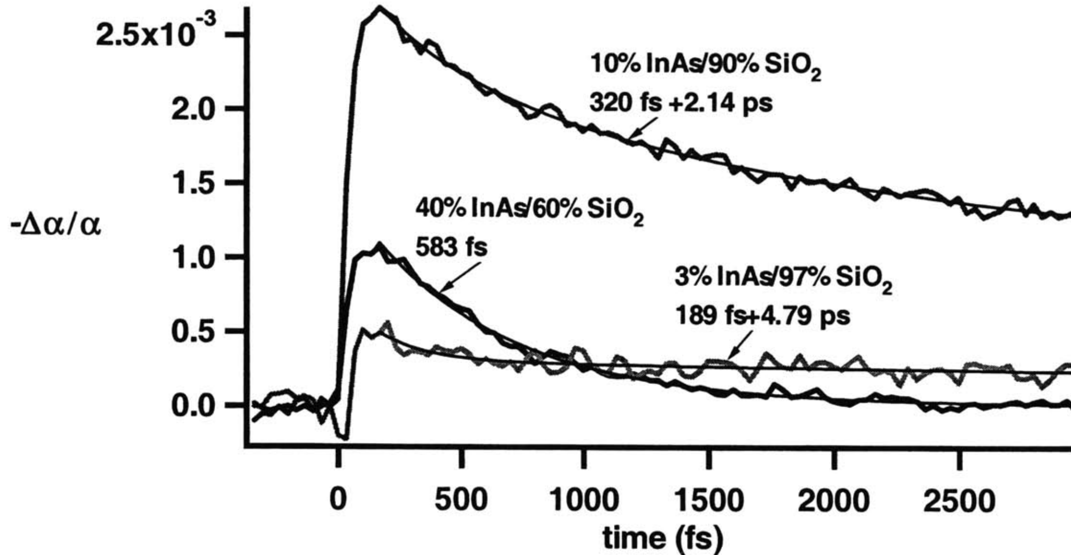

Figure 5-14. Degenerate pump-probe measurements at 800 nm on InAs-doped silica films with different InAs/SiO_2 ratios. The black lines show the results of fitting the data with exponential or double exponential functions, and the relaxation time constants are labeled for each curve. The pump power was 90 mW and the probe power was 0.4 mW, both focused to a 20 μm radius spot on the sample. The measured saturation fluences are given in the text.

From this figure, it is clear that the 10% InAs/90% SiO_2 film has the largest magnitude signal and therefore the lowest saturation fluence, although the mechanism by which this occurs was not clear at this point. The saturation fluences of these films were calculated using equation (5.28). The saturation fluence was 29.5 mJ/cm^2 for the 10% InAs/90% SiO_2 film, 72 mJ/cm^2 for the 40% InAs/60% SiO_2 film, and 141 mJ/cm^2 for the 3% InAs/97% SiO_2 film. Another interesting observation is that the carrier relaxation times, obtained from fitting the data with exponential or double exponential functions, are generally faster with increasing InAs/SiO_2 ratio. A simple explanation for this comes from the fact that the absorption edge shifts to longer wavelengths as the InAs/SiO_2 ratio increases, and therefore states farther above the absorption edge are probed. In the 40% InAs/60% SiO_2 films, the probed states around 800 nm are far above the band minima (around 1700 nm from figure 5-12), and therefore only the fast scattering

out of the initial excited state is observed. In contrast, only states near the band edge are probed in the 3% InAs/97% SiO_2 films, and therefore a long decay is measured since electrons that are scattered out of the initial excited state settle at the bottom of the band and wait to recombine. Although this model serves to describe the carrier dynamics, it does not clearly explain the changes in magnitude of the pump-probe signal between samples with different InAs/SiO_2 ratios. Therefore, further experiments needed to be performed to understand the dependence of the saturation fluence on film parameters.

5.5.3 Wavelength dependence of the saturation fluence

The large pump-probe signal measured at 800 nm for the 10% InAs/90% SiO_2 film motivated experiments to explore the wavelength dependence of the saturation fluence in this film with the tunable Ti:sapphire-based pump-probe system. Degenerate wavelength-dependent pump-probe measurements were performed on the previously measured 10% InAs/90% SiO_2 film (shown in figures 5-11, 5-12 and 5-14) at center wavelengths of 750, 800, and 925 nm. The measurement at 800 nm used the full laser bandwidth of 250 nm, while the measurements at 750 and 925 nm each had a bandwidth of 100 nm centered around the laser wavelength. The pump and probe powers were 40 mW and 0.2 mW, respectively, focused to a 20 μm spot as before, with all other system parameters as previously described. Figure 5-15 depicts the result of the measurement.

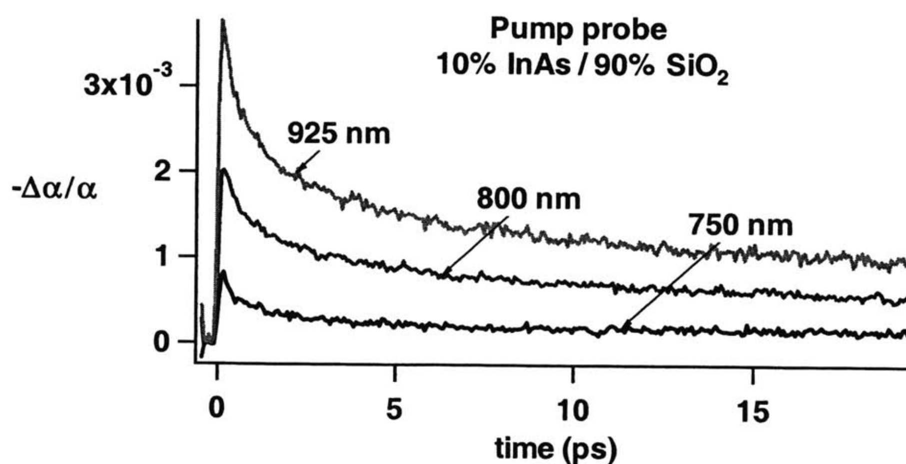

Figure 5-15. Degenerate pump probe measurement of a 10% InAs/90% SiO_2 film as a function of wavelength, showing a decrease in saturation fluence with excitation closer to the absorption

edge. 40 mW pump power and 0.2 mW probe power were focused to a 20 μm spot on the sample, and a saturation fluence of 9.3 mJ/cm^2 was measured at 925 nm.

From this measurement, it is clear that the $-\Delta\alpha/\alpha$ signal increases as the pump-probe wavelength moves closer to the absorption edge. Since the saturation fluence is inversely proportional to the $-\Delta\alpha/\alpha$ signal, this implies that the saturation fluence decreases as the wavelength increases. The saturation fluences were 9.3 mJ/cm^2 at 925 nm, 17.5 mJ/cm^2 at 800 nm, and 42.5 mJ/cm^2 at 750 nm. It should be mentioned that improvements in the detector alignment were made between the measurements shown in figure 5-13 and 5-14, which led to the difference in the measured saturation fluences at 800 nm on the same film; both values are comparable to the 25 mJ/cm^2 saturation fluence of 10% InAs/90% SiO_2 films measured at 800 nm in previous work [45, 46, 154]. Therefore, it can be concluded from this experiment that operation close to the absorption edge is desirable to minimize the saturation fluence. This trend has also been observed in previous work on semiconductor-doped glasses [251].

These results motivated examination of the 40% InAs/60% SiO_2 films near their absorption edge to determine whether a similar wavelength dependence would be observed. The OPO-based pump-probe system operating at 1.5 μm was used to measure the dynamics of the 40% InAs/60% SiO_2 films near their absorption edge of ~1.7 μm. The system parameters (pump and probe powers, etc.) were as described in section 5.4.3, with pump powers of 124 mW and probe powers of ~8 mW, focused to a 20 μm spot on the sample. All measurements with this system were performed in collaboration with Juliet Gopinath and Professor Erich Ippen. The 10% InAs/90% SiO_2 and 3% InAs/97% SiO_2 films have no absorption at this wavelength and therefore no measurement was attempted. The results of these measurements on a 40% InAs/60% SiO_2 film sputtered at an RF power of 100 W for 15 minutes and annealed for 60 seconds at 600°C in nitrogen, with transmission curve similar to that shown in figure 5-12, are depicted in figure 5-16.

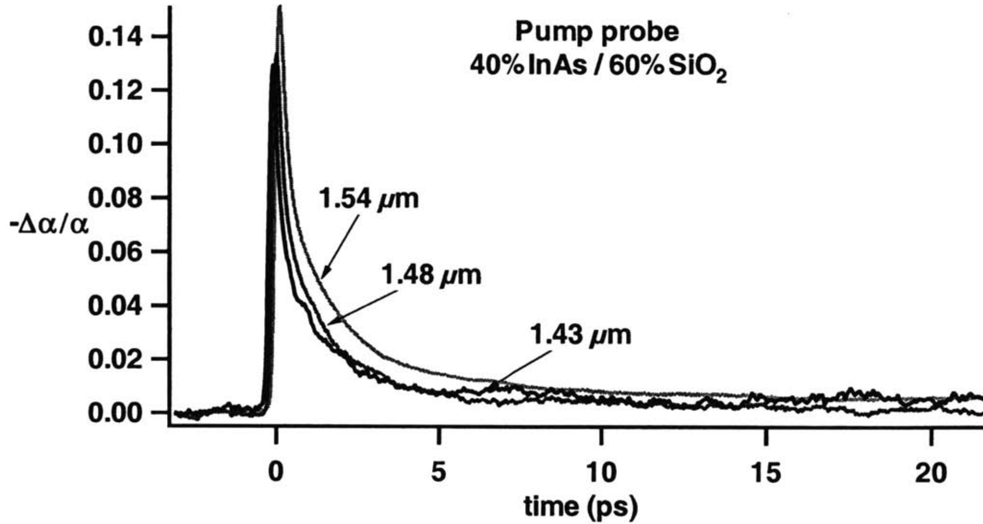

Figure 5-16. Tunable degenerate pump-probe measurements at wavelengths of 1.54 μm, 1.48 μm, and 1.43 μm on a 40% InAs/60% SiO_2 film. A pump power of 124 mW and a probe power of 8 mW were focused to a 20 μm spot on the sample, and a saturation fluence of 640 μJ/cm^2 at 1.54 μm was measured.

Several observations can be made from this measurement. As expected, the saturation fluence decreased with wavelength over the measured range (1.43-1.54 μm), although the decrease is not as drastic for this sample as for the 10% InAs/90% SiO_2 film shown in figure 5-15. This is expected since the transmission curve of the 40% InAs/60% SiO_2 film is much smoother than that of the 10% InAs/90% SiO_2 film (figure 5-12). It is worth mentioning that measurements on 3% InAs/97% SiO_2 films at wavelengths of 750, 800, and 900 nm revealed a decrease of the saturation fluence with wavelength as well. Therefore, the saturation fluence consistently decreases as the pump/probe wavelength is tuned closer to the absorption edge.

Perhaps the most important observation from figure 5-16 is the magnitude of the signal, as $-\Delta\alpha/\alpha$ is more than two orders of magnitude larger for 40% InAs/60% SiO_2 films at 1540 nm (figure 5-16) than at 800 nm (figure 5-14). The saturation fluence for this film was calculated from the pump pulse energy and spot size to be 640 μJ/cm^2 at 1.54 μm, significantly lower than the 72 mJ/cm^2 saturation fluence measured at 800 nm. This can be understood by noting that the 1.54 μm pump-probe wavelength is much closer to the ~1.7 μm absorption edge in this

measurement, and therefore the wavelength dependence of the saturation fluence has a strong effect. It is also important to note that the 640 μJ/cm^2 saturation fluence of the 40% InAs/60% SiO_2 films at 1.54 μm is more than an order of magnitude lower than the lowest measured saturation fluence of the 10% InAs/90% SiO_2 films (9.3 mJ/cm^2 at 925 nm from figure 5-15), even though both films were measured near their respective absorption edges. This was unexplained at this point, and will be discussed in section 5.5.4.

5.5.4 Fluence-dependent pump-probe measurements at 1.54 μm

Fluence-dependent dynamics have been observed in several pump-probe measurements on saturable absorber devices [245-248]. In these experiments, semiconductor saturable mirrors consisting of InGaAs quantum wells grown in an InP half-wave layer on a DBR by MBE were measured at 1.5 μm using the same pump-probe system described in section 5.4.3. These measurements revealed significant changes in the carrier dynamics with pump fluence. For low fluences, near the device saturation fluence, the pump-probe trace had a fast bleaching component and a slower recombination component, as is normally observed in pump-probe experiments on semiconductor quantum wells. However, at high fluences, free carrier absorption (FCA) and two-photon absorption (TPA) increase and eventually dominate the carrier dynamics, which could have important implications for laser dynamics when these devices are applied to laser mode-locking.

These effects were investigated for the semiconductor-doped silica film saturable absorbers. Pump-probe measurements were taken at 1.54 μm while varying the incident pump and probe fluences. The ratio of pump and probe fluences was kept to 10:1 or greater in order to avoid exciting carriers with the probe pulses. The pump and probe powers were 124 and 7.5 mW for the high fluence trace and 40 and 4 mW for the low fluence trace, with the spot focused to 20 μm radius. The result of these measurements on the 40% InAs/60% SiO_2 film with the linear transmission curve shown in figure 5-12 is displayed in figure 5-17. At low fluences, a characteristic similar to those displayed in figure 5-16 was measured, although a small hump on the trace is seen. The hump disappeared for still lower fluences (not shown) and the dynamics

appeared identical to those in figure 5-16. The hump significantly increased for a higher fluence of 118 μJ/cm^2.

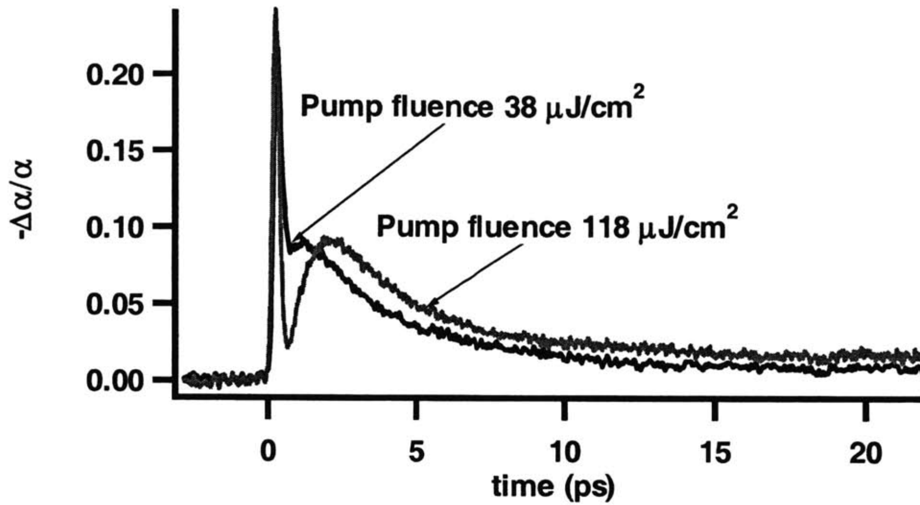

Figure 5-17. Fluence-dependent pump-probe measurement at 1.54 μm on the 40% InAs/60% SiO_2 film with the transmission curve shown in figure 5-12. The experimental parameters are given in the text.

These dynamics can be attributed to TPA and FCA effects occurring at high fluences. The width of the first peak at high fluence is due to the TPA component and corresponds to the pulse cross correlation [245], since TPA only occurs when the two pulses are overlapped in time and space. The carriers generated at high energy states by TPA and FCA at early delay times decay down to the states that are pumped and probed, saturating these states and resulting in the second peak in the data. These dynamics may strongly affect mode-locked laser operation, since typical intracavity fluences are on the order of a few mJ/cm^2. The stabilization against Q-switched mode-locking is expected to increase, while the threshold for multiple-pulsing may be lowered [248].

It is important to note that these samples are composed of semiconductor nanocrystallites doped into a silica film, while the previous work focused on quantum well samples; however, the observed dynamics that are similar to the effects observed in the quantum well samples are most likely due to the relatively weak confinement in these 40% InAs/60%SiO_2 films and broad size distribution of the nanocrystallites. Also, the fluences used here are still well below the

saturation fluence, while similar dynamics were observed in the quantum well samples for incident fluences above the saturation fluence. The pump-probe signal increased with wavelength at all fluence levels tested.

5.5.5 Pump-probe measurements at 1.26 μm

Pump-probe measurements at 1.26 μm were also performed on the 40% InAs/60% SiO_2 films to examine an intermediate wavelength between 800 and 1500 nm. The Cr:forsterite-based pump-probe system parameters were as described in section 5.4.3, with 70 mW pump power and 0.7 mW probe power focused to a 20 μm spot on the sample. The film shown in figure 5-12 is measured at 1.26 μm and the result is depicted in figure 5-18.

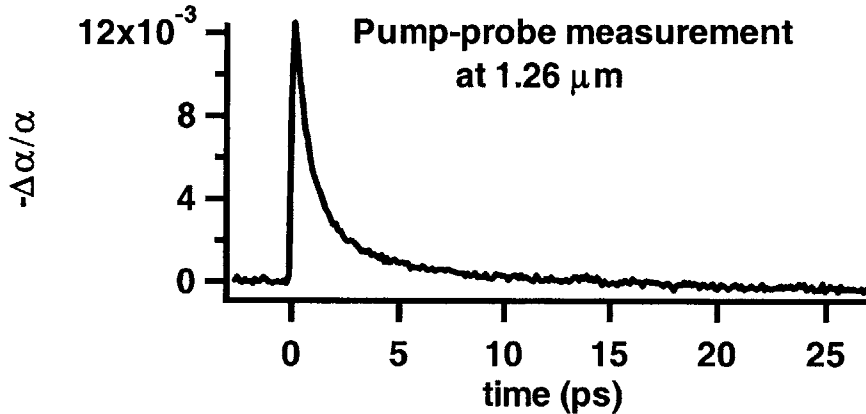

Figure 5-18. Degenerate pump-probe measurement at 1.26 μm of the 40% InAs/60% SiO_2 film with the transmission curve shown in figure 5-12. 70 mW pump power and 0.7 mW probe power were focused to a 20 μm spot on the sample. The saturation fluence of this sample was 4.05 mJ/cm^2.

A saturation fluence of 4.05 mJ/cm^2 is calculated from the trace shown in figure 5-18. This is greater than the saturation fluence of 640 $\mu J/cm^2$ at 1.54 μm; however, it is still significantly lower than the 25 mJ/cm^2 saturation fluence measured at 800 nm on the films used to self-start KLM in Ti:sapphire [45, 46, 154]. Therefore, this implies that these 40% InAs/60% SiO_2 films can be used to self-start mode-locking in a Cr:forsterite laser.

Comparison of the pump-probe measurements for 10% InAs/90% SiO_2 films measured at 800 nm (figures 5-14 and 5-15) with the measurements on 40% InAs/60% SiO_2 films at 1.26 μm (figure 5-18) indicate that the nanocrystallite size is a significant factor in determining the saturation fluence of the device. The saturation fluence decreases significantly when comparing the 40% InAs films with larger nanocrystallites (Γ_{sat}=4.05 mJ/cm^2 at 1.26 μm) to the 10% InAs films with smaller nanocrystallites (Γ_{sat}=17.5 mJ/cm^2 at 800 nm). The pump-probe wavelengths are approximately the same distance from the absorption edge in both cases (~400 nm), since the absorption edge is around 1200 nm for the 10% InAs film and 1700 nm for the 40% InAs film. Therefore, the wavelength-dependent effects observed when tuning the pump-probe wavelength for a certain sample (figures 5-15 and 5-16) should not appreciably influence the interpretation of the data. This indicates that the differences in nanocrystallite size between the two films are the most likely cause of the large difference in saturation fluence.

The combination of the nanocrystallite size dependence with the dependence of the saturation fluence on wavelength could explain the dynamics in figure 5-14, where the 40% InAs films were excited too far above the absorption edge to have appreciable saturable absorption, and the nanocrystallites in the 3% InAs films were too small to saturate easily. The extremely low saturation fluence of 640 μJ/cm^2, measured on the 40% InAs films at 1.54 μm, can also be explained since the nanocrystallites are large and the pump-probe wavelength is very close to the absorption edge. Therefore, from this sub-section as well as section 5.5.2, it can be concluded that nanocrystallite size and operating wavelength relative to the absorption edge are very important parameters in determining the saturation fluence of a semiconductor-doped silica film saturable absorber and may enable further optimization of the saturable absorber properties.

5.5.6 Effect of RTA temperature variance on absorption saturation dynamics

The annealing temperature of the 10%InAs/90% SiO_2 films was varied to determine the effect of RTA on the nonlinear absorption saturation dynamics. Annealing is expected to modify the surface properties of the nanocrystallites; nanocrystallites with better surface properties are anticipated to have lower saturation fluence. The films with transmission characteristics shown in figure 5-13 were measured in pump-probe experiments. Figure 5-19 depicts the changes in

the measured pump-probe signal at 800 nm, obtained with the Ti:sapphire-based system with 90 mW pump power and 0.4 mW probe power focused to a 57 μm spot, with the other parameters as described in section 5.4.2, as a function of annealing temperature.

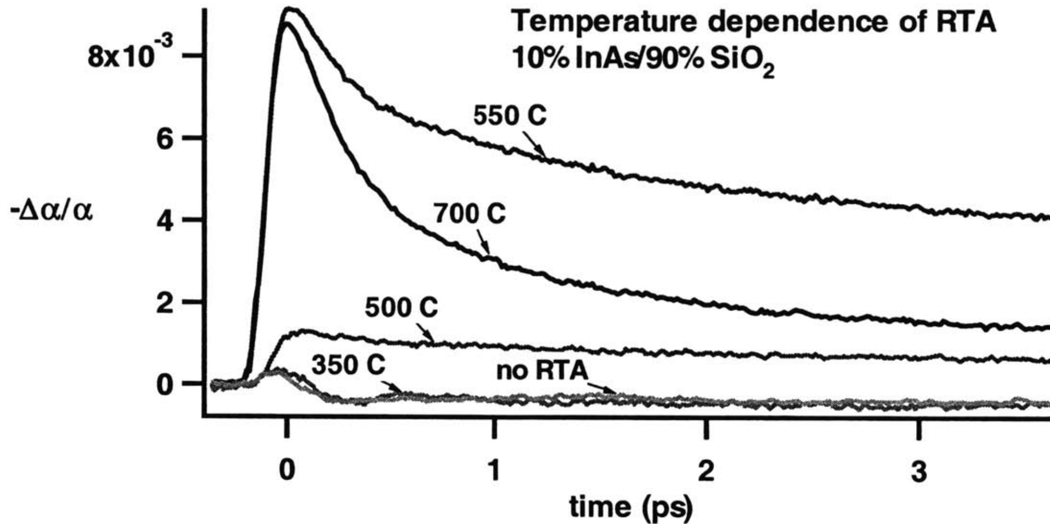

Figure 5-19. Degenerate pump probe measurement of a 150 nm thick 10% InAs/90% SiO_2 film at 800 nm as a function of rapid thermal anneal temperature. Discrete changes in the dynamics as a function of annealing temperature are observed. The pump power was 90 mW and the probe power was 0.4 mW, both focused to a 57 μm spot on the sample.

Distinctive changes in the absorption saturation dynamics were observed as the annealing temperature was varied from 350-700°C. For an unannealed sample as well as a sample annealed at 350°C, a negative pump-probe signal was measured, indicating induced absorption, which has been observed by other authors and attributed to the formation of biexciton states, free carrier absorption, photodarkening, and band gap renormalization [219, 221]. In our case, the low pump fluences and nanocrystallites smaller than the Bohr radius rule out band gap renormalization and biexciton state formation. No permanent changes were observed, making photodarkening unlikely. Therefore, a mechanism similar to free carrier absorption in bulk semiconductors is most likely the origin of the induced absorption. The absorption of light photons by excited carriers and their subsequent transitions to higher energy states would explain the induced absorption, particularly with the large size distribution of nanocrystallites and the broad laser spectrum. Induced absorption was consistently observed with unannealed samples.

In the range of 400-500°C, the absorption saturation was positive but small, and a saturation fluence of ~10 mJ/cm^2 was measured. At temperatures of 550°C and above, the absorption saturation was large, resulting in a saturation fluence of 1.08 mJ/cm^2. It should be noted that although the saturation fluence for this 10% InAs/90% SiO_2 film (1.08 mJ/cm^2) appears to be lower than in previous measurements (17.5 mJ/cm^2 from figure 5-15), the sample measured in figures 5-14 and 5-15 was also measured at the same time and found to have a similar signal magnitude as the films annealed at 550°C and above, suggesting that the differences in the measured saturation fluence of 10% InAs/90% SiO_2 films are primarily due to system alignment and position of the spot on the sample. Samples annealed at 700°C had a faster relaxation time than those annealed at 550-600°C, although the magnitude of the signal and therefore the saturation fluence was nearly the same as that of the sample annealed at 550°C. The latter trend agreed with that measured in previous work [46], although temperatures below 500°C were not tested in those experiments. Overall, as previously demonstrated higher annealing temperatures seem to be effective in improving the surface quality of the nanocrystallites and thereby reducing the saturation fluence. However, the discrete changes in the pump-probe signal as a function of RTA temperature were unexplained and further investigations would have to be performed.

It was hypothesized that the RTA temperature dependence shown in figure 5-17 was due to the relation of the glass melting and transition temperatures [203, 228] of the silica matrix surrounding the nanocrystallites to the RTA temperature. Therefore, films with InAs nanocrystallites doped into a borosilicate glass matrix (Ohara Optics, S-FSL5) and deposited on sapphire substrates were fabricated to test the dependence of the absorption saturation dynamics on the glass matrix composition. The films were 10% InAs and 90% borosilicate glass; the composition of the glass was ~55-65% SiO_2, 15-25% K_2O, and 10-20% B_2O_3. The films were annealed in nitrogen for 60 seconds as in the other experiments. Pump-probe measurements on these films using the same experimental conditions as the measurements depicted in figure 5-18 demonstrated that unlike the SiO_2-based films, the pump probe signal did not change discretely with annealing temperature, instead increasing continuously as the RTA temperature increased (figure 5-20). However, at high annealing temperatures the dynamics were very similar to those measured with a SiO_2 matrix, and there was no significant improvement in the saturation fluence

(1.03 mJ/cm^2 for the films annealed at 550 and 600°C). From these experiments, it was clear that the choice of glass material affects the absorption saturation dynamics.

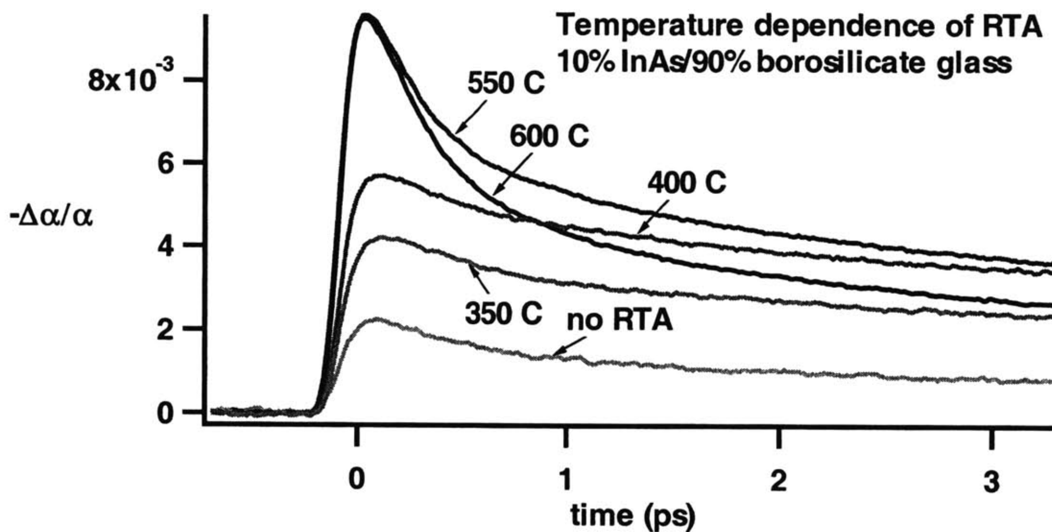

Figure 5-20. Degenerate pump probe measurement of a 150 nm thick 10% InAs/90% borosilicate glass film at 800 nm as a function of RTA temperature. The absorption saturation dynamics change continuously as a function of RTA temperature. The experimental parameters were identical to those in figure 5-19.

The difference in annealing temperature dependence between films fabricated with InAs doped into a SiO_2 matrix and films fabricated with InAs doped into a borosilicate glass matrix can possibly be explained by examining the different melting points of the composite films. The melting point of InAs is 1215 K, that of SiO_2 is 1983 K, and that of the borosilicate glass is ~1000 K. The eutectic point of each film is the temperature for a phase transition from solid to liquid for the composite film, which may be lower than the melting point of each film constituent [252, 253]. Therefore, if the eutectic point for the composite InAs/glass film is within the range of the annealing temperature, then the film will partially melt during the RTA process and its properties will be different after cooling down. Different eutectic points for the SiO_2-based films and the borosilicate glass-based films would cause the RTA process to affect the film properties in different ways and could explain the dynamics observed in our experiments. For example, the difference in glass matrices would change the variation of nanocrystallite surface properties with RTA temperature for the SiO_2-based films as compared to the borosilicate glass-based films, which could modify the saturation fluence. However, it should be noted that the eutectic point is

typically defined for a homogeneous sample; the InAs-doped glass films are not homogeneous since the InAs nanocrystallites exist as discrete elements scattered throughout the film. An alternative explanation could be based on the relation of the annealing temperature to the glass melting and transition temperatures, which will be different for the silica-based film and the borosilicate glass-based film. Overall, these experiments demonstrate that the choice of glass and annealing temperature has an important effect on the absorption saturation dynamics that must be considered when designing non-epitaxially grown semiconductor-doped silica films.

5.5.7 Effect of other fabrication parameters on absorption saturation dynamics

Fabrication parameters including the doping level of the InAs target, annealing time, and substrate temperature during the sputtering run were also varied to gauge their effect on the saturation fluence as measured in pump-probe experiments at 800 nm. It has been shown that higher substrate temperatures during sputtering result in larger nanocrystallites [155, 250, 254]. The substrate temperature was varied between 0 and 300°C during sputtering runs with the 10% InAs/90% SiO_2 target in an attempt to obtain larger nanocrystallites in the InAs-doped silica films. The RF power was 100 W and the sputtering time was 30 minutes as before. The samples were subsequently annealed at 600°C for 60 seconds in nitrogen. It was found that the dynamics were very similar in all cases, with a slightly faster relaxation time for a substrate temperature of 300°C. The magnitude of the pump-probe signals, along with the carrier dynamics obtained from the measurement, were nearly identical to the trace in figure 5-15 taken at 800 nm. Linear transmission measurements also did not show a significant red shift of the absorption edge. Other researchers have observed growth of InAs nanocrystallites on NaCl single crystal substrates only at temperatures higher than 250°C [250]. This combined with the fact that the substrate temperature may not be accurately known since it was measured far away from the substrate platform may explain the lack of nanocrystallite growth with substrate temperature in our samples.

The doping level of the InAs semiconductor chips was also varied to determine its effect on the saturation fluence; it was possible that doping the semiconductor chips with electrons or holes could saturate some of the conduction or valence band states and therefore make them

unavailable for optical transitions, effectively lowering the saturation fluence. N-type InAs chips with a carrier concentration of 3 x 10^{18} cm^{-3} were glued onto a borosilicate glass target in a 10% InAs/90% glass ratio. Films were deposited on sapphire substrates at a sputtering power of 100 W for 30 min. Pump-probe experiments at 800 nm revealed no significant change in the saturation fluence when compared to the samples made with undoped InAs, implying that the density of states was not a strong factor in determining the saturation fluence. However, it should be noted that the InAs-doping level in the semiconductor chips glued to the target could be different than the doping level in the InAs nanocrystallites within the sputtered films, which would affect these results.

10% InAs/90% SiO_2 films were fabricated and annealed in nitrogen at 600°C for varying times. Pump-probe measurements at 800 nm revealed a roughly continuous increase of the pump-probe signal up to annealing times of 30 seconds, after which the signal saturated and decreased for long annealing times of 1 hour. The relaxation times also became faster as the annealing time increased. This demonstrated that variation of the RTA time did not help lower the saturation fluence. The annealing gas was also varied; RTA in air, oxygen, and forming gas (95% N_2/5% H_2) was demonstrated, with no improvement in the saturation fluence.

A sapphire target was also installed, with the goal of putting a capping layer on the films to prevent material from diffusing out during the RTA process as was observed in previous work [154]; this could also decrease the saturation fluence. Sapphire layers were deposited and their thickness was calibrated with photolithography to determine the deposition rate. The deposition rate was measured to be ~1.5 nm/min at 100 W RF power. A sapphire layer with ~100 nm thickness was deposited on a 10% InAs/90% SiO_2 film grown at 100 W RF power for 30 minutes (~150 nm thickness) on a sapphire substrate, and the structure was annealed in nitrogen for 60 seconds at 600°C. The saturation fluence decreased slightly with the addition of the sapphire cap layer; this decrease was not significant in working towards the goal of developing devices with lower saturation fluence.

5.6 X-ray diffraction measurements on semiconductor-doped silica film saturable absorbers

X-ray diffraction (XRD) measurements were performed on the semiconductor-doped silica film saturable absorbers to determine their crystallinity and its variation with annealing temperature. This is a standard technique used to determine crystallinity and crystallite size for samples such as semiconductor-doped silica films [155, 255, 256]. The nanocrystallites in these films are usually polycrystalline, with several crystalline domains oriented in different directions within each nanocrystallite. The measurements were performed with a Rigaku 185 mm Bragg Brettano diffractometer, with x-rays generated by a Rigaku 18kW rotating anode x-ray generator, both located in the Center for Materials Science and Engineering at MIT. Measurements were done under the guidance of Joseph Adario. The 10% InAs/90% SiO_2 films with linear and nonlinear optical properties previously investigated as functions of RTA temperature (figures 5-13 and 5-19) were measured in x-ray diffraction. The results of these measurements are shown in figure 5-21.

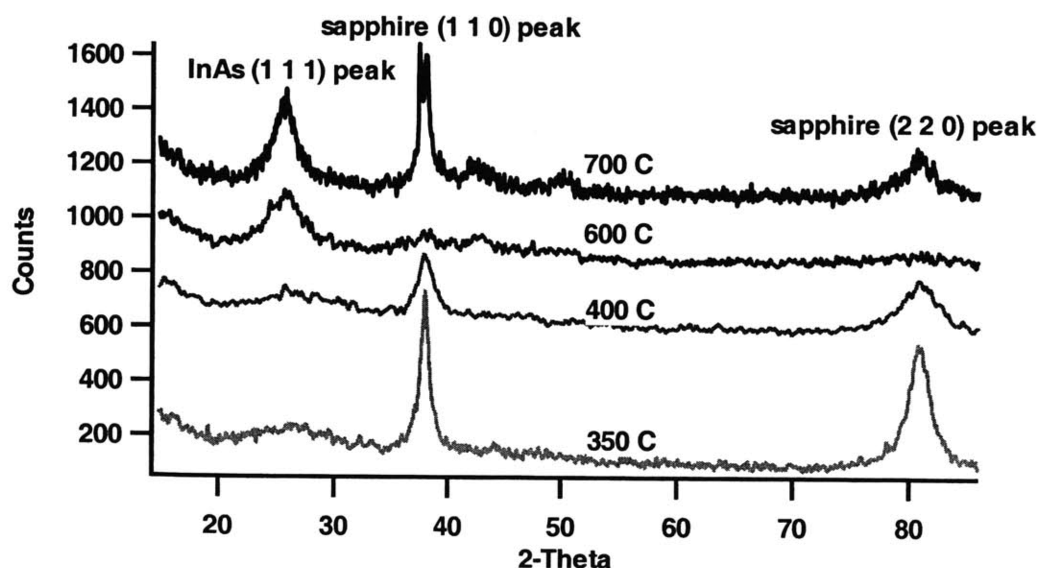

Figure 5-21. X-ray diffraction measurement of 10% InAs/90% SiO_2 films annealed at different temperatures for 60 seconds in nitrogen; the nonlinear optical properties of these films are shown in figure 5-19. The traces are displaced vertically for clarity and the data was smoothed.

From these measurements, several observations can be made. These InAs-doped silica films have a polycrystalline structure as expected, although it is difficult to see more than one peak for the samples annealed at lower temperatures. Although the sapphire substrates were not oriented, two peaks that are most likely due to these substrates is observed in some of the traces. These peaks seemed to be dependent upon the sample orientation in the diffractometer, but could not completely be eliminated for all samples. The width of the InAs (1 1 1) peak narrows with increasing RTA temperature; it is very broad (2θ=7.5° for an RTA temperature of 350°C) for low RTA temperatures and becomes relatively narrow (2θ=1.7° for an RTA temperature of 700°C) at higher annealing temperatures. For the films annealed at 600°C and 700°C, the InAs (2 2 0) and (3 1 1) peaks can faintly be observed. Earlier experiments on thicker films revealed these peaks more clearly. These particular peaks were also observed in previous work describing the fabrication and characterization of RF sputtered semiconductor-doped silica films [155, 254].

The width of the peaks can be related to the average nanocrystallite diameter, D, by

$$D = 0.9\lambda / \beta \cos\theta , \tag{5.29}$$

where λ is the wavelength of the x-ray source (1.54 angstroms with this system) and β is the FWHM of the XRD peak at the angle θ [155, 256]. Using this equation, the average diameter of the nanocrystallites in the InAs-doped films was calculated. At an RTA temperature of 700°C, the nanocrystallite size calculated from the (1 1 1) peak was 10.4 nm, while at an RTA temperature of 350°C, the nanocrystallite size was 2.5 nm. Therefore, this data appears to demonstrate that the nanocrystallite size increases with increasing anneal temperature. However, this should translate into a corresponding shift in the linear absorption edge from equation (5.11). As shown in figure 5-13, the absorption edge is approximately at the same position in all films, without the shift that would be expected from the difference in nanocrystallite size calculated from the XRD data. Therefore, it is likely that the nanocrystallites do not significantly change in size, and other effects influence the broadening of the XRD peaks.

X-ray diffraction measures the crystalline structure of the sample. If the crystalline structure of the sample is mixed or not well-defined, the XRD peaks will appear broadened. For example, in previous work both cubic and hexagonal structures existed in CdSe and CdS films, leading to the broadening of the XRD lines [155]. Imperfections in the crystal lattice and

crystallite anisotropy also lead to line broadening, as does the size distribution of the nanocrystallites (which is large in RF sputtered films) [256]. Equation (5.29), also known as the Scherrer equation, is valid for samples without significant lattice strain or other imperfections, and therefore films grown using RF sputtering, which have a large number of defects and imperfections, may exhibit line broadening in XRD measurements independent of the crystallite size. Another likely mechanism for the narrowing of the XRD peaks is changes in the structure of the polycrystalline grains within each nanocrystallite; the individual grains may grow and change orientation with increase in RTA temperature, narrowing the XRD lines. From these XRD measurements, it can be concluded that increasing the RTA temperature may "anneal out" some of the lattice defects and imperfections in RF sputtered InAs-doped silica films and may also influence the polycrystalline structure within each nanocrystallite, both effects which would makes the XRD lines narrower.

5.7 Fast dephasing times in semiconductor nanocrystallites and their effect on the saturation fluence

The presented experimental data provides a comprehensive characterization of the linear and nonlinear optical properties as well as the structural properties of the InAs-doped silica film saturable absorbers grown by RF sputtering. This data was carefully examined with the goal of understanding the origin of the high saturation fluence in semiconductor-doped silica film saturable absorbers. As previously discussed, the major trends in the data were the reduction of the saturation fluence with operation closer to the absorption edge, increased nanocrystallite size, and increased rapid thermal annealing temperature. The saturation fluence was not strongly affected by n-doping the InAs chips, increasing the substrate temperature, or depositing a sapphire cap layer on the InAs-doped film.

Absorption saturation has previously been linked to the electron-hole recombination time [251]. Larger nanocrystallites were found to have lower saturation fluence in single beam absorption saturation experiments with picosecond pulses. For recombination times shorter than the exciting pulse duration, the saturation intensity is a more appropriate parameter than the

saturation fluence, as described in chapter 2. Since the saturation intensity of the material depends both on the absorption cross-section and the absorption saturation recovery time (from equation (2-34)), shorter recovery times would increase the saturation intensity. Therefore, if the recovery time depended on nanocrystallite size, corresponding changes in the absorption saturation would be observed in the single beam experiments. However, this mechanism would not apply to the data presented in this thesis, since the time resolution of the pump-probe experiments (17-60 fs) is significantly faster than the absorption saturation recovery time (hundreds of fs to several ps).

In previous work, an argument based on the fast polarization dephasing time, T_2, in semiconductor nanocrystallites was proposed to explain the high saturation fluence of the semiconductor-doped silica film saturable absorbers [154]. The dephasing time is given by the temporal duration of the coherent regime that exists for short times after photoexcitation of a semiconductor as described in section 5.2.3. The saturation fluence can be linked to the dephasing time using the following argument. The saturation fluence is given by equation (2.38), re-stated here:

$$\Gamma_{sat} = \frac{h\nu}{\sigma_A} \tag{5.30}$$

where ν is the laser frequency and σ_A is the absorption cross-section. The absorption cross-section for a homogeneously broadened transition can be expressed by

$$\sigma_A(\nu) = \frac{|d|}{\gamma} L(\nu - \nu_0, \gamma) \tag{5.31}$$

where d is the dipole matrix element for the transition, γ is the homogeneous linewidth, and $L(\nu-\nu_0,\gamma)$ is a Lorentzian function normalized to unity at the center frequency ν_0. Finally, the dephasing time T_2 is inversely proportional to γ through the relation

$$\gamma = \frac{2}{T_2}. \tag{5.32}$$

Equations (5.30)-(5.32) can be found in ref. [47]. The combination of these expressions shows that the saturation fluence is inversely proportional to the polarization dephasing time.

Several authors have investigated the dephasing time in semiconductor quantum dots [257-262]. Fast polarization dephasing times of a few fs have been measured in semiconductor-doped glasses using methods based on incoherent light sources [258, 259]. In previous research, the dephasing time of chemically grown small CdSe nanocrystallites was measured using femtosecond photon-echo techniques [260, 261]. These measurements revealed a dependence of the dephasing time on nanocrystallite size and surface quality as well as sample temperature [261]. The dephasing time increased with nanocrystallite size, better surface quality, and lower temperature. The dependence on nanocrystallite size and surface quality was suggested to be due to coupling to surface states and scattering on impurity defect sites at the surface. The surface quality would also depend on the host material for the quantum dots (in this case a polymer matrix). The temperature dependence was due to interaction with phonons. Dephasing times on the order of tens of femtoseconds were measured for these samples, with the fastest time of ~25 fs at a temperature of 240 K. In quantum dots with radii greater than the Bohr radius, carrier-carrier scattering also becomes an important dephasing mechanism since more than one electron-hole pair can be excited per dot [262].

A dependence of the saturation fluence on the nanocrystallite size, annealing temperature (which influences surface quality) and the excitation wavelength relative to the absorption edge was observed in the experiments described in this chapter. This implies that the dephasing time may play a significant role in interpreting these results. RF sputtered semiconductor-doped silica films are expected to have a high density of defects in the sputtered films due to the rough deposition method, resulting in dephasing times even faster that those in semiconductor-doped glasses. This would produce a large amount of surface states and defects, scattering excited carriers and destroying coherence with the incident light field within a few femtoseconds. Annealing at high temperatures reduces the surface defect density of the films, increasing the dephasing time and reducing the saturation fluence as seen in the experiments of section 5.5.6.

The saturation fluence for films doped with larger nanocrystallites would be also less dependent on surface properties due to the lower surface-to-volume ratio and should therefore decrease, matching the experimentally observed trend (section 5.5.5). This can also be viewed by regarding the larger nanocrystallites as having properties approaching the bulk

semiconductor. As described in chapter 3, bulk semiconductors are not suitable for saturable absorber applications since their saturation fluence is too low, necessitating the invention of the A-FPSA [127]. Therefore, larger nanocrystallites would be expected to have optical properties similar to that of the bulk, with lower saturation fluences.

The dephasing time has also been shown to decrease with excitation above the band gap [258] due to the higher kinetic energy of the excited carriers, which agrees with the results of the experiments described in section 5.5.3. Finally, nanocrystallites with increased crystalline order should also have longer dephasing times, which is supported by the XRD measurements on 10% InAs/90% SiO_2 films as a function of RTA temperature that show an increase in crystallinity with RTA temperature, along with the pump-probe data (figures 5-19 and 5-20) demonstrating that the saturation fluence decreases with increasing RTA temperature.

The experimental data described in this chapter consistently support the explanation of the high saturation fluence in InAs-doped silica films by their fast dephasing times. A more direct method of testing this hypothesis would be to measure the dephasing times using four-wave mixing, femtosecond photon echoes, or incoherent light-based techniques while varying fabrication parameters. This would lead to greater understanding of the carrier relaxation and dephasing dynamics in these materials. Spectral hole burning experiments have also been used to measure the dephasing times, as the width of the measured spectral hole is inversely proportional to the dephasing time and is given for an inhomogeneously broadened transition by $\omega_{sh}=3/T_2$, where ω_{sh} is the width of the spectral hole and T_2 is the polarization dephasing time [263]. The wavelength-dependent pump-probe measurements described in section 5.5.3 reinforce the hypothesis that semiconductor-doped silica films grown by RF sputtering have extremely fast dephasing times, since no spectral hole was observed over a wavelength range of 175 nm; i.e., the pump-probe signal was positive between 750 and 925 nm. This corresponds to a maximum dephasing time of 6.3 fs, which is very fast and would lead to a high saturation fluence; the actual dephasing time is probably much shorter since the spectral hole was not resolved in this measurement.

Overall, the fast polarization dephasing time in RF sputtered semiconductor-doped silica film saturable absorbers may be the primary limitation in achieving lower saturation fluences and better self-starting performance. Further reductions in the saturation fluence could be accomplished by increasing the dephasing time of the semiconductor-doped silica films. Hydrogen passivation has been shown to reduce defects in thin films, including polycrystalline superlattices [264], RF sputtered GaAs films [265], and CdSe microcrystallites [266]. This is done by annealing the samples in a hydrogen atmosphere at temperatures of a few hundred degrees Celsius for several hours. The hydrogen fills up (passivates) dangling bonds at the interfaces and thereby reduces defects at the boundary. The absorption saturation increased in passivated CdSe microcrystallites as compared to unpassivated samples [266]. This method could not be tested due to the lack of a suitable system for annealing in a hydrogen atmosphere.

The composition of the glass matrix has also been shown to affect the dephasing time. Weakly confined CdS quantum dots were grown in a borosilicate glass matrix and their dephasing times were measured by nondegenerate four-wave mixing; samples with dephasing times as large as 280 fs at room temperature were fabricated [203, 262]. The experiments presented in section 5.5.3 of this thesis on 10% InAs/90% borosilicate glass films attempted to duplicate those results. The composition of the borosilicate glass used in those experiments was similar to that used in previous work; however, the RF sputtering technique used to deposit the films most likely introduced a large amount of defects into the films, reducing the dephasing time, and therefore no significant improvement in the saturation fluence was observed.

Recently, semiconductor nanocrystallites fabricated by colloidal synthesis have exhibited excellent optical properties, including optical gain and stimulated emission [208, 226]. The size distribution of these samples is very low (~5-15%) with this fabrication technique, allowing quantum confinement effects (such as discrete peaks in the linear absorption spectrum) to be observed. These chemically synthesized strongly confined CdSe and CdS nanoparticles often have an additional layer of ZnS overcoating each quantum dot, which significantly improves their surface properties. These samples would be expected to have a much longer dephasing time than RF sputtered semiconductor-doped silica films, since similar samples were measured to have dephasing times of tens of femtoseconds as described earlier in this section [261]. Large

$\Delta\alpha/\alpha$ signals of ~7×10^{-2} were obtained from these samples in pump-probe experiments, nearly an order of magnitude greater than those obtained for the 10% InAs films measured in this work. This result reinforces the relation between saturation fluence and dephasing time. Therefore, this indicates that the excellent surface properties of colloidally grown nanocrystallites result in a longer dephasing time, which could be important in laser mode-locking applications. Colloidally synthesized samples with PbSe nanocrystallites in a liquid solution were obtained (from J. Steckel in Professor Bawendi's group at MIT), with an absorption peak at 1270 nm. The Cr:forsterite-based pump-probe system was used to measure the samples; however, no signal was detected. This could be due to thermal effects, since the earlier pump-probe experiments were performed with low repetition rate lasers [208, 226]. The absorption peak of the samples could also have been shifted away from the peak of the laser spectrum (~1260 nm), since the sample properties tended to change after a few days. However, chemically synthesized quantum dots incorporated into films have great potential for mode-locking applications and should be further explored.

5.8 Guidelines for the design of non-epitaxially grown semiconductor-doped silica films saturable absorbers

Guidelines were formulated from the experimental results described in this chapter to optimize the saturation fluence of semiconductor-doped silica film saturable absorbers for a given laser system. From comparing figures 5-15 and 5-18, it is apparent that films with larger nanocrystallites have significantly lower saturation fluence than those with smaller nanocrystallites. It is also clear that the films should have an absorption edge close to the laser wavelength, since this also lowers the saturation fluence (figures 5-15 and 5-16). Therefore, the semiconductor material and semiconductor/glass ratio should be chosen to satisfy these two criteria for a certain operating wavelength. Finally, the annealing temperature should be above 550°C for strong absorption saturation based on the results displayed in Figures 5-19 and 5-20; however, the optimum temperature may vary for different semiconductor and glass materials. The carrier relaxation time can also be tailored for a particular application by varying the annealing temperature.

The small nanocrystallites used in the previous work demonstrating self-starting KLM in a Ti:sapphire laser limit the minimum achievable saturation fluence. The guidelines described above can be applied to develop a saturable absorber with lower saturation fluence for mode-locking a Ti:sapphire laser. Operation near the absorption edge can be achieved by changing the semiconductor/glass ratio to experimentally position the absorption edge in the 850-900 nm wavelength range. A semiconductor with a larger bulk band gap than InAs should be chosen (ideally with bulk band gap in the 1000-1500 nm range), such that it would only be weakly quantum confined with large nanocrystallites for operation around 800 nm. Alloys such as $In_xGa_{1-x}As$ could be used to more precisely control the bulk band gap and optimize the absorption edge of the semiconductor-doped silica films. Finally, the glass matrix and RTA temperature should be chosen to optimize the signal measured in pump-probe experiments at 800 nm. These improvements should result in significantly lower saturation fluence, enabling self-starting saturable absorber mode-locking without KLM.

In addition, as previously mentioned, knowledge and control of the film structural properties may be useful in optimizing the properties of semiconductor-doped silica film saturable absorbers by relating structural and optical properties. This may be best accomplished with epitaxial or chemical growth techniques, which allow precise control of the size, shape, surface properties, and size distribution of the quantum dots. Fabrication of samples with well known structural properties and optically characterizing them would yield a significant amount of information on the relationship between structural and optical properties. For example, fabrication and characterization of quantum dots with circular, box-like, or cylindrical shapes could reveal a relationship between the dot shape and the saturation fluence. The remaining challenge would be to devise a method for controlling parameters such as the quantum dot shape with RF sputtering or other simple fabrication techniques to develop an extremely versatile device.

In conclusion, guidelines for designing and fabricating non-epitaxially grown semiconductor-doped silica films with optimized saturation fluence for a given laser system were developed, based on extensive characterization of the linear and nonlinear optical properties of

these devices. A novel pump-probe system with independently tunable pump and probe wavelengths from 700-950 nm was developed for wavelength-dependent device characterization. The saturation fluence was found to be dependent on nanocrystallite size, wavelength of operation relative to the absorption edge, and rapid thermal annealing temperature. Differences in the absorption saturation dynamics for different glass matrix materials were also observed. It was found that films annealed at high temperatures (above 550°C for the samples tested) with large nanocrystallites and an absorption edge near the laser wavelength were optimal for laser mode-locking applications. X-ray diffraction measurements showed an increase in crystallinity with RTA temperature. Finally, a mechanism based on the fast dephasing time in semiconductor-doped silica films was proposed to explain the high saturation fluence in these devices. The guidelines developed in this chapter were applied to the development of a non-epitaxially grown semiconductor saturable absorber for mode-locking a Cr:forsterite laser, to be described in the next chapter.

Chapter 6

Self-starting mode-locking in a Cr:forsterite laser using non-epitaxially grown semiconductor-doped silica films

6.1 Introduction

In the previous chapter, guidelines for designing and fabricating semiconductor-doped silica films saturable absorbers were developed. These guidelines were based on extensive characterization of the linear and nonlinear optical properties of the saturable absorbers while varying parameters such as nanocrystallite size, annealing time and temperature, glass matrix composition, and pump-probe wavelength relative to the absorption edge. It was found that operation close to the absorption edge, large nanocrystallites, and high annealing temperatures were optimum for saturable absorber applications. The next step is to apply these guidelines to develop a saturable absorber for a particular solid-state laser system. Ti:sapphire is the most common solid-state laser system; however, self-starting KLM in this laser with non-epitaxially grown saturable absorbers has already been demonstrated [45]. Although this result could possibly be improved with the knowledge gained from the device characterization results reported in the previous chapter, a more novel application would be to develop a saturable absorber for a different laser system.

In this chapter, non-epitaxially grown semiconductor-doped silica film saturable absorbers for modelocking a Cr:forsterite laser are demonstrated. Section 6.2 describes the Cr:forsterite gain medium. In section 6.3, the design and fabrication of 40% InAs/60% SiO_2 saturable absorber films deposited on sapphire substrates is described. The laser cavity and addition of a second fold for focusing onto the saturable absorber device are discussed in section 6.4. The application of these devices for self-starting KLM in the Cr:forsterite laser, producing

25 fs pulses with 91 nm bandwidth, is described in section 6.5. Saturable absorber mode-locking without KLM is also demonstrated and its intracavity dispersion dependence investigated in this section. Further attempts at reducing the pulse duration are also discussed.

6.2 Cr:forsterite laser system

The Cr:forsterite (Cr:Mg_2SiO_4) laser was chosen for demonstrating the concept of optimizing a non-epitaxially grown saturable absorber for a particular laser system. Cr:forsterite is a well known solid-state laser material tunable from 1130-1367 nm, with a center wavelength around 1260 nm [113]. It has a broad gain bandwidth of over 200 nm (see table 4.1) and has been used to generate pulses as short as 14 fs [91]. The operating wavelength is near the zero dispersion wavelength of ordinary optical fiber, making this an important source for communications. Cr:forsterite also has applications in optical coherence tomography due to its high transmission in tissue [267]. Finally, by frequency doubling the output, the wavelength range previously dominated by dye laser systems can be accessed in an all solid-state system [268].

Lasing was first obtained in Cr:forsterite in 1988 [269]. Cr:forsterite can be pumped by several sources due to its broad absorption band, and lasing has been demonstrated using a pulsed, frequency doubled Nd:YAG laser at 532 nm [269], a cw Ti:sapphire laser at 740 nm [270], and a cw Yb:fiber laser operating at 1053 nm [271] as well as the most commonly used cw Nd:YAG laser at 1064 nm [272]. The latter two pump sources are compact and stable and are easily obtained from many manufacturers. Diode pumping at 980 nm has also been used to demonstrate a compact cw source at 1260 nm [273]. One drawback of Cr:forsterite is its low thermal conductivity, making thermal lensing effects important in cw and mode-locked operation [113, 114, 183]. Low doping of crystals can be used to minimize these effects.

Mode-locked operation of Cr:forsterite was first demonstrated using active mode-locking and synchronous pumping techniques, generating picosecond pulse durations [274]. Kerr lens mode-locking initiated with an acousto-optic modulator was first demonstrated in Cr:forsterite in

1993, generating 60 fs pulses with 85 mW output power [275]. KLM was then demonstrated with no external initiation mechanism [276] and was optimized to generate pulses as short as 25 fs [277]. The shortest pulses of 14 fs were obtained in 2001 [91], with the laser that was modified for use in this work; it will be described in section 6.3. As described in chapter 3, semiconductor saturable absorbers have also been used to mode-lock Cr:forsterite, obtaining self-starting 20 fs pulses with 90 nm bandwidth with the assistance of KLM [43]. Semiconductor-doped silica film saturable absorbers used in a transmissive geometry have no bandwidth limitations other than the saturable absorption itself, and therefore similar pulse durations and bandwidths should be possible with these absorbers as with the previous epitaxially grown semiconductor saturable absorbers.

6.3 Transmissive saturable absorber device design

The guidelines developed in chapter 5 were applied to the design of an absorber for Cr:forsterite. To obtain large nanocrystallites while setting the band edge near 1260 nm, a material with a bulk band gap of ~1700-2000 nm could be chosen. Mild quantum confinement could shift this band edge to ~1300 nm, resulting in large nanocrystallites and operation near the absorption edge. GaSb has a bulk band edge of ~1750 nm [278] and would appear to be suitable for this application. However, in previous work [158] it was shown that sputtered GaSb+SiO_2 films lost their optical quality after annealing, making them unsuitable for laser applications. Other materials considered, such as InSb, PbS, and PbSe all had bulk band gaps comparable to that of InAs [278]. Therefore, since InAs had been extensively studied in this and previous work, it was chosen as the semiconductor dopant.

In chapter 5, experiments characterizing the dependence of the nonlinear optical properties on glass matrix variation were also described, and no significant improvement was observed for annealing temperatures above 550 °C. Therefore, SiO_2 was chosen as the host matrix for the InAs quantum dots, and an annealing temperature of 600 °C was selected. The InAs/SiO_2 ratio was set at 40/60, since this resulted in fairly large nanocrystallites with an absorption edge in the IR (figure 5-12), near the operating wavelength of Cr:forsterite. The

saturation fluence of these films had also been measured at 1.26 μm in pump-probe experiments and found to be 4.05 mJ/cm^2, which should be sufficient for self-starting KLM in Cr:forsterite. Previous experiments with saturable absorbers based on thin wedged colored glass filters mounted on sapphire substrates [153] demonstrated self-starting mode-locking with saturation fluences of 1 mJ/cm^2, comparable to the saturation fluence of the 40% InAs/60% SiO_2 films, and therefore it may be possible to self-start saturable absorber mode-locking without KLM as well.

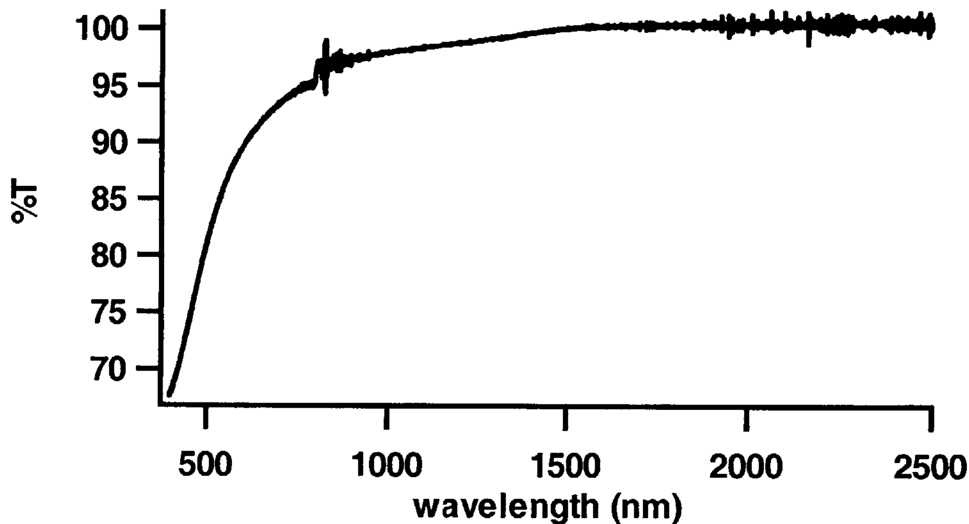

Figure 6-1. Linear transmission of the 40% InAs/60% SiO_2 films used in Cr:forsterite laser mode-locking experiments. The noise near 800 nm is due to a detector change in the Cary spectrophotometer.

InAs-doped silica film saturable absorbers were designed for laser mode-locking experiments at 1.26 μm. 40% InAs/60% SiO_2 films were sputtered at an RF power of 25 W for 30 seconds at an argon pressure of 5 mTorr onto 3 mm thick 0° oriented sapphire substrates. As in the previous work, sapphire was chosen for its high thermal conductivity. Sapphire is a birefringent material and must be oriented correctly to minimize birefringence effects that would destroy mode-locking. The substrates were oriented with the optic axis parallel to the surface normal. The films were annealed at 600 °C for 60 seconds at atmospheric pressure to improve their absorption saturation dynamics. The films had 1% absorption at 1.3 μm; their linear transmission is shown in figure 6-1. The absorption edge of these films is around 1500 nm, close to the lasing wavelength of 1260 nm. The difference in linear transmission curves between these

films and the thicker films used in the pump probe experiments of chapter 5 can be attributed to the growth of some larger nanocrystallites in the thicker films, shifting the absorption edge to longer wavelengths.

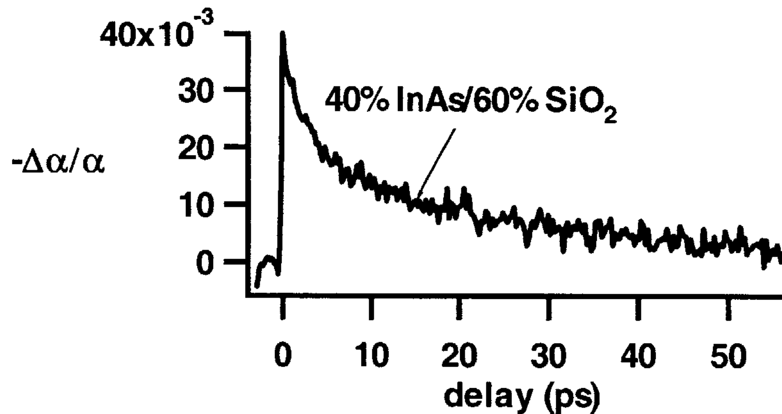

Figure 6-2. Pump-probe measurement at 1.26 μm on a thin 40% InAs/60% SiO_2 film used for mode-locking a Cr:forsterite laser.

The saturation fluence of this film was also measured at 1.26 μm using the Cr:forsterite-based pump-probe system described in chapter 5; the result is shown in figure 6-2. The saturation fluence of this device is calculated to be 1.07 mJ/cm^2 at 1.26 μm. This implies that the saturation fluence decreases with decreasing film thickness, which was an unexpected effect. Experiments exploring this are currently in progress. The carrier relaxation times in this film are also significantly longer than in the thicker film that was examined in figure 5-18. This thin 40% InAs/60% SiO_2 film should work well for self-starting KLM and possibly saturable absorber mode-locking without KLM in Cr:forsterite.

6.4 Laser cavity design

The laser used in these experiments consists of a 5 mm Cr:forsterite crystal with α=2.4 cm^{-1}, pumped by a diode-pumped Nd:YAG laser in a standard z cavity at 100 MHz. Pumping with a Yb:fiber laser was also implemented and did not significantly affect the pulse duration or output power; the results reported in this chapter were obtained with the Nd:YAG pump source.

Broadband double chirped mirrors (DCMs) along with two PBH71 prisms separated by 5 cm were used for dispersion compensation. The reflectivity of the DCMs is shown in figure 6-3 (a), and the dispersion of the Cr:forsterite crystal, PBH71 prisms, and DCMs, along with the total intracavity dispersion, are shown in figure 6-3 (b).

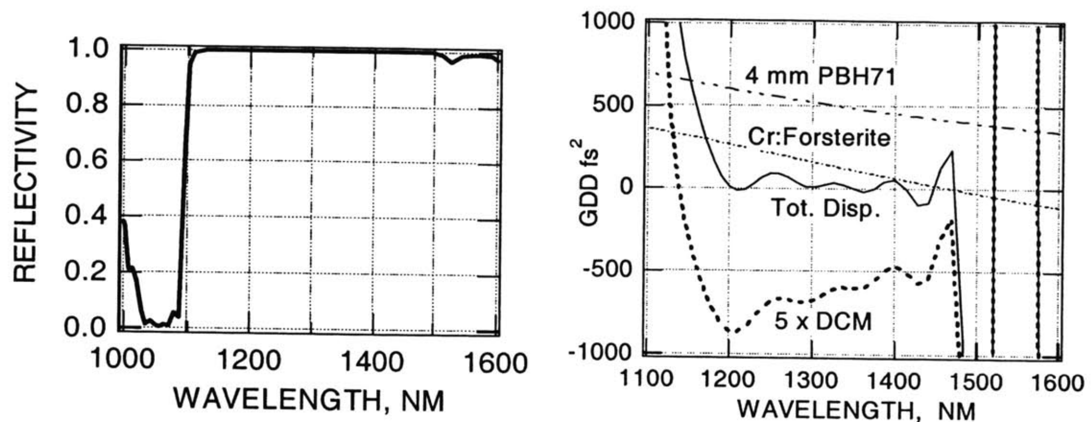

Figure 6-3. (a) Reflectivity of the DCMs used in the Cr:forsterite laser. The reflectivity is greater than 99.8% from 1.1 to 1.5 μm. (b) Group delay dispersion of the Cr:forsterite crystal, PBH71 prisms, and DCMs, plotted with the total intracavity dispersion.

The zero dispersion wavelength of many materials is around 1.3 μm, and therefore higher order dispersion plays a significant role in pulse shaping in Cr:forsterite lasers. The PBH71 prism material was chosen due to its favorable ratio of second to third-order dispersion (about 1) in this wavelength range, enabling a nearly flat total dispersion characteristic with wavelength from 1.2 to 1.4 μm when combined with the DCMs (figure 6-3 (b)). The second prism (P_2) and the end mirror were mounted on a stage to initiate mode-locking. The cavity was purged with nitrogen to remove the effects of water absorption at 1.45 μm, enabling 14 fs pulse generation [91].

In this work, the laser cavity was modified by replacing the DCM high reflector with a second fold consisting of a curved R=5 cm DCM and an R=7.5 cm standard high reflecting end mirror (figure 6-4). The separation of the two mirrors was set for a unity q parameter transformation. The incidence angle on the 5 cm DCM was set to 13 degrees to compensate for the astigmatism introduced by the 3 mm thick sapphire substrate, as calculated from equation (2-52). The DCMs had dispersion characteristics identical to those reported in ref. [91]. The output

coupler (OC) was moved to the prism arm. The saturable absorber was placed at Brewster's angle at the focus of the second fold. The spot size on the saturable absorber was approximately 25 μm; this small spot was necessary due to the relatively high saturation fluence of these devices. The cavity was not purged in initial experiments.

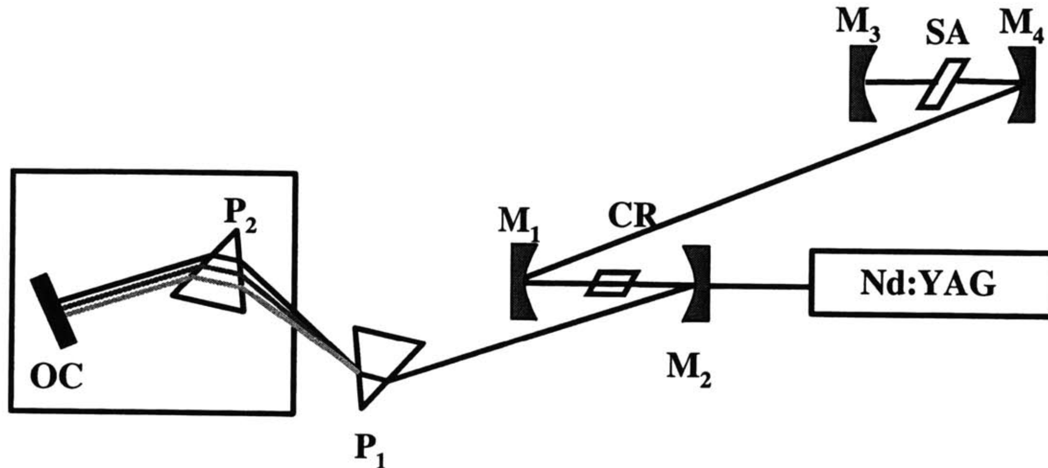

Figure 6-4. Schematic diagram of Cr:forsterite laser with additional fold. CR: crystal; M_1, M_2: 10 cm ROC DCM; M_3: 7.5 cm ROC standard high reflector; M_4: 5 cm ROC DCM; SA: non-epitaxially grown semiconductor saturable absorber; P_1, P_2: PBH71 prisms; OC: 0.5% output coupler.

6.5 Self-starting Kerr lens mode-locking

The laser cavity was first optimized for KLM in a standard 4-mirror cavity configuration with no second fold, with a 1% output coupler in the non-prism arm. The output coupler (OC) and end mirror (HR) positions were then exchanged, and the 1% output coupler was replaced with a 0.5% output coupler to increase the intracavity fluence on the saturable absorber. KLM could not be initiated in this cavity without a saturable absorber since the stage with the second prism (P_2) and output coupler had to be fixed at a prism separation of 5 cm to avoid displacement of the output beam when shaking the stage. Two extracavity DCMs were added after the OC for dispersion compensation. The end mirror was then replaced by the additional cavity fold for

focusing onto the saturable absorber. The crystal was cooled with a Pelltier cooler, and the temperature was set to 0 °C for these experiments.

Initially, a blank sapphire substrate was placed in the saturable absorber position in the second fold to optimize laser operation in this cavity. When the sapphire blank was replaced by an InAs-doped saturable absorber positioned at the focus of the second fold, self-starting mode-locking without KLM was obtained. With optimization of the intracavity dispersion and mirror separations, self-starting KLM was obtained. Pulse durations were measured using interferometric autocorrelation with a 100 μm thick BBO crystal. The shortest pulse duration was 25 fs with a bandwidth of 91 nm as shown in figure 6-5. The time-bandwidth product was 0.408. The pulses are not transform-limited, probably due to excess self-phase modulation (SPM) and uncompensated higher order dispersion from the sapphire substrate.

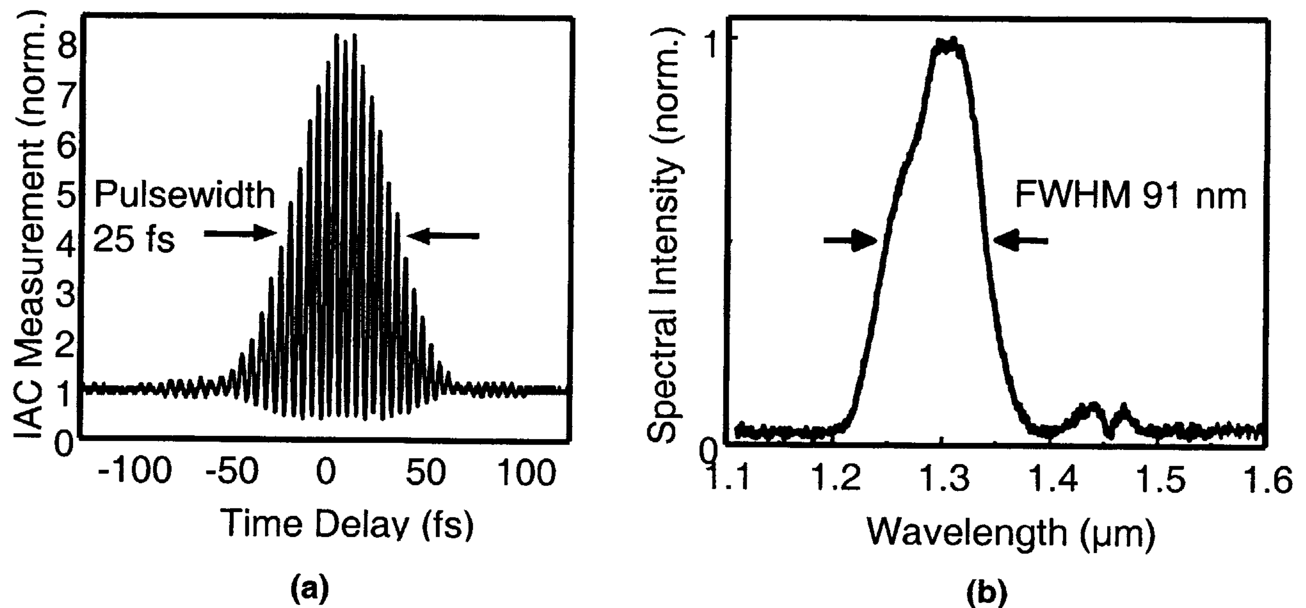

Figure 6-5. Interferometric autocorrelation (a) and spectrum (b) of self-starting KLM in Cr:forsterite using non-epitaxially grown InAs-doped silica films. Self-starting 25 fs pulses with a bandwidth of 91 nm were generated.

Self-starting KLM operation was maintained while the saturable absorber position was varied over approximately 1 mm. This emphasizes the low saturation fluence of this device, since self-starting was relatively insensitive to the focused spot size on the absorber. The

threshold for cw lasing was 4.2 W. Self-starting KLM was obtained at 4.4 W pump, with 37 mW mode-locked output power obtained at the maximum pump power of 4.8 W.

Another measure of the saturable absorber performance is the mode-locking build-up time. From equation (2-35) and the accompanying discussion, lower saturation fluences lead to faster mode-locking build-up times. The mode-locking build-up time in the previous work on self-starting KLM in a Ti:sapphire laser was relatively slow, on the order of 50 ms. In this work, it was measured by chopping the pump beam and observing the output on a fast photodiode. Mode-locking build-up times (MLB) as fast as 4.8 ms were measured, supporting the order of magnitude reduction in saturation fluence measured in pump probe experiments.

Experiments were also performed to investigate the use of the InAs-doped films for pure saturable absorber mode-locking without KLM. The laser was set to operate in a part of the stability region where KLM did not occur. Self-starting saturable absorber mode-locking was obtained; however, intensity autocorrelations showed that the output consisted of a short pulse with a long background pulse. This can be explained using equations (2.24) and (2.25), restated here:

$$\tau_{FWHM} = 1.76 \cdot \frac{4|D|}{\delta E_p}, \tag{6.1}$$

defining the pulsewidth τ for a given net intracavity group delay dispersion D, pulse energy E_p, and δ, the SPM coefficient for the Cr:forsterite crystal, and

$$\frac{D_g}{\tau^2} < 2q_0 \tag{6.2}$$

the pulse stability condition, with q_0 the saturable absorber modulation depth and D_g the gain dispersion.

The width of the shorter soliton-like pulse is fixed by the cavity parameters in (2.24); however, from the stability condition (2.25), the low modulation depth of the saturable absorber devices cannot support such a short pulse. The short pulse sheds energy to a cw background that develops into a longer background pulse with a duration set by the recovery time of the saturable

absorber. To stabilize the short pulse, the dispersion could be increased, which would make the soliton-like pulse longer but eliminate the background pulse.

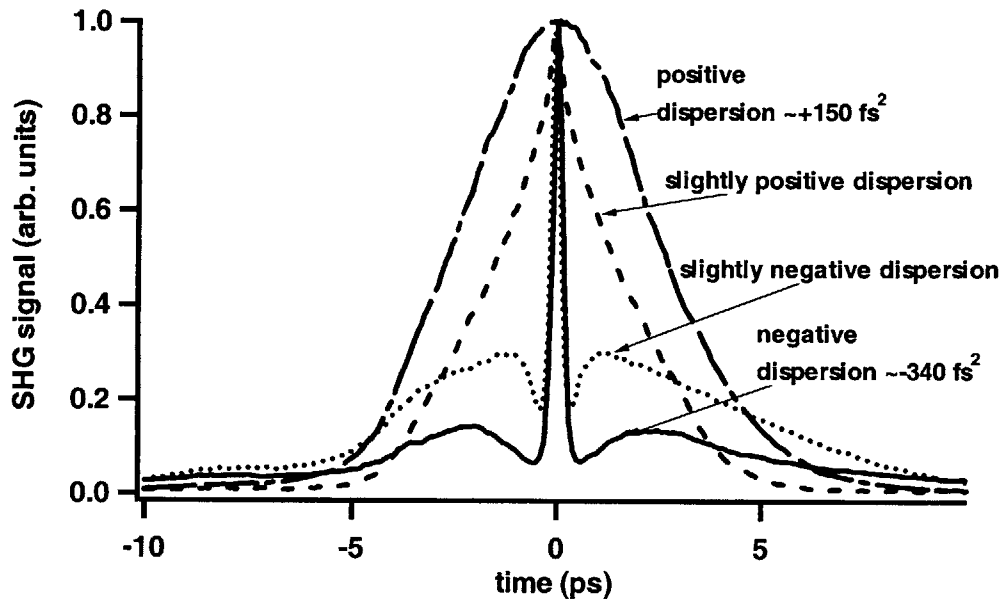

Figure 6-6. Intensity autocorrelations at different dispersion operating points for saturable absorber mode-locking without KLM. The peak intensity of the longer background pulse decreases as the negative dispersion increases.

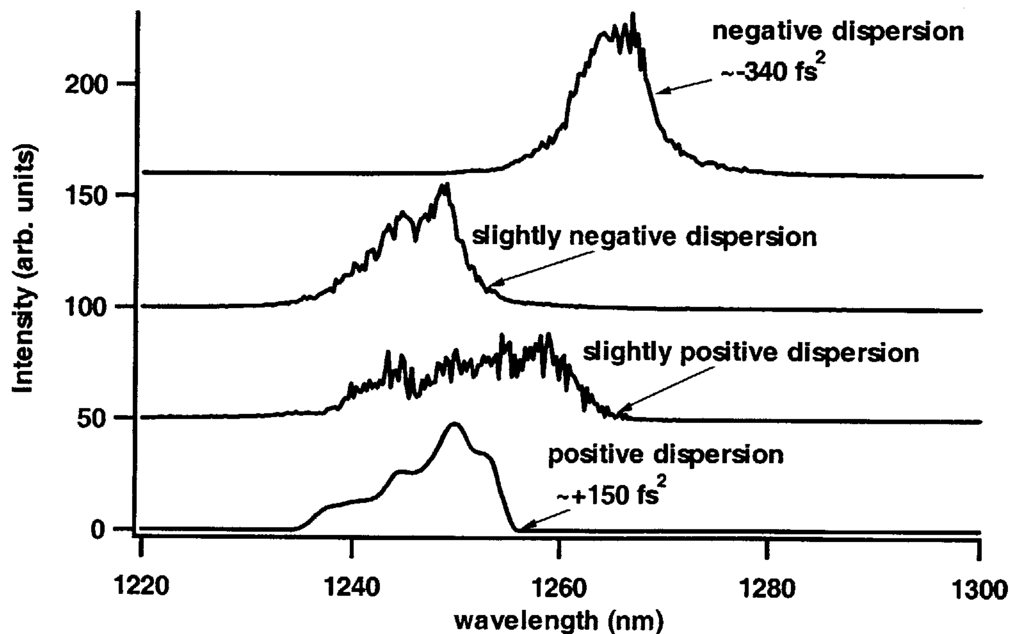

Figure 6-7. Spectra at different dispersion operating points for saturable absorber mode-locking without KLM.

Autocorrelation measurements of the pulses for different intracavity dispersion operating points agree with theoretical expectations (figure 6-6). The corresponding spectra are shown in figure 6-7. For small positive dispersions, a long pulse with 5.3 ps duration is generated. The corresponding spectrum has a bandwidth of 11 nm and the pulse is strongly chirped. As the intracavity dispersion is made increasingly negative, a short soliton-like pulse of ~150 fs duration is generated with a longer background pulse. For more negative values of dispersion, the intensity of the longer background pulse decreases and the spectrum shifts to longer wavelengths. Pulse shaping would be improved if the saturable absorber saturation fluence was reduced, modulation depth was increased, or the relaxation dynamics were made faster. In this experiment, increasing the prism separation and decreasing the prism insertion would add more negative dispersion and eliminate the background pulse. However, due to table space constraints, the prism separation could not be increased beyond 8 cm, and the background pulse could not be completely eliminated.

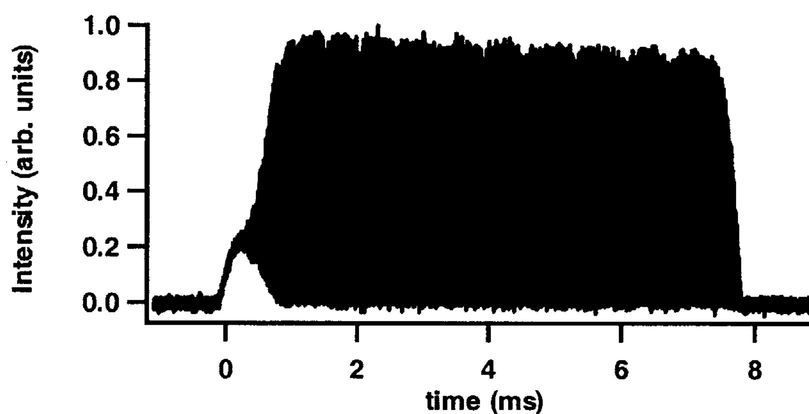

Figure 6-8. Measured mode-locking build-up time for pure saturable absorber mode-locking with large negative dispersion. The MLB is the time from zero to the peak intensity.

The mode-locking build-up time was also measured for pure saturable absorber mode-locking in large negative dispersion (figure 6-8). The pump beam was chopped at 63 Hz and the output was detected with a fast photodiode. The MLB was approximately 1 ms in this configuration, faster than that with KLM, although a small background pulse still existed.

Subsequent experiments attempted to reduce the pulse duration from this laser system by purging the cavity with nitrogen to remove the effects of water absorption at 1.45 μm. In the previous experiments demonstrating 14 fs pulse generation [91], this increased the spectral bandwidth from 90 nm to 250 nm after optimization of the laser cavity. Since the only bandwidth limitation of the InAs-doped silica film saturable absorbers when used in a transmissive geometry is the increasing absorption on the short wavelength side of the spectrum, it was expected that this would increase the bandwidth of the self-starting Cr:forsterite laser.

The cavity was enclosed and purged with nitrogen at a very low pressure of <5 psi, to avoid disturbing mode-locking by introducing turbulence due to the nitrogen flow into the beam path. However, when the cavity was optimized for self-starting mode-locking with the InAs-doped silica films, no improvement in the spectrum was observed. This can most likely be explained by the inability to fine tune the dispersion by changing the prism separation. When operating in the four mirror cavity, the mode-locked spectrum was very sensitive to the prism separation. The prism separation and insertion introduce GDD, as well as third order dispersion and other higher order dispersion terms. It was experimentally observed in the four mirror cavity that insertion or deinsertion of the prisms into the beam was not sufficient for generating the broadest spectrum; control of the prism separation was also critical to obtain the shortest pulses. When a saturable absorber was used, the prism separation was fixed and could not be adjusted. Therefore, this critical parameter could not be used to fine tune the dispersion operating point, limiting generation of the shortest pulses. In later work, it was found that the InAs-doped silica film saturable absorbers could support bandwidths of ~130 nm in a cavity with optimized dispersion [279], supporting this argument.

In conclusion, non-epitaxially grown InAs-doped silica films were demonstrated for self-starting mode-locking in Cr:forsterite lasers [280]. The guidelines developed in the previous chapter were applied to create saturable absorbers suitable for mode-locking Cr:forsterite. Almost a one order of magnitude reduction of the saturation fluence was achieved compared to previous work. The saturable absorber films were used to self-start KLM in Cr:forsterite, generating 25 fs pulses with 91 nm bandwidth. Finally, saturable absorber mode-locking without KLM was demonstrated and its dependence on dispersion examined. These results demonstrate

the ability to design, fabricate, and apply non-epitaxially grown saturable absorbers to self-start mode-locking in a variety of laser systems. The versatility and ease of fabrication of these devices make non-epitaxially grown semiconductor films very promising for short pulse generation.

Chapter 7
Conclusion

This thesis has reported on the development and application of both epitaxially and non-epitaxially grown saturable absorbers for femtosecond solid-state laser mode-locking. The two major thrusts of this research were the use of an epitaxially grown saturable Bragg reflector (SBR) to mode-locking an extended cavity Cr:LiSAF laser pumped by inexpensive single mode diodes and the further development and application to laser mode-locking of non-epitaxially grown semiconductor-doped silica film saturable absorbers.

An extended cavity Cr:LiSAF laser pumped by inexpensive single mode diodes and mode-locked with an SBR was developed to provide an inexpensive source of femtosecond pulses with pulse energies and durations comparable to those from standard Ti:sapphire lasers. The diode pump source was designed and implemented, producing 137 mW pump power at the crystal position. A four mirror cavity design was developed to test the diode pump source, generating 28.5 mW cw power from the Cr:LiSAF laser. A multi-pass cavity was designed and introduced into the laser cavity to increase pulse energies and an SBR was used as the mode-locking mechanism. Using prisms for dispersion compensation, 43 fs pulses with 18.5 nm bandwidth were produced at an 8.4 MHz repetition rate. The pulse energy was 0.66 nJ in this configuration. In a prismless cavity, the laser generated 39 fs pulses with 20 nm bandwidth. The repetition rate was 8.6 MHz and the pulse energy was 0.75 nJ. Slope efficiencies up to 12.8% were measured, indicating that laser output powers can be scaled to higher output powers and pulse energies as higher power pump diodes become available. This low cost source of femtosecond pulses generates pulse energies and durations that will make it a cost-effective alternative to standard Ti:sapphire lasers in many applications.

The drawbacks associated with epitaxially grown saturable absorbers motivated the further development of semiconductor-doped silica films grown by RF sputtering, which had

previously been used to self-start Kerr lens mode-locking (KLM) in a Ti:sapphire laser but had a high saturation fluence, limiting device performance in some applications. A novel pump-probe system with independent pump and probe wavelength tunability from 700-1000 nm based on a 5.5 fs Ti:sapphire laser was developed for device characterization as a function of wavelength, with the goal of discovering trends that would aid in reducing the saturation fluence. A minimum time resolution of 17 fs was demonstrated for a laser bandwidth of 250 nm. Pump-probe experiments were performed to measure the saturation fluence as a function of fabrication and characterization parameters, including nanocrystallite size, rapid thermal annealing (RTA) temperature, and pump and probe wavelengths relative to the absorption edge of the films. Films with different glass matrix compositions were also investigated to understand the dependence of the measured pump-probe signal on RTA temperature. X-ray diffraction measurements were performed as a function of RTA temperature to examine the structural properties of the films. From these experiments, it was found that films with larger nanocrystallites, RTA temperatures greater than 550°C, and absorption edges near the lasing wavelength exhibited the lowest saturation fluences. These trends could be explained by the fast exciton dephasing time in these semiconductor-doped silica films grown by RF sputtering. Saturation fluences as low as 640 $\mu J/cm^2$ were achieved at 1.54 μm using 40% InAs/60% SiO_2 films deposited on a sapphire substrate and annealed in nitrogen at 600°C for 60 seconds.

Based on these results, InAs-doped silica films grown by RF sputtering were designed for use in a Cr:forsterite laser. The saturation fluence of these 40% InAs/60% SiO_2 films was measured by pump-probe experiments to be 1.07 mJ/cm^2 at 1.26 μm. These films were used in a transmissive geometry to self-start KLM in a Cr:forsterite laser, producing 25 fs pulses with 91 nm bandwidth. The use of these devices to self-start saturable absorber mode-locking without KLM was also investigated, and it was found that the low modulation depth and insufficient negative dispersion limited ultrashort pulse generation.

Many directions can be explored in extending this research. As stated in chapter 4, the performance of the Cr:LiSAF laser can be improved in several ways. The SBR design could be modified to increase the reflectivity bandwidth and also the magnitude of the reflectivity. The saturable loss could also be increased while decreasing the non-saturable loss. Recent work has

demonstrated a monolithically integrated broad bandwidth SBR used to self-start mode-locking in a Cr:forsterite laser, generating 30 fs pulses [281]. Applying this technology to the Cr:LiSAF laser should improve the pulse duration and output pulse energy, generating sub-20 fs pulses. The MPC mirror design could also be modified to be more suitable for Cr:LiSAF, since these mirrors were originally designed for Ti:sapphire lasers. Improvements in the mirror reflectivity and bandwidth would increase the output pulse energy and decrease the pulse duration. This would enable more compact laser designs, as currently the mirrors must be separated by 2 meters since more than 4 bounces on each mirror in a single pass introduces too much loss into the cavity for efficient mode-locked operation. Designs similar to those demonstrated in reference [282] could be used, resulting in a compact femtosecond source with pulse energies and durations comparable to Ti:sapphire. It is expected that higher power single spatial mode pump diodes should become available soon, and the use of these diodes will also improve pulse energies and output powers from the Cr:LiSAF laser. This may also enable KLM in the Cr:LiSAF laser without an SBR, which should lead to sub-20 fs pulse durations with appropriate dispersion compensation. Another possibility would be to pump the laser crystal from both sides with two diode pump sources, increasing the pump power by a factor of 2. Finally, a second fold to focus onto a material with high nonlinearity could be added to the cavity for additional self-phase modulation, and in combination with a hard aperture could also provide a mode-locking mechanism.

Several applications can be conceived for the extended cavity Cr:LiSAF laser in its current form. The pulse energies of 0.75 nJ, comparable to those from the 5.5 fs Ti:sapphire laser used for the pump-probe experiments described in chapter 5, would enable pump-probe experiments at 860 nm using this source, which may not have been possible with previous single mode diode-pumped Cr:LiSAF systems. The low repetition rate would also reduce thermal effects that often influence the results of experiments performed using higher repetition rate sources. In addition, this source could be used for efficient terahertz wave generation using a PPLN crystal [283] or a dipole antenna consisting of metal lines deposited on GaAs [4]. The extended cavity Cr:LiSAF laser would be a good seed oscillator for amplified systems, either in a Cr:LiSAF-based amplified system similar to that in ref. [284] or to replace an expensive solid-state or argon-pumped Ti:sapphire oscillator. The factor of ~5 increase in pulse energy over

other single mode diode-pumped systems would reduce the amplification required in later stages and thereby reduce the cost and complexity of the overall system.

The Cr:LiSAF laser could also be used in a four mirror cavity, mode-locked with the SBR to generate ~40 fs pulses with 20 nm bandwidth, in several applications such as white light generation with a photonic crystal fiber [184], optical communications [285] and optical analog to digital conversion [10]. The shorter pulse durations demonstrated here may offer performance advantages in these applications when compared to previous single mode diode-pumped Cr:LiSAF lasers.

The guidelines developed in this thesis for designing semiconductor-doped silica film saturable absorbers can be applied to design a saturable absorber for any laser system. Careful choice of the semiconductor and glass materials, along with the RTA temperature, to produce a film with large nanocrystallites having good surface quality and an absorption edge near the lasing wavelength should produce semiconductor-doped silica films with low saturation fluence. An obvious extension of this research would be to apply a 40% InAs/60% SiO_2 film to self-starting mode-locking, with and without KLM, in a Cr:YAG laser. The low saturation fluence in these films at 1.54 μm should enable mode-locking without KLM. Devices could subsequently be designed to mode-lock other laser systems, including Nd:YLF and Nd:YAG, although these lasers would only generate picosecond pulses due to their limited gain bandwidths. With an appropriate choice of semiconductor, saturable absorbers could be designed to mode-lock the Cr:LiSAF laser developed as part of this thesis, overcoming the bandwidth limitation of the epitaxially grown SBR used for mode-locking.

Several other avenues of research remain to be explored with semiconductor-doped silica films. Previous attempts at incorporating these films into a reflective mirror structure were only marginally successful, increasing KLM stability in a Ti:sapphire laser but without self-starting KLM [158]. It would be worthwhile to explore this further and understand why these devices did not self-start KLM, since calculations indicated that they should have lower saturation fluence than transmissive devices. The problems with these devices were most likely due to imperfections in the growth process, and therefore the use of a magnetron sputtering system may

overcome those difficulties. The ability to decrease the saturation fluence, demonstrated in this work, would also improve the performance of these reflective saturable absorbers. Devices could also be incorporated into dielectric mirror structures such as double-chirped mirrors, enabling dispersion compensation and saturable absorption in a single broad bandwidth structure.

Further experiments could be performed to measure the dephasing times in semiconductor-doped silica films by four-wave mixing or incoherent light-based techniques. This would establish a clear connection between the saturation fluence and dephasing time. As suggested in chapter 5, the use of other growth techniques for quantum dot-based saturable absorbers, such as epitaxial or chemical growth, may improve performance due to the better surface properties and expected longer dephasing times in these devices. The ability to control the quantum dot structural properties with these fabrication techniques and relate them to the optical properties may also yield insight into the optimization of these devices. Although these fabrication techniques are much more complex than RF sputtering, the versatility of quantum dot-based devices could still lead to improvements over quantum well-based saturable absorbers. Devices based on quantum wires, such as carbon nanotubes or oxide nanowires, could also be considered in the further development of semiconductor saturable absorbers.

Techniques such as hydrogen passivation for increasing the dephasing time by improving the nanocrystallite surface properties could also be explored. Some possibilities include incorporating the InAs nanocrystallites into a semiconductor matrix such as GaAs; this could improve the surface properties of the nanocrystallites through pseudo-lattice matching between the InAs dots and GaAs matrix, since the lattice constants of the materials are similar. These devices would only work at wavelengths greater than ~1 μm due to absorption in the GaAs matrix. Other materials without absorption at the lasing wavelength could be doped into the films in the hope of modifying the surface properties of the nanocrystallites. Another possibility would be to use an RF sputtering system capable of increasing substrate temperatures above 300°C, which could increase the crystallinity of the nanocrystallites and thereby increase the dephasing times. Finally, lasers mode-locked with non-epitaxially grown semiconductor-doped silica film saturable absorbers would provide a stable, self-starting source of ultrashort laser pulses for many of the applications listed in the introduction.

The future development and application of semiconductor saturable absorbers to femtosecond solid-state laser mode-locking appears extremely promising. Lasers mode-locked with semiconductor saturable absorbers are already commercially available. With the fast pace of improvements in this field, reliable, self-starting ultrashort pulsed lasers should be a valuable tool in many fields of research for years to come.

Appendix A

RF sputtering procedure

This appendix describes the procedure for deposition of a thin film using the Denton Discovery 18 magnetron RF sputtering system.

Substrate preparation:

1. Rinse the substrate with acetone, methanol, and deionized water in that order.
2. Dry the substrate with an air dryer, let dry for several minutes.

Loading the samples into the system:

3. Vent the loadlock using the automatic venting procedure, making sure the gate valve is closed and the chamber is under high vacuum (~10^{-7} Torr).
4. Remove the loadlock cover and load the substrates on the substrate platform.
5. Close the loadlock cover.
6. Start the automatic loadlock pump procedure; this pumps the loadlock down to a pressure of ~10^{-4} Torr and subsequently starts the automatic chamber pump procedure.
7. Once the chamber pump procedure has started, open the gate valve.
8. Manually advance the substrate platform into the chamber, making sure the platform is in the "UP" position.
9. Once the substrate platform is fully advanced into the chamber, bring the substrate platform to the "DOWN" position.
10. Retract the platform holding claw from the chamber.
11. Close the gate valve and wait until the chamber is pumped down to a pressure below 10^{-6} Torr (the deposition runs described in this thesis were typically done at $5x10^{-7}$ Torr).

Sputtering system preparation:

12. Make sure the system cooling water is turned on and the argon gas pressure in the supply tank is set to ~10-20 psi.

13. Turn on the RF power controller.
14. Set the argon flow to the desired value (typically 55-60 sccm for a pressure of 5.15-5.2 x 10^{-3} Torr) and make sure the controller is turned on and reading zero.
15. Set the substrate temperature to the desired value (if the substrate heater is being used).
16. Set the substrate platform rotation speed to the desired value.
17. Make sure the shutter is closed on the target to be sputtered.
18. Turn the substrate rotation on.
19. Turn the substrate temperature on if that option is being used.

Target cleaning (pre-sputtering the target with the shutter closed to remove impurities from the target surface):

20. Turn on the RF power and wait for the automatic matching network to reduce the reflected power to zero.
21. Turn the argon gas on and watch for the plasma to ignite.
22. If the plasma does not ignite, turn the RF power off and turn the gas flow off. Wait for the chamber pressure to go below ~10^{-5} Torr. Open the shutter, turn on the RF power, and turn on the argon gas again. As soon as the plasma ignites, close the shutter.
23. Wait 10 minutes to ensure a clean target surface.

Film deposition:

24. Open the shutter.
25. Wait for the desired time duration of the sputtering run, monitoring the argon flow and pressure (pressure should be 5.15-5.2 x 10^{-3} Torr).
26. Close the shutter.
27. Turn off the RF power.
28. Turn off the argon gas.
29. Turn off the substrate heater and substrate platform rotation.
30. Wait for the chamber pressure to drop below 10^{-5} Torr.

Sample removal:

31. Open the gate valve.

32. Manually advance the platform holding claw into the chamber, making sure that the claw is in the "DOWN" position.
33. Once the platform holding claw is fully advanced into the chamber, bring the holding claw to the "UP"position.
34. Retract the substrate platform from the chamber.
35. Once the platform is fully removed from the chamber, close the gate valve.
36. Vent the loadlock using the automatic loadlock venting procedure.
37. Remove the loadlock cover.
38. Remove the samples from the loadlock.
39. Close the loadlock cover.
40. Start the automatic loadlock pumping procedure, which should lead to the automatic chamber pumping routine and return the chamber to high vacuum.

Appendix B

Optics used in the Cr:LiSAF laser

Standard commercially available mirrors:

Manufacturer	Mirror	Diameter	Radius	Reflectivity
Alpine Research Optics (ARO)	M1, M2	1”	10 cm	High reflector
Alpine Research Optics (ARO)	DM, HR, M3, M4	1”	Plane	High reflector
Layertec	M10	0.5”	20 cm	High reflector
CVI	OC	1”	Plane	R=99%

Double chirped mirrors (designed by Dr. Uwe Morgner and Professor Franz Kaertner, and fabricated by V. Scheuer):

Mirror	Diameter	Radius	Reflectivity
M1	0.5”	10 cm	High reflector
M3, M4, M5, M9	0.5”	Plane	High reflector
M6	1.5”	Plane	High reflector
M7	1.5”	4 m	High reflector
M8	0.25”	4 m	High reflector

Other optics:

CR-3 x 3 x 5 mm optical path length Cr:LiSAF crystal, 1.5% doping, obtained from VLOC corporation

PR1, PR2-Fused silica prisms, 1” high, from CVI

P1-Uncoated diverging lens, 2" diameter, R=-100 mm

P2-AR coated achromatic lens (400-700 nm), 0.5" diameter, R=76.3 mm

PBS-Polarizing beam splitter, 1" square

WP-$\lambda/2$ wave plate, AR coated (670 nm)

References

1. R. W. Schoenlein, S. Chattopadhyay, H. H. W. Chong, T. E. Glover, P. A. Heimann, C. V. Shank, A. A. Zholents and M. S. Zolotorev, "Generation of femtosecond pulses of synchrotron radiation", *Science,* **287**, 2237, 2000.

2. C. W. Siders, A. Cavalleri, K. Sokolowski-Tinten, C. Toth, T. Guo, M. Kammler, M. Horn von Hoegen, K. R. Wilson, D. von der Linde and C. P. J. Barty, "Detection of non-thermal melting by ultrafast x-ray diffraction", *Science,* **286**, 1340, 1999.

3. A. Rundquist, C. G. Durfee III, Z. Chang, C. Herne, S. Backus, M. Murnane and H. C. Kapteyn, "Phase-matched generation of coherent soft x-rays", *Science,* **280**, 1412, 1998.

4. D. M. Mittleman, R. H. Jacobsen and M. C. Nuss, "T-ray imaging", *IEEE J. Sel. Top. Quant. Elect.,* **2**, 679, 1996.

5. S. T. Cundiff, J. Ye and J. L. Hall, "Optical frequency synthesis based on mode-locked lasers", *Rev. Sci. Inst.,* **72**, 3749, 2001.

6. D. J. Jones, S. A. Diddams, J. K. Ranka, A. Stentz, R. S. Windeler, J. L. Hall and S. I. Cundiff, "Carrier-envelope phase control of femtosecond mode-locked lasers and direct optical frequency synthesis", *Science,* **288**, 635, 2000.

7. D. Huang, E. A. Swanson, C. P. Lin, J. S. Schuman, W. G. Stinson, W. Chang, M. R. Hee, T. Flotte, K. Gregory, C. A. Puliafito and F. J.G., "Optical coherence tomography", *Science,* **254**, 1178, 1991.

8. W. Drexler, U. Morgner, F. X. Kaertner, C. Pitris, S. A. Boppart, X. D. Li, E. P. Ippen and J. G. Fujimoto, "In vivo ultrahigh resolution optical coherence tomography", *Opt. Lett.,* **24**, 1221, 1999.

9. M. C. Nuss, W. H. Knox and U. Koren, "Scalable 32 channel chirped-pulse WDM source", *Elect. Lett.,* **32**, 1311, 1996.

10. P. W. Juodawlkis, J. C. Twichell, G. E. Betts, J. J. Hargreaves, R. D. Younger, J. L. Wasserman, F. J. O'Donnell, K. G. Ray and R. C. Williamson, "Optically sampled analog-to-digital converters", *IEEE Trans. Microwave Theory and Tech.,* **49**, 1840, 2001.

11. D. S. Chemla and J. Shah, "Ultrafast dynamics of many-body processes and fundamental quantum mechanical phenomena in semiconductors", *Proc. Natl. Acad. Sci.,* **97**, 2437, 2000.

12. H. Rabitz, R. de Vivie-Riedle and K. Kompa, "Whither the future of controlling quantum phenomena?" *Science,* **288**, 824, 2000.

13. A. Baltuska, T. Udem, M. Uiberacker, M. Hentschel, E. Goulielmakis, C. Gohle, R. Holzwarth, V. S. Yakovlev, A. Scrinzi, T. W. Hansch and F. Krausz, "Attosecond control of electronic processes by intense light fields", *Nature,* **421**, 611, 2003.

14. P. M. Paul, E. S. Toma, P. Breger, G. Mullot, F. Auge, P. Balcou, H. G. Muller and P. Agostini, "Observation of a train of attosecond pulses from high harmonic generation", *Science,* **292**, 1689, 2001.

15. M. Hentschel, R. Kienberger, C. Spielmann, G. A. Reider, N. Milosevic, T. Brabec, P. Corkum, U. Heinzmann, M. Drescher and F. Krausz, "Attosecond metrology", *Nature,* **414**, 509, 2001.

16. M. Drescher, M. Hentschel, R. Kienberger, G. Tempea, C. Spielmann, G. A. Reider, P. Corkum and F. Krausz, "X-ray pulses approaching the attosecond frontier", *Science,* **291**, 1923, 2001.

17. R. Ell, U. Morgner, F. X. Kärtner, J. G. Fujimoto, E. P. Ippen, V. Scheuer, G. Angelow and T. Tschudi, "Generation of 5 fs pulses and octave-spanning spectra directly from a Ti:sapphire laser", *Opt. Lett.,* 2001.

18. G. Mourou and D. Umstader, "Extreme light", *Scientific American*, 81, 2002.

19. A. L. Schawlow and C. H. Townes, "Infrared and optical masers", *Phys. Rev.,* **112**, 1940, 1958.

20. T. H. Maiman, "Stimulated optical radiation in ruby", *Nature,* **187**, 493, 1960.

21. L. E. Hargrove, R. L. Fork and M. A. Pollack, "Locking of He-Ne laser modes induced by synchronous intracavity modulation", *Appl. Phys. Lett.,* **5**, 4, 1964.

22. A. J. DeMaria, D. A. Stetser and H. Heynau, "Self mode-locking of lasers with saturable absorbers", *Appl. Phys. Lett.,* **8**, 174, 1966.

23. H. W. Mocker and R. J. Collins, "Mode competition and self-locking effects in a Q-switched ruby laser", *Appl. Phys. Lett.,* **7**, 270, 1965.

24. E. P. Ippen, C. V. Shank and A. Dienes, "Passive modelocking of the cw dye laser", *Appl. Phys. Lett.,* **21**, 348, 1972.

25. C. V. Shank and E. P. Ippen, "Subpicosecond kilowatt pulses from a modelocked cw dye laser", *Appl. Phys. Lett.,* **24**, 373, 1974.

26. R. L. Fork, C. H. B. Cruz, P. C. Becker and C. V. Shank, "Compression of optical pulses to six femtoseconds by using cubic phase compensation", *Opt. Lett.,* **12**, 483, 1987.

27. P. F. Moulton. Ti-doped sapphire: tunable solid-state laser. *Optics News* **Nov./Dec.**, 9 (1982).

28. P. F. Moulton, "Spectroscopic and laser characteristics of Ti:Al_2O_3", *J. Opt. Soc. Am. B,* **3**, 125, 1986.

29. D. E. Spence, P. N. Kean and W. Sibbett, "60-fsec pulse generation from a self-mode-locked Ti:Sapphire laser", *Opt. Lett.,* **16**, 42, 1991.

30. M. Nisoli, S. De Silvestri, O. Svelto, R. Szipöcs, K. Ferenz, C. Spielmann, S. Sartania and F. Krausz, "Compression of high energy laser pulses below 5 fs", *Opt. Lett.,* **22**, 522, 1997.

31. A. Baltuska, Z. Wei, M. S. Pshenichnikov and D. A. Wiersma, "Optical pulse compression to 5 fs at 1 MHz repetition rate", *Opt. Lett.,* **22**, 102, 1997.

32. C. G. Durfee III, A. Rundquist, S. Backus, C. Herne, M. Murnane and H. C. Kapteyn, "Phase matching of high-order harmonics in hollow waveguides", *Phys Rev. Lett.,* **83**, 2187, 1999.

33. P. B. Corkum, "Above-threshold ionization in the long-wavelength limit", *Phys Rev. Lett.,* **62**, 1259, 1989.

34. T. Brabec and F. Krausz, "Intense few-cycle laser fields: Frontiers of nonlinear optics", *Rev. Mod. Phys.,* **72**, 545, 2000.

35. G. G. Paulus, F. Grasbon, H. Walther, P. Villoresi, M. Nisoli, S. Stagira, E. Priori and S. De Silvestri, "Absolute-phase phenomena in photoionization with few-cycle laser pulses", *Nature,* **414**, 182, 2001.

36. U. Keller, K. J. Weingarten, F. X. Kärtner, D. Kopf, B. Braun, I. D. Jung, R. Fluck, C. Hönninger, N. Matuschek and J. Aus der Au, "Semiconductor saturable absorber mirrors (SESAMs) for femtosecond to nanosecond pulse generation in solid-state lasers", *IEEE J. Sel. Top. Quant. Elect.,* **2**, 435, 1996.

37. S. Tsuda, W. H. Knox, S. T. Cundiff, W. Y. Jan and J. E. Cuningham, "Mode-locked ultrafast solid-state lasers with saturable Bragg reflectors", *IEEE J. Sel. Top. Quant. Elect.,* **2**, 454, 1996.

38. I. D. Jung, F. X. Kärtner, N. Matuschek, D. H. Sutter, F. Morier-Genoud, Z. Shi, V. Scheuer, M. Tilsch, T. Tschudi and U. Keller, "Semiconductor saturable absorber mirrors supporting sub-10 fs pulses", *Appl. Phys. B,* **65**, 137, 1997.

39. F. X. Kärtner, I. D. Jung and U. Keller, "Soliton modelocking with saturable absorbers", *IEEE J. Sel. Top. Quant. Elect.,* **2**, 540, 1996.

40. D. H. Sutter, G. Steinmeyer, L. Gallmann, N. Matuschek, F. Morier-Genoud, U. Keller, V. Scheuer, G. Angelow and T. Tschudi, "Semiconductor saturable-absorber mirror assisted Kerr-lens mode-locked Ti:sapphire laser producing pulses in the two-cycle regime", *Opt. Lett.,* **24**, 631, 1999.

41. S. Tsuda, W. H. Knox, E. A. d. Souza, W. Y. Jan and J. E. Cunningham, "Femtosecond self-starting passive mode locking using an AlAs/AlGaAs intracavity saturable Bragg reflector," *Conference on Lasers and Electro-Optics*, talk CWM6, 1995.

42. V. P. Yanovsky, A. Korytin, F. Wise, A. Cassanho and H. Jenssen, "Femtosecond diode-pumped Cr: LiSGAF lasers", *IEEE J. Sel. Top. Quant. Elect.,* **2**, 465, 1996.

43. Z. Zhang, K. Torizuka, T. Itatani, K. Kobayashi, T. Sugaya, T. Nakagawa and H. Takahashi, "Broadband semiconductor saturable-absorber mirror for a self-starting mode-locked Cr:forsterite laser", *Opt. Lett.,* **23**, 1465, 1998.

44. D. J. Ripin, J. T. Gopinath, H. M. Shen, A. A. Erchak, G. S. Petrich, L. A. Kolodziejski, F. X. Kartner and E. P. Ippen, "Oxidized GaAs/AlAs mirror with a quantum-well saturable absorber for ultrashort-pulse Cr4+:YAG laser", *Opt. Comm.,* **214**, 285, 2002.

45. I. P. Bilinsky, J. G. Fujimoto, J. N. Walpole and L. J. Misaggia, "Semiconductor-doped silica saturable absorber films for solid state laser mode locking", *Opt. Lett.,* **23**, 1766, 1998.

46. I. P. Bilinsky, J. G. Fujimoto, J. N. Walpole and L. J. Misaggia, "InAs-doped silica films for saturable absorber applications", *Appl. Phys. Lett.,* **74**, 2411, 1999.

47. A. E. Siegman. *Lasers* (University Science Books, Mill Valley, California, 1986).

48. W. Siebert. *Circuits, signals and systems* (MIT Press, Cambridge, MA, 1986).

49. S. T. Cundiff, "Phase stabilization of ultrashort optical pulses", *J. Phys. D,* **35**, R43, 2002.

50. H. A. Haus, "Mode-locking of lasers", *IEEE J. Sel. Top. in Quant. Elect.,* **6**, 1173, 2000.

51. J. A. Valdmanis, R. L. Fork and J. P. Gordon, "Generation of optical pulses as short as 27 fs directly from a laser balancing self-phase modulation, group-velocity dispersion, saturable absorption, and saturable gain", *Opt. Lett.,* **10**, 131, 1985.

52. H. A. Haus, "Theory of mode locking with a slow saturable absorber", *IEEE J. Quant. Elect.,* **11**, 736, 1975.

53. A. Owyoung, R. W. Hellwarth and N. George, "Intensity-induced changes in optical polarization in glasses", *Phys. Rev. B,* **12**, 628, 1972.

54. J.-C. Diels and W. Rudolph. *Ultrashort Laser Pulse Phenomena* (Academic Press, Boston, 1996).

55. I. P. Christov, M. M. Murnane, H. C. Kapteyn, J. Zhou and C. P. Huang, "Fourth-order dispersion-limited solitary pulses", *Opt. Lett.,* **19**, 1465 1994.

56. D. H. Sutter. *New frontiers of ultrashort pulse generation*, Dept. of Physics, Swiss Federal Institute of Technology, 2000.

57. G. P. Agrawal. *Nonlinear Fiber Optics* (Academic Press, Inc., 1989).

58. F. X. Kärtner, J. A. d. Au and U. Keller, "Mode-locking with slow and fast saturable absorbers - what's the difference?" *IEEE J. Sel. Top. Quant. Elect.,* **4**, 159, 1998.

59. H. A. Haus, "Theory of modelocking with a fast saturable absorber", *J. Appl. Phys.,* **46**, 3049, 1975.

60. H. A. Haus, J. G. Fujimoto and E. P. Ippen, "Structures for additive pulse modelocking", *J. Opt. Soc. Am. B,* **8**, 2068, 1991.

61. H. A. Haus, J. G. Fujimoto and E. P. Ippen, "Analytic theory of additive pulse and Kerr lens mode locking", *IEEE J. Quant. Elect..* **28**, 2086, 1992.

62. O. E. Martinez, R. L. Fork and J. P. Gordon, "Theory of passively modelocked lasers including self-phase modulation and group-velocity dispersion", *Opt. Lett.,* **9**, 156, 1984.

63. C. Spielmann, P. F. Curley, T. Brabec and F. Krausz, "Ultrabroadband femtosecond lasers", *IEEE J. Quant. Elect.,* **30**, 1100, 1994.

64. Y. Chen, F. X. Kärtner, U. Morgner, S. H. Cho, H. A. Haus, J. G. Fujimoto and E. P. Ippen, "Dispersion managed mode-locking", *J. Opt. Soc. Am. B,* **16**, 1999, 1999.

65. D. Huang, M. Ulman, L. H. Acioli, H. A. Haus and J. G. Fujimoto, "Self-focusing-induced saturable loss for laser mode locking", *Opt. Lett.,* **17**, 511, 1992.

66. T. Brabec, P. F. Curley, C. Spielmann, E. Wintner and A. J. Schmidt, "Hard-aperture Kerr-lens mode locking", *J. Opt. Soc. Am. B,* **10**, 1029, 1993.

67. G. Cerullo, S. De Silvestri and V. Magni, "Self-starting Kerr lens mode-locking of a Ti:sapphire laser", *Opt. Lett.,* **19**, 1040, 1994.

68. G. Cerullo, S. De Silvestri, V. Magni and L. Pallaro, "Resonators for Kerr-lens mode-locked femtosecond Ti:sapphire lasers", *Opt. Lett.,* **19**, 807, 1994.

69. E. P. Ippen, L. Y. Liu and H. A. Haus, "Self-starting condition for additive-pulse modelocked lasers", *Opt. Lett.,* **15**, 183, 1990.

70. F. Krausz, T. Brabec and C. Spielmann, "Self-starting passive modelocking", *Opt. Lett.,* **16**, 235, 1991.

71. H. A. Haus and E. P. Ippen, "Self-starting of passively mode-locked lasers", *Opt. Lett.,* **16**, 1331, 1991.

72. I. D. Jung, F. X. Kärtner, L. R. Brovelli, M. Kamp and U. Keller, "Experimental verification of soliton modelocking using only a slow saturable absorber", *Opt. Lett.,* **20**, 1892, 1995.

73. F. X. Kärtner and U. Keller, "Stabilization of soliton-like pulses with a slow saturable absorber", *Opt. Lett.,* **20**, 16, 1995.

74. F. X. Kärtner, L. R. Brovelli, D. Kopf, M. Kamp, I. Calasso and U. Keller, "Control of solid-state laser dynamics by semiconductor devices", *Opt. Eng.,* **34**, 2024, 1995.

75. R. Fluck, I. D. Jung, G. Zhang, F. X. Kärtner and U. Keller, "Broadband saturable absorber for 10 fs pulse generation", *Opt. Lett.,* **21**, 743, 1996.

76. H. Haug and S. W. Koch. *Quantum theory of the optical and electronic properties of semiconductors* (World Scientific, Singapore, 1993).

77. H. A. Haus, "Parameter ranges for cw passive modelocking", *IEEE J. Quant. Elect.,* **12**, 169, 1976.

78. J. Shah. *Ultrafast spectroscopy of semiconductors and semiconductor nanostructures* (Springer Verlag, Berlin, 1996).

79. S. T. Cundiff, W. H. Knox, E. P. Ippen and H. A. Haus, "Frequency dependent mode size in broadband Kerr-lens mode locking", *Opt. Lett.,* **21**, 662, 1996.

80. L. Xu, G. Tempea, A. Poppe, M. Lenzner, C. Spielmann, F. Krausz, A. Stingl and K. Ferencz, "High-power sub-10-fs Ti:sapphire oscillators", *Appl. Phys. B,* **65**, 151, 1997.

81. H. A. Haus. *Waves and fields in optoelectronics* (Prentice Hall, Inc., Englewood Cliffs, NJ, 1984).

82. H. W. Kogelnik, E. P. Ippen, A. Dienes and C. V. Shank, "Astigmatically compensated cavities for cw dye lasers", *IEEE J. Quant. Elect.,* **8**, 373, 1972.

83. E. B. Treacy, "Optical pulse compression with diffraction gratings", *IEEE J. Quant. Elect.,* **5**, 454, 1969.

84. R. L. Fork, O. E. Martinez and J. P. Gordon, "Negative dispersion using pairs of prisms", *Opt. Lett.,* **9**, 150, 1984.

85. J. Zhou, G. Taft, C.-P. Huang, M. M. Murnane, H. C. Kapteyn and I. P. Christov, "Pulse evolution in a broad-bandwidth Ti:sapphire laser", *Opt. Lett.,* **19**, 1149, 1994.

86. Z. Zhang, K. Torizuka, T. Itatani, K. Kobayashi, T. Sugaya and T. Nakagawa, "Femtosecond Cr:forsterite laser with modelocking initiated by a quantum well saturable absorber", *IEEE J. Quant. Elect.,* **33**, 1975, 1997.

87. S. Uemura, "Dispersion compensation for a femtosecond Cr:LiSAF laser", *Jap. J. Appl. Phys.,* **37**, 133, 1998.

88. P. C. Wagenblast, U. Morgner, F. Grawert, T. R. Schibli, F. X. Kartner, V. Scheuer, G. Angelow and M. J. Lederer, "Generation of sub-10-fs-pulses from a Kerr-lens mode

locked Cr3+:LiCAF laser oscillator using third order dispersion compensating double-chirped mirrors", *Opt. Lett.*, **27**, 1726, 2002.

89. D. Ripin. *A few cycle Cr^{4+}:YAG laser and optical studies of photonic crystals*, Dept. of Physics, MIT, 2002.

90. U. Morgner, F. X. Kärtner, S. H. Cho, H. A. Haus, J. G. Fujimoto, E. P. Ippen, V. Scheuer, G. Angelow and T. Tschudi, "Sub-two cycle pulses from a Kerr-Lens modelocked Ti:sapphire laser", *Opt. Lett.*, **24**, 411 1999.

91. C. Chudoba, J. G. Fujimoto, E. P. Ippen, H. A. Haus, U. Morgner, F. X. Kärtner, V. Scheuer, G. Angelow and T. Tschudi, "All-solid-state Cr:forsterite laser generating 14 fs pulses at 1.3 um", *Opt. Lett.*, **26**, 292, 2001.

92. N. Matuschek, F. X. Kärtner and U. Keller, "Theory of double-chirped mirrors", *IEEE J. Sel. Top. Quant. Elect.*, **4**, 197, 1998.

93. R. Szipöcs, K. Ferencz, C. Spielmann and F. Krausz, "Chirped multilayer coatings for broadband dispersion control in femtosecond lasers", *Opt. Lett.*, **19**, 201, 1994.

94. R. Szipöcs and A. Kohazi-Kis, "Theory and design of chirped dielectric laser mirrors", *Appl. Phys. B*, **65**, 115, 1997.

95. L. Xu, C. Spielmann, F. Krausz and R. Szipöcs, "Ultrabroadband ring oscillator for sub-10-fs pulse generation", *Opt. Lett.*, **21**, 1259, 1996.

96. N. Matuschek, F. X. Kärtner and U. Keller, "Exact coupled-mode theories for multilayer interference coatings with arbitrary strong index modulations", *IEEE J. Quant. Elect.*, **33**, 295, 1997.

97. F. X. Kärtner, N. Matuschek, T. Schibli, U. Keller, H. A. Haus, C. Heine, R. Morf, V. Scheuer, M. Tilsch and T. Tschudi, "Design and fabrication of double-chirped mirrors", *Opt. Lett.*, **22**, 831, 1997.

98. N. Matuschek, F. X. Kärtner and U. Keller, "Analytic design of double-chirped mirrors with custom tailored dispersion characteristics", *IEEE J. Quant. Elect.*, **5**, 129 1999.

99. K. Naganuma, K. Mogi and H. Yamada, "Group-delay measurement using the Fourier transform of an interferometric cross correlation generated by white light", *Opt. Lett.*, **15**, 393, 1990.

100. F. X. Kärtner, U. Morgner, T. R. Schibli, E. P. Ippen, J. G. Fujimoto, V. Scheuer, G. Angelow and T. Tschudi, "Ultrabroadband double-chirped mirror pairs for generation of octave spectra", *J. Opt. Soc. Am. B*, **18**, 882, 2001.

101. A. Baltuska, Z. Wei, M. S. Pshenichnikov, D. A. Wiersma and R. Szipöcs, "All-solid-state cavity dumped sub-5-fs laser", *Appl. Phys. B*, **65**, 175, 1997.

102. V. Magni, G. Cerullo and S. De Silvestri, "ABCD matrix analysis of propagation of gaussian beams through Kerr media", *Opt. Comm.,* **96**, 348, 1993.

103. V. Magni, G. Cerullo, S. De Silvestri and A. Monguzzi, "Astigmatism in Gaussian-beam self-focusing and in resonators for Kerr-lens mode locking", *J. Opt. Soc. Am. B,* **12**, 476, 1995.

104. B. E. Bouma and J. G. Fujimoto, "Compact Kerr-lens-mode-locked resonators", *Opt. Lett.,* **21**, Jan. 15, 1996.

105. T. Brabec, C. Spielmann, P. F. Curley and F. Krausz, "Kerr lens mode locking", *Opt. Lett.,* **17**, 1292, 1992.

106. M. Piché and F. Salin, "Self-mode locking of solid-state lasers without apertures", *Opt. Lett.,* **18**, 1041, 1993.

107. A. Penzkofer, M. Wittmann, M. Lorenz, E. Siegert and S. Macnamara, "Kerr lens effects in a folded-cavity four-mirror linear resonator", *Opt. and Quant. Elect.,* **28**, 423, 1996.

108. B. Bouma, M. Ramaswamy-Paye and J. G. Fujimoto, "Compact resonator designs for mode-locked solid-state lasers", *Appl. Phys. B,* **B65**, 213, 1997.

109. E. J. Grace, A. Ritsataki, P. M. W. French and G. H. C. New, "New optimization criteria for slit-apertured and gain-apertured KLM all-solid-state lasers", *Opt. Comm.,* **183**, 249, 2000.

110. M. Ramaswamy-Paye and J. G. Fujimoto, "Compact dispersion-compensating geometry for Kerr-lens mode-locked femtosecond lasers", *Opt. Lett.,* **19**, 1756, 1994.

111. A. Bartels, T. Dekorsy and H. Kurz, "Femtosecond Ti:sapphire ring laser with a 2-GHz repetition rate and its application in time-resolved spectroscopy", *Opt. Lett.,* **24**, 996, 1999.

112. S. Uemura and K. Torizuka, "Generation of 12-fs pulses from a diode-pumped Kerr-lens mode-locked Cr:LiSAF laser", *Opt. Lett.,* **24**, 780, 1999.

113. A. Sennaroglu, "Broadly tunable Cr^{4+}-doped lasers in the near infrared and visible", *Prog. Quant. Electr.,* **26**, 287, 2002.

114. A. Sennaroglu and B. Pekerten, "Experimental and numerical investigation of thermal effects in end-pumped Cr^{4+}:forsterite lasers near room temperature", *IEEE J. Quant. Elect.,* **34**, 1996, 1998.

115. Y. P. Tong, P. M. W. French, J. R. Taylor and J. G. Fujimoto, "All-solid-state femtosecond sources in the near infrared", *Opt. Comm.,* **136**, 3, 1997.

116. D. T. Reid, M. Padgett, C. McGowan, W. E. Sleat and W. Sibbett, "Light-emitting diodes as measurement devices for femtosecond laser pulses", *Opt. Lett.,* **22**, 233, 1997.

117. J. K. Ranka, A. L. Gaeta, A. Baltuska, M. S. Pshenichnikov and D. A. Wiersma, "Autocorrelation measurement of 6-fs pulses based on the two-photon-induced photocurrent in a GaAsP photodiode", *Opt. Lett.,* **22**, 1344, 1997.

118. I. D. Jung, F. X. Kärtner, J. Henkmann, G. Zhang and U. Keller, "High-dynamic-range characterization of ultrashort pulses", *Appl. Phys. B,* **65**, 307, 1997.

119. R. Trebino and D. J. Kane, "Using phase retrieval to measure the intensity and phase of ultrashort pulses: frequency-resolved optical gating", *J. Opt. Soc. Am. B,* **10** 1993.

120. D. J. Kane and R. Trebino, "Characterization of arbitrary femtosecond pulses using frequency-resolved optical gating", *IEEE J. Quant. Elect.,* **29** 1993.

121. R. Trebino, K. W. DeLong, D. N. Fittinghoff, J. Sweetser, M. A. Krumbügel and B. Richman, "Measuring ultrashort laser pulses in the time-frequency domain using frequency-resolved optical gating", *Rev. Sci. Instrum.,* **68**, 1 1997.

122. G. Taft, A. Rundquist, M. M. Murnane, I. P. Christov, H. C. Kapteyn, K. W. DeLong, D. N. Fittinghoff, M. A. Krumbugel, J. N. Sweetser and R. Trebino, "Measurement of 10-fs laser pulses", *IEEE J. Sel. Top. Quant. Elect.,* **2**, 575, 1996.

123. A. Baltuska, M. S. Pshenichnikov and D. A. Wiersma, "Second-harmonic generation frequency-resolved optical gating in the single-cycle regime", *IEEE J. Quant. Elect.,* **35**, 459, 1999.

124. C. Iaconis and I. A. Walmsley, "Spectral phase interferometry for direct electric-field reconstruction of ultrashort optical pulses", *Opt. Lett.,* **23**, 792, 1998.

125. C. Iaconis and I. A. Walmsley, "Self-referencing spectral interferometry for measuring ultrashort optical pulses", *IEEE J. Quant. Elect.,* **35**, 501, 1999.

126. L. Gallmann, D. H. Sutter, N. Matuschek, G. Steinmeyer, U. Keller, C. Iaconis and I. A. Walmsley, "Characterization of sub-6-fs optical pulses with spectral phase interferometry for direct electric-field reconstruction", *Opt. Lett.,* **24**, 1314, 1999.

127. U. Keller, D. A. B. Miller, G. D. Boyd, T. H. Chiu, J. F. Ferguson and M. T. Asom, "Solid-state low-loss intracavity saturable absorber for Nd:YLF lasers: an antiresonant semiconductor Fabry-Perot saturable absorber", *Opt. Lett.,* **17**, 505, 1992.

128. S. Tsuda, W. H. Knox, E. A. d. Souza, W. Y. Jan and J. E. Cunningham, "Low-loss intracavity AlAs/AlGaAs saturable Bragg reflector for femtosecond mode locking in solid-state lasers", *Opt. Lett.,* **20**, 1406, 1995.

129. I. D. Jung, F. X. Kärtner, N. Matuschek, D. H. Sutter, F. Morier-Genoud, G. Zhang, U. Keller, V. Scheuer, M. Tilsch and T. Tschudi, "Self-starting 6.5 fs pulses from a Ti:sapphire laser", *Opt. Lett.,* **22**, 1009, 1997.

130. J.-M. Hopkins, G. J. Valentine, B. Agate, A. J. Kemp, U. Keller and W. Sibbett, "Highly compact and efficient femtosecond Cr:LiSAF lasers", *IEEE J. Quant. Elect.*, **38**, 360, 2002.

131. B. Agate, B. Stormont, A. J. Kemp, C. T. A. Brown, U. Keller and W. Sibbett, "Simplified cavity designs for efficient and compact femtosecond Cr:LiSAF lasers", *Opt. Comm.*, **205**, 207, 2002.

132. M. N. Islam, E. R. Sunderman, C. E. Soccolich, I. Bar-Joseph, N. Sauer, T. Y. Chang and B. I. Miller, "Color center lasers passively mode locked by quantum wells", *IEEE J. Quant. Elect.*, **25**, 2454, 1989.

133. P. W. Smith, Y. Silberberg and D. A. B. Miller, "Modelocking of semiconductor diode lasers using saturable excitonic nonlinearities", *J. Opt. Soc. Am. B*, **2**, 1228, 1985.

134. L. R. Brovelli, U. Keller and T. H. Chiu, "Design and operation of antiresonant Fabry-Perot saturable semiconductor absorbers for mode-locked solid-state lasers", *J. Opt. Soc.Am. B*, **12**, 311, 1995.

135. S. Gupta, J. F. Whitaker and G. A. Mourou, "Ultrafast carrier dynamics in III-V semiconductors grown by molecular-beam epitaxy at very low substrate temperatures", *IEEE J. Quant. Elect.*, **28**, 2464, 1992.

136. A. J. Lochtefeld, M. R. Melloch, J. C. P. Chang and E. S. Harmon, "The role of point defects and arsenic precipitates in carrier trapping and recombination in low-temperature grown GaAs", *Appl. Phys. Lett.*, **69**, 1465, 1996.

137. P. W. E. Smith, S. D. Benjamin and H. S. Loka, "Tailoring of trap-related carrier dynamics in low-temperature-grown GaAs", *Appl. Phys. Lett.*, **71**, 1156, 1997.

138. B. C. Collings, J. B. Stark, S. Tsuda, W. H. Knox, J. E. Cunningham, W. Y. Jan, R. Pathak and K. Bergman, "Saturable Bragg reflector self-starting passive modelocking of a Cr^{4+}:YAG laser pumped with a diode-pumped Nd:YVO_4 laser", *Opt. Lett.*, **21**, 1171, 1996.

139. J. Aus der Au, D. Kopf, F. Morier-Genoud, M. Moser and U. Keller, "60-fs pulses from a diode-pumped Nd:glass laser", *Opt. Lett.*, **22**, 307, 1997.

140. C. Hönninger, G. Zhang, U. Keller and A. Giesen, "Femtosecond Yb:YAG laser using semiconductor saturable absorbers", *Opt. Lett.*, **20**, 2402, 1995.

141. I. D. Jung, L. R. Brovelli, M. Kamp, U. Keller and M. Moser, "Scaling of the antiresonant Fabry-Perot saturable absorber design toward a thin saturable absorber", *Opt. Lett.*, **20**, 1559, 1995.

142. S. Schon, M. Haiml, L. Gallmann and U. Keller, "GaAs absorber layer growth for broadband AlGaAs/flouride SESAMs", *J. Cryst. Growth*, **227**, 172, 2001.

143. D. Kopf, G. Zhang, R. Fluck, M. Moser and U. Keller, "All-in-one dispersion-compensating saturable absorber mirror for compact femtosecond laser sources", *Opt. Lett.,* **21**, 486, 1996.

144. G. J. Spuhler, S. Reffert, M. Haiml, M. Moser and U. Keller, "Output-coupling semiconductor-saturable absorber mirror", *Appl. Phys. Lett.,* **78**, 2733, 2001.

145. Z. Zhang, K. Torizuka, T. Itatani, K. Kobayashi, T. Sugaya and T. Nakagawa, "Self-starting mode-locked femtosecond forsterite laser with a semiconductor saturable-absorber mirror", *Opt. Lett.,* **22**, 1006, 1997.

146. Z. Zhang, K. Torizuka, T. Itatani, K. Kobayashi, T. Sugaya and T. Nakagawa, "Femtosecond Cr:forsterite laser with mode locking initiated by a quantum-well saturable absorber", *IEEE J. Quant. Elect.,* **33**, 1975, 1997.

147. D. Kopf, K. J. Weingarten, L. Brovelli, M. Kamp and U. Keller, "Diode-pumped 100-fs passively mode-locked Cr:LiSAF using an A-FPSA", *Opt. Lett.,* **19**, 2143, 1994.

148. D. Kopf, A. Prasad, G. Zhang, M. Moser and U. Keller, "Broadly tunable femtosecond Cr:LiSAF laser", *Opt. Lett.,* **22**, 621, 1997.

149. D. Kopf, G. Zhang, M. Moser, U. Keller, M. A. Emanuel, R. J. Beach and J. A. Skidmore, "High-power femtosecond diode-pumped Cr:LiSAF laser," *Advanced Solid-State Lasers,* 1997.

150. D. Kopf, U. Keller, M. A. Emanuel, R. J. Beach and J. A. Skidmore, "1.1-W cw Cr:LiSAF laser pumped by a 1-cm diode-array", *Opt. Lett.,* **22**, 99, 1997.

151. N. Sarukura, Y. Ishida, T. Yanagawa and H. Nakano, "All solid-state cw passively mode-locked Ti:sapphire laser using a colored glass filter", *Appl. Phys. Lett.,* **57**, 229, 1990.

152. P. T. Guerreiro, S. Ten, N. F. Borrelli, J. Butty, G. E. Jabbour and N. Peyghambarian, "PbS quantum-dot doped glasses as saturable absorbers for mode locking of a Cr:forsterite laser", *Appl. Phys. Lett.,* **71**, 1595, 1997.

153. I. P. Bilinsky, R. P. Prasankumar and J. G. Fujimoto, "Self-starting mode locking and Kerr-lens mode locking of a Ti:Al_2O_3 laser by use of semiconductor-doped glass structures", *J. Opt. Soc. Am. B,* **16**, 546, 1999.

154. I. P. Bilinsky. *Novel saturable absorber materials and devices for laser modelocking*, Dept. of Physics, Massachusetts Institute of Technology, 1999.

155. K. Tsunetomo, H. Nasu, H. Kitayama, A. Kawabuchi, Y. Osaka and K. Takiyama, "Quantum size effect of semiconductor microcrystallites doped in SiO2-glass thin films prepared by RF-sputtering", *Jap. J. Appl. Phys.,* **28**, 1928, 1989.

156. K. Tsunetomo, M. Yamamoto and Y. Osaka, "CuCl microcrystallite-doped SiO_2 glass thin films prepared by RF sputtering", *Jap. J. Appl. Phys.,* **30**, L764, 1991.

157. S. Kaneko, H. Nasu, T. Ikegami, J. Matsuoka and K. Kamiya, "Effect of preparation conditions on the properties of CdSe microcrystal-doped SiO_2 glass thin films prepared by RF-sputtering", *Jap. J. Appl. Phys.,* **31**, 2206, 1992.

158. R. P. Prasankumar. *Novel saturable absorber devices grown using RF and magnetron RF sputtering*, Dept. of Electrical Engineering and Computer Science, MIT, 1999.

159. L. K. Smith, S. A. Payne, W. L. Kway, L. L. Chase and B. H. T. Chai, "Investigation of the Laser Properties of Cr^{3+}:$LiSrGaF_6$", *IEEE J. Quant. Elect.,* **28**, 2612, 1992.

160. S. A. Payne, L. L. Chase, H. W. Newkirk, L. K. Smith and W. F. Krupke, "Cr:LiCAF: a promising new solid-state laser material", *IEEE J. Quant. Elect.,* **24**, 2243, 1988.

161. S. A. Payne, L. L. Chase, L. K. Smith, W. L. Kway and H. Newkirk, "Laser performance of $LiSrAlF_6$:Cr^{3+}", *J. Appl. Phys.,* **66**, 1051, 1989.

162. A. Miller, P. LiKamWa, B. H. T. Chai and E. W. V. Stryland, "Generation of 150-fs tunable pulses in Cr:LiSAF", *Opt. Lett.,* **17**, 195, 1992.

163. J. M. Evans, D. E. Spence, W. Sibbett, B. H. T. Chai and A. Miller, "50-fs pulse generation from a self-mode-locked Cr:LiSrAlF6 laser", *Opt. Lett.,* **17**, 1447, 1992.

164. P. LiKamWa, B. H. T. Chai and A. Miller, "Self-mode-locked Cr^{3+}:$LiCaAlF_6$ laser", *Opt. Lett.,* **17**, 1438, 1992.

165. N. H. Rizvi, P. M. W. French and J. R. Taylor, "50-fs pulse generation from a self-starting cw passively mode-locked Cr:LiSrAlF6 laser", *Opt. Lett.,* **17**, 877, 1992.

166. N. H. Rizvi, P. M. W. French and J. R. Taylor, "Generation of 33-fs pulses from a passively mode-locked Cr^{3+}:$LiSrAlF_6$ laser", *Opt. Lett.,* **17**, 1605, 1992.

167. I. T. Sorokina, E. Sorokin, E. Wintner, A. Cassanho, H. P. Jenssen and M. A. Noginov, "Efficient cw TEM00 and femtosecond Kerr-lens modelocked Cr:LiSrGaF laser", *Opt. Lett.,* **21**, 204, 1996.

168. I. T. Sorokina, E. Sorokin, E. Wintner, A. Cassanho, H. P. Jenssen and R. Szipöcs, "Sub-20 fs pulse generation from the mirror dispersion controlled Cr:LiSGaF and Cr:LiSAF lasers", *Appl. Phys. B,* **65**, 245, 1997.

169. I. T. Sorokina, E. Sorokin, E. Wintner, A. Cassanho, H. P. Jenssen and R. Szipocs, "14-fs pulse generation in Kerr-lens mode-locked prismless Cr:LiSGaF and Cr:LiSAF lasers: observation of pulse self-frequency shift", *Opt. Lett.,* **22**, 1716, 1997.

170. P. M. W. French, R. Mellish and J. R. Taylor, "Modelocked all-solid-state diode-pumped Cr:LiSAF laser", *Opt. Lett.,* **18**, 1934, 1993.

171. M. J. P. Dymott and A. I. Ferguson, "Self-mode-locked diode-pumped Cr:LiSAF laser", *Opt. Lett.,* **19**, 1988, 1994.

172. M. J. P. Dymott and A. I. Ferguson, "Self-mode-locked diode-pumped Cr:LiSAF laser producing 34-fs pulses at 42-mW average power", *Opt. Lett.,* **20**, 1157, 1995.

173. F. Falcoz, F. Balembois, P. Georges and A. Brun, "Self-starting self-mode-locked femtosecond diode-pumped Cr:LiSAF laser", *Opt. Lett.,* **20**, 1874, 1995.

174. S. Uemura and K. Torizuka, "Development of a diode-pumped Kerr-lens mode-locked Cr:LiSAF laser", *IEEE J. Quant. Elect.,* **39**, 68, 2003.

175. V. P. Yanovsky, F. W. Wise, A. Cassanho and H. P. Jenssen, "Kerr-lens mode-locked diode-pumped Cr:LiSGAF laser", *Opt. Lett.,* **20**, 1304, 1995.

176. K. Gäbel, P. Ruβbüldt, R. Lebert, P. Loosen, R. Poprawe, H. Heyer and A. Valster, "Diode pumped, chirped mirror dispersion compensated, fs-laser", *Opt. Comm.,* **153**, 275, 1998.

177. K. Gäbel, P. Ruβbüldt, R. Lebert and A. Valster, "Diode pumped Cr^{3+}:LiCAF fs-laser", *Optics Communications,* **157**, 327, 1998.

178. S. Uemura and K. Torizuka, "Characteristics of 10-fs diode-pumped Kerr-lens mode-locked Cr:LiSAF and Cr:LiSGAF lasers," *Conference on Lasers and Electro-Optics*, talk CME6, 2002.

179. P. C. Wagenblast, U. Morgner, F. Grawert and F. X. Kartner, "12 fs, diode-pumped Cr^{3+}:LiCAF laser," *to be presented, Conference on Laser and Electro-Optics,* 2003.

180. G. J. Valentine, J.-M. Hopkins, P. Loza-Alvarez, G. T. Kennedy, W. Sibbett, D. Burns and A. Valster, "Ultralow-pump-threshold, femtosecond Cr^{3+}:$LiSrAlF_6$ laser pumped by a single narrow-stripe AlGaInP laser diode", *Opt. Lett.,* **22**, 1639, 1997.

181. J.-M. Hopkins, G. J. Valentine, W. Sibbett, J. Aus der Au, F. Morier-Genoud, U. Keller and A. Valster, "Efficient, low-noise, SESAM-based femtosecond Cr^{3+}:$LiSrAlF_6$ laser", *Opt. Comm.,* **154**, 54, 1998.

182. B. Agate, A. J. Kemp, C. T. A. Brown and W. Sibbett, "Efficient, high-repetition rate femtosecond blue source using a compact Cr:LiSAF laser", *Opt. Express,* **10**, 824, 2002.

183. A. A. Ivanov, B. I. Minkov, G. Jonuauskas, J. Oberle and C. Rulliere, "Influence of Cr^{4+} ion concentration on cw operation of forsterite laser and its relation to thermal problems", *Opt. Comm.,* **116**, 131, 1995.

184. R. Holzwarth, M. Zimmerman, T. Udem, T. W. Hansch, P. Russbuldt, K. Gabel, R. Poprawe, J. C. Knight, W. J. Wadsworth and P. S. J. Russell, "White light frequency comb generation with a diode-pumped Cr:LiSAF laser", *Opt. Lett.,* **26**, 1376, 2001.

185. S. A. Payne, W. F. Krupke, L. K. Smith, W. L. Kway, L. D. DeLoach and J. B. Tassano, "752 nm Wing-Pumped Cr:LiSAF laser", *IEEE J. Quant. Elect.,* **28**, 1188, 1992.

186. S. H. Cho, B. E. Bouma, E. P. Ippen and J. G. Fujimoto, "Low-repetition-rate high-peak power Kerr-lens mode-locked Ti:Al_2O_3 laser using a multiple-pass cavity", *Opt. Lett.,* **24**, 417, 1999.

187. S. H. Cho, F. X. Kärtner, U. Morgner, E. P. Ippen, J. G. Fujimoto, J. E. Cunningham and W. Knox, "Generation of 90-nJ pulses with a 4 MHz repetition rate Kerr-lens mode-locked Ti:Al_2O_3 laser operating with net positive and negative intracavity dispersion", *Opt. Lett.,* **26**, 560, 2001.

188. D. Herriott, H. Kogelnik and R. Kompfner, "Off-axis paths in spherical mirror interferometers", *Appl. Opt.,* **3**, 523, 1964.

189. D. Herriott and H. J. Schulte, "Folded optical delay lines", *Appl. Opt.,* **4**, 883, 1965.

190. P.-L. Hsiung. *High-speed path length scanning for optical coherence tomography*, Dept. of Dept. of Electrical Engineering and Computer Science, MIT, 2000.

191. A. Sennaroglu and J. G. Fujimoto, "Design criteria for Herriott-type multi-pass cavities for ultrashort pulse laser", *Opt. Express,* **11**, 1106, 2003.

192. R. P. Prasankumar, Y. Hirakawa, A. M. Kowalewicz, F. X. Kartner, J. G. Fujimoto, U. Morgner and W. Knox, "An 8.6 MHz extended cavity femtosecond Cr:LiSAF laser pumped by single spatial mode diodes," *Conference on Lasers and Electro-optics, talk CFA2,* 2003.

193. R. P. Prasankumar, Y. Hirakawa, A. M. Kowalevicz, F. X. Kaertner, J. G. Fujimoto and W. Knox, "An extended cavity femtosecond Cr:LiSAF laser pumped by low cost diode lasers", *Optics Express, to be published,* 2003.

194. D. Kopf, F. X. Kärtner, K. J. Weingarten and U. Keller, "Diode-pumped modelocked Nd:glass lasers using an A-FPSA", *Opt. Lett.,* **20**, 1169, 1995.

195. A. Imamoglu. The optical properties of nanoshells. *Opt. and Photon. News* **13**, 22 (2002).

196. D. Gammon and D. G. Steel. Optical studies of single quantum dots. *Phys. Today* **55**, 36 (2002).

197. P. M. Petroff, A. Lorke and A. Imamoglu. Epitaxially self-assembled quantum dots. *Phys. Today*, 46 (2001).

198. H. J. Eisler, V. C. Sundar, M. G. Bawendi, M. Walsh, H. I. Smith and V. Klimov, "Color-selective semiconductor nanocrystal laser", *Appl. Phys. Lett.,* **80**, 4614, 2002.

199. D. Bimberg, N. Kirstaedter, N. N. Ledentsov, Z. I. Alferov, P. S. Kop'ev and V. M. Ustinov, "InGaAs-GaAs quantum dot lasers", *IEEE J. Sel. Top. Quant. Electron.,* **3**, 196, 1997.

200. G. Chen, N. H. Bonadeo, D. G. Steel, D. Gammon, D. S. Katzer, D. Park and L. J. Sham, "Optically induced entanglement of excitons in a single quantum dot", *Science,* **289**, 1906, 2000.

201. D. P. DiVincenzo, "Real and realistic quantum computers", *Nature,* **393**, 113, 1998.

202. L. Banyai and S. W. Koch. *Semiconductor quantum dots* (World Scientific, Singapore, 1993).

203. U. Woggon. *Optical properties of semiconductor quantum dots* (Springer, Berlin, 1996).

204. P. Maly, "Ultrafast laser spectroscopy of semiconductor nanocrystals", *Czech. J. Phys.,* **52**, 645, 2002.

205. N. W. Ashcroft and N. D. Mermin. *Solid state physics* (Saunders College Publishing, Fort Worth, 1976).

206. M. S. Dresselhaus. *6.732 course notes, Physics of Solids II* (Massachusetts Institute of Technology, Cambridge, MA, 2001).

207. N. Peyghambarian, S. W. Koch and A. Mysyrowicz. *Introduction to semiconductor optics* (Prentice Hall, Englewood Cliffs, New Jersey, 1993).

208. V. I. Klimov, A. A. Mikhailovsky, S. Xu, A. Malko, J. A. Hollingsworth, C. A. Leatherdale, H.-J. Eisler and M. G. Bawendi, "Optical gain and stimulated emission in nanocrystal quantum dots", *Science,* **290**, 314, 2000.

209. J. J. Sakurai. *Modern quantum mechanics* (ed. S. F. Tuan) (Addison-Wesley, Reading, MA, 1994).

210. D. J. Griffiths. *Introduction to quantum mechanics* (Prentice-Hall, Englewood Cliffs, NJ, 1995).

211. S. Schmitt-Rink, D. A. B. Miller and D. S. Chemla, "Theory of the linear and nonlinear optical properties of semiconductor microcrystallites", *Phys. Rev. B,* **35**, 8113, 1987.

212. L. Brus, "Quantum crystallites and nonlinear optics", *Appl. Phys. A,* **53**, 465, 1991.

213. A. L. Efros and A. L. Efros, "Interband absorption of light in a semiconductor sphere", *Sov. Phys. Semicond.,* **16**, 772, 1982.

214. L. E. Brus, "Electron-electron and electron-hole interactions in small semiconductor nanocrystals: The size dependence of the lowest excited electronic state", *J. Chem. Phys.,* **80**, 4403, 1984.

215. J. C. Maxwell-Garnett, *Philos. Trans. R. Soc. London,* **203**, 385, 1904.

216. A. Othonos, "Probing ultrafast carrier and phonon dynamics in semiconductors", *J. Appl. Phys.,* **83**, 1729, 1998.

217. O. D. Mücke, T. Tritschler, M. Wegener, U. Morgner and F. X. Kärtner, "Signatures of carrier-wave Rabi-flopping in GaAs", *Phys. Rev. Lett.*, **87**, (057401, 2001.

218. H. Haug and A.-P. Jauho. *Quantum kinetics in transport and optics of semiconductors* (Springer, Berlin, 1996).

219. N. Peyghambarian, B. Fluegel, D. Hulin, A. Migus, M. Joffre, A. Antonetti, S. W. Koch and M. Lindberg, "Femtosecond optical nonlinearities of CdSe quantum dots", *IEEE J. Quant. Elect.*, **25**, 2516, 1989.

220. S. H. Park, R. A. Morgan, Y. Z. Hu, M. Lindberg, S. W. Koch and N. Peyghambarian, "Nonlinear optical properties of quantum-confined CdSe microcrystallites", *J. Opt. Soc. Am. B,* **7**, 2097, 1990.

221. G. Tamulaitis, V. Gulbinas, G. Kodis, A. Dementjev, L. Valkunas, I. Motchalov and H. Raaben, "Optical nonlinearities of glass doped with PbS nanocrystals", *J. Appl. Phys.*, **88**, 178, 2000.

222. U. Bocklemann and G. Bastard, "Phonon scattering and energy relaxation in two-, one-, and zero-dimensional electron gases", *Phys. Rev. B,* **42**, 8947, 1990.

223. T. Sosnowski, T. B. Norris, H. Jiang, J. Singh, K. Kamath and P. Bhattacharya, "Rapid carrier relaxation in $In_{0.4}Ga_{0.6}As$/GaAs quantum dots characterized by differential transmission spectroscopy", *Phys. Rev. B,* **57**, R9423, 1998.

224. U. Woggon, H. Giessen, F. Gindele, O. Wind, B. Fluegel and N. Peyghambarian, "Ultrafast energy relaxation in quantum dots", *Phys. Rev. B,* **54**, 17681, 1996.

225. V. I. Klimov and D. W. McBranch, "Femtosecond 1P-to-1S electron relaxation in strongly confined semiconductor nanocrystals", *Phys. Rev. Lett.*, **80**, 4028, 1998.

226. V. I. Klimov, D. W. McBranch, C. A. Leatherdale and M. G. Bawendi, "Electron and hole relaxation pathways in semiconductor quantum dots", *Phys. Rev. B,* **60**, 13740, 1999.

227. J. Urayama, T. B. Norris, J. Singh and P. Bhattacharya, "Observation of phonon bottleneck in quantum dot electronic relaxation", *Phys. Rev. Lett.*, **86**, 4930, 2001.

228. R. E. Hummel and K. H. Guenther. *Handbook of optical properties:Volume I, Thin films for optical coatings* (CRC Press, Boca Raton, FL, 1995).

229. R. F. Bunshah. *Handbook of deposition technologies for films and coatings* (Noyes Publications, Park Ridge, 1994).

230. N. F. Borrelli, D. W. Hall, H. J. Holland and D. W. Smith, "Quantum confinement effects of semiconducting microcrystallites in glass", *J. Appl. Phys.*, **61**, 5399, 1987.

231. P. Roussignol, D. Ricard, C. Flytzanis and N. Neuroth, "Phonon broadening and spectral hole burning in very small semiconductor particles", *Phys. Rev. Lett.,* **62**, 312, 1989.

232. Y. Kanemitsu, H. Tanaka, T. Kushida, K. S. Min and H. A. Atwater, "GaAs nanocrystals fabricated by sequential ion implantation: structural and luminescence properties", *Physica E,* **7**, 322, 2000.

233. M. L. Reed and J. D. Plummer, "Chemistry of Si-SiO_2 interface trap annealing", *J. Appl. Phys.,* **63**, 5776, 1988.

234. L. S. Wang, M. S. Lin, C. S. Yoo and F. S. Huang, "Improvement of oxide quality by rapid thermal annealing in N_2", *J. Appl. Phys.,* **74**, 3966, 1993.

235. K. L. Hall, G. Lenz, E. P. Ippen and G. Raybon, "Heterodyne pump-probe technique for time-domain studies of optical nonlinearities in waveguides", *Opt. Lett.,* **17**, 874, 1992.

236. J.-P. Foing, M. Joffre, J.-L. Oudar and D. Hulin, "Coherent effects in pump-probe experiments with chirped pump pulses", *J. Opt. Soc. Am. B,* **10**, 1143, 1993.

237. S. L. Palfrey and T. F. Heinz, "Coherent interactions in pump-probe absorption measurements: the effect of phase gratings", *J. Opt. Soc. Am. B,* **2**, 674, 1985.

238. R. P. Prasankumar, I. Hartl, J. T. Gopinath, E. P. Ippen, J. G. Fujimoto, P. Mak and M. F. Ruane, "Ultrafast dynamics of non-epitaxially grown semiconductor-doped silica film saturable absorbers," *Quantum Electronics and Laser Science Conference,* 2001.

239. S. Bourquin, R. P. Prasankumar, F. X. Kartner, J. G. Fujimoto, T. Lasser and R. P. Salathe, "High-speed femtosecond pump-probe spectroscopy using a smart pixel detector array", *Opt. Lett., to be published,* 2003.

240. S. Bourquin, P. Seitz and R. P. Salathe', "Two-dimensional smart detector array for interferometric applications", *Elect. Lett.,* **37**, 975, 2001.

241. S. Bourquin, P. Seitz and R. P. Salathe', "Optical coherence tomography based on a two-dimentional smart detector array", *Opt. Lett.,* **26**, 512, 2001.

242. W.-Z. Lin, R. W. Schoenlein, J. G. Fujimoto and E. P. Ippen, "Femtosecond absorption saturation studies of hot carriers in GaAs and AlGaAs", *IEEE J. Quant. Elect.,* **24**, 267, 1988.

243. R. W. Schoenlein, W. Z. Lin, E. P. Ippen and J. G. Fujimoto, "Femtosecond hot-carrier energy relaxation in GaAs", *Appl. Phys. Lett.,* **51**, 2134, 1987.

244. J. T. Gopinath. *The effect of proton bombardment on semiconductor saturable absorber structures*, Dept. of Electrical Engineering and Computer Science, MIT, 2000.

245. P. Langlois, M. Joschko, E. R. Thoen, E. M. Koontz, F. X. Kaertner, L. Kolodziejski and E. P. Ippen, "High fluence ultrafast dynamics of semiconductor saturable absorber mirrors", *Appl. Phys. Lett.,* **75**, 3841, 1999.

246. M. Joschko, P. Langlois, E. R. Thoen, E. M. Koontz, E. P. Ippen and L. Kolodziejski, "Ultrafast hot-carrier dynamics in semiconductor saturable absorber mirrors", *Appl. Phys. Lett.,* **76**, 1383, 2000.

247. J. T. Gopinath, E. R. Thoen, E. M. Koontz, M. E. Grein, L. Kolodziejski and E. P. Ippen, "Recovery dynamics in proton-bombarded semiconductor saturable absorber mirrors", *Appl. Phys. Lett.,* **78**, 3409, 2001.

248. E. R. Thoen, E. M. Koontz, M. Joschko, P. Langlois, T. R. Schiblil, F. X. Kaertner, E. P. Ippen and L. Kolodziejski, "Two-photon absorption in semiconductor saturable absorber mirrors", *Appl. Phys. Lett.,* **74**, 3927, 1999.

249. I. Tanahashi, A. Tsujimura, T. Mitsuyu and A. Nishino, "Optical properties of CdS microcrystallite-doped SiO_2 glass thin films", *Jap. J. Appl. Phys.,* **29**, 2111, 1990.

250. J. Shi, K. Zhu, W. Yao and L. Zhang, "Growth of InAs nanocrystals embedded in SiO_2 films by radio-frequency magnetron cosputtering", *J. Crystal Growth,* **186**, 480, 1998.

251. D. W. Hall and N. F. Borrelli, "Absorption saturation in commercial and quantum-confined $CdSe_xS_{1-x}$-doped glasses", *J. Opt. Soc. Am. B,* **5**, 1650, 1988.

252. W. D. Callister. *Materials science and engineering: an introduction* (John Wiley, New York, 2003).

253. L. H. Van Vlack. *Elements of materials science* (Addison-Wesley, Reading, 1964).

254. H. Nasu, J. Matsuoka and K. Kamiya, "Preparation and optical properties of semiconductor-microcrystal-doped SiO_2 glass thin films by rf-sputtering", *J. Non-Cryst. Solids,* **178**, 148, 1994.

255. B. D. Cullity. *Elements of x-ray diffraction* (Addison-Wesley, Reading Menlo Park, 1980).

256. H. P. Klug and L. E. Alexander. *X-ray diffraction procedures* (John Wiley & Sons, New York, 1974).

257. P. Borri, W. Langbein, S. Schneider, U. Woggon, R. L. Sellin, D. Ouyang and D. Bimberg, "Exciton relaxation and dephasing in quantum-dot amplifiers from room to cryogenic temperature", *IEEE J. Sel. Top. Quant. Elect.,* **8**, 984, 2003.

258. G. L. Huang and H. S. Kwok, "Femtosecond dephasing times in semiconductor microcrystals measured with incoherent light", *J. Opt. Soc. Am. B,* **9**, 2019, 1992.

259. L. H. Acioli, A. S. L. Gomes, J. M. Hickmann and C. B. de Araujo, "Femtosecond dynamics of semiconductor-doped glasses using a new source of incoherent light", *Appl. Phys. Lett.,* **56**, 2279, 1990.

260. R. W. Schoenlein, D. M. Mittleman, J. J. Shiang, A. P. Alivisatos and C. V. Shank, "Investigation of femtosecond electronic dephasing in CdSe nanocrystals using quantum-beat-suppressed photon echoes", *Phys. Rev. Lett.,* **70**, 1014, 1993.

261. D. M. Mittleman, R. W. Schoenlein, J. J. Shiang, V. L. Colvin, A. P. Alivisatos and C. V. Shank, "Quantum size dependence of femtosecond electronic dephasing and vibrational dynamics in CdSe nanocrystals", *Phys. Rev. B,* **49**, 14435, 1994.

262. U. Woggon and M. Portune, "Femtosecond dephasing in CdS quantum dots determined by nondegenerate four-wave mixing", *Phys. Rev. B,* **51**, 4719, 1995.

263. C. H. Brito Cruz, J. P. Gordon, P. C. Becker, R. L. Fork and C. V. Shank, "Dynamics of spectral hole burning", *IEEE J. Quant. Elect.,* **24**, 261, 1988.

264. R. Tsu, E. H. Nicollian and A. Reisman, "Passivation of defects in polycrystalline superlattices and quantum well structures", *Appl. Phys. Lett.,* **55**, 1897, 1989.

265. L. H. Ouyang, D. L. Rode, T. Zulkifli, B. Abraham-Shrauner, N. Lewis and M. R. Freeman, "Hydrogenated amorphous and microcrystalline GaAs prepared by radio-frequency magnetron sputtering", *J. Appl. Phys.,* **91**, 3459, 2002.

266. U. Woggon, M. Muller, I. Ruckmann, J. Kolenda and M. Petrauskas, "Influence of hydrogenation of defects at the microcrystallite-glass interface on the nonlinear optics of CdSe microcrystallites", *Phys. Stat. Sol.,* **160**, K79, 1990.

267. B. E. Bouma, G. J. Tearney, I. P. Bilinsky, B. Golubovic and J. G. Fujimoto, "Self-phase-modulated Kerr-lens mode-locked Cr:forsterite laser source for optical coherence tomography", *Opt. Lett.,* **21**, 1839, 1996.

268. A. Sennaroglu, "Continuous-wave broadly tunable intracavity frequency-doubled Cr^{4+}:forsterite laser", *IEEE J. Sel. Top. Quant. Elect.,* **8**, 474, 2002.

269. V. Petricevic, S. K. Gayen and R. R. Alfano, "Laser action in chromium-doped forsterite", *Appl. Phys. Lett.,* **52**, 1040, 1988.

270. B. Golubovic, B. E. Bouma, I. P. Bilinsky, J. G. Fujimoto and V. P. Mikhailov, "Thin crystal, room-temperature Cr^{4+}:forsterite laser using near-infrared pumping", *Opt. Lett.,* **21**, 1993, 1996.

271. V. Shcheslavskiy, V. V. Yakolev and A. Ivanov, "High-energy self-starting femtosecond Cr^{4+}:Mg_2SiO_4 oscillator operating at a low repetition rate", *Opt. Lett.,* **26**, 1999, 2001.

272. V. Petricevic, S. K. Gayen and R. R. Alfano, "Continuous-wave laser operation of chromium-doped forsterite", *Opt. Lett.,* **14**, 612, 1989.

273. J. M. Evans, V. Petricevic, A. B. Bykov, A. Delgado and R. R. Alfano, "Direct diode-pumped continuous-wave near-infrared tunable laser operation of Cr^{4+}:forsterite and Cr^{4+}:Ca_2GeO_4", *Opt. Lett.,* **22**, 1171, 1997.

274. A. Seas, V. Petricevic and R. R. Alfano, "Continuous-wave mode-locked operation of a chromium-doped forsterite laser", *Opt. Lett.,* **16**, 1668, 1991.

275. A. Seas, V. Petricevic and R. R. Alfano, "Self-mode-locked chromium-doped forsterite laser generates 50 fs pulses", *Opt. Lett.,* **18**, 891, 1993.

276. Y. Pang, V. Yanovsky, F. Wise and B. I. Minkov, "Self-mode-locked Cr:forsterite laser", *Opt. Lett.,* **18**, 1168, 1993.

277. V. Yanovsky, Y. Pang, F. Wise and B. I. Minkov, "Generation of 25-fs pulses from a self-modelocked Cr:forsterite laser with optimized group-delay dispersion", *Opt. Lett.,* **18**, 1541, 1993.

278. S. V. Kershaw, M. Harrison, A. L. Rogach and A. Kornowski, "Development of IR-emitting colloidal II-VI quantum-dot materials", *IEEE J. Sel. Top. Quant. Elect.,* **6**, 534, 2000.

279. T. R. Schibli, personal communication, 2002.

280. R. P. Prasankumar, C. Chudoba, J. G. Fujimoto, P. Mak and M. F. Ruane, "Self-starting mode locking in a Cr:forsterite laser by use of non-epitaxially-grown semiconductor-doped silica films", *Opt. Lett.,* **27**, 1564, 2002.

281. S. N. Tandon, J. T. Gopinath, T. R. Schibli, G. S. Petrich, L. A. Kolodziejski, F. X. Kaertner and E. P. Ippen, "Saturable absorbers with large area broadband Bragg reflectors for femtosecond pulse generation," *Conference on Lasers and Electro-Optics, talk CWM5,* 2003.

282. A. Sennaroglu, A. M. Kowalevicz, F. X. Kaertner and J. G. Fujimoto, "High performance, compact, prismless, low-threshold 30 MHz Ti:Al_2O_3 laser", *Opt. Lett., to be published,* 2003.

283. Y. S. Lee, T. Meade, T. B. Norris and A. Galvanauskas, "Tunable narrow-band terahertz generation from periodically poled lithium niobate", *Appl. Phys. Lett.,* **76**, 3583, 2001.

284. A. Isemann, H. Hundertmark and C. Fallnich, "Diode-pumped Cr:LiCAF fs regenerative amplifier system seeded by an Er-doped mode-locked fiber laser", *Appl. Phys. B,* **74**, 299, 2002.

285. L. Boivin, M. Wegmueller, M. C. Nuss and W. H. Knoz, "110 Channels x 2.35 Gb/s from a single femtosecond laser", *IEEE Photon. Tech. Lett.,* **11**, 466, 1999.

3571-79